

**Low-frequency local field potentials in primate motor cortex  
and their application to neural interfaces**

*Thomas Morley Hall*

Candidate: A9921268

Thesis submitted for the degree of:

*Doctor of Philosophy*

Institute of Neuroscience, Newcastle University

Supervisors:

Professor Andrew Jackson

Professor Stuart N. Baker

November 2017





# Abstract

For patients with spinal cord injury and paralysis, there are currently very limited options for clinical therapy. Brain-machine interfaces (BMIs) are neuroprosthetic devices that are being developed to record from the motor cortex in such patients, bypass the spinal lesion, and use decoded signals to control an effector, such as a prosthetic limb.

The ideal BMI would be durable, reliable, totally predictable, fully-implantable, and have generous battery life. Current, state-of-the-art BMIs are limited in all of these domains; partly because the typical signals used—neuronal action potentials, or ‘spikes’—are very susceptible to micro-movement of recording electrodes. Recording spikes from the same neurons over many months is therefore difficult, and decoder behaviour may be unpredictable from day-to-day. Spikes also need to be digitized at high frequencies ( $\sim 10^4$  Hz) and heavily processed. As a result, devices are energy-hungry and difficult to miniaturise. Low-frequency local field potentials (*lf*-LFPs;  $< 5$  Hz) are an alternative cortical signal. They are more stable and can be captured and processed at much lower frequencies ( $\sim 10^1$  Hz).

Here we investigate rhythmical *lf*-LFP activity, related to the firing of local cortical neurons, during isometric wrist movements in Rhesus macaques. Multichannel spike-related slow potentials (SRSPs) can be used to accurately decode the firing rates of individual motor cortical neurons, and subjects can control a BMI task using this synthetic signal, as if they were controlling the actual firing rate. *Lf*-LFP-based firing rate estimates are stable over time – even once actual spike recordings have been lost. Furthermore, the dynamics of *lf*-LFPs are distinctive enough, that an unsupervised approach can be used to train a decoder to extract movement-related features for use in biofeedback BMIs. Novel electrode designs may help us optimise the recording of these signals, and facilitate progress towards a new generation of robust, implantable BMIs for patients.

*T, A, D, R, S and U*  
*Ne obliviscamur*

# Acknowledgements

I'd mainly like to thank Andy Jackson – my supervisor and mentor. It's difficult to think of a single word of this thesis, a single line of MATLAB code, a single byte of data, a single embryonic idea, that would have been possible without his guidance. His extraordinary mind and work ethic are evident from his scientific record. And having worked with him for several years, I can also attest to his thoughtfulness, empathy, his desire to help people via his research, his level of care for his monkeys, and his patience (which I'm sure I've tested beyond sensible limits with this thesis). His recent promotion to Professor is well-deserved testament to his hard work, focus and leadership. Congratulations, Professor Jackson!

Secondly, I'd like to thank Jen Tulip: the other person without whom this thesis wouldn't have been possible. Always with a smile on her face; her work with the primates, and constant attention to their welfare, helped me to enjoy and value my time working with the monkeys.

Many thanks also to Stuart Baker, my second supervisor, and to Adrian Rees and Alex Thiele, for advising me at my progress review meetings. Thank you to Felipe De Carvalho, Wei Xu and Kia Nazarpour for assistance with monkeys and filter kernels! And a special thanks to Norman Charlton for his amazing skill with all things mechanical. The work described here was supported by a Research Studentship from the MRC, and Andy Jackson's laboratory (hence this work) is supported by the Wellcome Trust.

I've met and worked with so many brilliant people, both in Andy's lab and beyond, and I'd like to thank you all. To name but a few: Jonas, Kari, Claire S, D-mar, Ed, all of Bakerlab, Pradeep, Felix, 迪迪, Katherine, Bonne, and everyone in the CBC. Finally, a special thank-you to Sabine, and to all the amazing experiences we had together.

Things haven't been plain-sailing, and I'm eternally grateful to Mark and to my GP for their professional support. If any student or researcher reading this is feeling really down: do speak to someone. Heck, e-mail me if you need to ([thomasmhall@gmail.com](mailto:thomasmhall@gmail.com)).

Finally, I'd like to thank my family. I've lived with you while I've been writing up, and it's been so nice. I'm so grateful that you've been there to look after me, and feed me while I have no job, and read my thesis, and motivate me when I thought I would never get to the finish line. I couldn't have done it without you. I love you all!



# Declaration

I declare that this thesis has been written by me, that it represents my work (except, where indicated, other people's work being appropriately acknowledged), that it has not been submitted for any other degree or qualification, and that it has not been published elsewhere, other than in the peer-reviewed open-source articles listed below (on which I am an author).

— T M Hall, Newcastle upon Tyne, UK, November 2017

## Publications

### *Journal publications*

T M Hall, K Nazarpour, A Jackson (2014) Real-time estimation and biofeedback of single-neuron firing rates using local field potentials. *Nature Communications* **5**, doi:10.1038/ncomms6462.

T M Hall, F de Carvalho, A Jackson (2014). A common structure underlies low-frequency cortical dynamics in movement, sleep, and sedation. *Neuron* **83**(5), pp.1185–1199, doi:10.1016/j.neuron.2014.07.022.

A Jackson & T M Hall (2016) Decoding local field potentials for neural interfaces, *IEEE Transactions on Neural Systems and Rehabilitation Engineering* **99**, doi:10.1109/TNSRE.2016.2612001.

### *Peer-reviewed conference papers*

A Krasoulis, T M Hall, A Jackson, S Vijaykumar & K Nazarpour (2014). Generalizability of upper-limb muscle activity decoded using local field potentials. In *Proceedings of the IEEE Engineering in Medicine and Biology Society* **36**, Chicago USA, doi:10.1109/EMBC.2014.6943917



# Table of Contents

	<i>Page:</i>
Abstract.....	iii
Acknowledgements .....	v
Declaration.....	vii
Publications .....	vii
Table of Contents.....	ix
List of Figures.....	xiii
List of Tables .....	xvii
List of Equations.....	xviii
Chapter 1. General Introduction .....	1
1.1 Neural interfaces.....	1
1.1.1 Motivation .....	1
1.1.2 Invasive motor BMIs: current trends.....	6
1.1.3 Limitations of spike-controlled biomimetic BMIs .....	7
1.1.4 Biofeedback BMIs as an alternative to biomimetic BMIs .....	9
1.2 Local field potentials .....	10
1.2.1 Using LFPs as control signals for BMIs.....	11
1.2.2 LFPs during movement, and the rationale for studying low-frequency local field potentials (lf-LFPs) .....	13
1.2.3 Do lower signal frequencies actually permit lower power consumption?.....	16
1.3 Chapter summary.....	20
Chapter 2. General Methods .....	21
2.1 Subjects and behaviour .....	21
2.1.1 Non-human primate subjects .....	21
2.1.2 Wrist torque-controlled task .....	21
2.1.3 Brain-machine interface tasks .....	22
2.2 Electrode design and construction.....	24
2.2.1 Moveable tungsten microwire array .....	24

2.3	Surgical methods.....	26
2.3.1	Surgical planning .....	26
2.3.2	Surgical procedures.....	28
2.3.3	EMG electrode implantation.....	28
2.3.4	Cortical electrode implantation and transcutaneous titanium implant fixation	28
2.4	Electrophysiological recordings.....	30
2.4.1	TDT RZ2-based recording system.....	30
2.4.2	CED Power-1401–based recording system.....	30
2.4.3	EMG and task recording .....	31
2.5	Signal pre-processing and offline analysis.....	31
2.6	Statistical analysis .....	31
2.7	Chapter summary .....	31
Chapter 3. Spike-LFP relationships in motor cortex for use in BMI applications.....		33
3.1	Introduction.....	33
3.1.1	The low-frequency LFP (lf-LFP) during movement.....	33
3.1.2	Using the lf-LFP as a biofeedback BMI control signal .....	34
3.1.3	Modelling multichannel spike-LFP and LFP-spike relationships.....	35
3.2	Aims.....	36
3.3	Methods and Results .....	37
3.3.1	Experimental setup.....	37
3.3.2	Spike-triggered averaging of the LFP.....	37
3.3.3	The spike-related slow potential (SRSP) .....	39
3.3.4	Estimating low-frequency LFPs from neuronal firing rates .....	40
3.3.5	Estimating single-neuron firing rates from multiple lf-LFPs.....	46
3.4	Discussion .....	54
3.5	Chapter summary .....	59
Chapter 4. Stability, dimensionality and generalisation of LFP-based firing rate estimates, and their use in biofeedback BMIs .....		61
4.1	Introduction.....	61
4.1.1	Stability of LFP-based firing rate estimates.....	61
4.1.2	Dimensionality analysis of firing rate estimates .....	63
4.1.3	Generalisation and transferability of firing rate estimation .....	63
4.1.4	Biofeedback BMI using LFP-based firing rate estimates .....	64

4.2	Aims.....	65
4.3	Methods and Results.....	65
4.3.1	Stability of LFP-based firing rate estimates .....	65
4.3.2	Stability of trial-averaged LFP-based firing rate estimates .....	66
4.3.3	Dimensionality of LFP-based firing rate estimates .....	71
4.3.4	Generalisation and transferability of LFP-based estimation .....	76
4.3.5	Realtime biofeedback using LFP-based firing rate estimates .....	84
4.4	Discussion.....	89
4.5	Chapter summary.....	94
Chapter 5. Low-frequency cyclical cortical dynamics: exploring novel signals for BMIs .....		97
5.1	Introduction .....	97
5.1.1	Motivation .....	97
5.1.2	Multichannel lf-LFPs exhibit phase differences between channels .....	98
5.1.3	Wrist movements are correlated with realtime low-frequency cyclical activity in the lf-LFP.....	99
5.1.4	The importance of <u>local</u> lf-LFP sources and phase differences across electrodes 101	
5.1.5	Dynamical systems methods can be used to characterise these cyclical features 102	
5.1.6	The properties of these oscillations suggest that they reflect intrinsic dynamics of the motor cortex. ....	104
5.2	Aims.....	107
5.3	Methods and Results.....	108
5.3.1	Extracting dynamical features from multichannel lf-LFP —Motivation .....	108
5.3.2	‘jPCA’ approach.....	109
5.3.3	‘Areal velocity component’ (AVC)-based approach.....	112
5.3.4	Comparing the performance of AV-based approaches to conventional methods. 117	
5.3.5	Using areal velocity signals for biofeedback BMI control and exploring the underlying physiology of low-frequency cortical dynamics .....	129
5.4	Discussion.....	145
5.5	Chapter summary.....	154

Chapter 6. Hybrid geometric/moveable arrays for investigating the spatial nature of <i>lf</i> -LFPs in motor cortex.....	155
6.1 Introduction.....	155
6.2 Aims.....	158
6.3 Methods and Results.....	159
6.3.1 Hybrid electrode design and construction.....	159
6.3.2 Surgical implantation.....	161
6.3.3 Task and electrophysiological recording.....	161
6.3.4 Event-triggered average profiles across LMAs.....	162
6.3.5 Estimating neural firing rates with a minimal number of LFPs.....	164
6.4 Discussion.....	167
6.5 Chapter summary.....	169
Chapter 7. General Discussion.....	171
7.1 Summary and implications for the field.....	171
7.2 Future directions.....	175
References.....	177
Appendices.....	187
Appendix I: Specifications of dual “Long”-shank LMA.....	187
Appendix II: Specifications of dual “Short”-shank LMA.....	190
Indices.....	193
Index of acronyms and abbreviations.....	193
Conventions for mathematical variables.....	194
Index of common terms.....	194

# List of Figures

	<i>Page:</i>
<b>Figure 1-1</b> <i>A neuroprosthetic approach to spinal cord injury.</i> .....	2
<b>Figure 1-2</b> <i>LFP activity in the frequency domain, aligned to movement onset, averaged over many trials</i> .....	14
<b>Figure 2-1</b> <i>Illustration of the experimental setup and four main tasks performed by the monkeys</i> .....	22
<b>Figure 2-2</b> <i>Construction of the moveable tungsten microwire array used in this study.</i> .....	25
<b>Figure 2-3</b> <i>Illustration of a left lateral view of the macaque brain. (Actual size.)</i> .....	27
<b>Figure 2-4</b> <i>Photographs of example customised titanium implant</i> .....	27
<b>Figure 2-5</b> <i>Implantation of the cortical electrode array at the craniotomy site.</i> .....	29
<b>Figure 3-1</b> <i>Schematic of the spike-triggered averaging approach.</i> .....	38
<b>Figure 3-2</b> <i>Spike triggered average of the LFP and variation in amplitude of the STA lf-LFP with cortical area.</i> .....	39
<b>Figure 3-3</b> <i>Estimating lf-LFPs from firing rates.</i> .....	41
<b>Figure 3-4</b> <i>Neuron dropping curves for lf-LFP estimation</i> .....	43
<b>Figure 3-5</b> (Top; black box) <i>Conceptual illustration of experiment in which microwires were advanced</i> .....	44
<b>Figure 3-6</b> (Bottom) <i>Polarity inversion of SRSPs with increasing cortical depth.</i> .....	44
<b>Figure 3-7</b> <i>Principal component decomposition of the SRSP</i> .....	46
<b>Figure 3-8</b> <i>Method for estimating firing rates from lf-LFPs.</i> .....	49
<b>Figure 3-9</b> <i>Representative performance of firing rate estimation from lf-LFPs</i> .....	50
<b>Figure 3-10</b> <i>LFP- and PC-dropping curves for firing rate estimation.</i> .....	52

<b>Figure 3-11</b> <i>Task-relationship of actual and estimated firing rates.</i> .....	54
<b>Figure 3-12</b> <i>Examples of SRSP-like phenomena in macaque V1, documented by Rasch et al.</i> .....	55
<b>Figure 4-1</b> <i>Long-term stability and dimensionality of firing rate estimation.</i> .....	67
<b>Figure 4-2</b> <i>Actual and estimated trial-aligned firing rate profiles in Monkey D.</i> .....	68
<b>Figure 4-3</b> <i>Actual and estimated trial-aligned firing rate profiles in Monkey R.</i> .....	69
<b>Figure 4-4</b> <i>Clustering and PC analysis of the neural firing rate-space</i> .....	72
<b>Figure 4-5</b> <i>Firing rate estimation in principal component space.</i> .....	73
<b>Figure 4-6</b> <i>Generalisation of lf-LFP–based firing rate estimate across ‘cell-control’ BMI tasks.</i> .....	77
<b>Figure 4-7</b> <i>Comparison of model performance for MI vs. PMv neurons.</i> .....	80
<b>Figure 4-8</b> <i>Model performance for neurons with different actual firing rates.</i> .....	81
<b>Figure 4-9</b> <i>Performance of firing rate estimation for cells that are modulated to a greater or lesser extent with movement (wrist torque), as quantified by a torque modulation index (TMI).</i> .....	82
<b>Figure 4-10</b> <i>SRSP (spike-related slow potential) during ‘cell-control’ BMI task.</i> .....	83
<b>Figure 4-11</b> <i>Biofeedback BMI controlled by realtime LFP-based firing rate estimates.</i> .....	86
<b>Figure 4-12</b> <i>Trial-averaged data for cursor position and actual/estimated firing rate.</i> .....	86
<b>Figure 4-13</b> <i>Group data for actual firing rates of estimated neurons vs. all other neurons.</i> ..	89
<b>Figure 5-1</b> <i>Low-frequency LFP dynamics during isometric movements</i> .....	100
<b>Figure 5-2</b> <i>Areal velocity signals from low-dimensional LFP projections.</i> .....	103
<b>Figure 5-3</b> <i>Properties of low-frequency rotations with submovements of varying speed.</i> ...	105
<b>Figure 5-4</b> <i>LFP dynamics during sleep: Submovement- and K complex-related activity share a common low-frequency phase structure.</i> .....	106

<b>Figure 5-5</b> <i>Oscillation of neural firing rates during three movement types.</i> .....	109
<b>Figure 5-6</b> <i>Illustration showing the potential problems of using jPCA to find the best planes in multi-dimensional neural data</i> .....	112
<b>Figure 5-7</b> <i>Relationship between LFP-PCs and movement direction in three dimensions.</i> .	113
<b>Figure 5-8</b> <i>Illustration of the steps involved in the 'AVC'-based method of dimensionality reduction and AV signal calculation.</i> .....	116
<b>Figure 5-9</b> <i>Bimanual wrist-torque task</i> .....	119
<b>Figure 5-10</b> <i>Example section of data from the bimanual wrist-torque task</i> .....	122
<b>Figure 5-11</b> <i>Illustration of receiver-operating characteristics (ROC) analysis using wrist torque</i> .....	123
<b>Figure 5-12</b> <i>Example ROC analysis of AV-based signals generated using the jPCA-based method</i> .....	126
<b>Figure 5-13</b> <i>ROC analysis comparing performance of different feature-extraction techniques, with increasing numbers of LFPs</i> .....	128
<b>Figure 5-14</b> <i>Simple schematic of state space parameters</i> .....	130
<b>Figure 5-15</b> <i>Schematic of experimental setup for areal-velocity (AV)-controlled BMI task</i>	131
<b>Figure 5-16</b> <i>1-D BMI task and possible strategies to the redundant 2:1 mapping</i> .....	133
<b>Figure 5-17</b> <i>Example data from 1-D (2:1 mapping) AV-control BMI biofeedback task</i> .....	135
<b>Figure 5-18</b> <i>Weighting coefficients for each jPC plane</i> .....	135
<b>Figure 5-19</b> <i>Illustration of the various parameters related to the areal velocity</i> .....	136
<b>Figure 5-20</b> <i>Trial-averaged data from the 1-D (2:1 mapping) AV-control biofeedback BMI task, aligned to the end of the successful hold period</i> .....	138
<b>Figure 5-21</b> <i>'Solution space' plot for the 1-D (2:1 mapping) biofeedback BMI task</i> .....	139
<b>Figure 5-22</b> <i>The mechanisms of modulation of areal velocity in the 1-D (2:1 mapping) biofeedback BMI task.</i> .....	141

<b>Figure 5-23</b> <i>Areal velocity during 2-D AV-control biofeedback BMI task</i> .....	142
<b>Figure 5-24</b> <i>The mechanisms of modulation of areal velocity in the 2-D biofeedback BMI task.</i> .....	143
<b>Figure 5-25</b> <i>Behaviour of the local neurons during the 2-D AV-control biofeedback BMI task</i> .....	144
<b>Figure 5-26</b> <i>Comparison of different signal types from LFP recording</i> .....	150
<b>Figure 6-1</b> <i>Anatomy and histology around the central sulcus, and example MEA implantation</i> .....	156
<b>Figure 6-2</b> <i>Design of dual-shank LMA plus tungsten microwire hybrid array.</i> .....	160
<b>Figure 6-3</b> (right) <i>Schematic of relative locations of recording sites in Monkey U. (To scale.)</i> .....	162
<b>Figure 6-4</b> <i>Example submovement-triggered average from 76 electrodes in M1 in Monkey U.</i> .....	163
<b>Figure 6-5</b> <i>Example of using a minimal number (three) LFPs to estimate the firing rate of a single neuron recorded on a separate microwire. (To scale.)</i> .....	166

# List of Tables

Page:

<b>Table 1-1</b> <i>Comparative power consumption between a wide-band (&lt;10 kHz) data acquisition device and a low-frequency (&lt; 100 Hz) device</i> .....	18
<b>Table 4-1</b> <i>Generalisation of 1f-LFP-based firing rate decoders, trained on ‘torque task’ data and tested (validated) on data from ‘cell-control’ BMI tasks.</i> .....	78
<b>Table 4-2</b> <i>Comparison of using the ‘original’ model (trained on torque task data) vs. using an ‘updated’ model (trained on data from the specific cell-control block).</i> .....	79
<b>Table 6-1</b> (left) <i>Channel mapping in Monkey U. Note that channels 13–16 were not connected.</i> .....	162
<b>Table 6-2</b> <i>Performance of the best combination of channels from each category in firing rate estimation with three LMA channels.</i> .....	165

# List of Equations

Equation no.	Page:
1.1 <i>FPGA dynamic power consumption</i> .....	19
3.1 <i>Spike-triggered averaging (STA) (discrete notation)</i> .....	38
3.2                   — " — <i>(integral notation)</i> .....	38
3.3 <i>Multiple-input, multiple-output (MIMO) model</i> .....	40
3.4 <i>LFP estimation from multiple firing rates</i> .....	41
3.5 <i>Estimation of latent 'sources' using spike-related slow potentials</i> .....	48
3.6 <i>Calculation of 'inverse' LFP filter kernels</i> .....	48
3.7 <i>Firing rate estimation from lf-LFPs</i> .....	48
4.1 <i>Tuning index for task modulation of firing rates</i> .....	88
5.2 <i>Areal velocity as a function of angular velocity and radius</i> .....	103
5.3 <i>Areal velocity as a function of frequency and radius</i> .....	103
5.4 <i>Vector velocity as the derivative of vector position</i> .....	103
5.5                   — " —                   .....	103
5.6 <i>Areal velocity calculated by cross-product</i> .....	104
5.7 <i>Time invariant linear dynamical system (function notation)</i> .....	110
5.8                   — " — <i>(matrix notation)</i> .....	110
5.9 <i>Symmetric and skew-symmetric components of <math>\mathbf{M}</math></i> .....	110
5.10 <i>Scalar components of 3-D vectors <math>\mathbf{u}</math> and <math>\mathbf{v}</math></i> .....	114
5.11 <i>Vector cross-product of 3-D vectors, in terms of their scalar components</i> .....	114

<b>5.12</b> <i>Scalar components resulting from the vector cross-product</i> .....	115
<b>5.13</b> <i>Scalar components of areal velocity in three dimensions</i> .....	115
<b>5.14</b> <i>Definition of the 'areal velocity component' (AVC)</i> .....	115
<b>5.15</b> <i>Definition of the receiver-operator characteristic discrimination index</i> .....	124
<b>5.16</b> <i>Calculation of the tangential (cross-radial) velocity</i> .....	136
<b>5.17</b> <i>Relation of angular velocity, tangential velocity and radius</i> .....	136
<b>5.18</b> <i>Calculation of tangential velocity as a vector projection</i> .....	137

***An index of acronyms, abbreviations and conventions  
is provided at the end of this thesis.***



# Chapter 1. General Introduction

*In which I propose and explain the motivation for using local field potentials as control signals for motor brain machine interfaces.*

## 1.1 Neural interfaces

Neural interfaces are neuroprosthetic devices that interact directly with the nervous system. They have an electronic pathway by which biological control signals are recorded, usually from the central nervous system (CNS), then processed and transformed into an output signal that can be used to produce action in the environment, via an effector.

Brain-machine interfaces (BMIs) and brain-computer interfaces (BCIs) are a class of neural interface whose input signals come from the brain, and whose output signals control ‘machines’ (e.g. robotic arms) or computers (e.g. a cursor), respectively. The term neural interface is broader, and includes devices which produce action via other types of effector: for example, by stimulation of the CNS or muscles. Given the significant overlap between contemporary ‘machines’ and ‘computers’, the terms BMI and BCI are often used interchangeably, so in this thesis, I will use the term BMI for consistency. In discussions of broader application of the technology I will use the term neural interface where appropriate.

This thesis focusses mainly on *motor* BMIs, which allow control of an external effector—e.g. a computer cursor or a robotic arm—using signals recorded directly *from* the CNS (typically from the motor cortex). This is in contrast to *sensory* neural interfaces (e.g. retinal implants), which use stimulation (usually electrical) to deliver afferent sensory information from the environment directly *to* the CNS.

### 1.1.1 Motivation

#### 1.1.1.1 The clinical context

Neural interfaces offer considerable promise for restoring functional arm movement to patients with a number of clinical pathologies, including spinal cord or brainstem injury,

cerebrovascular events (stroke), multiple sclerosis and motor neuron disease (Daly and Wolpaw 2008).

In such diseases, if a ‘disconnect’ exists (at any point in the descending pathway) between a healthy, functioning cortex and the muscles, a chronic neural interface could theoretically be used to ‘bypass’ the lesion and control an external device, or re-animate a paralyzed limb by stimulating the muscles (Pfurtscheller et al. 2003; Moritz et al. 2008; Ethier et al. 2012) or spinal cord (Zimmermann et al. 2011) (**Figure 1-1**).

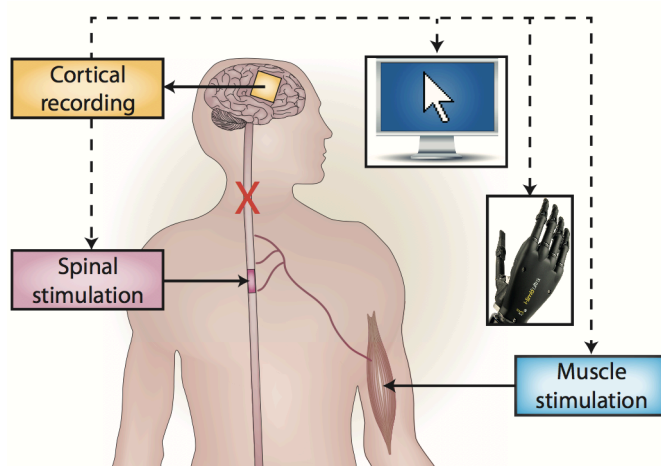


**Figure 1-1** A neuroprosthetic approach to spinal cord injury.

Schematic of an invasive BMI approach to treating spinal cord injury. Signals recorded from the brain can be used as control signals, either to reanimate the limb through spinal cord stimulation or muscle stimulation, or to control a variety of artificial effectors.

— Adapted from Jackson & Zimmermann (2012) *Nature Rev. Neurology* 8 (Nature Publishing Group).

Amongst these devastating pathologies, spinal cord injury is perhaps the most likely to be amenable to treatment with neural interfaces in the near future. Roughly three people per day in the UK and Ireland—mostly young adults—suffer a paralyzing spinal cord injury (Spinal Research 2017); most commonly due to a traumatic injury, such as a road-traffic accident (WHO 2013). Over half of those patients will suffer partial or complete tetraplegia, as well as other life-changing symptoms, such as incontinence and sexual dysfunction (NSCISC 2017). Of all of these symptoms, according to patients with tetraplegia, the highest priority for recovery is arm and hand function (Andersen, Burdick, et al. 2004).

### ***1.1.1.2 Therapeutic approaches***

Restoring function in a paralysed upper limb is currently a significant therapeutic challenge. There is no cure, and treatment options are few: limited mainly to physiotherapy and other rehabilitative interventions to preserve range-of-motion. However, in many patients with traumatic spinal cord transection, brain function is preserved. This means that they can still have the intention to move their limbs, and their primary motor cortex (M1) often still produces signals that would normally be associated with movement (Kokotilo et al. 2009), but these signals are unable to traverse the spinal cord lesion and reach the motoneurons and muscles. Such patients are also usually fully cognitively intact and aware of their circumstances, and often young: all factors which make this condition particularly devastating and important to treat, both for individuals and for society.

There are currently two main scientific proposals for curing spinal cord transection:

- i) stem-cell therapy, and
- ii) neuroprosthetic therapy.

Whilst stem-cell therapy (or other biological regenerative method) may eventually prove to be the ‘Holy Grail’ of curative therapy for spinal injury, it is a field in its infancy. It is by no means clear that stem-cells will ever be able to functionally re-connect a damaged spinal cord (Antonic et al. 2013); even less so, a damaged corticospinal tract – a specialised motor pathway which is essential to human hand dexterity (Lemon et al. 2004). It is important to note here, that in patients who have suffered incomplete spinal cord injury, the corticospinal tract may be damaged, but other pathways (e.g. the rubrospinal and reticulospinal tracts) may still be able to transmit signals past the lesion. In such patients, there is a particularly important role for targeted rehabilitative physiotherapy, as these ‘accessory’ tracts may be able to provide a substrate for considerable recovery of function (Baker 2011).

### ***1.1.1.3 Types of neural interface***

In comparison to cell-based therapy, the field of neuroprosthetics is surprisingly mature. Two main types of neural interface device exist: *invasive* and *non-invasive*. Non-invasive neural interfaces use recording methods that don’t require a device to be implanted in the CNS to record signals. For example, electroencephalography (EEG) captures signals from the brain at the scalp surface. Non-invasive devices have the advantage that the CNS is not damaged by

implantation, the skin remains intact—massively reducing the risk of infection—and no transcutaneous connectors or cables are required. However, brain signals are attenuated and spatially low-pass filtered by the skull and soft tissues, introducing artificial correlation between electrodes, and making source localisation very difficult (Srinivasan et al, 1998). Despite these limitations, there are already a huge number of motor BMI experiments employing EEG for controlling computers (McFarland et al. 2008), wheelchairs (Galán et al. 2008), robotic exoskeletons (Bhagat et al. 2016), and more.

Invasive neural interfaces are also surprisingly common. Indeed, there are already hundreds-of-thousands of people walking around with surgically-implanted neural interfaces, in the form of cochlear implants, which are a type of *sensory* neural interface that converts environmental information (sound) into electrical neural signals.

More relevant to this thesis, several volunteer patients in the USA have already received implantations of experimental BMI devices into their motor cortex, with which they can control robotic arms using only their brain activity (e.g. Simeral et al. 2011; Hochberg et al. 2012). Some patients even have hybrid sensorimotor BMIs, with electrodes in both motor and somatosensory cortices, which can provide both motor efference and sensory afference between the brain and a robotic limb (Flesher et al. 2016).

#### ***1.1.1.4 Limitations of the status quo***

Despite these amazing advances, there are three main bottlenecks that need to be addressed before invasive BMIs become clinically viable and widely available to patients:

- i) miniaturisation and subcutaneous implantation;
- ii) energy consumption and battery life; and
- iii) stability and longevity of the biological control signals

Current experimental motor BMI devices, using cortical implants, are highly susceptible to infection. The sheer size of the connectors and processing equipment required, means that the implants must have a transcutaneous component. Transcutaneous, foreign, non-biological materials are notoriously prone to infection, because they breach the natural skin-barrier and—however biocompatible the material—never undergo true integration with the surrounding skin and soft tissues. Extra-oral transcutaneous implants fail in 53% to 100% of cases – depending on a variety of factors (Pendegrass et al. 2007). The ideal solution to this

‘transcutaneous dilemma’ would be for the whole device to be implanted subcutaneously (including electrodes, connectors, cabling, processing unit, power supply and radio-communications), so that once the skin wounds are healed, no part of the device is exposed to the external environment, and the risk of infection is greatly reduced.

Currently, the size of electronics required for the complexity of such devices is a major limitation to miniaturisation, although this is likely to change with new technologies from the consumer mobile electronic device industry. Even then, however, there is still no current energy storage solution (e.g. electrochemical cell/battery) that can provide sufficient energy density to enable BMIs to be powered subcutaneously for a clinically-acceptable amount of time (decades, or at least years).

One possible solution to the issue of energy storage is to use a device which is powered inductively, using an electromagnetic radio-frequency (RF) transmitting coil (outside the body) and a receiving coil (under the skin). This system could either power the device directly or (more likely) recharge an implanted battery. However, inductive power transfer introduces numerous bioengineering challenges to the system. Firstly, the efficiency of inductive transfer is highly dependent on the orientation of the receiver coil, and very sensitive to the distance between the coils. The subcutaneous receiver coil can migrate surprisingly quickly (F. de Carvalho, personal communication), and render the power transfer insufficient to power the device (Amar et al. 2015). Secondly, the ability of a resonant circuit to retain energy increases with the frequency of RF transmission, but higher frequencies are more absorbed by subcutaneous tissues. Because of concerns about tissue damage caused by heating, tissue absorption of RF transmissions is tightly regulated, particularly in medical devices, by stringent specific absorption rate (SAR) limits set by regulators (Abiri et al. 2017). Thirdly, inductive power (by definition) requires implantation of AC circuits, as well as AC-DC rectifiers and regulators to ensure a ‘clean’ DC supply (e.g. at 3.3V) to the digital elements of the implanted device. Not only do these components generate heat, they also are potential sources of electromagnetic interference, which can contaminate the recording of tiny neural potentials or the operation of digital components (Sun et al. 2013).

The final major bottleneck of implanted BMIs (even if miniaturisation and power consumption/storage issues could be solved) is that there are still fundamental problems with the instability of signals that can be recorded from the brain using existing electrode technology.

***In this thesis:***

I will argue that the use of low-frequency cortical local field potentials (LFPs) as signals for controlling motor BMIs, may offer an elegant, low-level solution to all three of these bottlenecks, and thus present a new direction for the development of clinical motor BMIs.

**1.1.2 *Invasive motor BMIs: current trends***

To be clinically viable and justifiable, invasive BMIs for motor rehabilitation need to work with high precision (movements are accurate), low variability (movements are repeatable and predictable) and sufficient dimensionality (enough different movements, or ‘degrees of freedom’, can be controlled simultaneously). Devices should also have an appropriate longevity—ideally decades—to avoid device failure or repeated surgeries (Lebedev & Nicolelis 2006; Schwartz et al. 2006; Green & Kalaska 2011; Jackson & Fetz 2011).

In the existing literature, the neural signals typically used for invasive motor BMIs are the ‘spiking’ activity (action potential events) of neurons recorded from the motor cortex; most commonly the firing rates of multiple M1 neurons recorded simultaneously. There has been enormous progress in the use of these signals in BMIs over the last 20 years. This progress has only been possible because of experiments performed in non-human primates (NHPs); in particular, Rhesus macaque monkeys (*Macaca mulatta*). These primate models are essential for this field of study, because only Old World primates (such as the humans, other great apes, and macaques) have specialised corticospinal tracts, with dedicated monosynaptic connections between cortical neurons and motoneurons, that mediate the level of manual and digital dexterity that is fundamental to the function of the human forelimb (Lemon et al. 2004).

Models of varying mathematical complexity have been used to describe the relationship of motor cortical firing rates to a variety of kinematic forelimb movement parameters in these NHP models of human movement. Most commonly, these models are based on the apparent, and well-documented, cosine tuning of motor cortical neurons to movement direction (Georgopoulos et al., 1982). Based on these observed relationships, an electronic ‘decoder’ can be trained to estimate movement parameters from firing rates in realtime, and considerable success has been achieved in controlling multi-dimensional artificial effectors (Wessberg et al. 2000; Serruya et al. 2002; Taylor et al. 2002; Hochberg et al. 2006).

Such techniques are commonly called ‘biomimetic’ decoding approaches: they use observed relationships between cortical signals and natural arm movement kinematics, and attempt to decode and mimic this relationship when using these signals for controlling artificial effectors (Fagg et al. 2007).

### **1.1.3 *Limitations of spike-controlled biomimetic BMIs***

Spike-based biomimetic BMIs have achieved considerable success. Once they have been trained using a training dataset, they tend to be quick and intuitive for a subject to use (Serruya et al. 2002). However, they are still slow and jerky when compared to natural movements (Velliste et al. 2008), and they have several other limitations, which can be broadly divided into two categories:

- a) the limitations of using spikes, and
- b) the limitations of using biomimesis.

#### **1.1.3.1 *Limitations of using neuronal spiking for BMI control***

There are three main limitations of using neuronal spiking for BMI control. The reader will observe how these relate to the ‘bottlenecks’ already described on page 4.

i) *Stability*: Neuronal spiking activity recorded using extracellular electrodes tends to be unstable over time. Extracellular spike recordings are highly dependent on very close proximity (maximum ~300  $\mu\text{m}$ ; Henze et al. 2000) of the recording site to a healthy neuron. The micro-movement that unavoidably occurs at the brain-electrode interface, during normal daily activity, often causes spike waveform morphology to change, signal-to-noise ratios (SNRs) to decrease, or cells to be lost completely (Perge et al. 2013). Electrodes themselves can also become damaged or de-insulated (Barrese et al. 2013). Obtaining long-term stable recordings of the same single neurons therefore remains a considerable challenge at present (Bensmaia & Miller 2013).

In addition, the foreign-body reaction that the brain mounts against chronically-implanted electrodes leads to inflammation and reactive gliosis (Polikov et al. 2005). This gliosis can produce a neuron-poor zone around the electrode shank as well as increasing contact impedances (Andersen, Burdick, et al. 2004; Leach et al., 2010). These factors, as well as

neuronal death (Biran et al. 2005) lead to a gradual reduction in the number of neurons that can be recorded, over months to years (Suner et al. 2005).

ii) *Frequency content*: Spiking activity contains very high frequency components (up to ~10 kHz), and therefore digital spike recordings need to be sampled at very high frequencies (usually > 20 kHz). This places major limitations on implanted chronic devices, because the development of the low-power components required for sampling and transmitting multichannel data at such rates is still in its infancy (Kipke et al. 2008).

iii) *Processing power*: Identifying single-unit spiking activity through thresholding, feature-extraction and clustering is time-consuming and highly non-linear, making it computationally demanding and relatively complex to implement in hardware.

### ***1.1.3.2 Limitations of the biomimetic approach to BMIs***

There are five main limitations of using a biomimetic approach to BMIs:

i) In paralysed patients who are unable to produce any movement, it is difficult to train biomimetic decoders. It is admittedly not impossible; considerable success has been achieved in controlling computer cursors or robotic arms by training decoders whilst subjects are asked to make *imagined* movements (Hochberg et al. 2012). However, it is extremely difficult to accurately characterise the natural movement that the subject is imagining, therefore decoders trained in such a way are often unintuitive, and are not truly biomimetic: they require a period of learning.

ii) Decoders trained biomimetically may behave erratically with only slight changes in signal quality, and may need to be ‘retrained’ or refined every time they are used.

iii) Each decoder is highly dependent on an individual subject’s recording configuration and the choice of task data used to train the decoder. With current electrode technology, the decoders used are not generalisable between subjects, because the probability of finding a sample of neurons (from the millions of neurons in the motor cortex) that behave in a sufficiently similar way between two different subjects, is basically zero. Also, the performance of a decoder with a particular task may be almost entirely dependent on one or two neurons from the neuronal ensemble. As a result, biomimetic BMIs do not tend to generalise well between different tasks (Aflalo and Graziano 2006) or different individuals (or for that matter, between different species).

iv) The signals and algorithms used for biomimetic BMIs are often selected to be intuitive for subjects to use initially, but that does not necessarily mean that it is easy for subjects to *learn* how to *improve* their performance, especially if the signal-task relationship is also unstable. It may be preferable to choose signals that are less intuitive, but more stable, and easier for the subject to learn with salient feedback.

v) Biomimetic decoders are often based on ‘black-box’ decoder algorithms. This means that they are engineered to model a desired movement parameter from a selection of input signals in the ‘best’ way possible, according to mathematical optimisation algorithm, without necessarily being informed by knowledge of the underlying cortical physiology. As such, it can be difficult to ask scientific questions of the data from biomimetic BMI experiments about cortical function and plasticity.

#### **1.1.4 Biofeedback BMIs as an alternative to biomimetic BMIs**

An alternative to the biomimetic approach is called the ‘biofeedback’ BMI. This relies on the finding that subjects are able to learn to modulate an arbitrary neural signal, given appropriate, salient sensory feedback.

Early experiments showed that biofeedback was possible for the firing rates of single neurons (Fetz 1969), and it has subsequently been demonstrated that subjects can dissociate the firing rates of multiple single cortical neurons (e.g. Ganguly & Carmena 2009). It appears not to be necessary that the chosen cells are directionally tuned, or even that they are in the motor cortex (Moritz & Fetz 2011).

Biofeedback BMIs can therefore (within reason) be ‘abstract’ rather than intuitive: the relationship between neural signal and BMI output does not need to be naturalistic, as long as the feedback is salient enough for the brain to learn the relationship.

An analogy is useful here. A trowel is a tool that makes digging soil faster, more efficient and safer than using one’s bare hand. Using a trowel is simple and intuitive; it mimics the hand itself, and the neural and muscular activities that produce the desired effect are naturalistic: they map very closely to the activity seen without the trowel. The trowel is thus a *biomimetic tool*. In comparison, a *JCB* (mechanical excavator with a backhoe) is a tool that achieves the same task, but the hand movements that produce the effect (pushing levers) are non-naturalistic and are mapped in a highly abstract way to the effector. Controlling a backhoe

thus requires learning a new skill, but the feedback is salient, and once the mapping is learned, the effect is extremely powerful (arguably more powerful than the naturalistic approach). The *JCB* can therefore be thought of as a *biofeedback tool*.

#### **1.1.4.1 Advantages of biofeedback BMIs**

There are three key advantages of a biofeedback BMI over a biomimetic BMI.

- i) Rather than being designed for intuitiveness, BMIs can be designed for ease of learning. In this way, biofeedback BMIs can be thought of as a ‘tool’ that the brain finds easy to learn, and can offer enhanced function. This is as opposed to a biomimetic BMI, which is trying to replace function (a ‘prosthesis’) in a naturalistic (but perhaps limited) way (Jackson & Fetz, 2011).
- ii) They do not rely on a recorded neural signal being naturally tuned to a particular movement. Signals can instead be chosen on other merits, e.g. stability of recording (Andersen, Musallam, et al. 2004). Inputs could also be chosen on the basis that they reflect some more distributed, but abstract, feature of cortical movement representation. These (hypothetical) ‘features’ could form the basis of a BMI that would be less dependent on the precise tuning of individual neurons (and probably therefore less intuitive), but hopefully more generalisable between tasks and subjects.
- iii) By choosing the control signal, and linking the brain directly to the external effector (‘closing the loop’ using feedback), abstract biofeedback BMIs can offer an interesting and more direct insight into the way that the motor cortex learns to use new tools, independent of the confounding effects (e.g. filtering, resonance, delay) of the spinal cord, neuromuscular junction, muscles and skeleton.

## **1.2 Local field potentials**

The local field potential (LFP) is the low-pass filtered portion (typically below 300 Hz) of the high-bandwidth electrical signal recorded from the brain by penetrating electrodes (as opposed to surface electrodes). The LFP from a particular electrode is thought to represent a temporal and spatial integration of excitatory and inhibitory postsynaptic potentials from a volume of brain tissue around the recording site. Because such potentials are largely

generated in the dendrites, the LFP is often considered to represent the synaptic ‘input’ of the recorded group of neurons (Logothetis 2003; Buzsáki et al. 2012).

In the neocortex, the synaptic activity of pyramidal cells dominates the LFP signal. This is because of the elongated morphology of these cells (which makes them good open-field dipole generators), their extensive dendritic system, and their regimented arrangement (predominantly perpendicular to the cortical surface) meaning that their individual dipoles are likely to spatially summate (rather than cancel) to produce large amplitude LFP contributions. It is also important to note that there are undoubtedly several other contributions to the LFP signal other than synaptic potentials, including spike after-potentials, calcium transient currents and voltage-dependent membrane oscillations (Logothetis 2003; Buzsáki et al. 2012).

Whilst extracellular spiking activity is almost universally accepted to be detectable within a relatively small radius around a recording site (~100  $\mu\text{m}$ ), there is considerable debate as to the volume of tissue over which LFP signals are integrated; or to put it another way, the spatial ‘spread’ of the LFP signal from its source. Some recent studies suggest that the radius of spatial integration is small, around 200–400  $\mu\text{m}$  (Katzner et al. 2009; Xing et al. 2009), but a larger body of evidence supports the idea that signals spread from their sources, by volume conduction, over many millimetres, if not centimetres, and that an LFP recording includes a mixture of many such signals (Kreiman et al. 2006; Nauhaus et al. 2008; Kajikawa and Schroeder 2011).

### **1.2.1 Using LFPs as control signals for BMIs**

In view of the limitations of neural spiking as a control signal (particularly the stability problem), there is increasing interest in the use of LFPs for invasive BMIs. LFPs have a number of *prima facie* advantages over spikes as control signals.

#### **1.2.1.1 Advantages of LFP signals for BMIs**

i) Rather than just sampling from a single neuron (whose behaviour may be highly unrepresentative of the wider population), LFPs reflect the summation of postsynaptic potentials over at least a few hundred micrometres from the recording site (Berens et al. 2008; Katzner et al. 2009; Xing et al. 2009; Kajikawa & Schroeder 2011; Buzsáki et al. 2012; Einevoll et al. 2013).

- ii) Because LFPs represent a more spatially distributed signal that is dependent on a much larger population of neurons, they may be more robust to microscopic electrode movements and encapsulation of electrodes (Andersen, Musallam, et al. 2004; Flint et al. 2013), and kinematic information can be retrieved even from electrodes without clear spike activity (Flint, Lindberg et al. 2012; Wang et al. 2014).
- iii) Because they are temporally ‘slower’ than spikes, LFPs can be digitized at sampling rates *at least* two orders of magnitude lower than spikes ( $10^2$ – $10^3$  Hz vs.  $10^4$ – $10^5$  Hz) without violating the Nyquist limit. This also enables them to be transmitted wirelessly much more easily.
- iv) Lower electronic sampling, processing and transmission rates may allow lower power consumption. This in turn facilitates much smaller devices, longer battery life and wireless communication. If battery life, in particular, could be extended by decreasing consumption, rather than increasing energy storage capacity, then implantable clinical devices become much more achievable using existing electronic technology.

#### ***1.2.1.2 Disadvantages of LFP signals for BMIs***

Despite many decades of research, the origin of field potentials is generally less well understood than the origin of spikes. This may be because the physiology of the action potential is very well understood and extensively studied, and spike events are an intuitive manifestation of action potentials; whereas LFPs represent a complex (and much debated) mixture of signals, generated by the network activity of neurons at a huge range of scales.

Furthermore, with spiking, there is an ubiquitously accepted method of separating signal (spikes) from background noise: through high-pass filtering, thresholding and spike sorting. And the relationship of multichannel firing rates to a huge range of behaviours (motor, sensory and cognitive) is very extensively studied. It is also known that the firing rates of single (e.g. Fetz 1969) and multiple (e.g. Ganguly et al. 2011) neurons can be subject to operant conditioning in closed-loop BMIs, meaning that the brain can learn to improve motor BMI ‘skill’, given salient feedback (Jackson & Fetz 2011; Carmena 2013).

In contrast, the separation of signal from noise in LFPs is much more challenging, because thresholding is not meaningful, and even the identification of ‘what is signal and what is noise’ is not trivial. Moreover, even given a clean, multichannel LFP signal, it is not clear

exactly which *features* of this signal (for example, amplitude, phase, current-source density, power in various frequency bands, higher-order multichannel features) are best for BMI control, and particularly, which are amenable to learning through biofeedback.

### ***1.2.1.3 Use of LFPs for BMIs***

A number of groups have found that LFPs can be successfully used to control BMI devices. Some experience has been gained using the EEG, which can be thought of as a non-invasive version of the LFP, recorded at the scalp surface. Forearm kinematics can be decoded from EEG (Waldert et al. 2008; Bradberry et al. 2010), and multichannel EEG has been used in human subjects for controlling computer cursors (Fabiani et al. 2004) and wheelchairs (Galán et al. 2008).

Using recordings at the surface of the *brain* itself—via electrocorticography (ECoG) and epidural field recordings—has also been fruitful (Levine et al. 2000; Leuthardt et al. 2004; Slutzky et al. 2011). However, studies in monkeys have demonstrated that more information about movement kinematics can be decoded from the LFP than from planar surface recordings (Mehring et al. 2004; Flint, Lindberg et al. 2012). It is not yet clear whether this is simply because recordings at depth have a ‘cleaner’ signal (higher signal-to-noise ratio and less filtering by the extra-cerebral tissues), or whether there is additional information available when by combining multichannel LFP signals recorded at varying depths in the cortex (e.g. by sampling from different cortical layers).

## ***1.2.2 LFPs during movement, and the rationale for studying low-frequency local field potentials (lf-LFPs)***

LFPs are traditionally classified into frequency bands, which inherit their labels from the historical EEG nomenclature. In this thesis, we focus on the low-frequency LFP (*lf-LFP*), which we define as those LFP components below 5 Hz; corresponding approximately to the traditional ‘delta’ band (0.5–4 Hz) and lower (0.025–0.5 Hz) bands (Penttonen & Buzsáki 2003).

Goal-directed planning and movement in primary motor and premotor cortices in primates (at least in visuomotor tasks) is associated with peaks in the LFP power spectrum in three main frequency bands (O’Leary & Hatsopoulos 2006):

- a) ‘slow’ (< 5 Hz), here referred to as the *lf*-LFP, and also sometimes referred to as the local motor potential (LMP);
- b) ‘intermediate’ (16–30 Hz), commonly referred to as ‘beta’-band activity; and
- c) ‘high’ (30–200 Hz), commonly referred to as ‘gamma’-band activity; often split into ‘low gamma’ (30–60 Hz) and ‘high gamma’ (60–200 Hz).

Modulation of activity in all three bands is evident when motor cortical field potentials (typically LFPs from monkeys, or EEG from humans) are aligned to specific movement events during visuomotor tasks. For example (**Figure 1-2**), Rickert and colleagues (2005) calculated the average LFP amplitude spectrogram over many trials, by alignment and averaging relative to the onset of unimanual centre-out movements.

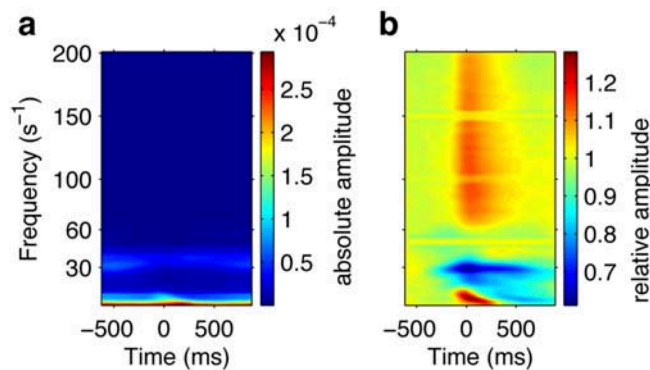


**Figure 1-2** LFP activity in the frequency domain, aligned to movement onset, averaged over many trials

- a) Time-resolved, absolute amplitude spectrum (arbitrary units) of average LFP activity recorded from a single electrode implanted in macaque motor cortex, shown relative to movement onset (time zero).
- b) Time-resolved amplitude spectrum, normalized to baseline amplitude.

— Reproduced from Figure 5a,b in Rickert et al (2005), *J. Neurosci.* **25** (Society for Neuroscience).

### 1.2.2.1 Beta-band LFP activity

Beta-band activity in the motor cortex generally has the highest amplitude prior to movement onset (O’Leary & Hatsopoulos 2006). Indeed, has been consistently shown that beta-band oscillations (reflecting synchrony) in the motor cortex tend to occur during periods of static posture—for example, just prior to movement, and during steady grip—and tend to disappear during periods of movement (Baker et al 1999), as is clearly seen in **Figure 1-2a**.

### 1.2.2.2 *Gamma-band LFP activity*

Gamma-band activity in the motor cortex (particularly high gamma), is associated with the onset and execution of movement. In the sensory cortices, specific gamma oscillations have been documented in association with particular stimuli (e.g. auditory, Brosch et al 2002; visual, Hermes et al 2015); in association cortices, gamma oscillations have been associated with sensory ‘binding’ and working memory (Tseng et al 2016); and in hippocampus, gamma oscillations are thought to have a functional role in memory encoding and retrieval (Colgin & Moser 2010). However, in the motor cortex, there is much less evidence of oscillatory gamma ‘peaks’; rather, there is broadband power across the gamma range during goal-directed movement. There is therefore considerable debate as to whether gamma activity has a functional role in the motor cortex, or whether it actually represents contamination due to simultaneous multi-unit spiking (Waldert et al 2013; Ray & Maunsell 2015).

As well as debate over the functional role of gamma oscillations in the motor cortex, there are also considerable technical issues with capturing and processing gamma band signals, in order to use them to produce a BMI control signal. Firstly, gamma band signals are extremely small in amplitude compared to lower-frequency LFP bands, as can be seen in the non-normalized amplitude spectrum in **Figure 1-2a**. The power distribution of LFP signals broadly follows a  $1/f^n$  relationship to frequency,  $f$ . That is to say, higher-frequency LFP signals naturally have much lower power than lower-frequency LFP signals. Recording gamma band signals therefore requires amplifiers capable of greater gain. Their small signal size also makes higher-frequency LFP signals considerably more susceptible to noise, leading to lower signal-to-noise ratios, and greater susceptibility to changes in electrode impedance.

### 1.2.2.3 *Low-frequency (lf)-LFP activity*

In contrast to beta and gamma-band LFPs, low-frequency LFPs (*lf*-LFPs) have considerable merits as candidate signals for BMI control. Firstly, they are large-amplitude, and their peak activity is clearly associated with goal-directed movement (e.g. **Figure 1-2b**). Secondly, and perhaps more importantly, an increasing number of studies are finding that *lf*-LFPs show very strong directional tuning, and that these low frequency bands perform better than any other for decoding kinematic parameters from motor cortical LFP (Mehring et al. 2004; Rickert et al. 2005; O’Leary & Hatsopoulos 2006; Asher et al. 2007; Waldert et al. 2008; Bansal et al. 2011; Flint, Lindberg et al. 2012). Thirdly, *lf*-LFPs exemplify the technical advantages of

LFPs for BMI control outlined in **Section 1.2.1**, above. In particular, their very low frequency means that they can be sampled, processed and transmitted at extremely low data rates, which should enable a dramatic reduction in power consumption (thus battery size), and thus potentially enable the future development of a miniaturised, ultra-low power device, which could be implanted subcutaneously.

### ***1.2.3 Do lower signal frequencies actually permit lower power consumption?***

Before proceeding, it is important to explore and validate, from an engineering perspective, this assertion that lower sampling, processing and transmission rates may enable BMI devices based on *lf*-LFPs to operate with lower power consumption.

In its most basic form, a typical data acquisition and processing device (such as a BMI) incorporates the following stages in its design. Each stage requires a certain amount of power, which contributes to the overall power consumption of the device:

- a) Amplification;
- b) Analogue filtering (most importantly, anti-aliasing with a low-pass filter cut-off below the Nyquist frequency);
- c) Analogue-to-digital conversion (ADC), that is ‘sampling’;
- d) Digital signal processing (DSP); and
- e) Output.

In each stage, power consumption is typically divided into ‘static’ (baseline) consumption, which is a required overhead, regardless of activity, and ‘dynamic’ consumption, which is dependent on the demand placed on the device by the user. Here (and in this thesis in general) I do not directly consider the power consumption at stage ‘e’ (output) of a device, as this will vary enormously depending on the selected application and output modality (e.g. wired/wireless transmission versus electrical stimulation; see **Figure 1-1**).

#### ***1.2.3.1 Power consumption of data acquisition***

Stages ‘a’ to ‘c’ represent data acquisition, which are most commonly performed together, within commercially-available specialised integrated circuits (ICs; ‘chips’), which are optimised to provide reliable and robust performance at low power draw. An excellent example of such a chip is the Intan RHD2132 Digital Electrophysiology Interface chip (Intan

Technologies, LLC, Los Angeles, CA, USA), which is widely used (including within our laboratory) as the ‘front-end’ (first data-acquisition stage) of many low-power, miniaturised data acquisition devices.

Intan provide dynamic power dissipation data for the RHD2132 (Intan, 2013), as follows (where supply voltage to the chip is a constant 3.3V, so power is proportional to current):

a)/b) Amplification/analogue filtering

*“Each amplifier consumes current in proportion to its upper cutoff frequency, approximately 7.6  $\mu\text{A}/\text{kHz}$  per amplifier.” (Intan, 2013)*

c) ADC

*“Baseline ADC current: Each ADC pulls 510  $\mu\text{A}$  of quiescent current to power various voltage references and bias current generators.*

*“ADC and MUX [multiplexer] dynamic current: The ADC/MUX assembly consumes additional current in proportion to the total sampling rate, approximately 2.14  $\mu\text{A}/(\text{kS}/\text{s})$ .” (Intan, 2013)*

Intan also provide data for static power consumption, and provide a worked example of power consumption when the device is operating as a wideband neural recording headstage, recording 32 channels at 20 kS/s (upper cutoff 10 kHz, allowing recording of spikes). These data can be seen in the left-hand column of

**Table 1-1** (adapted as per legend). In the right-hand column, I perform the same calculation for a putative device operating at a sampling rate of 200 S/s (upper cutoff 100 Hz), which is the minimum cutoff frequency of the RHD2132.

Component	i) 10 kHz 'wide-band' device (32 channels)	ii) 100 Hz 'low-frequency' device (32 channels)
Total sampling rate (including oversampling and reference channels)	$35 \times 20 \text{ kS/s}$ = 700 kS/s	$35 \times 200 \text{ S/s}$ = 7 kS/s
<b>a)/b) Amplification/filtering</b>		
Baseline amplifier array current	200 $\mu\text{A}$	200 $\mu\text{A}$
Amplifiers	$32 \times 7.6 \mu\text{A/kHz} \times 10 \text{ kHz Fc}$ = 2432 $\mu\text{A}$	$32 \times 7.6 \mu\text{A/kHz} \times 10 \text{ Hz}$ = 24.32 $\mu\text{A}$
<b>c) ADC</b>		
Baseline ADC current	510 $\mu\text{A}$	510 $\mu\text{A}$
ADC/MUX	$2.14 \mu\text{A}/(\text{kS/s}) \times 700 \text{ kS/s}$ = 1498 $\mu\text{A}$	$2.14 \mu\text{A}/(\text{kS/s}) \times 7 \text{ kS/s}$ = 14.98 $\mu\text{A}$
<b>Other static consumption</b>		
LVDS I/O	Off (assume SPI to nearby microcontroller)	Off (assume SPI to nearby microcontroller)
Impedance measurement	120 $\mu\text{A}$	120 $\mu\text{A}$
Temperature sensor	70 $\mu\text{A}$	70 $\mu\text{A}$
Supply voltage, auxiliary inputs	$4 \times 10 \mu\text{A}$ = 40 $\mu\text{A}$	$4 \times 10 \mu\text{A}$ = 40 $\mu\text{A}$
<b>TOTALS</b>		
Total supply current	4.87 mA	0.979 mA
Total power dissipation	$4.87 \text{ mA} \times 3.3 \text{ V}$ = 16.1 mW	$0.979 \text{ mA} \times 3.3 \text{ V}$ = 3.23 mW

**Table 1-1** Comparative power consumption between a wide-band (<10 kHz) data acquisition device and a low-frequency (< 100 Hz) device

Values are taken from the RHD2132 data-sheet (Intan, 2013). 'LVDS I/O', low-voltage differential signalling input/output. This is 'off' as it is assumed that the default standard serial peripheral interface bus (SPI) is used to communicate with a microcontroller. Two-fold oversampling is used in each case, to enable a fair comparison.

Reducing the sampling rate of the RHD2132 from 20 kS/s to 200 S/s achieves approximately a 5-fold reduction in power consumption, which would represent a very meaningful reduction for a battery-powered medical device. The limitation preventing a more significant reduction is the static consumption ('overhead') of the RHD2132, of 3.1 mW (which represents 96% of power dissipation in the low-frequency scenario).

However, a sampling rate of 200 S/s (per channel) is the lowest possible sampling rate that the RHD2132 can achieve. Also, the RHD2132 is also designed to be a versatile and multi-functional device, with a wide range of user-defined settings, and it is therefore not optimised for very low frequency operation. It is very likely that a purpose-built device, designed to filter, sample and process  $lf$ -LFPs—for instance, filtering below 5 Hz and sampling at 20 S/s—could operate with significantly lower static (and dynamic) consumption.

Whilst a number of ADC architectures are available, 'algorithmic' successive approximation register (SAR) ADCs are considered the most efficient (Dlugosz & Iniewski 2006) for ultra-low power scenarios (including being used in the RHD2132). Static consumption in ultra-low frequency SAR ADCs is a recognised issue in the biomedical engineering field, and comes

primarily from control logic overheads and current leakage (Zhang 2014). The former of these can be reduced in ultra-low frequency devices by maximising the simplicity of the ADC, to achieve the required sampling rate and resolution without the unnecessary and complex supplementary circuit logic (e.g. digital error correction) required for higher specifications. Current leakage can then also be mitigated by reducing the supply voltage to the ADC to the absolute minimum (e.g. 0.4V rather than 3.3V). Such approaches have been demonstrated to reduce the power dissipation of SAR ADCs to the tens-of-nanowatt ( $10^{-8}$  W) range (e.g. Zhang 2014).

### ***1.2.3.2 Power consumption of data processing***

Whilst the nature of the data acquisition stages of a low-power device based on *lf*-LFPs can be reasonably well assumed, the data processing architecture of such a device (stage ‘d’) is less clear at this point. It is therefore harder to estimate the potential power reduction that could be achieved by using lower frequencies. However, educated assumptions about power savings can be made by looking at an existing chip technology: namely field-programmable gate arrays (FPGAs).

FPGAs are integrated circuits which can be configured after manufacture, and are commonly used in a variety of digital signal processing (DSP) contexts, where hardware-level speed and efficiency is needed, but there is a requirement to be able to program certain parameters (e.g. filter coefficients). This is a very similar set of requirements to those of a low-frequency *lf*-LFP-based device.

Like acquisition hardware, FPGAs have both static and dynamic power dissipation. It is widely accepted that dynamic power consumption ( $P_d$ ) of an FPGA is directly proportional to the processing frequency (‘switching’ frequency,  $S$ ) of the chip (Arora 2016):

$$P_d = CV^2S \quad (1.1)$$

where  $C$  is the load capacitance and  $V$  is the operating voltage. Hence, 1000-fold reduction in switching frequency should lead to a proportional reduction in dynamic power consumption.

Like with ADCs, at low frequencies, the static consumption of an FPGA is likely to heavily dominate the overall power consumption. However, also like ADCs, purpose-designed

architecture (e.g. a custom-designed application-specific integrated circuit [ASIC], optimised for ultra-low frequencies) is likely to be able to also reduce static consumption considerably.

### 1.3 Chapter summary

- The use of spike signals for BMI-control is limited by spike instability, high-frequency signal management and complex processing.
- The use of LFP signals permits lower-frequency signal management, and potentially better stability.
- Biofeedback BMIs allow signal features to be chosen based on stability, ease of processing and ease of learning. Control strategies can be abstract, and we can rely on the ability of the brain to learn the required signal-effector mappings.
- This thesis focuses on the *lf*-LFP, which is defined as the LFP signal low-pass filtered at 5 Hz. The *lf*-LFP has considerable merits as a BMI input signal, compared to other LFP frequency bands.
- Dynamic power consumption of hardware essentially scales proportionally to signal frequency. It is likely that static power consumption can also be reduced through simplification of architecture. Ultra-low power consumption and miniaturisation could therefore be major benefits of a BMI device based on *lf*-LFPs, rather than on spikes or higher-frequency LFP bands.

# Chapter 2. General Methods

*In which I introduce the primate model and brain-machine interface task, and our methods for measuring and recording electrical signals from primate motor cortex.*

## 2.1 Subjects and behaviour

### 2.1.1 *Non-human primate subjects*

Five female monkeys (*Macaca mullata*) in total were used for different aspects of this study: Monkey A, Monkey D, Monkey R, Monkey S, and Monkey U (all aged approximately 5.5 years at the start of their respective experimental recording periods). Subjects were trained to sit in a primate chair, and voluntarily accept neck and arm restraint, and immobilisation of the left hand within a static manipulandum, but were not head-fixed. All animal procedures were carried out under appropriate UK Home Office licenses in accordance with the Animals (Scientific Procedures) Act 1986 (2013 revision), and were approved by the Local Research Ethics Committee of Newcastle University.

### 2.1.2 *Wrist torque-controlled task*

We trained subjects to perform a task in which two-dimensional (2-D) isometric left-wrist torque (measured by a static six-axis force/torque manipulandum; ATI Industrial Automation, Apex NC, USA) controlled the 2-D position of a circular cursor on a screen placed ~50 cm in front of the subject (**Figure 2-1, right**). We refer to this here as the ‘torque task’.

Each trial was initiated by the cursor entering a central circular ‘home’ region, reflecting zero torque (relaxation). A peripheral circular target appeared at one of eight positions spaced equally around a circumference centred on the home position. After a variable ‘cue’ period (between 1.2 and 2.4 s)—during which subjects had to remain in the home region—they were required to move the cursor to overlap the target for a fixed ‘hold’ period (0.6 s). If successful, subjects heard a reward tone, and were given a small piece of fruit reward by a researcher. There was no time limit for an individual trial. Around 300–500 trials were performed per day in a single session.

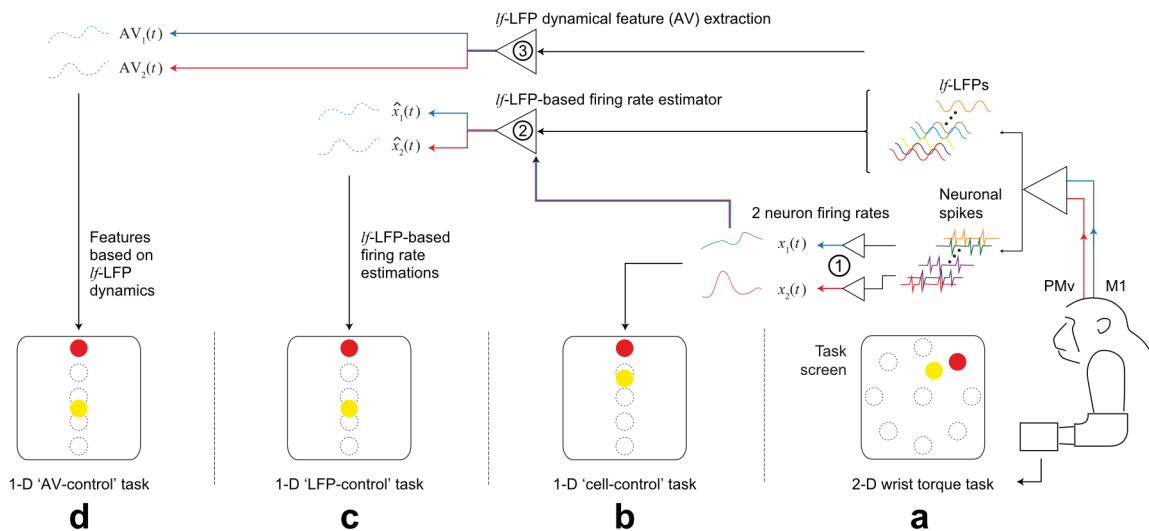


**Figure 2-1** Illustration of the experimental setup and four main tasks performed by the monkeys

Unless otherwise stated, neural recordings were made from the right cortical hemisphere, and behaviour was recorded at the left wrist.

- 2-D wrist torque-controlled task: torque recorded from the left wrist via a manipulandum and mapped to  $x$  and  $y$  co-ordinates of a 2-D task with 8 peripheral targets.
- 1-D 'cell-control' task: Firing rates calculated in real time, indicated by ①, and mapped 2-to-1 to up and down directions of a 1-D task with four targets.
- 1-D 'LFP-control' task: As per **b**, but with firing rate estimates calculated in real time from  $l_f$ -LFPs, indicated by ②.
- 1-D 'AV-control' task: "AV" is an abbreviation for areal velocity. It is a feature extracted from the dynamics of the multichannel  $l_f$ -LFP, indicated by ③. This experiment is explained in detail in the Methods of **Chapter 5**.

### 2.1.3 Brain-machine interface tasks

Following surgical implantation of electrodes in the right cortical hemisphere, subjects also performed one of three different types of biofeedback BMI task, in which 1-D screen cursor position was controlled by the normalized amplitude of signals derived from neural recordings, to acquire 1-D targets (**Figure 2-1, left**). A prototypical day's recording consisted of 50 trials of the torque task followed by 250–450 trials of a BMI task.

There were three main types of BMI task: 'cell-control', 'LFP-control' and 'AV-control'. Monkey A performed only the 'cell-control' task. Monkey D first performed a series of 'cell-control' sessions followed, after an intervening period of 6 months, by the 'LFP-control' task, based on a different sample of neurons, followed by the 'AV-control' task. Monkey R performed only the 'LFP-control' task. Monkey S performed the 'torque task' as well as a unique bimanual task described in **Chapter 5**. Monkey U only performed the 'torque task' during this experimental period.

### 2.1.3.1 ‘Cell-control’ BMI task.

In this task, 1-D cursor position was controlled by actual firing rates of neurons. In general, for BMI tasks we tried to choose neurons with large amplitude, clean spikes, but did not otherwise select based on task-related modulation of firing rate. Moreover, the axis of 1-D cursor movement under brain control was chosen at random so as to have no consistent relationship with the preferred direction of neurons.

Two neurons were discriminated during the ‘torque task’. The smoothed instantaneous firing rate ( $x$ ) of each neuron was calculated in realtime by convolution of spike times with a rectangular window (width 400 ms). Because the firing rates of different units were modulated over different ranges, we applied linear scaling to normalise firing rates to screen co-ordinates, based on the distribution of the firing rates obtained during the torque task. Each firing rate was mapped to normalised screen co-ordinates such that the 5<sup>th</sup>/95<sup>th</sup> centiles of this distribution corresponded to  $\pm 50\%$  (in screen co-ordinates, where 100 % represents the screen edge).

Targets appeared at four positions:  $-70\%$ ,  $-35\%$ ,  $35\%$  and  $70\%$ . Within a day’s experiment, for blocks of 100 trials each, one-dimensional cursor position,  $c$ , was controlled by the firing rate of one cell,  $x_{1(\text{norm})}$  or by the summed,  $(x_{1(\text{norm})} + x_{2(\text{norm})})/\sqrt{2}$ , or differential,  $(x_{1(\text{norm})} - x_{2(\text{norm})})/\sqrt{2}$ , firing rates of the two neurons, where the factor of  $1/\sqrt{2}$  was used to make all targets equidistant from the origin in the 2-D normalised neural space.

### 2.1.3.2 ‘LFP-control’ BMI task

In this task, the 1-D cursor position was controlled by the smoothed *estimated* firing rates of neurons. Each day, we built a model using data from the torque task that was then used to estimate simultaneously the firing rates of two neurons from *lf*-LFP data in realtime.

The two estimated firing rates were smoothed online using an exponential decay filter with a decay constant  $\lambda = 0.25$  s. Cursor position was then controlled by either the smoothed estimated firing rate of one neuron or by the difference between two smoothed firing rate estimates. Each firing rate estimate was mapped to normalised screen co-ordinates using the median and 5<sup>th</sup>/95<sup>th</sup> centiles of its distribution (as described for the ‘cell-control’ task).

Targets appeared at four positions:  $-70\%$ ,  $-35\%$ ,  $35\%$  and  $70\%$ . During one-cell control, the cursor position,  $c$ , was equal to the scaled estimated firing rate,  $\hat{x}_{1(\text{norm})}$ . During two-cell control,  $c = (\hat{x}_{1(\text{norm})} - \hat{x}_{2(\text{norm})})/\sqrt{2}$ .

### 2.1.3.3 ‘AV-control’ BMI task

In this task, cursor position was controlled by signals calculated directly from multichannel  $lf$ -LFP, without use of spike recordings. To do this, we used dynamical features of the multichannel  $lf$ -LFP. AV is an acronym for ‘areal velocity’. The methodology and results of this approach are the subject of **Chapter 5**, and are detailed there.

## 2.2 Electrode design and construction

For **Chapters 3 to 5** we used only moveable tungsten microwire electrode arrays. These are detailed in the following text. The development of a new type of hybrid array for recording  $lf$ -LFPs is the subject of **Chapter 6**, and details are given there.

### 2.2.1 Moveable tungsten microwire array

Each array consisted of 12 tungsten microwires ( $50\ \mu\text{m}$  diameter, impedance  $100\text{--}200\ \text{k}\Omega$  at  $1\ \text{kHz}$ ; Advent Research Materials, UK), passing through parallel polyimide guide tubes in two rows of six, aligned to the central or arcuate sulcus, with spacing of  $\sim 200\ \mu\text{m}$  within rows and  $\sim 2\ \text{mm}$  between rows. The arrays were made by hand, according to the design and methods given by Jackson and Fetz (2007), using nylon connector blocks (ITT Cannon, Irvine CA, USA), gold pins (ITT Cannon),  $50\ \mu\text{m}$  tungsten microwires, polyimide guide tubes (Cole-Parmer, London, UK) two-part silicone adhesive (Silastic®, Dow Corning, Auburn MI, USA) and two-part dental cement (see below). **Figure 2-2** is a reproduction of Figure 1 from Jackson & Fetz (2007), because understanding of the construction of the array is important to **Chapter 5** of this thesis.

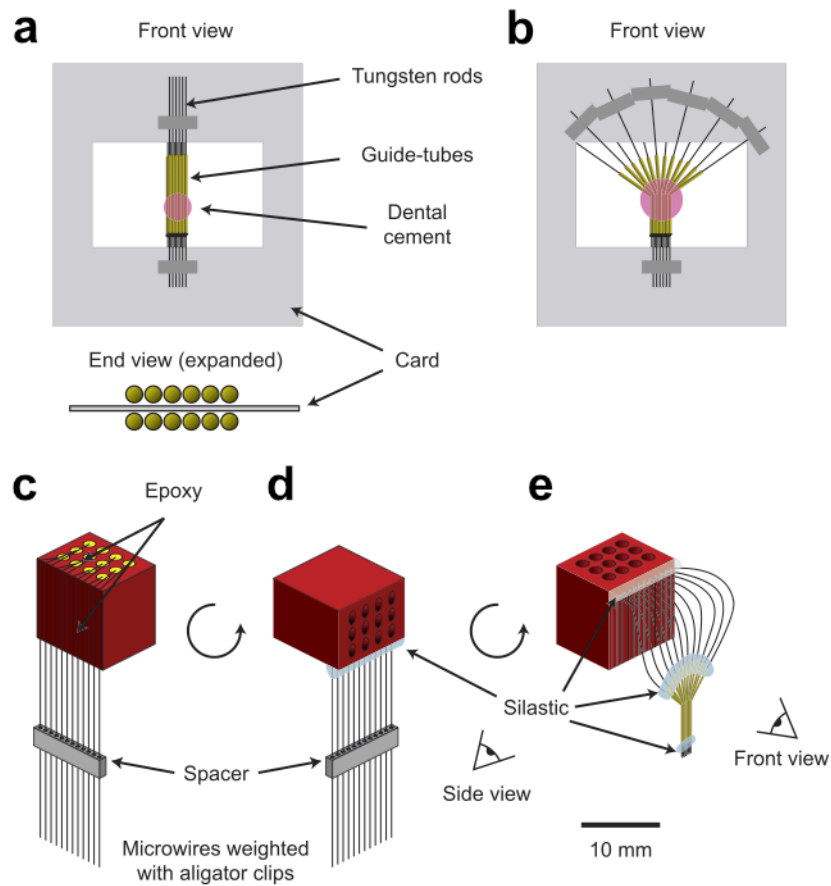


**Figure 2-2** Construction of the moveable tungsten microwire array used in this study.

- (a) Guide tubes were aligned on parallel tungsten rods and fixed with dental cement. Two rows of 6 tubes were positioned on each side of a piece of card to produce a  $6 \times 2$  array (see expanded end view).
- (b) Guide tubes were splayed at one end and more cement was applied.
- (c) Weighted microwires hung parallel along one side of the connector. Epoxy was applied to electrically insulate the contacts and fix the wires.
- (d) Connector block was rotated and *Silastic* was applied to the wires for strain relief.
- (e) Finished implant. Wires ran in loops from the connector block to the guide-tube array. Guide tubes were filled with antibiotic ointment and sealed at both ends with *Silastic*.

— Figure and legend reproduced from Jackson & Fetz (2007), *Journal of Neurophysiology* **98** Figure 1a–e, p. 3111 (American Physiological Society)

The implant was made in two stages. Individual components were first constructed and autoclave sterilised. The final implant was then constructed under sterile conditions, just prior to the surgery, and kept under sterile conditions until implantation.

Individual microwires could be moved to acquire new neuron recordings. Depending on the experiment, we left the microwires in place for many months at a time, or moved them as often as twice-per-week to obtain new signals.

## 2.3 Surgical methods

Chronic electrodes were implanted in primary motor cortex (M1) and ventral premotor cortex (PMv). PMv was targeted, in addition to M1, to enable between-area, as well as within-area comparison of spike-LFP and LFP-LFP relationships. PMv is particularly useful for this, because it demonstrates both direct (corticomotoneuronal) and indirect (via M1) control of forelimb muscles (Boudrias et al 2009).

### 2.3.1 Surgical planning

Structural magnetic resonance imaging (MRI) scans were performed on all subjects and imported into MATLAB (Mathworks, Natick MA, USA). Digital MRI images were rotated (using MATLAB function `MRIrotate.m`, S. Baker, Newcastle University) and a 3-D model of brain surface and bony cranium was generated from slices (using MATLAB function `ROIinator.m`, J. B. Zimmermann, Newcastle University).

2-D projections (in MATLAB) and 3-D images (in *Blender* software; Blender Foundation, Amsterdam, Netherlands) were used to locate the precise coordinates in each subject of M1 (antero-posterior ~11 mm, medio-lateral ~15 mm) and PMv (AP ~20 mm, ML ~20 mm) in the right cortical hemisphere. **Figure 2-3** illustrates the surface anatomy of the macaque motor cortex, with approximate implant locations indicated. Please note that the illustration shows a view of the left hemisphere. We implanted our arrays in the right hemisphere, but the surface anatomy of the right motor cortex is an exact mirror of the left.

3-D rendering software and ‘3-D-printed’ acrylic skull models (Shapeways, Eindhoven, The Netherlands) were used to plan the location of all connectors and screws on the animal’s skull, and also to customise the size and shape of a titanium transcutaneous implant to each individual animal’s skull (**Figure 2-4**).

This titanium cranial implant was required to protect the electrode arrays and connectors from damage, and was sized and designed such that a battery-powered ‘Neurochip-2’ device (Zanos et al. 2011) could be installed if desired, for home-cage recordings. The customisation to skull shape was performed to minimise the footprint of the implant, and thus reduce the likelihood of peri-implant infection. Grade 5 titanium (Ti-6Al-4V) was used for areas in contact with living tissue, in order to maximise biocompatibility of the implant. The titanium

implant was degreased, cleaned with enzymatic cleaner, sonicated and autoclave sterilised prior to implantation.

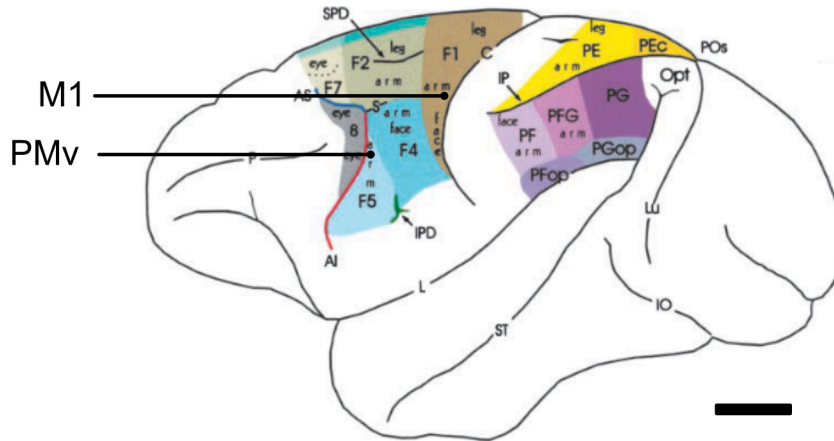


**Figure 2-3** Illustration of a left lateral view of the macaque brain. (Actual size.)

Nomenclature in the original source figure follows the convention of labelling ‘frontal’ (F) and ‘parietal’ (P) cortical areas. Relevant labels: **F1** (brown), primary motor cortex; **F5** (light blue), ventral premotor cortex; **C** (black line), central sulcus; **AS** (blue line), superior arcuate sulcus; **AI** (red line), inferior arcuate sulcus; **S** (black line), spur of the arcuate sulcus. Scale bar: 10 mm.

The label ‘**M1**’ indicates the approximate target for electrode implantation in the forearm/hand area of primary motor cortex, just anterior (rostral) to the central sulcus.

The label ‘**PMv**’ indicates the approximate target for electrode implantation in the forearm/hand area of ventral premotor cortex, just posterior (occipital) to the arcuate sulcus, and caudal to (below) the spur of the arcuate sulcus.

— Figure adapted from Geyer et al. (2000) *Anat. Embryol.* **202** (Springer-Verlag)

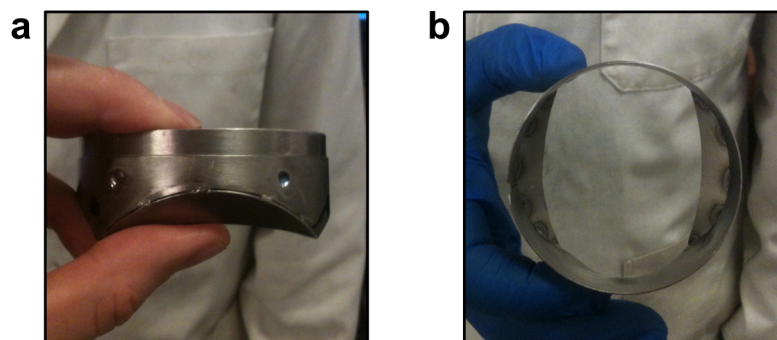


**Figure 2-4** Photographs of example customised titanium implant

(a) Right side view and (b) top view of a customised titanium implant for Animal S, prior to cleaning and autoclave sterilisation. The implant was profiled at front, back and sides to match the 3-D acrylic skull model of each animal.

### **2.3.2 Surgical procedures**

Surgery was performed in two stages: a first-stage surgery in which electromyography (EMG) electrodes were implanted, followed by a one-month period of recovery, followed by a second-stage surgery in which cortical electrodes and the titanium trans-cutaneous cranial implant were implanted. Two stages were used to minimise the length of anaesthetic periods, thereby to optimise recovery and reduce infection, but also to allow the animal a chance for acclimatisation and rehabilitation between surgeries.

All surgeries were performed under sterile conditions and under general anaesthesia induced with propofol (2–4 mg kg<sup>-1</sup>) and maintained with sevoflurane (minimum alveolar concentration 1.8–1.9 %) and alfentanil infusion (0.2 µg kg<sup>-1</sup> min<sup>-1</sup>). Ventilation was supported, and expired carbon dioxide concentration and peripheral oxy-/deoxy-haemoglobin ratio were monitored. An intra-arterial line and urethral catheter were inserted to monitor circulatory status, and intravenous fluid support was provided (Hartmann's saline, 5–10 ml kg<sup>-1</sup> h<sup>-1</sup>), while body temperature was maintained between 36.5 and 37.5 °C throughout. Animals received peri-operative methylprednisolone (5.4 mg kg<sup>-1</sup> h<sup>-1</sup>) and cefotaxime (250 mg, 2-hourly), as well as post-operative antibiotics (ceftiofur 3 mg kg<sup>-1</sup>), analgesia (meloxicam 0.2 mg kg<sup>-1</sup>) and steroids (methylprednisolone).

### **2.3.3 EMG electrode implantation**

Bipolar EMG electrodes, made from braided stainless-steel wire, with or without *Dacron* patches (Microprobes for Life Sciences, Gaithersburg MD, USA), depending on the animal, were implanted to record the activity of 6–10 forelimb muscles in the arms and hands. Wires were tunneled sub-cutaneously to a connector mounted on the subject's head. A ground wire with connector was connected to a skull screw on the subject's head.

### **2.3.4 Cortical electrode implantation and transcutaneous titanium implant fixation**

Guided by the prior surgical planning, we made individual craniotomies over primary motor cortex (M1) and ventral premotor cortex (PMv) of the right hemisphere. After dural resection, we placed a custom-made moveable microwire array (**Figure 2-5a**) and subdural surface

reference wire (de-insulated 50  $\mu\text{m}$  tungsten microwire) over each area. The craniotomy was sealed with cyanoacrylate glue, sterile compressed sponge (*Gelfoam*, Pfizer, Sandwich, UK) and gentamicin-impregnated antimicrobial dental acrylic (*Gent-C-ment*) (**Figure 2-5b**). It should be noted here that, unlike the other subjects, Monkey S received bilateral M1 implants, for reasons that are described in **Chapter 5**.

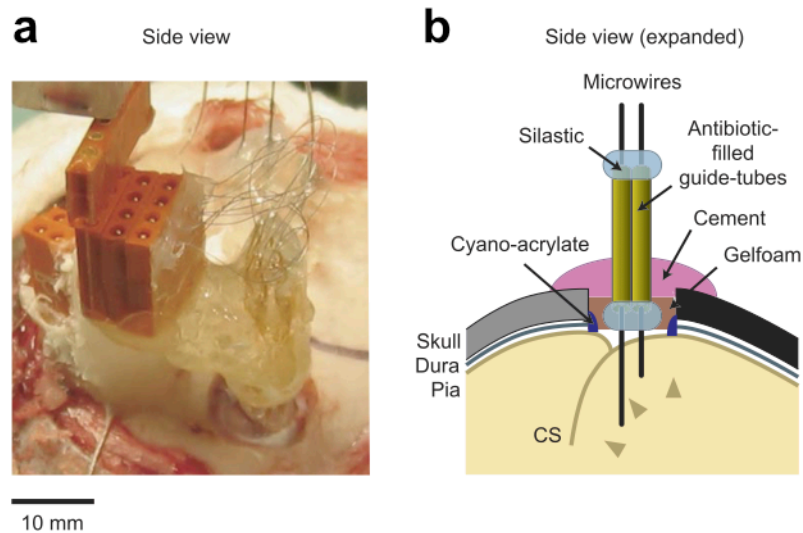


**Figure 2-5** *Implantation of the cortical electrode array at the craniotomy site.*

- (a) Implant as it was fixed to the skull during surgery. Microwires can be seen entering the brain through a craniotomy.
- (b) Cross section showing microwires penetrating the pia mater anterior to the central sulcus (CS) through a craniotomy and dural opening. Pia mater was bonded to the edge of the craniotomy with cyanoacrylate glue and the craniotomy was sealed with Gelfoam and dental cement.

— Figure and legend reproduced from Jackson & Fetz (2007), *Journal of Neurophysiology* **98** Figure 1f,g, p. 3111 (American Physiological Society)

During the same anaesthetic, skull screws were placed at mechanically advantageous locations in the skull, and the periosteum was sealed with a thin layer of *Super-Bond C&B* dental adhesive acrylic (Sun Medical, Moriyama City, Japan). The titanium cranial implant was then located on the skull, and fixed to the head using dental acrylic (*Simplex Rapid*, Kemdent, Swindon, UK). The skin and soft tissue margins were drawn together around the titanium implant using absorbable sutures, and the animal given post-operative care, as described above.

Animals recovered and returned to training for 1–2 weeks before the microwires were lowered into the cortex. Each microwire was advanced until clear spiking activity was heard.

Then, depending on the experiment, microwires were moved as often as two times per week, or left for many weeks recording the same signals.

## **2.4 Electrophysiological recordings**

Two different recording systems were used to acquire data for this thesis. Both recording systems were used with Monkeys A and D. Only the ‘TDT system’, described in the next section, was used with Monkeys R, S and U.

### **2.4.1 TDT RZ2-based recording system**

Unless otherwise stated, data were acquired using a Tucker Davis Technologies (TDT) RZ2 digital signal processor and acquisition system (TDT, Alachua FL, USA). Cortical signals were acquired by a digitizing pre-amplifier (48.8 kHz; frequency response 3 dB for 0.35 Hz–7.5 kHz, 6 dB for 0.2 Hz–8.5 kHz) from 24 microwire electrodes, relative to a subdural reference. Neuronal spiking activity was extracted by digitally band-pass filtering the raw signal (1–8 kHz) and thresholding. We classified single-unit spikes in a semi-supervised fashion using the TDT online principal component-based feature extraction and clustering software suite. In realtime BMI experiments, the *lf*-LFP was extracted from the raw signal online, by low-pass filtering at 5 Hz (digital biquad filter), before downsampling to 48.8 Hz.

### **2.4.2 CED Power-1401-based recording system**

Where specifically indicated, data were acquired using a system based around a CED Power-1401 acquisition system (Cambridge Electronic Design, Cambridge, UK). Signals were amplified and filtered into LFP and spike bands using two MPA8I headstages and a PGA1632 amplifier (Multichannel Systems, Reutlingen, Germany). LFP signals were amplified (gain 5000) and band-pass filtered (1 Hz to 300 Hz) before being sampled (1000 Hz) by the Power-1401. Spike activity was amplified (gain 10000), band-pass filtered (300 Hz to 8 kHz) and sampled (18.5 kHz), after which single-unit spikes were classified, in a supervised fashion, using the template-based online spike sorter of the Power-1401.

### **2.4.3 EMG and task recording**

EMG signals were amplified (gain 1000) using a differential alternating-current (AC) amplifier (A-M Systems, Sequim WA, USA) and band-pass filtered (10 Hz to 1 kHz with a 50 Hz notch filter) before being sampled by the TDT-RZ2 or Power-1401 (2 kHz). Torque produced at the manipulandum and a variety of task events were acquired using a NI-USB-6229 (National Instruments, Austin TX, USA) and sampled by the TDT-RZ2 or Power-1401 (100 Hz).

## **2.5 Signal pre-processing and offline analysis**

All offline analysis was performed in MATLAB. Channels were excluded from further analysis if visual inspection of the LFP signals indicated that the electrodes or their insulation were damaged (flat signals, consistent wideband noise or large artefacts). If not already extracted online, we extracted *lf*-LFP signals offline by low-pass filtering LFPs at 5 Hz (zero-phase 5<sup>th</sup>-order Butterworth filter, MATLAB), followed by downsampling to 48.8 Hz.

## **2.6 Statistical analysis**

Statistical analysis was performed in MATLAB and SPSS (IBM Corporation, Armonk NY, USA), and is described in detail in each of the individual chapters.

## **2.7 Chapter summary**

- Macaque subjects were implanted with moveable tungsten microwire electrodes in the right cortical hemisphere, in M1 and PMv.
- Awake, behaving recordings of neuronal spiking, LFP, EMG and torque were taken as the animals performed a centre-out, isometric wrist torque-controlled task, as well as several different BMI tasks, controlled either by neuronal firing rates, or by firing rate estimates derived from *lf*-LFP activity.
- A third type of BMI task, controlled by dynamical features in the multichannel *lf*-LFP, is introduced and described fully in **Chapter 5**.



# Chapter 3. Spike-LFP relationships in motor cortex for use in BMI applications

*In which I introduce low-frequency LFP phenomena associated with movement-related activity in primate motor cortex, and the concept of the spike-related slow potential (SRSP).*

## 3.1 Introduction

In **Chapter 1**, I introduced the LFP, and the *lf*-LFP specifically. I also introduced its merits as a motor BMI input signal. Here we explore the properties and utility of the *lf*-LFP in more detail; in particular, its relationship to cortical neuronal spiking.

### 3.1.1 *The low-frequency LFP (lf-LFP) during movement*

Historically (particularly based on early EEG studies), low-frequency LFP bands (< 5 Hz) have become associated with periods of behavioural inactivity in mammals, such as slow-wave sleep (Chauvette et al. 2011). During such periods, wide areas of cortex (and other non-cortical areas) become highly synchronized at low frequencies, and this is reflected by very high-amplitude, low-frequency features ('slow-waves') in the LFP/EEG, and highly correlated spiking (Steriade et al. 2001). Until recently though, there been relatively little focus on the *lf*-LFP during alert brain states, such as goal-directed movement. However, as already presented in **Section 1.2.2**, a number of recent studies have demonstrated that these low-frequency components contain a wealth of information about movement kinematics.

Physiologically speaking, the fact that kinematics can be decoded from the *lf*-LFP, with non-redundant information available from electrodes spaced as close as 350  $\mu\text{m}$  (Mehring et al. 2004; Rickert et al. 2005), is at odds with the concept that the *lf*-LFP signal only reflects widespread cortical synchrony. This fact supports the alternative hypothesis: that low-frequency activity in the motor cortex is at least in part generated at small spatial scales (within cortical area, so on the scale of millimetres) by the correlated activity of local populations of neurons, which for convenience, we refer to here as 'ensembles'.

According to such a hypothesis, each of these cortical ensembles may have its own behaviour during movement—reflecting some aspect of local cortical processing—whilst there could be only partial correlation *between* ensembles. Since *lf*-LFPs likely integrate over large spatial scales, any particular *lf*-LFP recording would therefore contain a *mixture* of multiple signals from relatively independent ‘sources’ (both local and distant), each transmitted by volume conduction to the electrode.

### **3.1.2 Using the *lf*-LFP as a biofeedback BMI control signal**

Unlike spiking activity, where firing rate modulation is relatively well-understood, it is unclear which specific *features* of the LFP can be brought under volitional control and would thus be applicable for closed-loop BMI applications. This is a particular problem for the *lf*-LFP, whose importance in relation to movement kinematics has only been appreciated relatively recently.

Some studies have suggested that LFP *power* may be a feature that is useful for closed-loop BMI. Power in the low-gamma range (30–50 Hz in cited study) can certainly be modulated under a biofeedback BMI paradigm (Engelhard et al. 2013) and the power of broader frequency bands has been shown to be modulated under a closed-loop biomimetic BMI paradigm (So et al. 2014). However, the majority of studies exploring the use of LFPs in closed-loop BMIs take a ‘black-box’ approach to generating biomimetic, kinematic decoders; for example, using Weiner filter cascades (Flint, Wright, et al. 2012; Flint et al. 2013; Scheid et al. 2013) or Kalman filters (Stavisky et al. 2015). Such supervised machine learning-based methods require no *a priori* understanding of the physiological characteristics of the *lf*-LFP to perform feature selection. Unfortunately, this is likely to hinder the applications of the *lf*-LFP signal beyond biomimetic decoding of kinematics.

Going beyond simple kinematic decoding of brain signals is likely to be important for the development of better BMIs. For example, it is known that acquisition of BMI skill is often associated with profound changes in the tuning of neurons contributing to the decoder (Taylor et al. 2002; Carmena et al. 2003; Ganguly et al. 2011). Although such changes can be reduced by recalibrating decoding algorithms online, neuroplasticity may nevertheless be beneficial for the retention of BMI skill, as well as resistance to interference from other tasks (Fan et al. 2014). These tuning changes indicate that the specific neuromotor mappings that subserve natural movements are unnecessary for learned BMI control (Jackson & Fetz 2011), and

likely reflect the ease with which the activity of individual neurons can be modulated under biofeedback paradigms (Fetz 1969; Hwang et al. 2013).

Based on these desirable properties of spike-based BMIs, we reasoned that, if we could identify *lf*-LFP components with a strong and consistent relationship to the firing rates of local neurons, then these should also be amenable to operant conditioning and therefore provide useful features for biomimetic BMIs. In addition, by using spike-related features in the *lf*-LFP (rather than firing rates directly), we would also be able to exploit the desirable properties of the *lf*-LFP: specifically, that it can be sampled on a time-scale comparable to kinematics (tens of Hertz), rather than on the time-scale of action potentials (tens of kilohertz).

### ***3.1.3 Modelling multichannel spike-LFP and LFP-spike relationships***

The correlation between single neurons and individual LFPs has been previously investigated using a range of techniques (Rasch et al. 2008; Rasch et al. 2009; Nauhaus et al. 2009; Okun et al. 2010; Zanos et al. 2012; Einevoll et al. 2013). However, to date there have been surprisingly few studies of the extent to which neural firing rates can be estimated from *multiple* LFPs and vice versa, perhaps in part due to the persisting assumption that multiple LFPs convey largely redundant information arising from the synchronous activity of many neurons (Berens et al. 2008; O'Leary & Hatsopoulos 2006; Hwang & Andersen 2013).

In the monkey visual cortex, a single LFP channel has been estimated by linear summation of multiple potentials associated with spike activity (Rasch et al. 2009; Nauhaus et al. 2009). Moreover, Rasch and colleagues (2008) found that in anaesthetised (but not awake) animals, the firing rate of a single neuron could be predicted from a single channel of LFP (Rasch et al. 2008). However, this study did not examine whether performance could be improved by using multiple LFPs. In the motor cortex, Bansal and colleagues (2011) have used multiple LFPs to decode the summed spiking activity of all neurons recorded on an electrode array (Bansal et al. 2011), but did not investigate the possibility of predicting the firing rates of individual neurons.

In **Section 3.1.1**, we hypothesised that each *lf*-LFP consists of a mixture of signals, coming from multiple sources within the cortex. If we use the common analogy of the 'cocktail party problem' (Cherry 1953), we can think of each *lf*-LFP signal as a 'microphone' signal, picking

up a mixture of sources ('voices') from a volume of tissue ('room'), as well as a considerable amount of correlated and uncorrelated noise (e.g. the pickup of movement artefacts and thermal Johnson-Nyquist noise, respectively). However, because each *lf*-LFP signal records a slightly different mixture of these sources, we can use source-separation techniques to infer the sources (finding a solution to the so-called 'inverse problem').

Our approach in this Chapter was to assume that the sources salient to movement generation are associated with concurrently-recorded spike activity from local ensembles. We therefore studied the relationship between the spiking of neurons and the multichannel *lf*-LFP.

Specifically, we investigated whether we could estimate the firing rate of individual neurons from the multichannel *lf*-LFP, with a view to using this signal (the *estimated firing rate*) as a biofeedback BMI control signal.

## 3.2 Aims

This Chapter therefore has three main aims:

**Aim 1:** To study the relationship between neuronal spiking and the multichannel *lf*-LFP in primary motor (M1) and ventral premotor (PMv) cortex.

**Aim 2:** To estimate the firing rate of individual neurons based on using source-separation techniques on the multichannel *lf*-LFP.

**Aim 3:** To quantify the performance of firing rate estimation, and compare the properties of firing rate estimates to actual firing rates.

## 3.3 Methods and Results

### 3.3.1 *Experimental setup*

Three subjects (monkeys D, R and A) performed the 2-D centre-out isometric wrist torque task described in **Section 2.1.2**. We recorded LFPs and spike activity using moveable microwire arrays implanted in the right M1 and PMv cortices, as described in **Section 2.4**.

### 3.3.2 *Spike-triggered averaging of the LFP*

Event-triggered averaging is a common approach in neuroscience for examining the temporal relationship between a point process (such as the spike times of a neuron, or the times of a behavioural event) and a waveform signal (such as an LFP recording or behavioural response). The spike-triggered average (STA) LFP,  $C(\tau)$ , is the average value of the LFP waveform,  $y(t)$ , in a time base,  $\tau$ , around when a spike is fired, over the duration ( $0 \rightarrow T$ ) of the recording (Dayan & Abbott 2005).

The STA-LFP represents the average LFP taken at the times of spike occurrences, and with proper normalization (division by the total number of spikes), is equivalent to the cross-correlation between the LFP and the spike train (Ito 2015) – a property that will become important later.

Working in the digital domain, where time,  $t$ , in the recording is discretised (according to the sampling interval), and signal amplitude is also discretised (according to the sampling depth): for a spike occurring at time  $t_i$ , we define a time window,  $t_i + \tau$ , around that spike (where  $\tau$  can be negative and positive) and use that window to capture a segment of the waveform signal,  $y(t_i + \tau)$ . We then sum these waveform segments over all  $n$  spikes in the recording,  $i = 1, 2, \dots, n$ , and normalise by dividing by the total  $n$ . (Method illustrated in **Figure 3-1**).

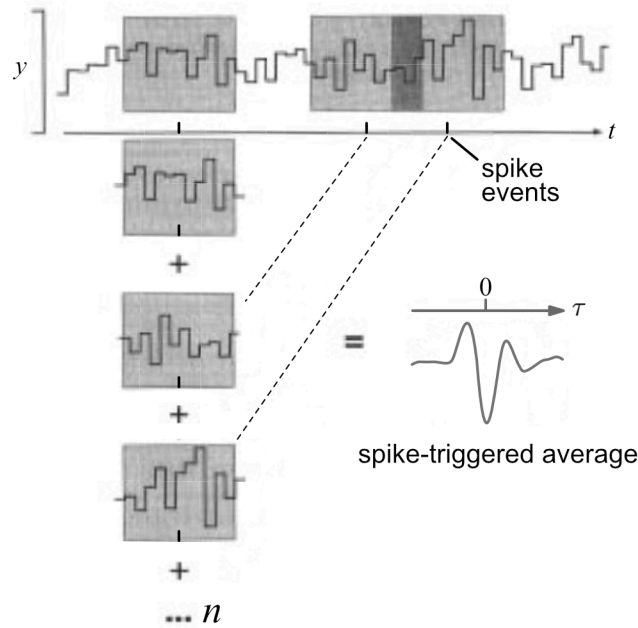


**Figure 3-1** Schematic of the spike-triggered averaging approach.

Iterative spike-triggered averaging approach, as described in the text.

— Figure adapted from Dayan & Abbott (2005) Figure 1.8 in *Theoretical Neuroscience* (MIT Press).

Thus,

$$C(\tau) = \frac{1}{n} \sum_{i=1}^n y(t_i + \tau) \quad (3.1)$$

The method shown in Equation 3.1 was used for calculation of spike-triggered averages in **Figure 3-2**, using an iterative approach in MATLAB, typically with a window width of  $-2 < \tau < 2$ .

Normalisation by the total number of spikes ( $n$ ) makes the STA equivalent to the cross-correlation between the waveform signal,  $y(t)$ , and the spike density function (instantaneous firing rate),  $x(t)$ . Therefore, (assuming sufficient data length and sampling rate), the STA is commonly approximated in the literature as an integral (that is, using continuous notation), in the form:

$$C(\tau) = \frac{1}{n} \int_0^T x(t)y(t + \tau) dt, \quad (3.2)$$

for the range  $-2 < \tau < 2$ . In this thesis, unless otherwise stated,  $x(t)$  was approximated by binning spikes into time bins with a width corresponding to the sampling interval of the corresponding LFP.

For clarity, for the remainder of this document, I will be expressing all functions relating to signal processing using this continuous (rather than discrete) notation.

### 3.3.3 The spike-related slow potential (SRSP)

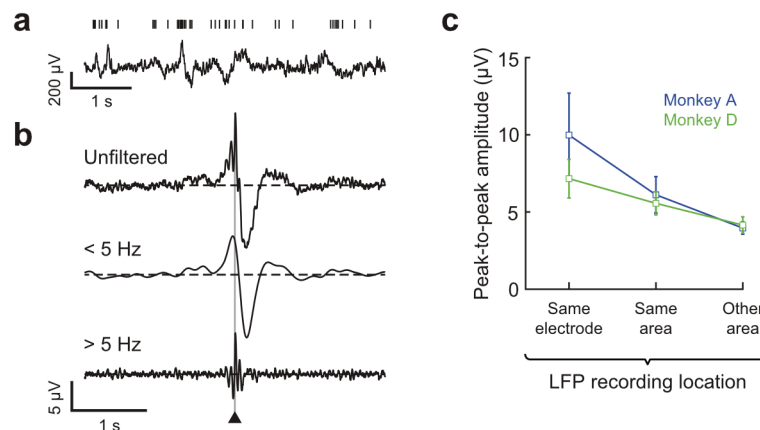


**Figure 3-2** Spike triggered average of the LFP and variation in amplitude of the STA lf-LFP with cortical area.

- (a) Representative spike raster of a single neuron (*top*) and representative LFP signal (*bottom*) recorded in M1 of Monkey D.
- (b) STA of LFP calculated using an iterative (discrete) approach, separated into full-bandwidth (*top*) low- (*middle*) and high-frequency (*bottom*) bands.
- (c) Mean peak-to-peak amplitude of STA of low-frequency LFP recorded on the same electrode as a neuron, other electrodes in the same cortical area (M1 or PMv) and electrodes in the other cortical area. Error bars show  $\pm$  standard error of the mean [s.e.m.] ( $n = 46$  neurons per monkey).

Spike-triggered averages (STAs) of the full-bandwidth LFP in our datasets (e.g. **Figure 3-2b**, *top*) typically exhibited beta-band ( $\sim 20$  Hz) phase-locking (revealed clearly by high-pass filtering  $> 5$  Hz; e.g. **Figure 3-2b**, *bottom*), as well as large and consistent low-frequency features, revealed clearly by low-pass filtering  $< 5$  Hz; e.g. **Figure 3-2b**, *middle*). We coined the term ‘spike-related slow-potentials’ (SRSPs) to refer to these low-frequency features, because they were spike-related (rather than event-related), and slow (low-frequency).

SRSPs were consistently observed in the STA-LFP, almost regardless of the choice of neuron, LFP channel or cortical area. However, we did find that there was considerable variation in the amplitude of the SRSP, and that this was systematically related to the relative locations of

the electrodes capturing the neuronal spiking and the LFP. The SRSP amplitude was typically largest in the LFP recorded from the same electrode as the spikes used to construct the average (**Figure 3-2c**). However, robust SRSPs were also observed in recordings from other electrodes within the same cortical area and—although smaller in amplitude—from the other cortical area (**Figure 3-2c**). Surprisingly, this suggested that the LFP contains a mixture of slow components reflecting the activity of both neighbouring *and distant* neural activity.

### 3.3.4 *Estimating low-frequency LFPs from neuronal firing rates*

To test this, we modelled the *lf*-LFP as a linear sum of contributions from the spike trains of multiple neurons. To achieve this, each spike train (firing rate) was convolved with a filter kernel that resembled the STA between that neuron and the *lf*-LFP of interest. As already discussed in **Section 3.3.2**, the normalised STA-LFP is equivalent to the cross-correlation between the firing rate and the LFP. However, with multiple inputs (firing rates), one also needs to consider the contribution of correlation between neurons. Therefore, rather than using the SRSP as a filter kernel directly, we used a system identification approach, to generate a filter kernel for each neuron, which resembled an SRSP waveform, but took account of the above subtlety.

To do this, the spike events of  $P$  neurons at time  $t$  (e.g. **Figure 3-3a**) were binned with the same sampling interval as the *lf*-LFP, demeaned and assigned to the  $P$ -dimensional vector  $\mathbf{x}(t)$ . *lf*-LFP vectors of  $Q$  recording channels were demeaned and assigned to the  $Q$ -dimensional vector  $\mathbf{y}(t)$ . We then used a ‘multiple-input, multiple-output’ (MIMO) model defined by the equation:

$$\mathbf{y}(t) = \int_{\tau_1}^{\tau_2} \mathbf{H}(\tau) \cdot \mathbf{x}(t + \tau) d\tau, \quad (3.3)$$

where  $\mathbf{H}(\tau)$  is an unknown  $Q$ -by- $P$  matrix of finite impulse response (FIR) filter kernels, that are a function of the time interval,  $\tau$ , relative to spike occurrence. For offline *lf*-LFP estimation, we used  $\tau_1 = -2.0$  s and  $\tau_2 = 2.0$  s. We used 75% of the duration of each torque tracking dataset as ‘training data’ for this model.

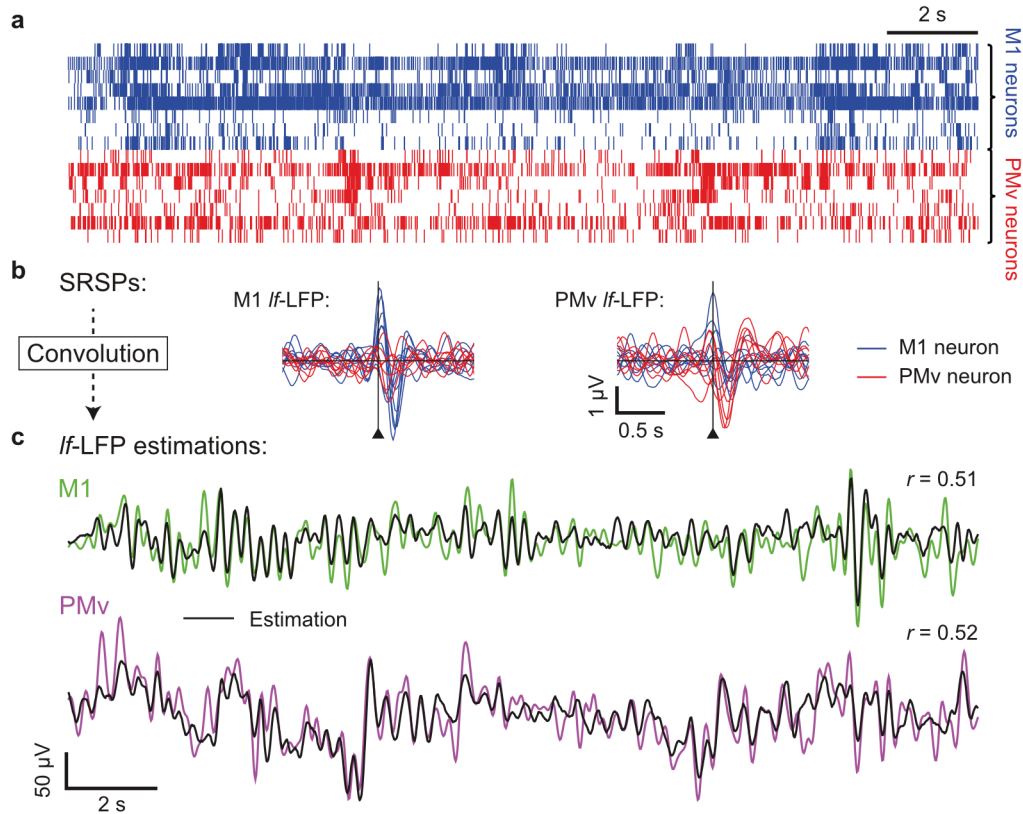


**Figure 3-3** Estimating lf-LFPs from firing rates.

- (a) Spike rasters for eight M1 (blue) and seven PMv neurons (red).
- (b) SRSPs for each neuron within a single M1 (left) or PMv lf-LFP (right).  $\blacktriangle$  Indicates time of spike.
- (c) lf-LFPs estimated using a linear model applied to validation data. Significance thresholds ( $p < 0.05$ , two-tailed; non-parametric bootstrap) for the indicated  $r$ -values were 0.07 and 0.11 for the M1 and PMv LFP, respectively. Data from monkey D.

We solved for the filter kernel matrix,  $\mathbf{H}(\tau)$ , of this system (**Figure 3-3b**) using the correlation-based approach of Perreault and colleagues, which is a computationally efficient approximation to least-squares regression under reasonable assumptions (Perreault et al. 1999; Westwick et al. 2006). Conceptually, an individual filter kernel element,  $h_{pq}(\tau)$ , from this matrix is very similar to the SRSP (and looks similar when plotted against  $\tau$ ), but it excludes contributions from the auto- and cross-correlation structure within multichannel firing rates.

Next, using these filter kernels, we produced lf-LFP estimates,  $\hat{\mathbf{y}}(t)$ , from firing rate data according to the same model with:

$$\hat{\mathbf{y}}(t) = \int_{\tau_1}^{\tau_2} \mathbf{H}(\tau) \cdot \mathbf{x}_{\text{val}}(t + \tau) d\tau \quad (3.4)$$

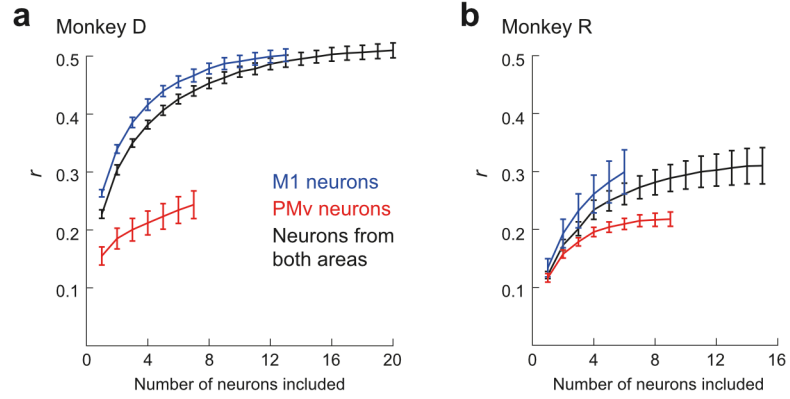
where  $\mathbf{x}_{\text{val}}(t)$  is firing rate data from validation data comprising the final 25% of the recording. The performance of the model was quantified by the Pearson's correlation coefficient,  $r$ , between the estimated  $lf$ -LFP,  $\hat{y}_q(t)$ , and the actual  $lf$ -LFP,  $y_q(t)$ . Using this method, we were reliably able to estimate  $lf$ -LFPs recorded from both M1 and PMv, with  $r$ -values on validation data of around 0.5 (e.g. **Figure 3-3c**).

#### **3.3.4.1 Performance with increasing numbers of neurons**

To determine how the quality of  $lf$ -LFP fit depended on the size of the neuronal sample, we estimated every  $lf$ -LFP channel in each cortical area ( $n = 10$ – $12$  LFPs, depending on subject and cortical area) using 120 random draws of  $P$  neurons (with replacement) increasing from one, up to the number of neurons available (Monkey D, max. 20 neurons; Monkey R, max. 15 neurons).

We found that the quality of fit ( $r$ ) increased monotonically as more neurons were included (**Figure 3-4**). The majority of useful information obtained from those recorded within the same cortical area as the estimated  $lf$ -LFP. But additional information was also obtained by including  $lf$ -LFPs from the other cortical area.

Estimating M1 *lf*-LFPs:



Estimating PMv *lf*-LFPs:

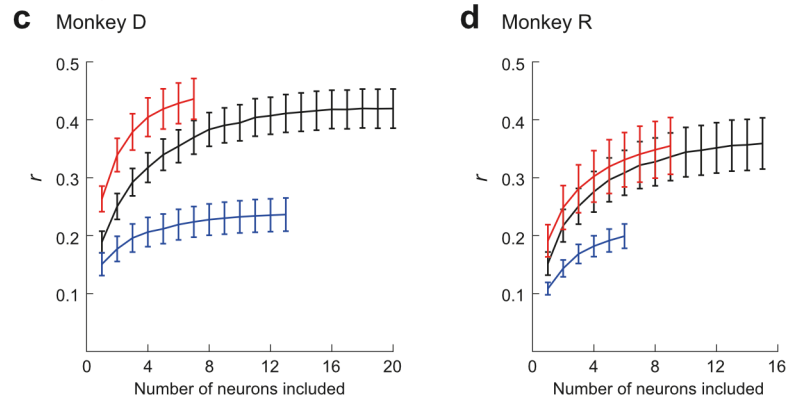


**Figure 3-4** *Neuron dropping curves for lf-LFP estimation*

- (a) Average correlation coefficient ( $r$ ) over validation data for M1 *lf*-LFPs in monkey D, estimated using an increasing number of neurons in M1 (blue), PMv (red) or both areas combined (black). Error bars show  $\pm$  s.e.m. ( $n=11$  *lf*-LFPs).
- (b) Same for M1 *lf*-LFPs in monkey R ( $n=10$ ).
- (c) Same for PMv *lf*-LFPs in monkey D ( $n=11$ ).
- (d) Same for PMv *lf*-LFPs in monkey R ( $n=12$ ).

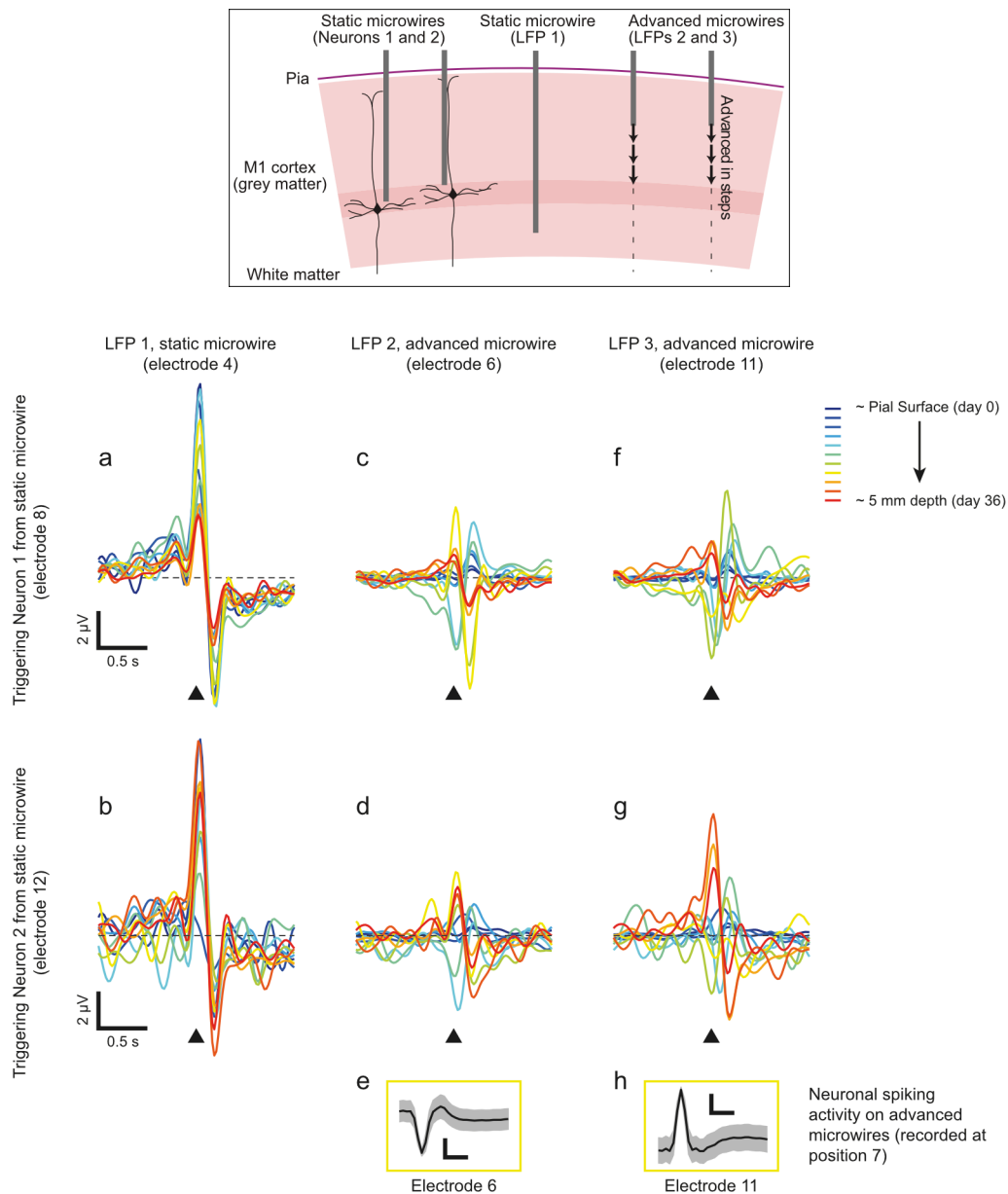


**Figure 3-5** (Top; black box) *Conceptual illustration of experiment in which microwires were advanced*

Two single neurons were recorded over thirty-six days from static microwires in M1 of Monkey D. *Lf*-LFP recordings were concurrently recorded from a static microwire located nearby in M1, and from two further M1 microwires whose depths were advanced manually by approximately 0.5 mm every 3 to 4 days under sedation. The relative locations of the electrodes in this figure are not meant to be interpreted literally. The figure merely illustrates the concept of the experiment.

**Figure 3-6** (Bottom) *Polarity inversion of SRSPs with increasing cortical depth.*

- (a–b) The polarity and shape of the SRSP from the static *lf*-LFP electrode remained highly consistent over time (with some minor variation in SRSP amplitude).
- (c–d, f–g) In contrast, the SRSP on the advanced electrodes gradually increased in amplitude with depth, before abruptly inverting polarity, then subsequently reducing in amplitude. Black arrows (▲) indicate time of triggering spike. Simultaneous spike recording from the advanced electrodes confirmed that the polarity inversion occurred within the cortical grey matter.
- (e, h) For example, spike shapes are shown from both advanced electrodes at position 7 (~ 3.5 mm depth, position corresponding to yellow line in the above panels); scale bars indicate 0.25 ms and 10  $\mu$ V.

#### **3.3.4.2 The local nature of the SRSP: polarity inversion with depth**

The nature of the SRSP (i.e. the filter kernels in the model) is fundamental to the results seen in the previous section. The results suggest that the SRSP reveals a signal component in the *lf*-LFP that is associated with the firing of a local cortical neuron. That is not to say that the signal in the *lf*-LFP is *due to* the activity of a *single* cell (the SRSP is much too large for that), but that there is an ensemble of neurons, represented by the recorded neuron, whose activity is making a relatively unique contribution to a particular *lf*-LFP signal.

To explicitly test the local nature of the SRSP, we performed an experiment in which, each day, we manually changed the depth of M1 electrodes on which we were recording *lf*-LFP signals, and analysed the changes in shape of the SRSPs, triggered by neurons from the same cortical area. The concept and details of this experiment are described in **Figure 3-5** and the results are described in **Figure 3-6** (and associated figure legends).

Most importantly, we found that the polarity of the SRSP inverted as we passed through the cortical grey matter. This strongly supports the hypothesis that the SRSP is being locally generated by a dipole source associated with the ensemble of neurons, of which the recorded neuron is a part. Polarity inversion occurs as the LFP electrode passes the depth equivalent to the zero-potential line of the dipole, where field potential inverts.

#### **3.3.4.3 SRSPs of individual neurons to multiple lf-LFPs**

We next used the SRSP to study the relationship between the spike train of each neuron and multiple LFP signals. To clarify: the reader should note that previously (e.g. **Figure 3-3**), we have been discussing the relationship between an individual *lf*-LFP and multiple neurons. We are now inverting this logic, and discussing the relationship between an individual neuron (whose spikes are used as ‘trigger events’ for the SRSP) and multiple *lf*-LFPs.

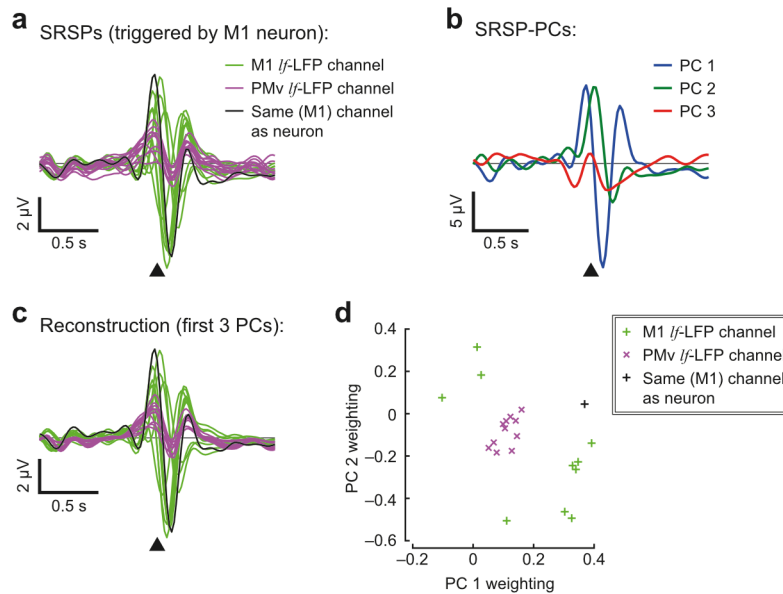


**Figure 3-7** *Principal component decomposition of the SRSP*

- (a) SRSPs of a single M1 neuron with multiple *lf*-LFPs from M1 (green) and PMv (purple) in Monkey D. Black trace shows the *lf*-LFP recorded on the same channel as the trigger neuron.  $\blacktriangle$  indicates time of spike.
- (b) First three principal components (PCs) of the SRSPs.
- (c) Reconstruction of the SRSPs in a using only the first three PCs.
- (d) Scatter plot showing the weightings of PC 1 and PC 2 used for this reconstruction.

We found that the SRSP associated with an individual neuron varied in both shape and polarity across different *lf*-LFP electrodes, particularly within the same cortical area as the trigger neuron (**Figure 3-7a**), despite the fact that *lf*-LFPs themselves appeared broadly similar. However, this variation could be explained by only a few principal components (PCs) (**Figure 3-7b,c**), suggesting that the contribution of a particular neuron to the multichannel *lf*-LFP comprised a limited number sources with distinct spatio-temporal profiles. The weightings of PCs in such reconstructions were particularly variable in size and polarity *within* a cortical area, and much less variable *across* cortical areas (**Figure 3-7d**), supporting the hypothesis that the sources in question are generated by the activity of local ensembles of neurons.

### 3.3.5 *Estimating single-neuron firing rates from multiple lf-LFPs*

On the basis of this, we developed a method to estimate these sources from the *lf*-LFP, and then used deconvolution to recover the firing rate of single neurons. To exclude the unlikely

possibility of action potential waveforms passing our low-pass filter, the  $lf$ -LFP recorded from the same electrode as the neuron was not used for its firing rate estimation.

### 3.3.5.1 Model design

In theory, we could apply the MIMO approach described in Equation 3.3 (Section 3.3.4; page 40) to solve directly the inverse problem of estimating firing rates from LFPs, simply by inverting the inputs and outputs. However, due to strong correlations between LFP inputs, we found that models fitted to the high-dimensional data suffered from instability and generalised poorly. Therefore, we reduced the dimensionality of the LFP data used as input to the MIMO model.

A common way to achieve this is by applying PC analysis to the LFP signals. However, the components of the LFP that are most informative about an individual neuron may not be those that capture the greatest overall variance. Instead we used a five-stage approach, guided by the biophysically reasonable assumption that the SRSP associated with each neuron is composed of a discrete number of components, as evidenced by our previous data (Figure 3-7).

(1) We built a forward MIMO model (as per Equation 3.3) with  $P$  neuronal firing rates,  $\mathbf{x}(t)$ , as inputs, and  $Q$   $lf$ -LFPs,  $\mathbf{y}(t)$ , as outputs, to generate the  $Q$ -by- $P$  matrix of filter kernels,  $\mathbf{H}(\tau)$ . Typically, we estimated two neuronal firing rates simultaneously (Figure 3-8a–c) and therefore the  $lf$ -LFPs from both of those electrode channels were excluded from the model. For offline firing rate estimation, we used  $\tau_1 = -2.0$  s and  $\tau_2 = 2.0$  s.

(2) We performed PC analysis on the filter kernels (Figure 3-8d). This was motivated by the observation that the variability of the SRSP across LFP channels could be captured by a small number of components, implying that only a discrete number of sources within the LFP are informative of the spiking of a given neuron. The first six SRSP-PCs were used for the remainder of the analysis, yielding  $\mathbf{h}'_p(\tau)$ , a vector of six filter kernels where the subscript indicates that these are appropriate for estimating cell  $p$ .

(3) At this stage, it would be possible to project the LFP directly onto the six SRSP-PC axes to achieve dimensionality reduction. However, such an approach would be suboptimal since, while these projections maximize the information about a given neuron, they do not minimize uncorrelated noise (which would not appear in the SRSP). Instead, for each neuron we first

obtained a ‘source estimate’ vector,  $\mathbf{s}_p(t)$ , (**Figure 3-8e**) by convolving the firing rate  $x_p(t)$  with the SRSP-PC kernels:

$$\mathbf{s}_p(t) = \int_{\tau_1}^{\tau_2} \mathbf{h}'_p(\tau) \cdot x_p(t + \tau) d\tau \quad (3.5)$$

(4) We then found the projection of the LFP data that best approximated this source estimate. Linear regression was performed between the source estimates,  $\mathbf{s}_p(t)$ , and the  $Q$  *lf*-LFPs,  $\mathbf{y}(t)$ , yielding a  $Q$ -by-6 ‘weighting matrix’  $\mathbf{M}_p$  (**Figure 3-8h**), which could be used to transform *lf*-LFP data into a six-dimensional ‘source projection’ vector,  $\mathbf{y}'_p(t)$ , that best fitted the six source estimates of neuron  $p$  (**Figure 3-8f**).

(5) For each neuron, we calculated an ‘inverse filter’ kernel vector,  $\boldsymbol{\kappa}_p(\tau)$ , to deconvolve the source projections for neuron  $p$  and produce an estimated firing rate (**Figure 3-8g**). To do this we fitted a new model, with source projections,  $\mathbf{y}'_p(t)$ , as inputs and the low-pass-filtered (5 Hz; zero-phase 5th-order Butterworth) actual firing rate,  $x_p(t)$ , as an output:

$$x_p(t) = \int_{\tau_1}^{\tau_2} \boldsymbol{\kappa}_p(\tau) \cdot \mathbf{y}'_p(t + \tau) d\tau \quad (3.6)$$

We found that the stability of this model (an inverse Wiener-Kolmogorov filter) could be improved by adding low-amplitude Gaussian noise (mean = 0; standard deviation [s.d.] =  $\overline{|\mathbf{y}'_p|}/100$ ) to each source projection before fitting, which is equivalent to adding a regularization term to penalize the sum-square of the filter kernels.

An ‘*lf*-LFP decoder’ for neuron  $p$  thus consisted of two elements: (i) the *lf*-LFP weighting matrix,  $\mathbf{M}_p$ ; and (ii) the inverse filter kernels,  $\boldsymbol{\kappa}_p(\tau)$ . Both were stored for later use in either online or offline firing rate estimation.

To test the model, validation *lf*-LFP data,  $\mathbf{y}_{\text{val}}$ , (either 25% of the recording, or data from another behavioural task/another day) were transformed by the weighting matrix,  $\mathbf{M}_p$ , and deconvolved using the inverse kernels to produce a firing rate estimate (**Figure 3-8i**) for a particular neuron:

$$\hat{x}_p(t) = \int_{\tau_1}^{\tau_2} \boldsymbol{\kappa}_p(\tau) \cdot \mathbf{M}_p \cdot \mathbf{y}_{\text{val}}(t + \tau) d\tau \quad (3.7)$$

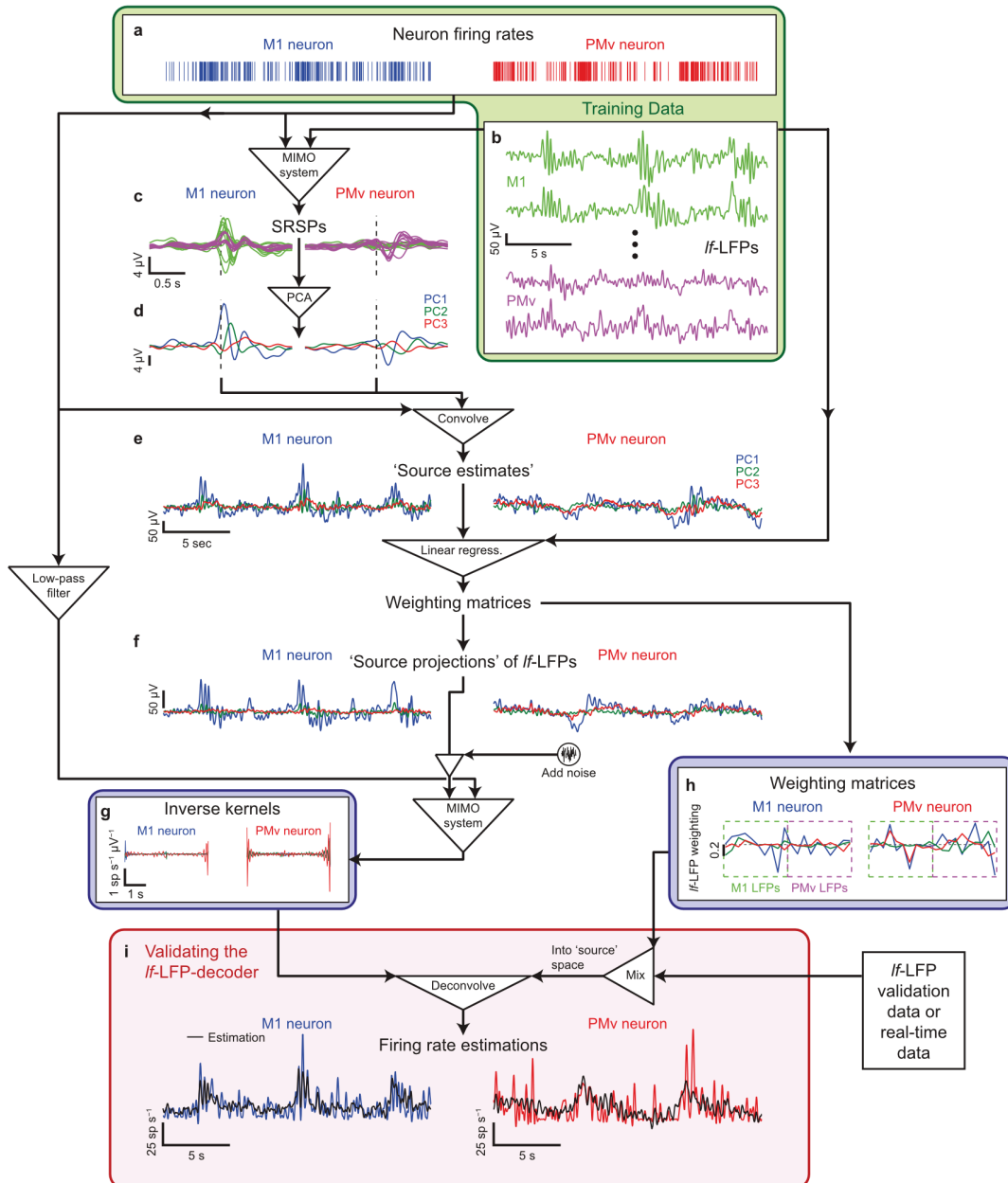


**Figure 3-8** Method for estimating firing rates from lf-LFPs.

Schematic illustration of the steps used to estimate the firing rates of two neurons. Green box represents training data. Blue boxes are the two elements of the linear model. Red box represents validating the model.

- Example rasters of an M1 neuron and PMv neuron. Binned firing rates ( $x_1$  and  $x_2$ ) were calculated and used for the succeeding steps.
- Four of the 20 lf-LFPs ( $y$ ) used in the model (22 in total, minus those recorded on the same channels as the estimated neurons).
- SRSP kernels ( $h_1$  and  $h_2$ ) for each neuron.
- SRSP-PC kernels ( $h'_1$  and  $h'_2$ ; first three shown).
- 'Source estimates' ( $s_1$  and  $s_2$ ) for each SRSP-PC.
- 'Source projections' ( $y'_1$  and  $y'_2$ ) of the lf-LFP that best fit the source estimates.
- Inverse filter kernels ( $\kappa_1$  and  $\kappa_2$ ) for each neuron.
- Weighting matrices ( $M_1$  and  $M_2$ ) for generating the lf-LFP source projections for each neuron.
- Firing rate estimates ( $\hat{x}_1$  and  $\hat{x}_2$ ) for each neuron based on deconvolution of source projections, compared against low-pass filtered actual firing rates.

### 3.3.5.2 Assessing model performance

The quality of firing rate estimation was quantified for each neuron using the Pearson correlation coefficient,  $r$ , between the low-pass-filtered actual firing rate,  $x_p(t)$ , and the estimated firing rate,  $\hat{x}_p(t)$ , over the validation data. Since successive samples of  $lf$ -LFPs or firing rates are not independent, the statistical significance of  $r$ -values (between estimated and actual data) cannot be inferred from parametric assumptions. Therefore, we estimated the distribution of  $r$ -values under the null hypothesis of no relationship by shifting (with circular wrapping) the actual and estimated data by all possible time-lags  $> 5$  s. The reported  $r$ -value was considered significant ( $p < 0.05$ , two-tailed) if it fell above the 97.5<sup>th</sup> centile of the resulting distribution.

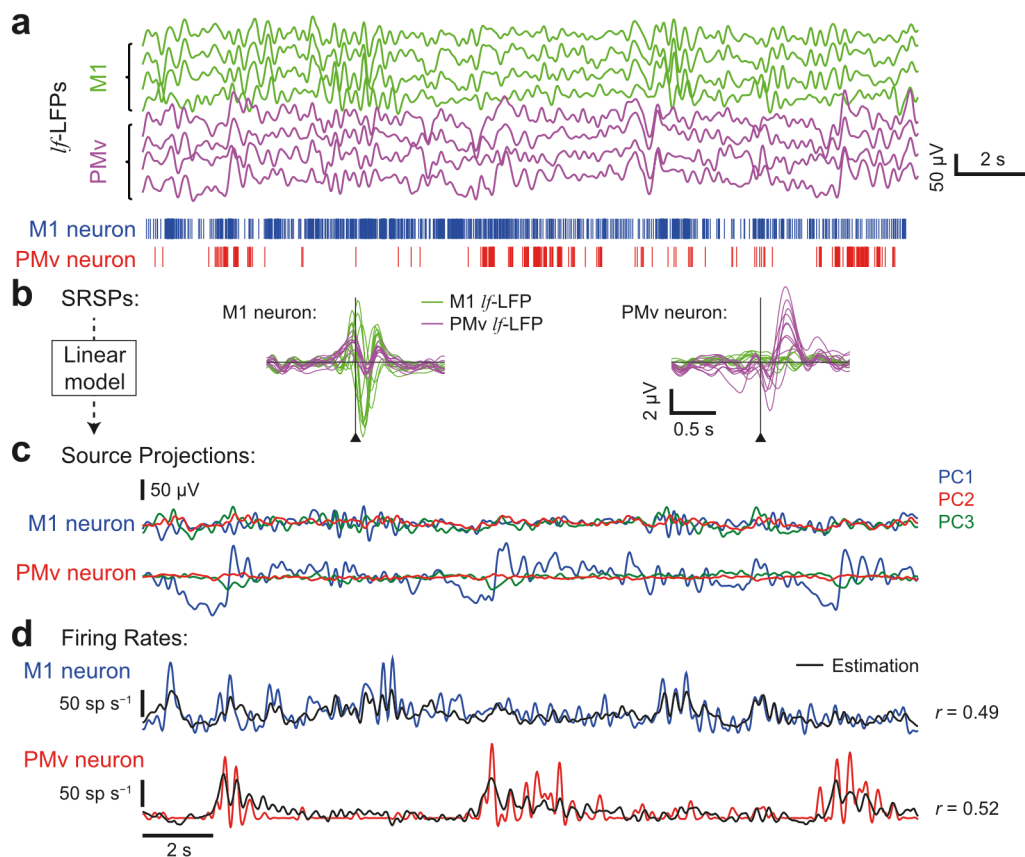


**Figure 3-9** Representative performance of firing rate estimation from lf-LFPs

- (a) Example  $lf$ -LFPs (top) and spike rasters (bottom) recorded from monkey D.
- (b) SRSPs across 20  $lf$ -LFPs associated with a single M1 (left) and PMv (right) neuron.
- (c) Source projections for each neuron, representing the  $lf$ -LFP mixture that best estimates the contribution of each SRSP-PC.
- (d) Firing rates estimated by deconvolution of source projections.  $R$ -values are those from testing on validation data.

**Figure 3-9** shows a representative validation performance using 20 LFPs (**Figure 3-9a, top**) to estimate the firing rate of single neurons (**Figure 3-9a, bottom**) in M1 and PMv. The LFPs on the same channels as the neurons of interest were excluded from the model. As expected, M1 neurons had dominant SRSPs in M1 LFPs, and PMv neurons had dominant SRSPs in PMv LFPs (**Figure 3-9b**).

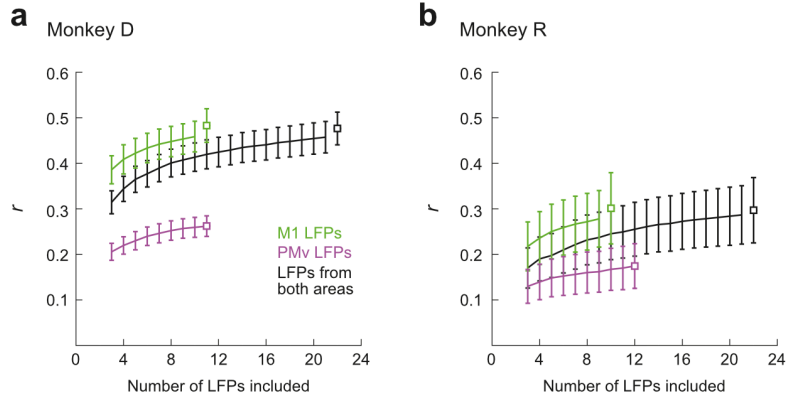
For each neuron, PCA was performed across all SRSPs, and the resulting SRSP-PCs (not shown) were convolved with the spike trains to generate ‘source estimates’ (not shown), which in turn were used to calculate the appropriate *lf*-LFP weightings ( $\mathbf{M}_1$  and  $\mathbf{M}_2$ , not shown) needed to calculate *lf*-LFP source projections (**Figure 3-9c**). These weightings, and the derived inverse filter kernels ( $\mathbf{\kappa}_1$  and  $\mathbf{\kappa}_2$ , not shown) could then be used to calculate firing rate estimates from LFP signals, either offline on validation data (e.g. **Figure 3-9d**), or online in near-real time.

Comparing our *lf*-LFP-based firing rate estimates to actual firing rates, on validation data, we saw typical *r*-values in the range 0.2–0.7, which was surprisingly good, considering that (a) estimations were performed on instantaneous firing rates (which are inherently very noisy), with no task or behavioural alignment, and (b) we excluded the LFP from the electrode on which the neuron of interest was recorded. Statistical significance of such estimates was calculated as described in **Section 3.3.5.2**, and the *r*-values of the example M1 and PMv neuron estimates in **Figure 3-9d** (0.49 and 0.52, respectively) were associated with significance thresholds of 0.11 and 0.10, respectively ( $p < 0.05$ , two-tailed; non-parametric bootstrap).

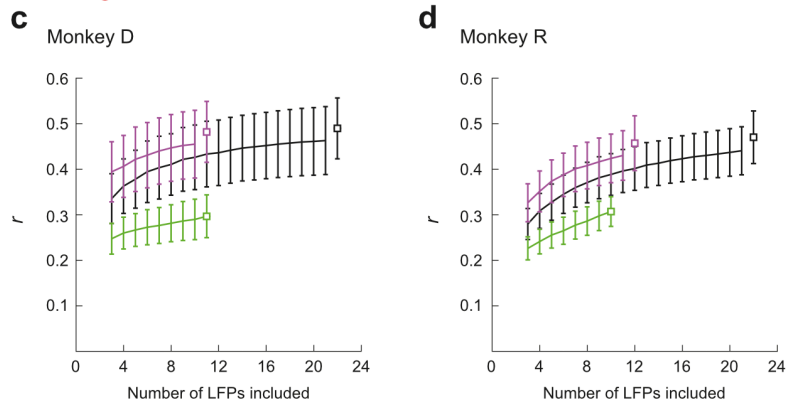
### **3.3.5.3 Performance with increasing numbers of *lf*-LFPs**

To determine how the quality of firing rate fit depended on size of the *lf*-LFP sample, every neuron’s firing rate was estimated using 120 random draws of  $Q$  *lf*-LFPs, increasing from three up to the number of channels available (excluding that recorded on the same electrode as the neuron of interest) and applying dimensionality reduction based on three SRSP-PCs (**Figure 3-10**).

Estimating M1 neurons:



Estimating PMv neurons:



Estimating neurons from both areas:

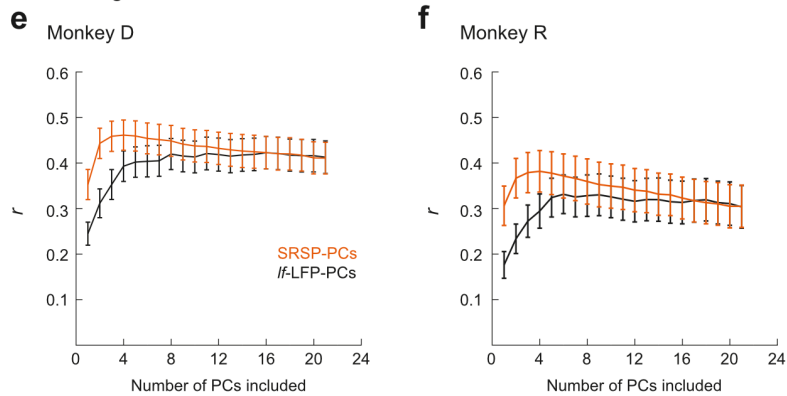


**Figure 3-10** LFP- and PC-dropping curves for firing rate estimation.

- (a) Average correlation coefficient over validation data for M1 neuron firing rates in monkey D, estimated from increasing numbers of *lf*-LFPs from M1 (green), PMv (purple) or both areas combined (black). Dimensionality reduction was performed using three SRSP-PCs. Open squares show the result when the *lf*-LFP on the same electrode as the estimated neuron was also included. Error bars show  $\pm$  s.e.m. ( $n = 13$  neurons).
- (b) Same for M1 neurons in monkey R ( $n = 6$ ).
- (c) Same for PMv neurons in monkey D ( $n = 7$ ).
- (d) Same for PMv neurons in monkey R ( $n = 9$ ).
- (e) Performance when estimating firing rates of all neurons in monkey D using increasing numbers of SRSP-PCs (orange), compared with a model based on PCs of *lf*-LFPs (black). All 22 LFPs were used (but with exclusion of the *lf*-LFP on the same electrode as each estimated neuron). Error bars show  $\pm$  s.e.m. ( $n=20$  neurons).
- (f) Same for all neurons in monkey R ( $n = 15$ ).

The quality of firing rate estimation increased with the number of *lf*-LFPs included in the model, with the most useful being within the same cortical area as the estimated neuron (**Figure 3-10a–d**). Firing rate estimation was only marginally improved by further inclusion of the *lf*-LFP recorded on the same electrode as the estimated neuron (**Figure 3-10a–d**, *open squares*). In each of the panels in **Figure 3-10**, error bars show the standard error of the mean (s.e.m.) across different channels, and are therefore are not artificially reduced by the large number of permutations averaged to estimate the mean for each channel.

We also wanted to determine how the quality of firing rate estimation depended on the number of SRSP-PCs. To do this, every neuron’s firing rate was estimated using all *lf*-LFPs (excluding that recorded on the same electrode as the neuron of interest) projected into a source estimate space with dimensionality increasing from one up to the number of channels available (that is, no dimensionality reduction). The quality of fit was compared against models based on increasing numbers of *lf*-LFP–PCs from one up to the number of channels available.

Estimation based on SRSP components out-performed models fitted directly to the PCs of the *lf*-LFPs (**Figure 3-10e,f**). Moreover, validation performance was optimal when only a limited number of sources were included – suggesting that each SRSP contains about three to four distinct components.

#### **3.3.5.4 Task-relationship of estimated firing rates**

Finally, we looked at the task-related behaviour of the firing rate estimate, and how this compared to the behaviour of the actual neuron. To do this, we began by calculating an event-triggered mean of the actual/estimated firing rate, aligned to the end of the hold period of the torque-tracking task. By averaging out the trial-to-trial variability in firing rates, it became even more clear how remarkably well we could estimate firing rates using only information derived from *lf*-LFPs (**Figure 3-11a**).

In effect, the single-trial firing rate of a neuron is itself a noisy estimate of the underlying task relationship of the neuron. (Hence why neuroscientists conventionally average over many trials to determine firing profiles.) And our *lf*-LFP–based estimate of firing rate is able to capture this task-relationship just as well as the actual firing rate. For example, for the neuron shown in **Figure 3-11a**, the *r*-value between actual and estimated trial-averaged firing rates

was 0.97, implying that we were capturing around 94% of the movement-related variation in the neural signal. We explore these task relationships further in **Chapter 4**.

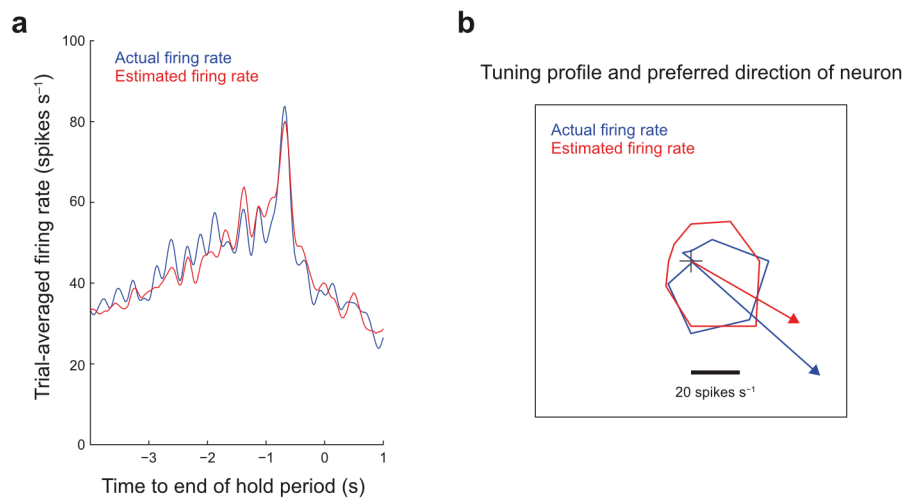


**Figure 3-11** Task-relationship of actual and estimated firing rates.

- (a) Mean firing rate across trials of an example M1 neuron (from Monkey D) aligned to the end of the ‘hold’ period of the torque task (55 trials). Blue line shows the trial-averaged actual firing rate (lowpass filtered at 5 Hz). Red line shows the trial-averaged LFP-based estimate for the same neuron.
- (b) Polar plot of actual and estimated firing rates for different target positions (average of 1 s prior to the end of the hold period, with baseline firing rate subtracted). Also shown is the ‘preferred direction’, calculated as the vector sum of the tuning profile.

Finally, we separated trial-aligned responses to each of the eight peripheral targets in the torque-task, and found that the actual directional tuning profile and ‘preferred direction’ of the neuron of interest could be satisfactorily retrieved from *lf*-LFP-based firing rate estimates (**Figure 3-11b**).

### 3.4 Discussion

Overall in this chapter, we have presented results demonstrating that single-neuron firing rates can be estimated from multichannel *lf*-LFP recordings in motor cortex using simple linear models. LFP-based estimates capture around 25% of the variance of instantaneous firing rates of individual neurons, but considerably more of the variance of trial-averaged firing rates.

Cortical *lf*-LFPs recorded by multi-electrode arrays are often assumed to contain only redundant information arising from the activity of large neuronal populations; perhaps because of the association of low-frequency activity with slow-wave sleep, during which

neurons become highly synchronized across wide areas of cortex and subcortical structures. Here we show that, if you look at them in the right way, multichannel *lf*-LFPs in monkey motor cortex actually each contain a slightly different mixture of distinctive slow potentials that reflect the activity of local neuronal populations, as well as neuronal populations in neighbouring areas of cortex. These findings are in agreement with a number of recent studies (Einevoll et al. 2007; Nauhaus et al. 2012; Rasch et al. 2009). However, to our knowledge, this is the first demonstration that the different mixtures contained within multiple *lf*-LFPs can be separated for estimation of single neuron firing rates\*.

Rasch and colleagues (2008; 2009) studied spike LFP relations in primary visual cortex (V1) of anaesthetised macaques during spontaneous activity and visual stimulation, and found STA features very similar to our SRSPs (**Figure 3-12**). Using these, they generated a linear model similar to ours to estimate an *lf*-LFP from neuronal spiking on the same channel (Rasch et al. 2009), with comparable results to ours. They also found these features to be robust, and had some success extrapolating their filters across electrodes, across cortical areas (visual to temporal) and even across subjects, supporting the idea that these features are widespread. However, they did not combine multiple neuronal contributions linearly in their *lf*-LFP estimations.

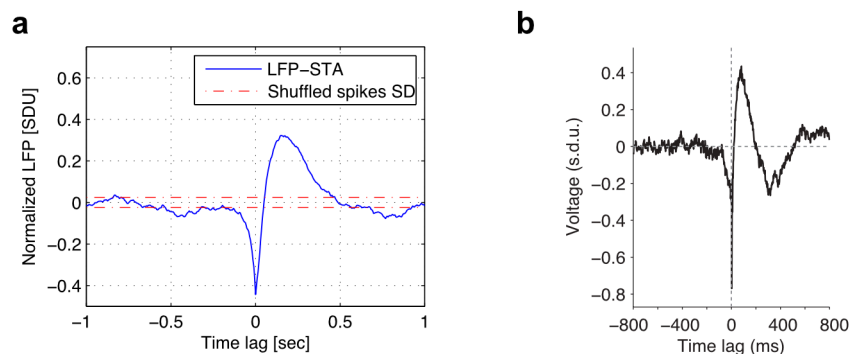


**Figure 3-12** Examples of SRSP-like phenomena in macaque V1, documented by Rasch et al.

- (a) Spike-LFP relationships in V1 of an anaesthetised monkey during movie stimulation.
  - Reproduction: Figure 2A from Rasch et al. (2008), *J. Neurophysiol.* (American Physiological Society).
- (b) A Wiener-Kolmogorov filter used for linear estimation of an LFP from a neuronal spike train during spontaneous activity in V1 of an anaesthetised monkey.
  - Reproduction of part of Figure 2A from Rasch et al. (2009), *J. Neurosci.* (Society for Neuroscience).

\* Note: These findings have been published as Hall, Nazarpour & Jackson (2014)

The same group also used LFP to estimate single-unit firing (Rasch et al. 2008), and found that a linear model performed 90% as well as a non-linear model. They found that the *lf*-LFP (both phase and power) was valuable for estimating firing rates, and (like in our SRSPs), the spike-related features were most informative between  $-50$  and  $+500$  ms around the spike time. They found that the same relationships held for both spontaneous and stimulus-driven activity. They noted that variance in their model performance was high between electrodes, and suggested that this may be due to electrode locations and depths, but they did not combine multichannel data in their estimations and, to our knowledge, the work presented here by us is the first time this has been tried.

Given that LFPs are population signals, the accuracy with which it is possible to resolve individual neurons is surprising, especially since neural synchrony inevitably confounds the inference of causal effects from STAs. The use of linear models, incorporating multiple recorded cells, can only partially mitigate this problem. Clearly, given its large amplitude and slow time course, the SRSP attributed by the model to each recorded cell must contain contributions from unrecorded (but correlated) neurons in the local network. The effects of correlation in the neural space are explored further in **Chapter 4**.

The origin and spatial extent of the LFP remains a subject of debate, with estimates ranging from a few hundred micrometres (Katzner et al. 2009; Xing et al. 2009) to several millimetres (Kajikawa & Schroeder 2011). Here, we observed robust SRSPs varying in shape and polarity within *lf*-LFPs recorded on different electrodes throughout the same cortical area as the trigger neuron. We can largely rule out recording artefacts (for example, room noise, head movements and electromyogram contamination) being a cause of these phenomena, since the SRSP reversed polarity within the grey matter and *lf*-LFPs were most informative of the firing rates of neurons within the same cortical area. Although we cannot discount the presence in our LFP recordings of artefacts uncorrelated with spiking activity, these would only reduce the accuracy with which we could estimate firing rates.

Unfortunately, using our moveable tungsten microwire arrays, we do not have a measure of the relative spatial location of our recording sites in the cortex (other than coarsely based on their implantation site), or of cortical depth of our recording sites (other than by coarsely advancing electrodes). We were also not able to perform post mortem tract reconstruction, because the multiple insertions and retractions of the moveable tungsten microwires mean that there are multiple, crossing paths present in post mortem tissue. Therefore, we cannot say for

sure whether the spatial extent of the SRSP reflects volume conduction of local sources, or synchronization of broader neuronal populations within each cortical area (Canolty et al. 2010), or the effect of a ‘traveling wave’ of activity across the cortex (e.g. Nauhaus et al. 2012).

Speculatively, we suggest that our data are most consistent with the first hypothesis: that (at least low-frequency) LFP is conducted over many millimetres or centimetres, likely by volume conduction. This is because neurons in one cortical area (e.g. M1) were correlated with features in the SRSP on LFP electrodes in the other cortical area (around 10 mm away). These signals from the ‘remote’ cortical area were much more stereotyped than those from the local cortical area, but nevertheless provided information that was non-redundant with respect to other ‘remote’ electrodes.

We are unable to provide further scientific insight here into the spatial properties of the *lf*-LFP, nor into the depth profile of the SRSP and SRSP-PCs, without a geometrically-arranged recording array. **Chapter 6** of this thesis describes some of our early work in designing and recording from such an array, in order to address these limitations.

It is important to note the similarities of our SRSPs to spike-LFP relationships reported in macaque visual cortex (Rasch et al. 2008; Rasch et al. 2009) and rat somatosensory and prefrontal cortex (Okun et al. 2010), which suggest that the SRSP may reflect a ubiquitous feature of cortical organization rather than a unique property of motor cortex.

A possible mechanism that could account for low-frequency SRSP components occurring several hundred milliseconds after spike activity is gamma-aminobutyric acid type-B receptor (GABA<sub>B</sub>)-mediated recurrent inhibition (Destexhe et al. 2001; Carracedo et al. 2013); since the slow kinetics of the G-protein-coupled receptor give rise to extracellular potentials that can be delayed substantially relative to cell activity (Dine et al. 2014). Other possible mechanisms intrinsic to the cortex include slow hyperpolarization-activated  $I_h$  currents, which contribute to low-frequency resonances in cortical neurons (Hutcheon et al. 1996).

Alternatively, reciprocal connections with the thalamus form feedback loops that are thought to contribute to delta-frequency oscillations (Destexhe 1998). Whilst we cannot rule out an extra-cortical feedback loop, our results are more suggestive of intra-cortical mechanisms, since one might expect extra-cortical loops to have more global, synchronising effects, rather than local effects on small ensembles of neurons.

In fact, our finding that the SRSP contains 3–4 distinct components suggests that multiple processes likely contribute. Because different electrodes record different mixtures of these components, we are able to extract information about firing rates that may not be present in global measures such as overall LFP power in broad frequency bands. Moreover, information in LFPs is highly layer-dependent (Einevoll et al. 2007; Markowitz et al. 2011), and variation in electrode depth within our recording array appears beneficial for extracting non-redundant spike-related features from multiple LFP channels. This may additionally help explain why decoding of LFPs typically outperforms surface recordings from the brain or scalp.

Large regression models can suffer from over-fitting and instability, especially when inputs are highly correlated – as in the case with multiple LFPs (Hwang & Andersen 2013). However, the distinct SRSP components associated with each neuron allowed us to develop a biophysically-principled approach to dimensionality reduction, which improved model validation and out-performed PC regression. The assumption of a linear relationship between *lf*-LFP and spike activity is likely suboptimal, although (as noted above) evidence from the primary visual cortex suggests that nonlinear approaches may yield only marginal improvements (Rasch et al. 2008).

Experiments in the anaesthetised visual cortex suggest there may be distinct information contained in the *lf*-LFP compared with gamma-band LFPs and spikes (Belitski et al. 2008), and that inclusion of these higher frequencies improves prediction of spiking (Rasch et al. 2008). LFP spectra in the awake motor cortex are characterized by strong activity in the beta-band, but this is typically suppressed during movement, when spiking activity shows the greatest modulation. This motivated our use of the low-frequency band for firing rate estimation. Nevertheless, it is possible that the inclusion of higher frequency bands could further improve performance, albeit at the cost of increased computational complexity.

The instability of single-unit recordings is currently a major challenge for invasive neuroprostheses, but the wide spatial extent of the SRSP that we have seen here—across electrodes within the same cortical area, and with evidence of spread to neighbouring cortical areas—suggests the *lf*-LFP may be less sensitive to micro-motion than extracellular spike recordings. This may make *lf*-LFP-based estimates of firing rate a particularly suitable signal for chronic, implanted BMIs. Moreover, the ability to infer firing rates from *lf*-LFP would be generally applicable for any neuroprosthetic application requiring long-term monitoring of neural activity.

### 3.5 Chapter summary

- The spike-related slow potential (SRSP) is a consistent feature seen in recordings from macaque motor cortex (and also other cortical areas).
- The SRSP contains a mixture of spike-related signals from multiple sources. Multiple electrodes sample different mixtures of these sources.
- Based on this, we can decode the firing rate of individual neurons from multichannel *lf*-LFP recordings with surprising accuracy, even though the channels on which the predicted units are recorded are not included in the decoder.
- The ability to infer firing rates from *lf*-LFP is potentially applicable to any neural interface application requiring long-term monitoring of neural activity, including chronic, implantable motor BMIs.



# Chapter 4. Stability, dimensionality and generalisation of LFP-based firing rate estimates, and their use in biofeedback BMIs

*In which we investigate the stability of LFP-based firing rate estimates over time, their dimensionality compared to actual firing rate data, their generalisation across a range of behavioural tasks, and finally, their use in an LFP-controlled biofeedback BMI task.*

## 4.1 Introduction

### 4.1.1 *Stability of LFP-based firing rate estimates*

As already introduced in **Chapter 1**, one of the most crucial challenges of invasive BMIs is that current implantable electrode technologies do not have the lifespan required for clinical use (many years or decades are required). Micro-motion of electrodes leads to daily changes in the shape and number of action potential recordings. In even the most refined experiments in human subjects, this generally necessitates recalibration of spike-based decoders at the beginning of every experimental session (e.g. Hochberg et al. 2012). This can typically only be done using powerful lab-based equipment, which is not only time-consuming, but impractical for any neuroprosthetic designed to be used day-to-day by patients, for activities of daily living.

An increasingly accepted solution in the literature is to not even try to isolate single units, and simply use unsorted threshold crossings from each electrode (so-called “multi-unit spikes”; e.g. Flint et al. 2016). However, electrode de-insulation, inflammation and gliosis, and neuronal death still lead to a gradual reduction in the number of neurons that can be recorded.

In **Chapter 3** of this thesis, we introduced a potentially parsimonious solution to the problem of neuron stability. We can estimate the firing rate of single neurons (at least on the same time-scale as movement kinematics) using only low-frequency field potentials, recorded on other electrodes. LFPs are theoretically easier to record stably over long time-periods than

spikes, because they are less dependent on precise proximity to single neurons, and they originate from ensembles of neurons (rather than from one neuron) (Andersen et al. 2004).

LFPs have long been postulated as a more stable alternative to spikes (Pesaran et al. 2002). Certainly, long-term recordings in monkeys suggest that movement-related information can be decoded from the LFP signal, even in the absence of clear spike activity (Flint, Lindberg et al. 2012; Stavisky et al. 2015). Experiments with ECoG have suggested that field recordings are comparable in performance to single-unit activity for decoding forearm movements, and with far superior stability, out to 250 days (Chao et al. 2010). But surprisingly few studies have studied closed-loop BMIs controlled solely by LFPs.

Hwang and Andersen (2009) used LFPs from posterior parietal cortex in a closed-loop BMI, but only as a binary gating signal. It has also been shown that gamma band LFP oscillations can be volitionally controlled in a biofeedback BMI paradigm (Engelhard et al. 2013). More recently, 2D continuous LFP-based BMI control has been demonstrated, using an adaptive controller (So et al. 2014). However, to my knowledge, only one group has explicitly demonstrated the stability of a motor cortical LFP-based closed-loop BMI: showing stable performance over 210 days using a decoder trained from a single recording session, with no retraining (Flint, Wright & Slutzky, 2012; Flint et al. 2013). The performance of the subjects remained constant or improved slightly over the seven months of the study. More recently, the same group published a closed-loop study concluding that LFPs were significantly more stable than even multi-unit spikes. Particularly informative, and particularly stable, were high-gamma power and the local motor potential (LMP), which reflects the  $lf$ -LFP time domain signal (Flint et al. 2016).

In this Chapter, we aim to quantify the stability of our LFP-based firing-rate decoders over many weeks. This is challenging, because our performance measure assumes that the actual firing rate of the selected neuron is being accurately captured by discriminated spike crossings. However, this may not be true over long periods of time, as the spike recording is likely to change as a result of the problems outlined above. Unfortunately, it is therefore impossible in this type of experiment to know the absolute ‘ground truth’ firing rate of the neuron for the purposes of quantifying model performance. In this chapter, we therefore also quantify stability in terms of the task-related behaviour of the firing rate estimate over time.

## 4.1.2 Dimensionality analysis of firing rate estimates

As mentioned in **Chapter 1**, there is a common assumption that *lf*-LFP activity reflects synchronisation of wide areas of cortex, and that therefore recording multiple channels of *lf*-LFP will yield multiple redundant signals. Also, because the *lf*-LFP power can be an order of magnitude larger than the LFP power in the gamma band, and because simulations show that low-frequency LFP components have a much larger spatial reach than higher frequencies (Łęski et al. 2013), there is also a common assumption that the *lf*-LFP reflects the activity of relatively large populations of cells.

Both of these assumptions would lead one to the prediction that redundancy of  $Q$  channels of *lf*-LFP should be very high, compared to the same number of channels of spike recording, because large-scale correlation and averaging of activity across thousands of neurons would mean that signals would all covary according to a very small number of explanatory, or ‘latent’ variables (Cunningham & Yu 2014). In contrast to these predictions—and therefore in disagreement with these assumptions—we showed in **Chapter 3** that by looking for *lf*-LFP features associated with neural spiking, we could reveal a rich mixture of multiple spike-related sources within the multichannel *lf*-LFP.

However, in **Chapter 3**, we only considered the scenario where we were estimating, at most, two neurons: one from M1 and one from PMv. Rather than estimating the unique firing rate profile of each neuron, we may actually have been estimating only two latent (hidden) variables within the neural space, which described correlated firing within M1 and PMv, respectively. To address this concern, in this Chapter, we demonstrate the offline estimation, using a single MIMO model, of the firing rate of all neurons recorded simultaneously on our electrodes. We also further investigate our ability to estimate ranked dimensions of the neural space, in order to exclude the possibility that we are simply estimating latent components reflecting correlated population activity.

## 4.1.3 Generalisation and transferability of firing rate estimation

### 4.1.3.1 Generalisation

Here, we use the term *generalisation* as a statistical concept, meaning the ability of a model to estimate output values for previously unseen data. For example, in our results to this point, we

have used generalisation as a test of model performance, by training our decoders on 75% of a recording, but using the remaining 25% of the recording as ‘unseen data’ for validation.

However, this only represents generalisation of the *lf*-LFP–spike model within the same recording, which is the most lenient scenario. One could imagine that the LFP features (SRSPs), on which our method relied, might be based on particular patterns of neural firing and correlation seen specifically during the isometric torque task data on which the decoders were trained, and may not generalise to more naturalistic, and less stereotyped, movements. In this Chapter, we therefore test the performance of our firing rate decoders on data from different behavioural scenarios.

#### **4.1.3.2 Transferability**

*Transferability* of a research finding is the extension of that finding outside of the original sample, to the wider population, or different population. I have deliberately avoided the word ‘*generalisability*’ here (even though this may be a more correct term), and used the term *transferability*, to avoid confusion with the term *generalisation* (which is reserved above). In this Chapter, we investigate how transferable our findings are across different types of neuronal firing pattern. Specifically:

- i) Does firing rate estimation perform equally well in M1 and PMv?
- ii) Does firing rate estimation only work for neurons with very fast or very slow firing rates?
- iii) Can we only estimate neurons whose activity is associated with overt movement?

None of these questions are a direct test of transferability (that would require additional experiments that are outside the scope of this thesis), but they provide evidence for or against the argument that SRSPs (and firing rate estimates dependent thereon) are a general property of motor cortical neurons and the method is therefore transferable to other scenarios.

#### **4.1.4 Biofeedback BMI using LFP-based firing rate estimates**

In **Chapter 3**, we presented evidence that offline LFP-based firing rate estimates produce an accurate prediction of actual firing rates, on a single-trial basis. In the first section of this chapter, we will demonstrate that these estimates are remarkably stable. Finally, as an extreme test of the specificity of *lf*-LFP–spike relationships to particular neurons, we wanted to use

firing rate *estimates* as control signals in a realtime biofeedback BMI task, whilst monitoring the *actual* firing rates of those neurons, to see whether our models were specific enough to allow the subjects to separate the activity of the selected neurons from that of other neighbouring neurons.

## 4.2 Aims

This Chapter therefore has four main aims:

**Aim 1:** To study the stability of LFP-based firing rate estimates over time.

**Aim 2:** To study the latent dimensionality of LFP-based firing rate estimates, compared to the latent dimensionality of the actual neural space.

**Aim 3:** To study the generalization of *lf*-LFP-based models across different behavioural scenarios.

**Aim 4:** To test the specificity of *lf*-LFP–spike relationships, using a realtime biofeedback BMI task, controlled by *estimated* firing rates of neurons.

## 4.3 Methods and Results

### 4.3.1 *Stability of LFP-based firing rate estimates*

#### 4.3.1.1 *Methods*

To assess the stability of the relationship between *lf*-LFPs and firing rates, we recorded the same ensemble of neurons over a prolonged period (Monkey D:  $P = 20$  neurons,  $Q = 22$  *lf*-LFPs; over 45 days. Monkey R:  $P = 8$  neurons,  $Q = 22$  *lf*-LFPs, over 23 days). Each day, we performed a torque task experiment (50 trials), as described in **Section 2.1.2**.

On day zero, we used the method described in **Section 3.3.5.1** to build a single model (decoder) to simultaneously estimate the firing rates of  $P$  neurons using  $Q$  *lf*-LFPs. Unlike previously, where we excluded *lf*-LFPs on the electrodes with neurons of interest, we were unable to do this here, because otherwise there would be insufficient *lf*-LFPs available.

Therefore all 22 *lf*-LFPs were included in the model. We then tested the performance of this decoder on data from the torque task experiment on each of the successive days.

For comparison to this static decoder ('Original model', unchanged throughout the duration of the experiment) we also refitted the decoder each day ('Updated model') and validated it within-day.

#### **4.3.1.2 Results**

Models fitted to data recorded on day zero were able to estimate firing rates of almost all neurons simultaneously from validation *lf*-LFP data recorded during that session. (Day zero: Monkey D, 20/20 neurons estimated above significance threshold, mean *r*-value 0.47, range 0.23–0.74; Monkey R, 7/8 neurons; mean *r*-value 0.27, range 0.03–0.56) (**Figure 4-1a,b**, data at *day zero*).

We then used the same model parameters to predict cell activity on subsequent days. Performance of the model using parameters from day zero was stable for most neurons throughout the recording period. (Last day: Monkey D, 20/20 neurons; mean *r*-value 0.31, range 0.06–0.57; Monkey R, 5/8 neurons; mean 0.16, range –0.11 to 0.51). Remarkably, performance was only slightly improved by fitting new parameters on each day (**Figure 4-1c,d**).

#### **4.3.2 Stability of trial-averaged LFP-based firing rate estimates**

Whilst the performance values in the previous figure may not seem very impressive on first glance (*r*-values of ~0.75 at best, corresponding to around 56% of variance explained), one needs to consider that these estimates are being done on a single-trial basis, with no averaging. As discussed in **Section 3.3.5.4** (page 53), single-trial firing rates are extremely noisy estimates of the underlying task relationship of the neuron. In fact, one could argue that we are asking even more of our decoder than single-trial performance, because we are not excluding data from the inter-trial periods of the task (e.g. returning to the home target), when neural behaviour may be even less consistent and predictable.

Next, therefore, we examined how well the trial-averaged (event-aligned) modulation of single-neuron firing rates (aligned to the end of the successful hold period) could be retrieved from LFP-based estimates.

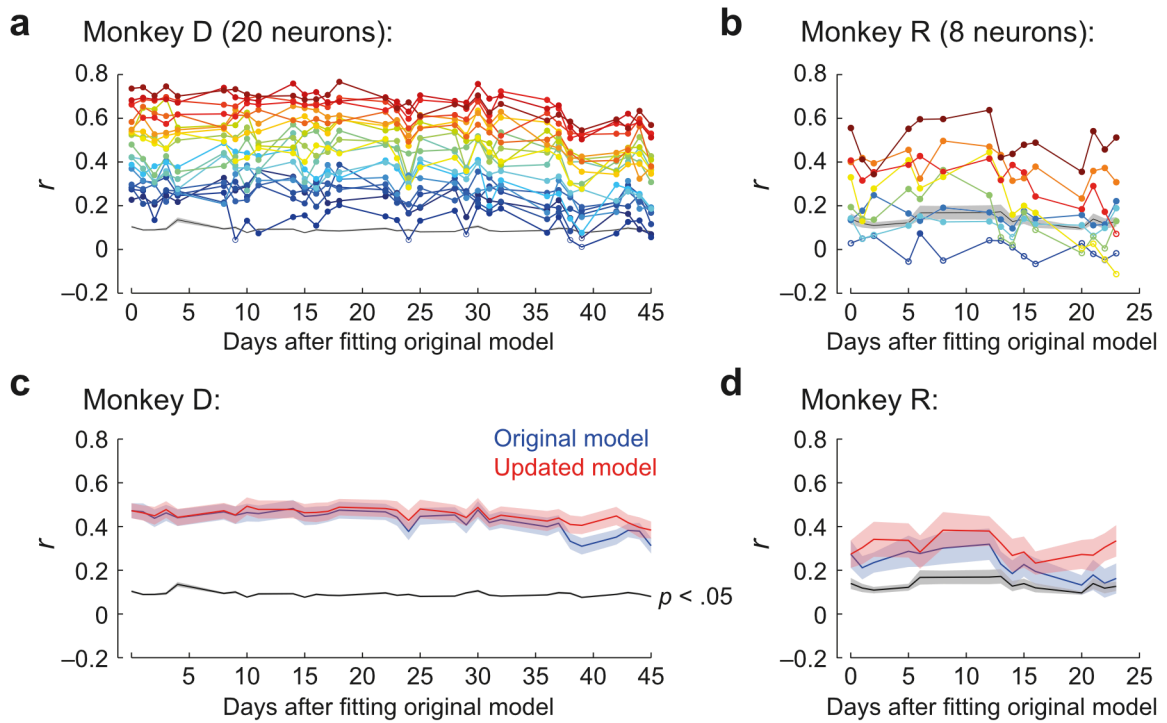


**Figure 4-1** Long-term stability and dimensionality of firing rate estimation.

- (a) Estimation of 20 neurons' firing rates, using 22 *lf*-LFPs in monkey D, over 45 days, without model updating. Filled circles indicate significant estimates ( $p < 0.05$ , two-tailed; non-parametric bootstrap). Neurons are colour-coded according to quality of estimation on day 0. Black line shows an illustrative significance threshold (mean threshold of  $n=20$  neurons; shading shows  $\pm$  s.e.m), although each firing rate undergoes its own significance test.
- (b) Same for monkey R; 8 neurons, using 22 *lf*-LFPs, over 23 days.
- (c,d) Performance (mean correlation coefficient) of the original model (blue, fitted to data on day 0) versus an updated model (red, fitted to the data daily). Shading shows  $\pm$  s.e.m. (monkey D,  $n = 20$  neurons; monkey R,  $n = 8$  neurons).

#### 4.3.2.1 Methods

We used the same decoders, built on day zero, as we used for **Figure 4-1a,b**. On day zero, we calculated the trial-averaged firing rate profile (including all eight target directions) of the actual firing rate of each of the  $P$  neurons, aligned to the end of the successful hold period. We then calculated the trial averaged estimated firing rate profile of each neuron, and compared the two trial-averaged signals (actual and estimated) using Pearson's correlation coefficient,  $r$  (just as in **Section 3.3.5.4**). Next, we used the same decoder (from day zero), to estimate firing rates on day 1 and on the final day of the experiment, and compared the trial-aligned firing rate estimates on those days to the actual firing rate profile on day zero. In this way, we used the actual firing rate profile on day zero as the 'ground truth' for the true task-related behaviour of the neuron over the duration of the experiment.

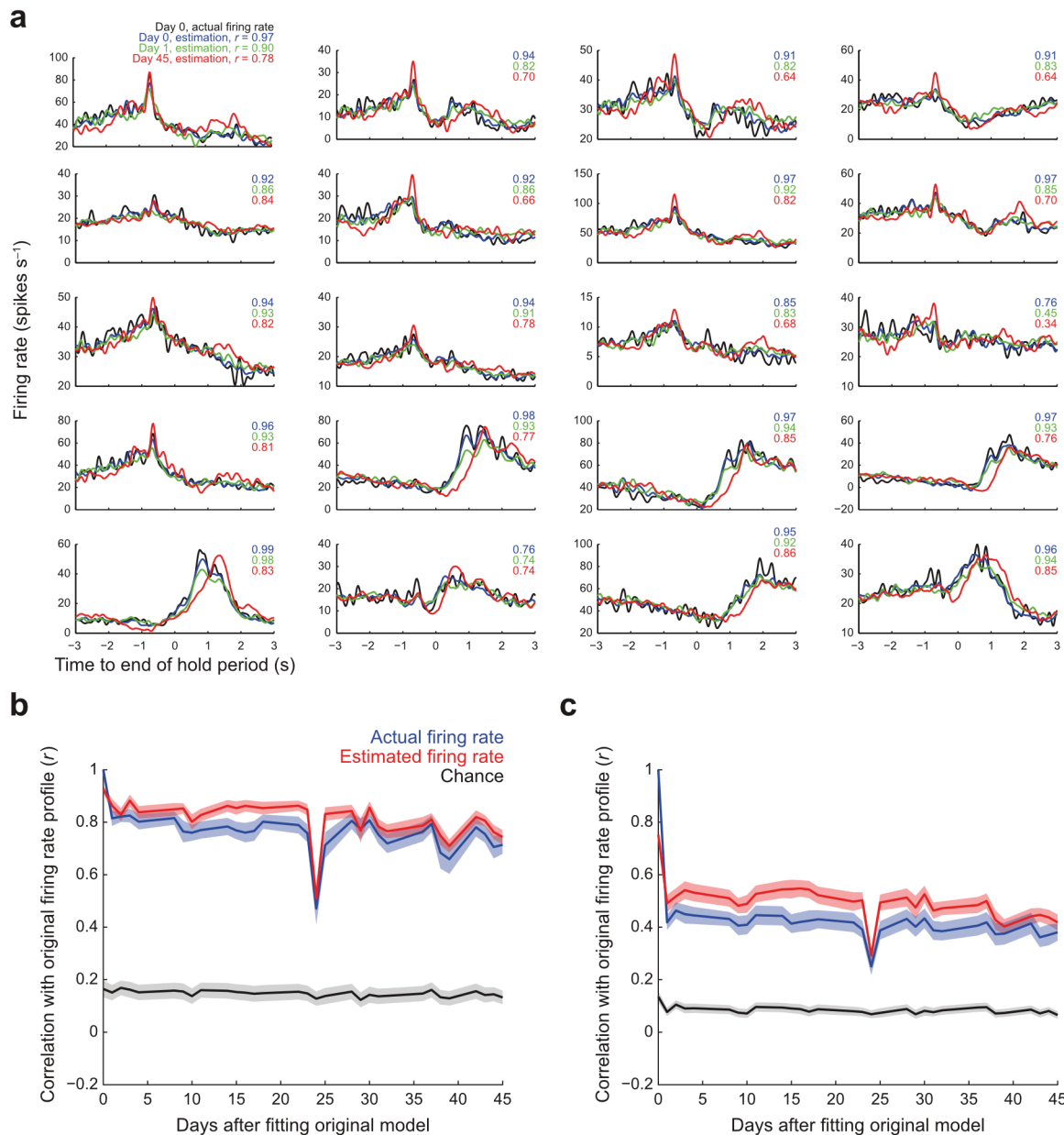


**Figure 4-2** Actual and estimated trial-aligned firing rate profiles in Monkey D.

- (a) Each sub-panel shows data for one of the 20 neurons from the sessions shown in **Figure 4-1a**. *Black trace*, shows the mean trial-aligned actual firing rate profile averaged over 50 trials of the torque task (including all eight target directions) on day zero; *Blue trace*, shows trial-averaged estimated firing rate profile derived from *lf*-LFP for the same trials; *Green trace*, shows the trial-averaged estimated firing rate profile for trials performed one day later; *Red trace*, shows the trial-averaged estimated firing rate profile on day 45. Inset numbers indicate the correlation coefficient ( $r$ ) between the actual firing rate profile on day 0 and the estimated firing rate profile on days 0, 1 and 45.
- (b) *Red line*, shows the mean ( $n = 20$  neurons; shading indicates  $\pm$  s.e.m.) of the correlation coefficient ( $r$ ) between the trial-aligned actual firing rate profile on day zero and the trial-aligned LFP-based estimate of the firing rate profile on successive days. *Blue line*, shows the mean ( $\pm$  s.e.m.) correlation coefficient of the actual trial-aligned firing rate profile on day zero and the actual trial-aligned firing rate profile on successive days. *Black line* shows the mean ( $\pm$  s.e.m.) ‘chance’ correlation (see text).
- (c) Shows the same as panel **b**, but for trials separated according to target direction

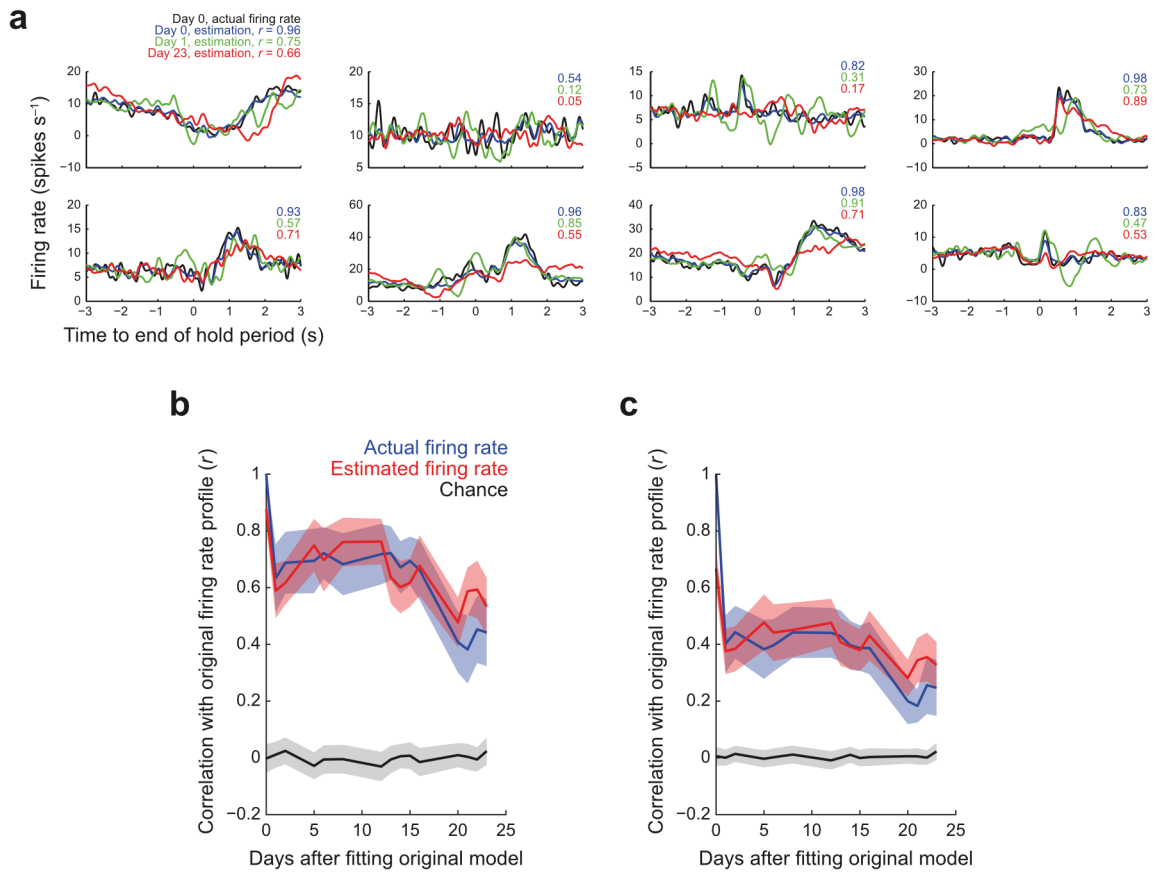


**Figure 4-3** Actual and estimated trial-aligned firing rate profiles in Monkey R.

As per **Figure 4-2**, but for the neurons shown in **Figure 4-1b**, recorded in Monkey R over 23 days ( $n = 8$  neurons; shading indicates  $\pm$  s.e.m.)

Then, we used the same ground truth to compare changes over time in the task-related behaviour of the actual firing rate, to changes in task-related behaviour of the estimated firing rate. As a measure of chance, we calculated the correlation between the trial-aligned actual firing rate profile on day zero and the trial-aligned estimated firing rate profile of a different neuron on successive days (i.e. the correlation that would be expected by chance if the LFP-based estimate did not capture firing rate modulations specific to the estimated neuron).

Finally, we performed this same analysis, but separated the trials by target direction ( $\sim 6$  trials each for the 8 circumferential targets in the torque task). To do this, correlation coefficients were calculated across the concatenation of firing rate profiles for the individual targets. Performance here is expected to be significantly worse, because not only do firing rate estimates have to capture target-indifferent task-related activity, they also have to capture subtle variations in firing rate profile of each neuron between the eight different targets.

### 4.3.2.2 Results

On day zero, the mean ( $\pm$  s.e.m.) correlation between the average firing rate of single neurons and the equivalent average of the LFP-based estimates was  $r = 0.93 \pm 0.06$  for monkey D and  $0.88 \pm 0.14$  for monkey R (**Figure 4-2a** and **Figure 4-3a**). These correlation coefficients are considerably higher than the  $r$ -values obtained for non-averaged data, suggesting that our method gave an unbiased estimate of task-related modulations of single neurons that converged towards the same trial-averaged profiles as the instantaneous firing rates. In these figures, it is clear that PMv neurons were commonly most modulated at the end of the trial, when the subject took food reward with the ipsilateral (right) hand.

On subsequent days, despite slight variation in the animals' behaviour, trial-averages of LFP-based estimates continued to resemble the actual trial-averaged firing rates from day zero ( $r$ -values on day 1:  $0.86 \pm 0.11$  for monkey D and  $0.59 \pm 0.26$  for monkey R;  $r$ -values on the last day:  $0.74 \pm 0.11$  and  $0.53 \pm 0.27$ ). Remarkably, trial-averaged LFP-based estimates were as similar to the day-zero profiles as were trial-averages of the actual firing rates on subsequent days (day 1:  $0.81 \pm 0.13$  for monkey D and  $0.63 \pm 0.32$  for monkey R; last day:  $0.71 \pm 0.15$  and  $0.44 \pm 0.32$ ; **Figure 4-2b** and **Figure 4-3b**).

It is important to note that variation in the monkey's behaviour from one day to the next limits the accuracy with which trial-averaged profiles on subsequent days resemble day zero, but this affects both real and estimated firing rate data equally (e.g. the downwards spike on day 24 in Monkey D, **Figure 4-2b**). In general, the LFP-based estimate performed at least as well as the actual firing rate throughout the recording, and was significantly greater than chance performance.

Comparable results were obtained when we compiled trial-averaged profiles for each target direction separately, albeit with lower  $r$ -values for both actual and estimated firing rates as a consequence of averaging over fewer trials (**Figure 4-2c** and **Figure 4-3c**).

Therefore, if we take as 'ground truth' the task-related modulation of a single neuron on day 0, this could be recovered from the LFP-based firing rate estimates at least as accurately as from the actual firing rate of the same neuron across the extended recording period. This was true in both animals.

We were still able to recover trial-averaged profiles from the LFP-based estimates even for the last sessions in our data sets before electrodes were moved to find new neurons, obtaining  $r$ -values of  $0.66 \pm 0.14$  for monkey D and  $0.57 \pm 0.34$  for monkey R, at time points corresponding to days 116 and 63, respectively. It is not possible to provide comparable values for the actual firing rates in these sessions since spike waveforms recorded on the electrodes had changed and/or deteriorated to the extent that the original ensemble of neurons could no longer be identified.

### ***4.3.3 Dimensionality of LFP-based firing rate estimates***

Although we could estimate the firing rate of all the individual neurons with considerable accuracy, we considered the alternative explanation that the neural activity was all highly correlated. Accordingly, we could hypothesise that, rather than estimating the unique features of each neural firing rate pattern, we would effectively be estimating latent (hidden) variables within the neural space, which described correlated population activity.

To examine whether subsets of highly-correlated cells were present in the data, we performed hierarchical cluster analysis on the neural space (using `linkage.m` from the MATLAB Statistics Toolbox). To measure the distance between clusters, we used the ‘correlation’ metric (one minus the sample correlation) and the ‘average’ method (unweighted average distance algorithm [UPGMA]). The resulting dendrogram was used to determine the order of cells in plots of the full pair-wise cross-correlation matrix between firing rates. In such plots, tightly-correlated ensembles would appear as clusters of high correlation values close to the main diagonal.

Although we found that the firing rates of neurons within the same cortical area exhibited higher correlation than between areas, we did not find clear evidence for smaller ensembles of tightly-correlated cells within each area (**Figure 4-4a–f**).

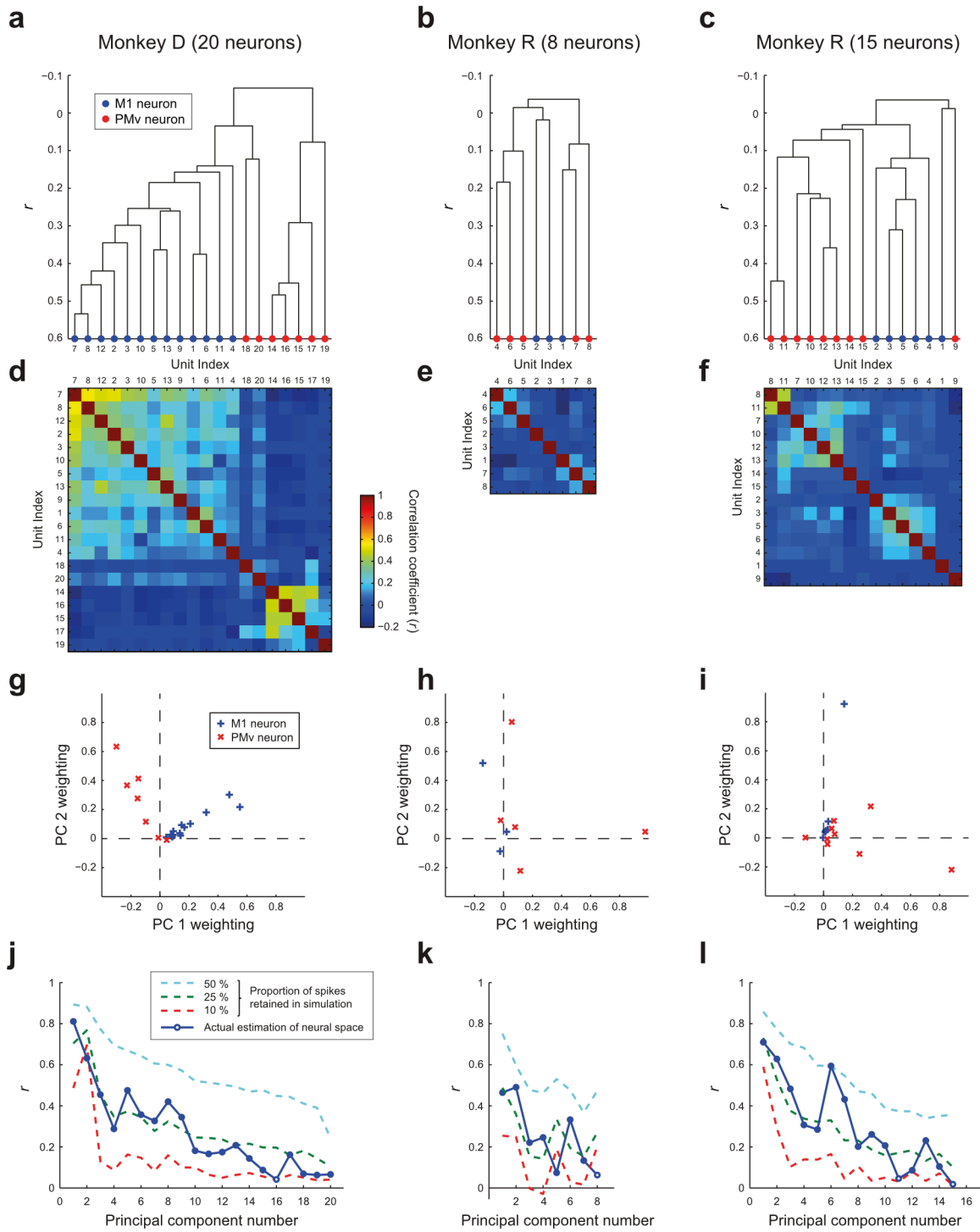


**Figure 4-4** Clustering and PC analysis of the neural firing rate-space.

(a) Dendrogram showing a hierarchical cluster tree based on correlations between the firing rates of 20 neurons in Monkey D (Same data as in **Figure 3-4a,c**, **Figure 3-10a,c,e** and **Figure 4-5a**).

(b) Same for 8 neurons in Monkey R (same data as in **Figure 4-5b**). (c) Same for another dataset in Monkey R with 15 neurons (same data as in **Figure 3-4a,c** and **Figure 3-10a,c,e**). Note that in all datasets, neurons within the same cortical area tend to be located on neighbouring branches of the tree.

(continued overleaf, bottom)

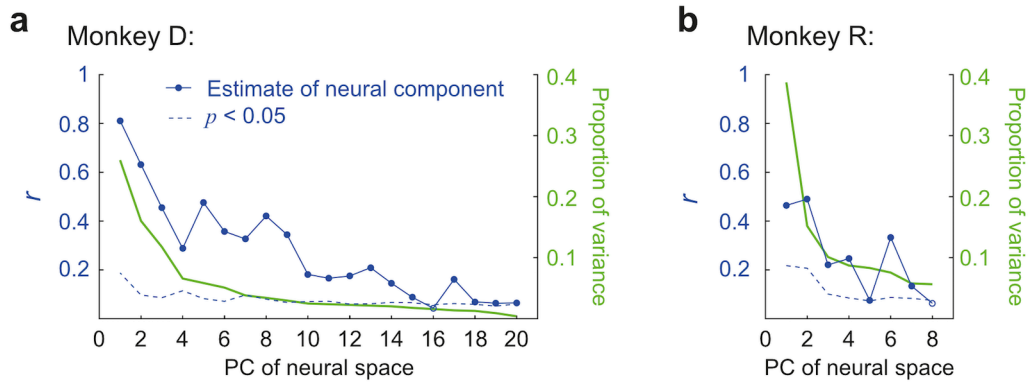


**Figure 4-5** *Firing rate estimation in principal component space.*

(a) Proportion of variance in actual firing rates of all neurons captured by each PC (*green*), and correlation coefficient on validation data for the projection of estimated firing rates onto the PCs of actual firing rates (*blue*) for Monkey D.

(b) Same for Monkey R.

Dashed line indicates  $p < 0.05$  significance threshold (two-tailed; non-parametric bootstrap).

---

**Figure 4-4** (*continued from previous page*)

(d-f) Full correlation matrix for the same datasets, ordered according to the corresponding cluster tree.

(g-i) Scatter plot of weightings for PC1 and PC2 of the high-dimensional neural space for the same datasets as shown in

(j-l) Simulation showing the effect of artificially introducing noise into the actual spike recordings by mixing a proportion of spikes between spike trains. Dashed lines show the effect of retaining 50%, 25% or 10% of spikes in the simulation. The drop-off seen in our ability to estimate higher order PCs of the neural space from *lf*-LFPs (solid blue line; see also **Figure 4-5a,b**) is comparable to estimates based on retaining 25% of the actual spike trains for each neuron. Filled circles indicate significant estimates ( $p < 0.05$ , two-tailed; non-parametric bootstrap).

Nevertheless, we considered the possibility that multichannel *lf*-LFPs might contain information only about a limited number of latent variables, corresponding to correlated components of the population activity. In this case, LFP-based firing rate estimates would predict only a few dimensions of the observed neural space.

To test this hypothesis, we calculated the PCs of the actual firing rates of all recorded neurons (low-pass filtered at 5 Hz), to find dimensions of the neural space that captured the greatest co-variation (**Figure 4-5**, *green lines*).

Approximately half of the total firing rate variance in both animals was explained by the first two PCs (which generally captured broad co-activation of neurons within M1 or PMv, **Figure 4-4g-i**), with the remainder distributed across the higher components. We then projected the LFP-based firing rate estimates of all neurons onto the same PC axes, and assessed their correlation with actual firing rates along each dimension using validation data (**Figure 4-5**, *blue lines*).

The highest correlations were obtained for the first two PCs, consistent with a previous observation that the total spiking within an area can be decoded from *lf*-LFPs (Bansal et al. 2011). However, we could also obtain statistically significant estimation of all but one of the higher PCs in each animal, suggesting fractionated components of the population activity were also contained within the LFP-based estimates. This was despite the fact that higher PCs captured less of the firing rate variability and would therefore be expected to have a lower signal-to-noise ratio.

#### **4.3.3.1 Simulation to introduce uniform artificial noise into spike trains**

There are two possible explanations for the drop-off in our ability to estimate higher neural PCs:

- i) LFP-based estimates are really only capturing a small number of latent variables within the neural space, or
- ii) Higher neural PCs have a lower amplitude, and as signal drops, the relative effect of noise increases: impacting the performance of LFP-based estimations of higher PCs.

To try to indicate which of these may be the case, we performed a simulation in which we artificially introduced uniform noise into the actual firing rates of neurons, and studied the

correlation between actual and ‘noisy’ firing rates along each of the PC axes of the neural space.

To do this, a proportion of spikes from each neuron were shuffled to spike trains of other neurons in the same recording. Whilst spikes from different neurons might not be independent (and therefore not represent random noise), we felt this shuffling was preferable to simply injecting synthetic noise, as it retained the overall statistical properties of the actual neural space. In effect, this simulated what might happen in a real experiment if spikes were misclassified to the wrong cell.

Our method was as follows: Using a recording with a total of  $P$  neurons, we retained a proportion,  $\sigma$ , (either 50%, 25% or 10%) of spikes selected randomly for each neuron. We then inserted a proportion,  $(1-\sigma)/(P-1)$ , of spikes from every other neuron into the spike train. This process was repeated for all  $P$  neurons, after which we calculated the low-pass-filtered (5 Hz as previously) and demeaned firing rates for each of the actual and ‘noisy’ spike trains. We then calculated the correlation coefficient ( $r$ ) between actual and ‘noisy’ firing rates along each of the PC axes of the neural space.

We found that the drop-off profile (with higher PCs) seen with our simulation of noise in the neural space (**Figure 4-4j-1**, *dashed lines*) was very comparable to the drop-off profile seen in our LFP-based estimation of the neural space (**Figure 4-4j-1**, *solid dark blue line*). This result was most consistent with explanation (ii) above. That is to say, our reduced ability to estimate higher PCs of the neural space using LFPs was likely because of a lower signal-to-noise ratio in higher components, rather than because our LFP-based estimations were limited to capturing a small number of latent variables.

Specifically, we found that performance of the LFP-based firing rate estimate over the entire neural space was comparable to firing rates calculated from actual spike data, in which 25% of spikes were correctly classified. This is consistent with the mean  $r$ -values for single-neuron estimation ( $\sim 0.5$ ), suggesting on average 25% of the true firing rate variation of individual neurons was captured by LFP-based estimates. Note, however, that while we here simulated the effect of noise by adding spikes from other neurons, the actual noise in our firing rate estimates did not have any consistent task relationship, since trial-averaged profiles converged on the true task-modulation of the single neurons (e.g. **Figure 4-2**, page 68).

#### **4.3.4 Generalisation and transferability of LFP-based estimation**

To test generalisation, we were interested to see whether the relationship between *lf*-LFPs and neural firing was preserved across tasks that required the generation of specific patterns of neural activity (rather than isometric torque) to successfully acquire targets. To do this, we explored how well models built on data recorded during the isometric torque task could be used to estimate firing rates during various biofeedback BMI tasks. We also used these data to test for transferability of the LFP-based firing rate estimation method.

##### **4.3.4.1 Methods**

For these experiments, we used the ‘cell control’ experimental paradigm described in **Section 2.1.3.1** (page 23), with the CED-based recording system (**Section 2.4.2**), in Monkeys D and A. Firstly, we performed a typical 50-trial torque tracking task. We trained a decoder from this data for estimating the firing rates of two neurons from up to 13 *lf*-LFPs (16 recording channels, minus one broken channel, and two channels on which the neurons-of-interest were recorded).

During the next phase of the experiment, the position of a one-dimensional (1-D) cursor was controlled in realtime by either:

- i) the firing rate of one arbitrarily chosen cell,
- ii) the summed firing rates of two cells or
- iii) the difference in firing rates of two cells, as per **Section 2.1.3.1**.

##### **4.3.4.2 Results: Generalisation**

Firstly, it is noteworthy that in general, firing rate estimates based on data from the CED system performed less well than those with the TDT-based system. This was primarily because fewer *lf*-LFPs were available with the CED-based system, but also because the 1 Hz high-pass filtering of the LFPs recorded with the CED-based system removed some informative frequencies.

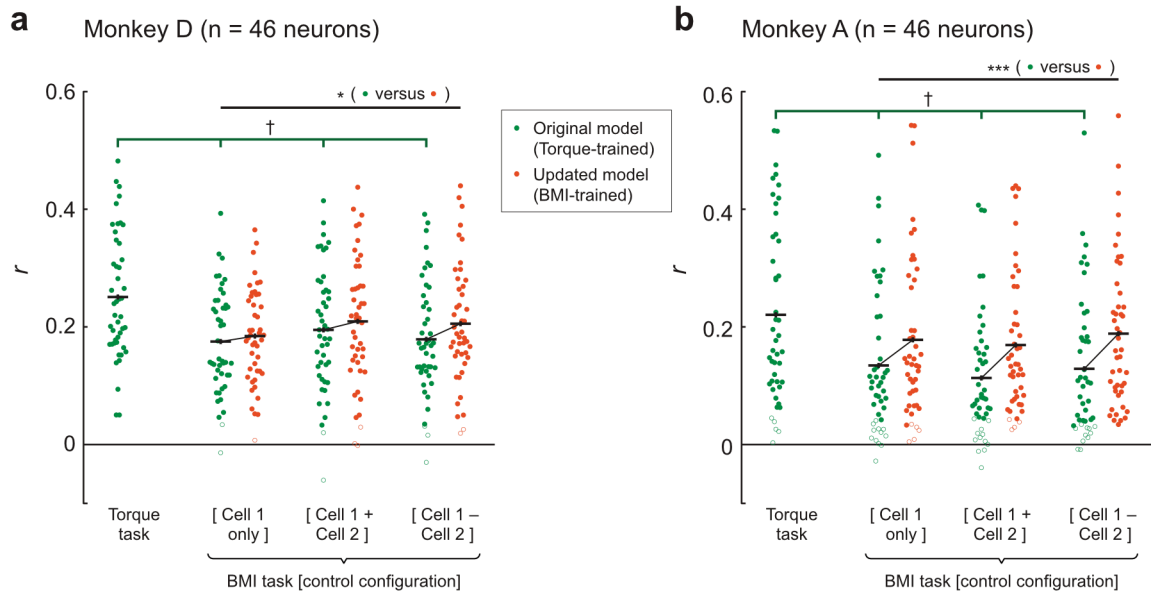


**Figure 4-6** Generalisation of lf-LFP-based firing rate estimate across ‘cell-control’ BMI tasks.

(a) Performance ( $r$ ) of firing rate estimate using a model built on the torque task data (green, ‘Torque-trained’) tested on validation data from three different ‘cell-control’ BMI tasks. Also shown is performance of model built on data from the same BMI condition as the validation data (orange, ‘BMI-trained’). Data from Monkey D; 23 experiments with 2 neurons per experiment;  $n = 46$  neurons (31 M1 neurons and 15 PMv neurons).

(b) The same for Monkey A; 23 experiments with 2 neurons per experiment;  $n = 46$  neurons (27 M1 and 19 PMv neurons).

Open circles indicate individual neurons whose firing rate estimate was non-significant by non-parametric bootstrap test ( $p < 0.05$ , two-tailed).

†,  $p < .001$  by one-way repeated-measures (rm-)ANOVA; \*,  $p < 0.05$  by two-way ANOVA; \*\*\*,  $p < .001$  by two-way rm-ANOVA.

We tested the generalisation of this model using data recorded during ‘cell-control’ tasks, during which the natural correlation between the two estimated neurons (and likely between many other recorded and unrecorded neurons) is explicitly disrupted by the requirements of the task. The results are presented in **Figure 4-6a,b** (green data) and the statistics are presented in **Table 4-1**.

	Monkey D	Monkey A
<b>Torque Task</b>	46/46 (100%)	41/46 (89%)
Mean $r \pm$ s.e.m	0.251 $\pm$ 0.016	0.221 $\pm$ 0.023
<b>Cell 1 only</b>	44/46 (96%)	34/46 (74%)
Mean $r \pm$ s.e.m	0.175 $\pm$ 0.013	0.135 $\pm$ 0.018
<b>Cell 1 + Cell 2</b>	44/46 (96%)	34/46 (74%)
Mean $r \pm$ s.e.m	0.195 $\pm$ 0.016	0.113 $\pm$ 0.016
<b>Cell 1 – Cell 2</b>	43/46 (96%)	35/46 (74%)
Mean $r \pm$ s.e.m	0.180 $\pm$ 0.014	0.129 $\pm$ 0.018
<b>One-way rm-ANOVA</b> Factor: test task type (torque, cell1_only, cell1+cell2, cell1-cell2)	$F_{2.7,120.7} = 23.6$ $p < 0.001$	$F_{3,135} = 24.3$ $p < 0.001$
Notes:	– Shapiro-Wilk test for normality passed ( $p > 0.05$ ). – Greenhouse-Geisser correction of DOF because Mauchly's test of sphericity failed ( $p < 0.05$ )	– Transformation: $Y' = \ln(Y + 0.05)$ – Then Shapiro-Wilk test passed ( $p > 0.1$ )

**Table 4-1** Generalisation of lf-LFP-based firing rate decoders, trained on 'torque task' data and tested (validated) on data from 'cell-control' BMI tasks.

Numbers in grey rows indicate fraction (and percentage) of neurons with significant validation performance. s.e.m., standard error of the mean;  $F$ , ANOVA  $F$ -statistic with DOF in subscript.

In both animals, there was a modest (~30% on average) but significant drop ( $p < 0.001$ ) in the performance of firing rate estimation across tasks, suggesting that decoders trained on torque tracking data have some difficulty generalising to BMI data. The result is still surprisingly good, considering the noticeable difference in the subjects' behaviour during the cell-control BMI tasks.

To test this possibility, we compared our 'original' torque-task-trained models with 'updated' models: trained using data from the same 'cell control' BMI task as the validation. The results are presented in **Figure 4-6a,b**, above (*green data vs. orange data*) and the statistics in **Table 4-2**, below.

	Monkey D		Monkey A	
	Original decoder (Torque-trained)	Updated decoder (BMI-trained)	Original decoder (Torque-trained)	Updated decoder (BMI-trained)
<b>Cell 1 only</b>				
Mean $r \pm$ s.e.m	0.175 $\pm$ 0.013	0.184 $\pm$ 0.012	0.135 $\pm$ 0.018	0.178 $\pm$ 0.021
<b>Cell 1 + Cell 2</b>				
Mean $r \pm$ s.e.m	0.195 $\pm$ 0.016	0.209 $\pm$ 0.016	0.113 $\pm$ 0.016	0.169 $\pm$ 0.017
<b>Cell 1 - Cell 2</b>				
Mean $r \pm$ s.e.m	0.180 $\pm$ 0.014	0.206 $\pm$ 0.015	0.129 $\pm$ 0.018	0.189 $\pm$ 0.019
<b>Two-way rm-ANOVA</b>				
<b>Factor:</b> decoder type (original, updated)	$F_{1,45} = 5.31$ $p = 0.026$		$F_{1,45} = 65.3$ $p < 0.001$	
<b>Factor:</b> test task type (torque, cell1_only, cell1+cell2, cell1-cell2)	$F_{2,90} = 3.33$ $p = 0.040$		$F_{2,90} = 1.91$ $p = 0.15$	
<b>Interaction:</b>	<i>n.s.</i>		<i>n.s.</i>	

**Table 4-2** Comparison of using the ‘original’ model (trained on torque task data) vs. using an ‘updated’ model (trained on data from the specific cell-control block).

Abbreviations as per Table 4-1; *n.s.*, not significant.

These results demonstrated that an updated decoder was able to perform moderately but significantly better than the original decoder (5–13% improvement in Monkey D,  $p = 0.026$ ; 23–33% improvement in Monkey A,  $p < 0.001$ ). This confirmed that there are some limitations to the ability of the torque-trained decoder to generalise to the different behavioural scenario of the cell-control task. Nevertheless, given the very abstract and non-naturalistic nature of the cell-control BMI task, the ability of our LFP-based firing rate decoders to generalise across different behavioural scenarios is reassuring.

#### 4.3.4.3 Transferability: Does cortical area in which the neuron is located affect performance of LFP-based firing rate estimation?

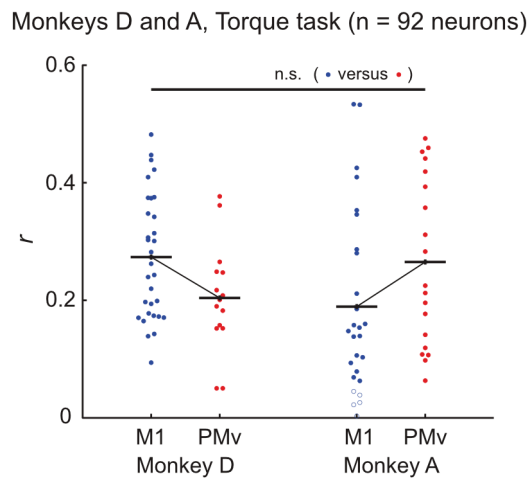


**Figure 4-7** Comparison of model performance for M1 vs. PMv neurons.

Comparison of model performance ( $r$ ) for M1 (blue) and PMv (red) neurons during the torque task in Monkey D (left) and Monkey A (right). n.s., not significant by two-way independent samples ANOVA ( $F < 1$  and  $p > 0.05$ ). Open circles indicate individual neurons whose firing rate estimate was not significant by non-parametric bootstrap test ( $p < 0.05$ , two-tailed). Data met all assumptions of two-way independent samples ANOVA.

Overall, we found no significant difference in our ability to estimate M1 and PMv neurons (two-way independent samples ANOVA, effect of Factor Area,  $F_{1,88} = 0.016$ , n.s.; effect of Factor Monkey,  $F_{1,88} = 0.181$ , n.s.), although a significant interaction was found between factor Monkey and factor Area ( $F_{1,88} = 6.78$ ,  $p = 0.011$ ), with M1 neurons estimated better in Monkey D and PMv neurons better in Monkey A (Figure 4-7).

#### 4.3.4.4 *Transferability: Does the underlying neuronal firing rate affect performance of LFP-based firing rate estimation?*

Monkeys D and A, Torque task (n = 92 neurons)

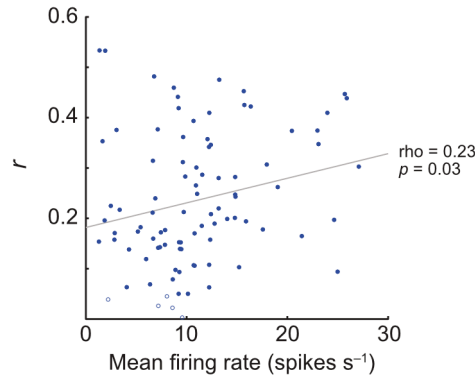


**Figure 4-8** *Model performance for neurons with different actual firing rates.*

Estimation performance ( $r$ ) vs. mean actual firing rate for all 92 neurons (46 neurons from each subject). Dashed shows simple least-squares regression line, with correlation coefficient,  $\rho$  and  $p$ -value of the regression. Open circles indicate individual neurons whose firing rate estimate was not significant by non-parametric bootstrap test ( $p < 0.05$ , two-tailed).

We were able to estimate neurons with a very wide range of firing rates, although performance was positively correlated with mean firing rate (**Figure 4-8**; regression line,  $\rho = 0.23$ ,  $p = 0.03$ ).

#### 4.3.4.5 *Transferability: Is the performance of firing rate estimation dependent on the association of neuronal activity with movement?*

We considered the possibility that our SRSP-based method may be dependent on sensory afferent signals from the arm and hand, being generated secondary to movement. If this were the case, this would impact our ability to estimate neuronal firing rates in situations where sensory feedback was absent: the most obvious example being a paralysed patient who can display movement intention, but is not able to generate overt movement. To test this, we investigated whether our ability to estimate the firing rate of a neuron was dependent on that neuron's association with wrist torque.

Using data from the one-cell control task (*Cell 1 only*) from both subjects, we quantified the degree to which neuronal firing rate modulation was associated with movement of the wrist, across each of the four targets, using a 'torque modulation index' (TMI). This was calculated

from the gradient of the linear regression of average absolute torque (during the hold period) against target position (in screen coordinates). TMI was normalised by the torque-position gain during the torque control task. Thus, a TMI value of less than one indicated that, during cell control, the monkey modulated torque less to acquire targets than during the torque task, while a value of zero indicated no overall modulation of torque for the different BMI targets.

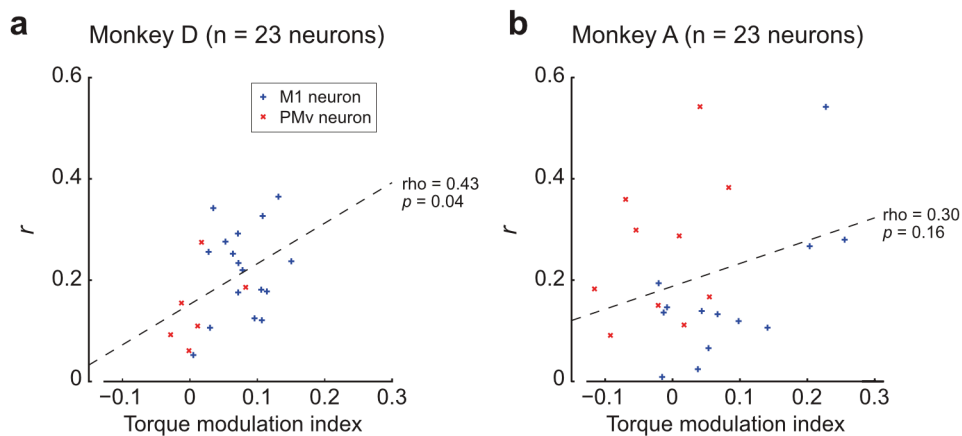


**Figure 4-9** Performance of firing rate estimation for cells that are modulated to a greater or lesser extent with movement (wrist torque), as quantified by a torque modulation index (TMI).

- (a) Performance ( $r$ ) of firing rate estimation vs. TMI for the ‘Cell 1 only’ cell-control BMI task in Monkey D ( $n = 23$  neurons).
- (b) Same for Monkey A ( $n = 23$  neurons). Data are plotted separately for M1 (blue ‘+’) or PMv (red ‘x’) neurons.

Dashed line shows least-squares regression through all points with correlation coefficient, rho, and  $p$ -value.

We found a weak correlation (significant in one animal) between the TMI and the performance of our LFP-based firing rate estimate (Monkey D, correlation coefficient = 0.43,  $p = 0.04$ ; Monkey A, correlation coefficient = 0.30,  $p = 0.16$ ). However, LFP-based firing rate estimation performed well in many cases even when the behaviour involved minimal torque modulation (**Figure 4-9**). Obviously, using this method, we could not account for firing rate modulation associated with movements of other joints that we were not monitoring.

Finally for this section, we studied one example PMv neuron from Monkey A in greater depth during the one-cell control task—whose firing rate modulation was not directly correlated with the production of torque—to explore whether there were any changes in the shape of the SRSP under different firing rate conditions.

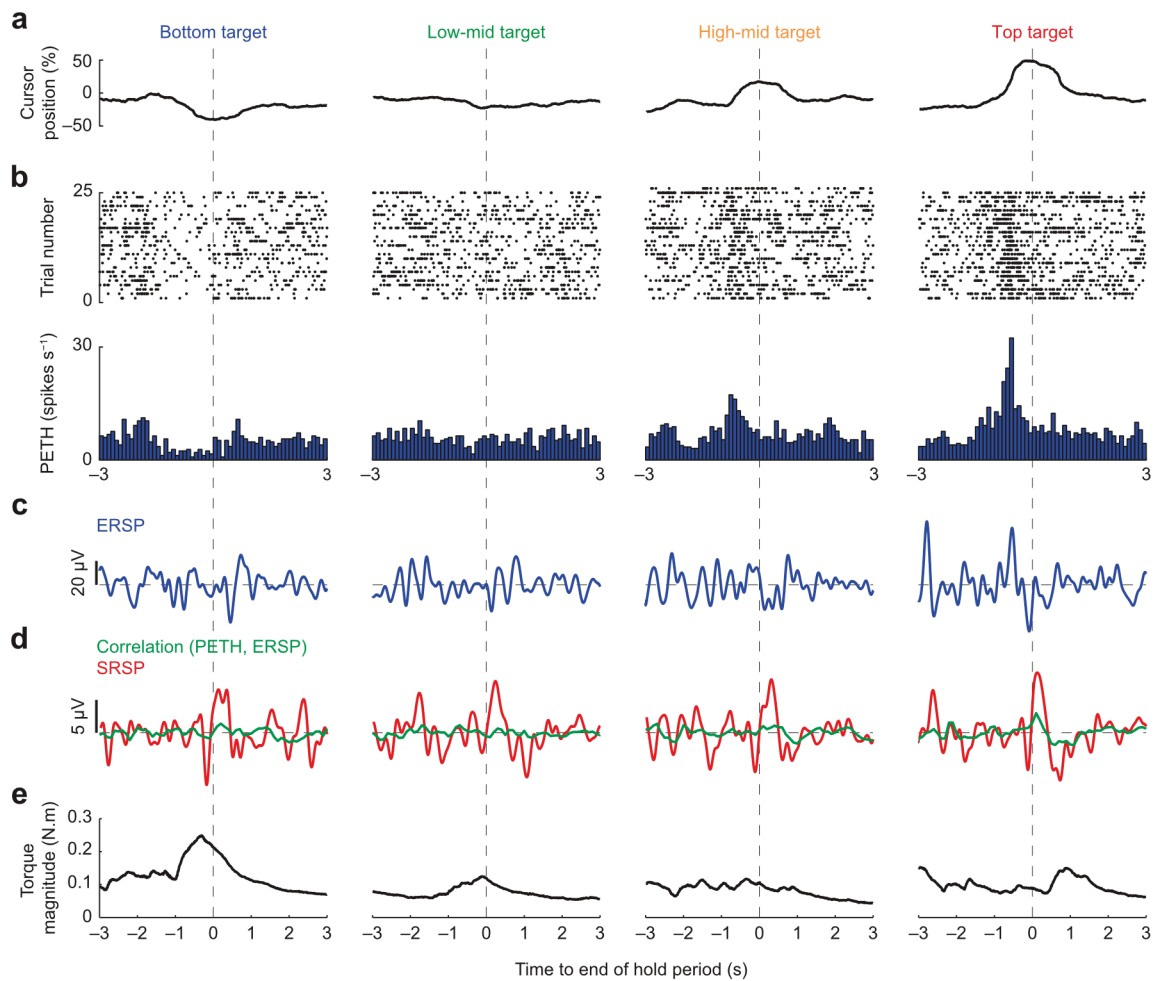


**Figure 4-10** SRSP (spike-related slow potential) during ‘cell-control’ BMI task.

- (a) Trial-averaged cursor position, aligned to end of hold period, during the 1-D ‘cell-control’ BMI task in which Monkey A controlled the firing rate of a single PMv neuron.
- (b) Spike raster and peri-event spike time histogram (PETH) of the controlling neuron.
- (c) Trial-aligned average of an lf-LFP on another PMv channel, labelled as the ‘event-related slow potential’ (ERSP).
- (d) Red, spike-related slow-potential (SRSP) of the lf-LFP for only those spikes shown above. Green, cross-correlation of the ERSP and PETH shown above.
- (e) Trial-aligned average wrist torque magnitude.

In the example session shown in **Figure 4-10**, Monkey A performed 100 trials of the 1-D ‘cell-control’ task (cursor position **Figure 4-10b**) by modulating the firing rate of a single PMv neuron (**Figure 4-10b**) to acquire 4 different targets while the isometric torque generated by the left wrist was monitored. Acquisition of the bottom target (reduced firing rate) was associated with wrist torque (**Figure 4-10e**), but the other targets were achieved without any consistent overt movement.

STAs of the *lf*-LFP (revealing the SRSP) from a second PMv electrode were compiled using only spikes within  $\pm 3$  s of the end of successful trials for each target (**Figure 4-10d**, *red traces*). Although noisy due to the small number of events, a positive *lf*-LFP peak followed the trigger spike in each case, even for those targets which were not associated with the generation of torque (middle and top targets). Indeed, the SRSP was remarkably consistent across targets with very different trial-averaged firing rate profiles (**Figure 4-10b**).

This may seem counter-intuitive, especially since the trial-averaged *lf*-LFP does not show any obvious modulation for these targets (**Figure 4-10c**). Indeed, we can assess the SRSP that would be expected from task-related co-variation in firing rate and *lf*-LFP by calculating the cross-correlation between the trial-averaged firing rate and trial-averaged *lf*-LFP (**Figure 4-10d**, *green traces*). The peaks in these correlations are about an order of magnitude smaller than the true STA, suggesting that the SRSP does not merely represent co-variation between signals that are time-locked to task events or wrist movements. Rather the SRSP includes correlations between firing rate and *lf*-LFP that vary trial-to-trial, and therefore do not survive averaging aligned to task events.

#### **4.3.5 Realtime biofeedback using LFP-based firing rate estimates**

So far, using offline analyses, we have demonstrated that firing rates can be estimated from *lf*-LFPs, that the multichannel *lf*-LFP captures the majority of the latent dimensionality of the neural space, that firing rate estimations capture a large proportion of the variance of task-aligned firing rate modulation, that LFP-based models generalise reasonably well across different behavioural scenarios, and that LFP-based firing rate estimation is almost certainly not just an artefact of a specific, esoteric experimental setup.

Finally for this chapter, we performed realtime biofeedback BMI experiments controlled by the *estimated* firing rates of neurons. Our hypothesis was that we would be able to drive changes in the *actual* activity of specific neurons, by providing *only lf*-LFP-based feedback of their firing rates to the subject. If true, this would provide a powerful demonstration that *lf*-LFP-based firing rate estimates are able to separate the activity of individual neurons from the general neuronal population.

#### 4.3.5.1 *Methods: Experimental setup and analysis of behaviour*

For online firing rate estimation during the ‘LFP-control’ BMI task, we trained a decoder to estimate the firing rate of one or two neurons, based on an initial 50 trials (~ 5 mins) of the torque-task. We used the same approach as offline (as described in **Section 3.3.5.1**), but with  $\tau_1 = -1.8$  s and  $\tau_2 = 0.2$  s, such that online firing rate estimation was delayed by 0.2 s relative to the realtime data. Again, we excluded *lf*-LFPs from those electrodes used to record the selected neurons.

Once we had built our decoder for a particular day, we stored the *lf*-LFP weighting matrices,  $\mathbf{M}_1$  and  $\mathbf{M}_2$ , and inverse filter kernels,  $\mathbf{\kappa}_1$  and  $\mathbf{\kappa}_2$ . Then, using these parameters, the projection of *lf*-LFP signals into the source space and subsequent inverse filtering were implemented on hardware digital signal processors within the TDT-RZ2 using the TDT Realtime Processor Visual Design Studio (RPvdsEx) software.

Monkeys then performed the 1-D biofeedback BMI task (in configurations *Cell 1 only* and *Cell 1 – Cell 2*) but rather than being controlled by the actual firing rates of one or two neurons, the cursor position was controlled by *estimated* firing rates. We called this experiment ‘LFP-control’ BMI, and further details of the experimental setup have already been given in **Section 2.1.3.2**.

Generally, cursor position data (and thus firing rates) were analysed by aligning to the end of the successful hold period. Because a trial had no set length (and therefore continued until the animal successfully acquired the presented target), the end of the trial was chosen to enable direct comparison between firing rates in each of the various biofeedback contingencies.

However, we also wanted to check that subjects were controlling the cursor position (modulating firing rates) in a goal-directed way, by excluding the null hypothesis that firing rates were modulated randomly and targets thereby acquired by chance. To do this, cursor position data were instead aligned to the ‘go’ cue (the point in the task at which subjects were cued to start making directed movement towards a peripheral target). The mean cursor position for each trial was then calculated over the first 1 second after the go cue. The sample of mean cursor positions for the top-most (70%) target were then compared to the sample for the bottom-most target (–70%) using the independent two-sample *t*-test (MATLAB function `ttest2.m`), with the null hypothesis of no difference.

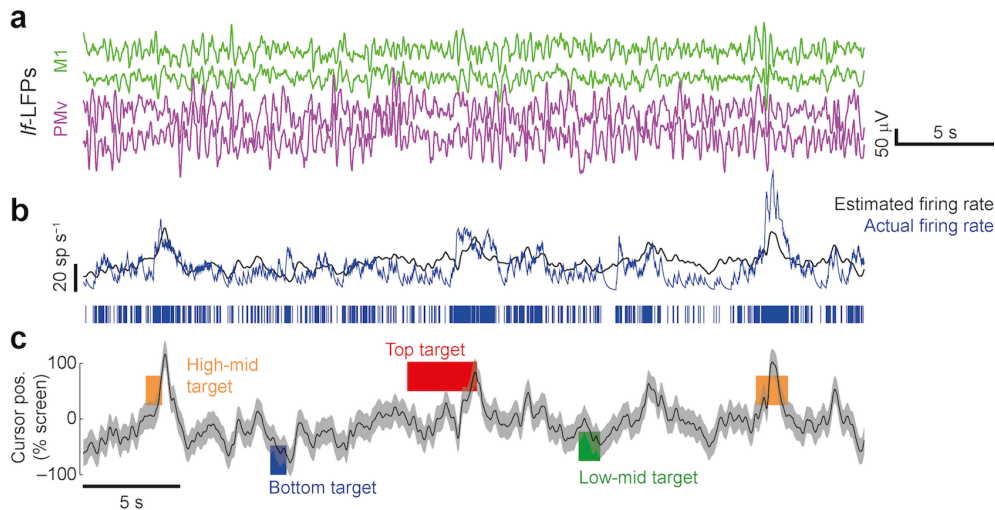


**Figure 4-11** Biofeedback BMI controlled by realtime LFP-based firing rate estimates.

- (a) Example if-LFPs (4 shown of 18) as monkey D controlled a BMI cursor using the estimated firing rate of an M1 neuron.
- (b) Realtime estimated and actual firing rates and spike raster.
- (c) Cursor and target positions (shading indicates cursor and target width).

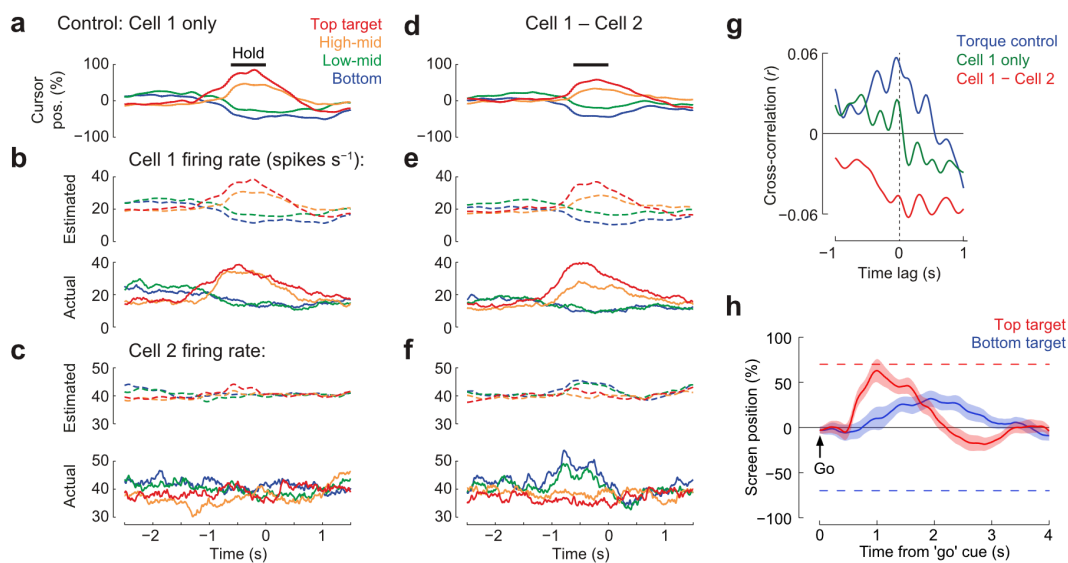


**Figure 4-12** Trial-averaged data for cursor position and actual/estimated firing rate.

- (a) Trial-averaged cursor position aligned to end of the successful hold period.
- (b) Trial-averaged estimated and actual firing rates of Cell 1 (the controlling M1 neuron).
- (c) Trial-averaged estimated and actual firing rates of Cell 2 (a non-controlling M1 neuron).
- (d–f) As in a–c, but now for a task controlled by the difference between estimated firing rates of Cell 1 and Cell 2.
- (g) Cross-correlation of the actual firing rates of Cell 1 and Cell 2 during the initial torque task and subsequent ‘LFP-control’ BMI tasks.
- (h) Mean cursor trajectories (across trials) aligned to the ‘go’ cue for the top (70%, red) and bottom (–70%, blue) targets for a representative experiment in Monkey D, where cursor position was controlled by the estimated firing rate of Cell 1 (as in panel a). Shading indicates  $\pm$ SEM. Dashed lines indicate the centres of the respective targets. There was no time-out, so trial length depended on speed of target acquisition, with some trials taking longer than the four seconds shown here.

#### 4.3.5.2 Results: Realtime control of firing rate estimates

Monkeys were rapidly able to control the cursor position based on the estimated firing rate of a single neuron (or the differential firing rates [estimated] of two neurons). A section of electrophysiological and behavioural data from a typical LFP-control session (here involving one-‘cell’ control with an M1 neuron) is presented in **Figure 4-11**. It is important to note the sample of neurons used for these LFP-control experiments was completely new, so the subjects had not previously experienced control of these particular neurons in any other form of BMI task.

Monkeys were able to both increase and decrease the estimated firing rates of single neurons (**Figure 4-12a–c**), but more importantly, they could achieve simultaneous independent control of two estimates when each moved the cursor in opposite directions (**Figure 4-12d–f**). It is important to emphasise at this point, that both neurons were being estimated in realtime, and simultaneously, from the *same* set of  $\sim 20$  *lf*-LFPs (minus the two LFPs on the same electrodes as the selected neurons).

Moreover, although we imposed no direct constraints on the activity of the underlying neurons, monkeys nevertheless performed the task by modulating the *actual* firing rates of the chosen neurons (**Figure 4-12b,c,e,f**), and the correlation between neurons changed in accordance with the imposed biofeedback contingency (**Figure 4-12g**).

We found that both animals consistently found it easier to increase, rather than decrease estimated firing rates. (This was a finding we also noted in those experiments [above, **Section 4.3.4.2**] where cursor position was controlled by *actual* firing rate [data not shown]).

Correspondingly, we found that target-directed cursor movement for targets associated with increased estimated firing rate (‘top’ targets) was considerably more consistent and stereotyped (e.g. **Figure 4-12h, red**) than cursor movement for targets associated with decreased estimated firing rate (‘bottom’ targets; e.g. **Figure 4-12h, blue**), when aligned to the ‘go’ cue. Therefore, whilst it appears from **Figure 4-12h** that the subject is paradoxically making small upwards movements for the bottom target (*blue*), it is important to note that the trace shows the mean across trials of the first four seconds of 25 trials with this target. The downward movement of the cursor actually associated with trial success occurred with high temporal variability, and therefore a stereotypical behaviour was not captured in the mean in the same way as it was with the ‘top’ target. Nevertheless, cursor movement over the first

second following the go cue was significantly different between trials with the ‘top’ target and those with the ‘bottom’ target ( $p = 0.02$ ; independent two-samples  $t$ -test;  $n_{\text{up}} = 24$ ,  $n_{\text{down}} = 25$ ). The same result was seen in a representative experiment from Monkey R ( $p = 0.002$ ;  $n_{\text{up}} = 30$ ,  $n_{\text{down}} = 30$ ). It is also important to note that monkeys were not exposed to, or trained on, control of a particular neuron’s firing rate (either actual or estimated) prior to a particular day’s experiment. Each experiment therefore captured a period of operant conditioning, which necessarily required exploratory behaviour by the animal, especially at the beginning of the session. It’s likely that, given training with feedback from the *same* neuron over a number of days, subjects would be able to learn much more consistent and direct cursor movements, for both increases and decreases in (estimated) firing rate.

#### 4.3.5.3 *Methods: Analysis of group data*

We defined a tuning index to quantify the modulation of firing rate with target position. The actual firing rate of each cell was normalized to zero mean and unity variance over the ‘LFP-control’ BMI session. Firing rate profiles for each target were aligned to the end of successful trials and averaged separately for estimated and all other neurons. The task-modulation of firing rates was quantified using a tuning index, calculated for each neuron during the hold period of the task (adjusted for the 0.2 s delay in the firing rate estimation), according to:

$$\text{Tuning index} = \frac{\bar{x}_{\text{top}} - \bar{x}_{\text{bottom}}}{\bar{x}_{\text{top}} + \bar{x}_{\text{bottom}}} \quad (4.1)$$

where  $\bar{x}_{\text{top}}$  and  $\bar{x}_{\text{bottom}}$  are the mean firing rates of the neuron during the (adjusted) hold period across all trials for the top target and bottom target, respectively.

We analysed a total of 44 controlling (estimated) neurons, and 947 other neurons, across 44 sessions (22 each in Monkeys D and R). The distribution of tuning indices of controlling (estimated) neurons was compared to all other neurons using the Mann-Whitney  $U$ -test, because data were not normally distributed (by the Shapiro-Wilk test).

#### 4.3.5.4 Results: Group data

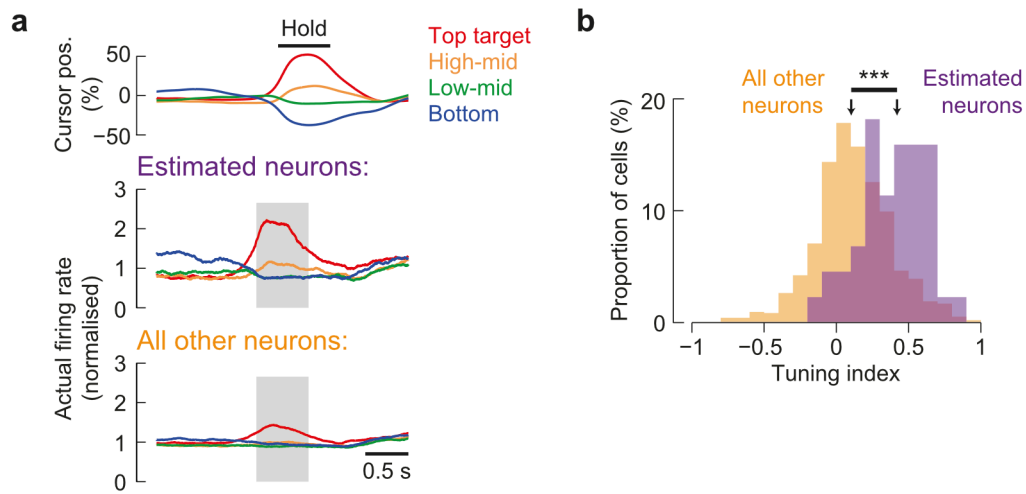


**Figure 4-13** Group data for actual firing rates of estimated neurons vs. all other neurons

- (a) Mean cursor position (top) across sessions where monkey D (22 sessions) or R (22 sessions) controlled the estimated firing rate of one neuron. Mean actual firing rates of controlling neurons (*middle*,  $n=44$ ) and all other cells (*bottom*,  $n=947$ ).
- (b) Tuning index (calculated within grey box in **k**) of the estimated neuron versus all other cells. ↓, median; \*\*\*  $p < 0.001$ , by Mann-Whitney  $U$  test, because data did not pass normality assumptions (Shapiro-Wilk,  $p = 0.05$ ).

Across 44 sessions in two animals, we found that the estimated neurons were significantly more tuned than the other recorded neurons (median tuning index of estimated neurons, 0.42; other neurons, 0.10;  $U = 9,140$ ,  $p < 0.001$ , two-tailed, by the Mann-Whitney  $U$ -test) (**Figure 4-13**).

## 4.4 Discussion

Firstly, in this Chapter, we have demonstrated that linear models for estimation of single-neuron firing rates from  $lf$ -LFPs are surprisingly stable in their performance over a number of weeks. In fact, with trial-averaged data, LFP-based estimates performed at least as well as actual firing rates in estimating ‘ground truth’ task-related neuronal behaviour. Remarkably, we were able to recover trial-averaged firing rate profiles out to 116 days (Monkey D) and 63 days (Monkey R). At this point spike waveforms had deteriorated so much that we could no longer identify the original neurons, but in theory, our LFP-based estimates of neuronal behaviour could probably have continued for longer, if it wasn’t that we had moved the electrodes to perform a different experiment.

The stability of signals based on the *lf*-LFP that we have documented here is consistent with the existing literature. Flint and colleagues have documented the stability of *lf*-LFP out to 210 days (Flint et al. 2013) and Chao and colleagues have similarly used ECoG out to 250 days (Chao et al. 2010). Furthermore, Flint and colleagues found that in a closed-loop BMI, movement-related *lf*-LFP signals (which they termed the LMP) were particularly informative, and more stable even than using multi-unit threshold crossings (Flint et al. 2016).

Unfortunately, due to the limitations of the geometry of our arrays, we cannot comment specifically on the reason for this stability at the electrophysiological or cellular level. But the fact that our SRSP features seem to originate from multiple sources within a cortical area (likely each corresponding to ensembles of many thousands of neurons), supports the theory that the *lf*-LFP is less sensitive to micromotion than extracellular spike recordings. Additionally, it seems plausible, that while gliosis and inflammation may displace or kill a single neuron, the *lf*-LFP should be relatively robust (as long as the LFP signal can reach the recording site by volume conduction), because it is generated as a result of the membrane potentials of a very large number of cells.

Future work in this area could explore the combination of spike-based signals and *lf*-LFPs via ‘hybrid’ decoder approaches. We envisage a scenario in which, soon after electrode implantation—while clean spike recordings can be obtained from many neurons—model parameters that relate the firing rates of these neurons to *lf*-LFPs could be calculated. While neuronal recordings remain stable, actual firing rates could be used for BMI control, but *lf*-LFP-based models may then allow estimated firing rates to be used after spike recordings have substantially deteriorated.

Alternatively, there is an increasing trend in the field towards using hybrid BMIs (spikes *with* LFP) as a matter of course (Flint et al. 2013; Gilja et al. 2015; Stavisky et al. 2015). LFP signals can be used to augment the performance achieved with spikes alone, and/or can be brought into use when spike signals are poor or absent. Understanding the relationship between neuronal spiking and the LFP in motor cortex will be critical to these endeavours, in order to inform which features of the LFP should be chosen. Whilst *lf*-LFP-based estimates of single neuron firing rate are one option, there may be more sophisticated models that can be discovered in the future through a better understanding of the generation of the LFP by cortical neural networks.

Secondly, we have shown that our LFP-based firing rate model is able to capture a large proportion of the structure present within the higher-dimensional neural space, rather than just capturing correlated components of population activity (reflecting widespread, synchronous activity, for example). When estimating the firing rates of 8–20 neurons simultaneously, we obtained significant prediction along all but one PC of the observed neural space. The quality of fit along each dimension could be simulated by adding noise uniformly across individual neurons, suggesting that the LFP-based estimates are not systematically biased to particular PCs. Moreover, when estimates of single neurons were used for realtime biofeedback, task-related firing rate modulations were largely confined to the targeted neuron.

Therefore, we conclude that the dimensionality of LFP-based estimates is comparable to the dimensionality of our multiple single-unit recordings. It remains to be seen whether this will stay true as the density of recording arrays increases. One possibility is that, as more of the network is sampled, the SRSP attributed to each recorded neuron will eventually converge on the true causal effect of its spiking. Alternatively, greater single-unit resolution may ultimately reveal tightly correlated ensembles beyond which SRSP-based separation becomes impossible.

Questions over the dimensionality of neural activity have an interesting relation to the apparent paradox of extreme redundancy in the motor cortex. M1 in macaques constitutes about 2.2% of the surface area of the cortex, and weighs around 1.4 g, with a cell density of around 75 million neurons per gram (Young et al. 2013) – meaning that there are approximately 100 million ( $10^8$ ) neurons in each macaque M1.

The theoretical number of degrees of freedom (DOFs) in the primate forelimb is many orders of magnitude lower. A reasonable estimate is 30 in the human: assuming there are 7 DOFs in the shoulder, elbow and wrist, for positioning of the hand, and around 22 DOFs in the intrinsic motion of the hand and digits (Rouse & Schieber 2015). The number of DOFs in the macaque forelimb is lower still, because they have considerably less individuated control over fine hand movements.

The *effective* number of independent DOFs of the primate forelimb is then considerably lower than this theoretical number, because

- a) natural movement almost never occurs in isolation at a single joint (Hager-Ross & Schieber 2000), and

- b) there is considerable evidence for muscular ‘synergies’ in the motor system: underlying patterns of simultaneous activity at multiple muscles, likely organised in the spinal cord (Hart & Giszter 2013), which mediate common natural movements (Rouse & Schieber 2015).

Therefore, we can see that there is considerable convergence in the motor system. From, in the order of,  $10^7$  neurons in the motor cortex encoding forelimb movement, to less than  $10^2$  DOFs of movement in both forelimbs: this considerable redundancy in the motor cortex has long been a source of interest for motor neuroscience researchers. As we see in our data, neurons within a cortical area certainly tend to be correlated. But in one study in rodent motor cortex, it was found that 96% of neurons contributed redundant predictive information about behavioural performance to their neuronal ensemble (Nandakumar et al. 2005).

Studies from the BMI field have shown that monkeys can use the firing rates of single neurons from M1 to control low-DOF BMIs (Fetz & Baker 1973). So, if each DOF of the forelimb could theoretically be encoded by the activity of, say, a single neuron, and there are less than 100 DOFs in forelimb movement, then why does the motor cortex require 10,000 times this number of neurons (and therefore a huge amount more energy) to control the forelimbs?

The answer is still a matter of investigation, but there is an emerging consensus that, rather than neurons encoding information independently, the motor cortex encodes information through the population activity of many thousands of neurons: in a high-dimensional space (the  $P$ -dimensional ‘neural space’), wherein each dimension corresponds to the activity of one neuron (Sadtlter et al 2014). Having more neurons than controlled DOFs allows for what is termed an ‘active space’, of dimensionality  $D$  (wherein activity leads to movement generation) and a ‘null space’, of dimensionality  $M = P - D$  (wherein activity produces no output) (Rouse & Schieber 2015).

*Why* this arrangement may exist is also an active question. One suggestion is simply that the null space acts as a repository for noise, allowing an ensemble of noisy neurons to encode their output more precisely in the active space, whilst their noise produces changes in the null space. A second possibility is that the null space permits preparatory activity to take place without producing movement (Churchland et al. 2010). A third possibility is that the null space permits more rapid adaptation of skills to new scenarios. There is evidence that

established patterns of activity take place within an ‘intrinsic manifold’ of the neural space—a ‘preferred’ sub-space which is constrained by the existing neural circuitry (Sadtlter et al. 2014)—and that the null space (the ‘uncontrolled manifold’) allows for the exploration of new trajectories when adapting a previously learned skill for use in a new context (Kaufman et al. 2014). Fourth and finally, the null space and active space may not be fixed, and the brain may be able to switch between multiple simultaneous representations of movement depending on context (Rouse & Schieber 2015).

Given that we have found that the dimensionality of LFP-based estimates is comparable to the dimensionality of our multiple single-unit recordings, it begs the question whether similar ‘active’ and ‘null’ spaces may be a feature of the high-dimensional LFP space, as seems to be the case with the neural space. Interestingly, Flint and colleagues have recently shown that projections of LFP features into a subspace relevant to a BMI task are significantly more stable over time than are projections into a “task-null” space (Flint et al. 2016). Given that LFPs are, by their nature, generated by correlated ensembles of neurons, and ‘subspace’ theories of neural redundancy seem to rely on subtle variations in correlation between individual neurons, there would appear to be a contradiction here. It may be that, as proposed by Flint and colleagues, “the brain is capable of different levels of control on mesoscopic (LFPs) and single-neuron scales ...” (Flint et al. 2016). More work is clearly needed in the future in this complex area.

Thirdly, in this Chapter, we have shown that *lf*-LFP/SRSP-based models generalise reasonably well between different behavioural scenarios. We have also shown that our model works on both M1 and PMv neurons, on neurons with a wide range of firing rates, and on neurons whose activity is modulated to a greater or lesser extent by movement.

These findings all bode well for the use of SRSP-based models in real-world BMIs. Models that are over-fitted to their specific training context generalise poorly to new scenarios. This is a very real concern in the field, given the current trend for simply trying to record more and more neurons in order to decode more kinematic parameters and control more DOFs. The ‘curse of dimensionality’ (Bellman 1957) dictates that the amount of data required grows exponentially with the dimensionality, in order to avoid sparsity. Because correlated noise can lead to overfitting at the initial regression, it is not necessarily the case that endlessly increasing the number of recorded neurons in a biomimetic decoder will increase BMI performance (Rouse & Schieber 2015).

It may be that we should take a different approach. Unlike biomimetic decoding, the biofeedback learning problem is one that must be solved by the brain rather than the system engineer. Biofeedback control signals can be chosen based on their stability over time, or other desirable characteristics, rather than simply whether they can predict movement parameters in a training dataset. Therefore, we could choose to use a relatively small number of *lf*-LFP-based signals (such as estimated firing rates), on the basis of their stability and ability to generalise, and allow patients to learn how to use them, via biofeedback, to control a prosthetic which has relatively few DOFs, but is very reliable and predictable in its behaviour. We propose that such a neuroprosthetic might be life-changing for a paralysed patient, who might get more independence from being able to control the position of their own bed (very predictably, and at relatively low cost), for example, rather than being able to control a multi-DOF robotic arm (which may not be very predictable, and may require recalibration every day). Likewise, the ability to infer firing rates from *lf*-LFPs is potentially applicable to any neuroprosthetic application requiring long-term monitoring of neural activity – not just motor BMIs.

Critical to this vision, and finally for this Chapter, we have demonstrated realtime, closed-loop control and operant conditioning of two neurons simultaneously, using biofeedback only of their *estimated* firing rates, derived solely from *lf*-LFP signals. The next step of demonstrating utility of these signals for BMIs, would be to show whether (or not) these realtime signals can truly transfer outside of the controlled experimental setup, into a more practical application, such as controlling a simple robotic effector, or even controlling electronic stimulation of the muscles or spinal cord, to ultimately enable re-animation of patients' own limbs.

## 4.5 Chapter summary

- Low-frequency LFP-based (SRSP-based) models for estimating the firing rates of single neurons were stable over weeks to months.
- LFP-based estimates captured around 25% of the variance of instantaneous firing rates and 75–85% of trial-averaged profiles, performing as well as the actual firing rates at reconstructing the task relationship of individual neurons on subsequent days.
- The dimensionality of LFP-based firing rate estimates was comparable to the dimensionality of our multiple single-unit recordings.

- LFP-based firing rate models generalised reasonably well across different behavioural contingencies.
- LFP-based firing rate estimates were sufficiently accurate and specific to permit operant conditioning of individual neuron firing rates using biofeedback based solely on *lf*-LFPs.



# Chapter 5. Low-frequency cyclical cortical dynamics: exploring novel signals for BMIs

*In which I describe the presence of intrinsic cyclical dynamics in the primate motor cortex, the potential origin and significance of this dynamical activity, and the potential use of these cyclical dynamics for brain-machine interface devices.*

## 5.1 Introduction

### 5.1.1 Motivation

In previous chapters, I have already introduced the existing state-of-the-art BMI decoder system. To summarise, this is typically:

- A. *Spike-based* – This requires that consistent neuronal spiking can be recorded for the expected life-span of the implanted device.
- B. *Biomimetic* – This requires that recorded neural activity has a sufficiently naturalistic relationship to certain movement parameters that the device is intuitive to control. This is somewhat down to chance, especially when the input space (number of neurons) is so small, relative to the number of neurons involved in the generation of natural movement.
- C. *Trained using labelled data* – Training a ‘black-box’ to decode movement intention from neural activity requires a supervised machine-learning algorithm. That is to say, the training data-set needs to be ‘labelled’ with certain kinematic parameters, or task events, in order to extract the informative features from the neural data. This labelling is usually possible in experimental models, but in paralyzed patients, who may not be able to perform a task, this labelling can be extremely difficult.
- D. *Unique* (to a specific subset of recorded neurons and experimental scenario) – This, combined with the ‘black-box’ nature of most decoders, and their indifference to the underlying physiology of the cortex, means that a decoder model generated for one scenario is unlikely to generalise well to other scenarios.

So far, we have shown that *lf*-LFPs can be used to estimate firing rates, and that NHP subjects are able to control and condition these estimates in a biofeedback BMI. Many of the limitations caused by items ‘A’ and ‘B’ in the above list, can thus be addressed. By using *lf*-LFPs, we can propose a system in which a patient’s BMI decoder would need to be trained and calibrated only once (soon after implantation), rather than being recalibrated every day. Then, following a period in which the subject learns the biofeedback paradigm, control of the interface should be both intuitive and robust to neuron loss. However, estimation of firing rates using *lf*-LFPs is still dependent on the successful recording of spikes. It would be ideal to do-away with this step altogether: to remove the need for costly high-frequency recording, processing, and spike-sorting.

Secondly, it would be ideal to address item ‘C’, by doing-away with using event-based labelling of training data. Firing rate estimation from *lf*-LFPs removes the necessity for kinematic labelling of data, but of course still requires labelled spike data, which come with the issues already discussed. Ideally, one could identify distinctive, physiologically-principled features from low-frequency activity in the cortex, which were consistently related to movement. Although these features might not be intuitive for the subject to control at first, they could be learned through biofeedback, assuming they provided salient feedback of movement-related neural activity and had good signal-to-noise ratio. Given that these low-frequency features are likely generated by much larger volumes of cortex than spikes, there is also perhaps a greater likelihood that decoders based on such features would be stable over time, but also, have characteristics that would generalise between behavioural scenarios.

In summary, an ‘ideal’ BMI would be based on robust and salient signals, that are easy to record and process (e.g. *lf*-LFPs) and ‘training’ the BMI decoder would be unsupervised (it would not require prior alignment to spike times or task events). As a fortunate by-product, such a device could also deal with three of the other bottlenecks of clinical device development: complexity, power consumption and size. Without the need to record or process spikes, the device could be based on much more simple electronics, and therefore have much lower power consumption and therefore longer battery life than current experimental devices.

### **5.1.2 *Multichannel lf-LFPs exhibit phase differences between channels***

In **Chapter 3**, we described the SRSP: essentially the spike-aligned *lf*-LFP. The SRSP has an underlying oscillatory structure, even if only for around one cycle (e.g. **Figure 3-2b**, page 39).

However, when looking across multiple LFP electrodes, it is clear that the phase of these oscillations varies across channels. Indeed, these phase-differences across channels are visible in the multichannel SRSP (e.g. **Figure 3-7a**, page 46). And without this phase difference, neither the identification of ‘sources’ within the *lf*-LFPs, nor the estimation of firing rates would be possible.

However, this multichannel oscillatory structure is not a phenomenon that is *only* seen when LFPs are aligned to spikes. Indeed, if we look at the firing rate patterns during a period of the torque-tracking task (e.g. **Figure 3-9a**, page 50), we see that oscillatory patterns in the 1–3 Hz range appear to be a feature of motor cortical recordings. That is to say, the presence of oscillatory structure in the SRSP is not an ‘artefact’ of aligning LFPs to thousands of spikes, but rather, appears to reflect more a more general and ongoing property of the motor cortex during movement.

We hypothesized that these oscillatory properties, visible in realtime recordings from subjects performing wrist-movement tasks, could be exploited in realtime, to develop a novel form of signal for BMI control.

### ***5.1.3 Wrist movements are correlated with realtime low-frequency cyclical activity in the lf-LFP***

A candidate for a useable signal—based on these low-frequency oscillations—was suggested by a separate, but simultaneous, series of experiments performed by me, Felipe de Carvalho and Andrew Jackson. The findings of these experiments are not presented as part of the results and conclusions of this thesis, because they were analysed and interpreted separately, primarily by Andrew Jackson. They are already available in published form (Hall, De Carvalho & Jackson 2014). Because this publication describes an essential step in our understanding of the *lf*-LFP, its relevant figures and findings are presented here, as part of the introduction to this Chapter.

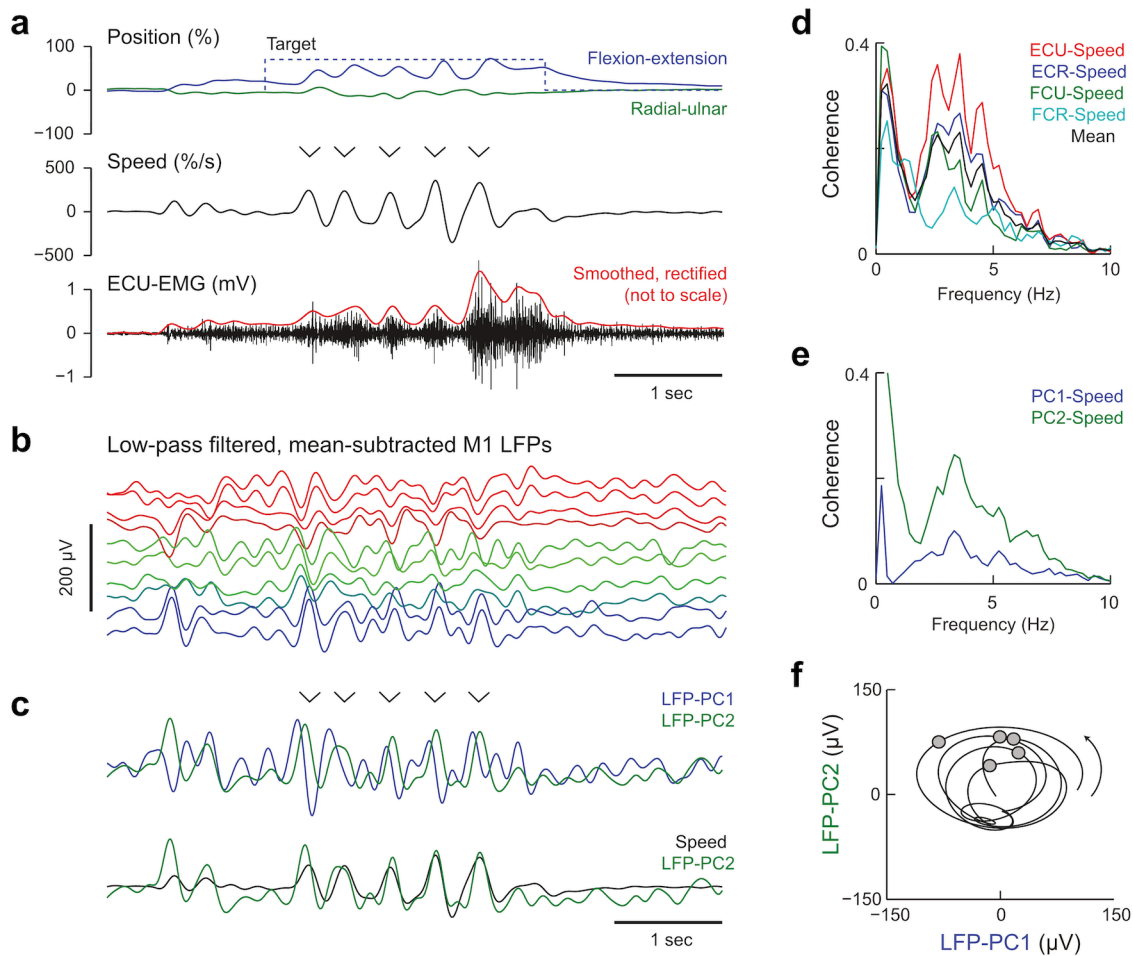


**Figure 5-1** Low-frequency LFP dynamics during isometric movements

- (a) *Top*: Position of cursor and target during one trial of the torque task. *Middle*: Radial cursor speed (arrows indicate submovements). *Bottom*: EMG from a wrist extensor muscle.
- (b) Low-pass filtered (< 5 Hz), mean-subtracted M1 LFPs. LFP traces are ordered and color-coded according to their phase relative to submovements.
- (c) Principal component decomposition of the M1 *lf*-LFPs.
- (d) Coherence between wrist muscles and cursor speed, with peak around 3 Hz.
- (e) Coherence between LFP-PCs and cursor speed.
- (f) LFP-PC trajectory for 2 s of the trial. Circles indicate times of submovements.

— Figure adapted from Hall, De Carvalho and Jackson (2014) *Neuron* **83**, Figures 1 & 2 (Cell Press).  
 Figures originally produced by A. Jackson.

In a centre-out task, we found that goal-directed isometric movements, rather than consisting of single, smooth trajectories, actually consisted of a series of submovements, occurring at a periodicity of  $\sim 2\text{--}3$  per second. These were most clearly revealed when the radial speed of the cursor—the derivative of the distance from the origin (**Figure 5-1a, top**)—was plotted against time (**Figure 5-1a, middle**). As would be expected, the EMG activity (e.g. **Figure 5-1a,**

*bottom*) of multiple wrist muscles was also highly coherent with these wrist submovements (**Figure 5-1d**).

More importantly, we saw clear periods of low-frequency (< 5 Hz) oscillatory activity in the *lf*-LFP that occurred during periods of movement (**Figure 5-1b**). These oscillations were closely synchronised to wrist submovements (coherent with cursor speed). However, very importantly, the phase of these *lf*-LFP oscillations varied across cortical electrodes.

The consistency of these oscillations, their phase relationships, and their correlation with submovement activity, were visualised by collapsing the multichannel *lf*-LFP space down into two components (PC1 and PC2) using principal component analysis. This revealed, even more clearly, that each cycle of the low-frequency cortical oscillation was associated with a submovement of the wrist, and that there was a consistent phase relationship across electrodes during these movement-associated oscillations – as illustrated by the consistent phase-relationship of the principal components, with PC1 always leading PC2; **Figure 5-1c**). Correspondingly, LFP-PCs were highly coherent with the speed of the cursor (**Figure 5-1e**).

Finally, the peak speed of the submovement consistently occurred at the same phase of each oscillatory cycle. This was most easily visualised in a state-space projection of PC1 vs. PC2 (e.g. **Figure 5-1f**), where it can be seen that these oscillations traced cyclical (circular or elliptical) paths, with both a consistent phase relationship (consistent direction of state-space rotation; anticlockwise) and consistent phase when peak cursor speed occurred ( $\pi/2$  radians, or ‘12 o-clock’, in this example).

#### **5.1.4 *The importance of local lf-LFP sources and phase differences across electrodes***

Firstly, it is important to note that these findings are consistent with the findings of the previous chapters of this thesis. In fact, they suggest (although do not prove) that multichannel SRSPs show phase differences between electrodes *because* the underlying LFPs contain these phase differences (and they are not averaged out by spike-triggering because firing rates also have modulation at these frequencies). This re-enforces our case that the motor-cortical *lf*-LFP is generated by local cortical sources (thus multiple electrodes can capture different phases), and that these local *lf*-LFP sources are intimately related to (if not causal to) the generation of submovements.

LFPs in these low frequency ranges are most commonly associated with NREM (non-rapid eye movement, also known as ‘slow-wave’) sleep. In this type of deep sleep, large parts of the brain, including large areas of the cortex, exhibit synchronised low-frequency oscillations (Amzica and Steriade 1997). The function and origin of these oscillations is not known, but is assumed to be related to homeostatic and regenerative processes in the brain during sleep (Tononi & Cirelli 2014), or perhaps memory consolidation (Diekelmann et al 2012).

Given this context, it is therefore very surprising and novel, firstly, to demonstrate evidence of local sources of *lf*-LFP activity in the motor cortex, which produce a specific *lack* of phase-synchronisation across electrodes within a single cortical functional area; and secondly, to demonstrate functional *lf*-LFP activity that is clearly related to task-directed behaviour (rather than sleep, rest or inattention).

We saw these movement-related low-frequency oscillations in all subject animals that we studied. Given their consistency, their movement-relation, their low-frequency nature and their apparently local (although as-yet mechanistically undefined) physiological origin in the motor cortex, we endeavoured to extract a movement-related signal from these multichannel oscillations which could be used for BMI control.

### ***5.1.5 Dynamical systems methods can be used to characterise these cyclical features***

The basis of our method for extracting a control signal was the projection of the multichannel LFP data into a two-dimensional state-space. Doing this, it became clear that faster submovements (those in which greater screen distance was covered by the cursor in unit time) were associated with ‘bigger’ rotations in the state-space projection.

To quantify the ‘size’ of rotation, we used the parameter *areal velocity*, which is the unit of area swept out by the state-space ‘particle’,  $\rho$ , about the origin, in unit time (expressed in S.I. units  $V^2/s$ ).

This parameter is dependent on both the rotational ‘speed’ (angular velocity) of the rotation (which corresponds to frequency of the oscillation) and the ‘size’ (radius) of the rotation (which corresponds to amplitude of oscillation). Specifically,

$$\mathbf{a}_\rho(t) = \frac{1}{2} \omega(t) |\mathbf{x}_\rho(t)|^2, \quad (5.2)$$

$$= \pi f(t) |\mathbf{x}_\rho(t)|^2, \quad (5.3)$$

Where  $\mathbf{a}_\rho(t)$  is the areal velocity,  $\omega(t)$  is the scalar angular velocity,  $\mathbf{x}_\rho(t)$  is the 2-D vector position (radius) of the particle,  $\rho$ , as a function of time,  $|\mathbf{x}_\rho(t)|$  is the magnitude of that vector (length of the radius), and  $f(t)$  is the frequency of the oscillation.

As a note of interest to the reader: The concept of areal velocity is commonly used when analysing the orbit of planets around **stars** (and constancy of areal velocity around an elliptical orbit is known as Kepler's second law).

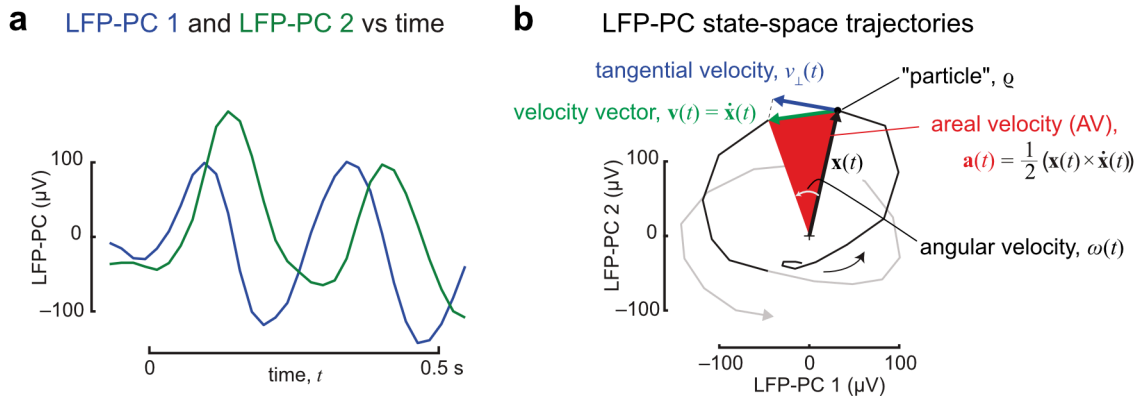


**Figure 5-2** Areal velocity signals from low-dimensional LFP projections.

- (a) Example of top two *lf*-LFP principal components (LFP-PCs) as time-series waveforms.
- (b) The same data, plotted as a 2-D state-space plot, showing the trajectory of the imagined “particle”,  $\rho$ , which is located at position/radius  $\mathbf{x}(t)$  from the origin at time,  $t$ . All other variables can be calculated from this position, and the change in position,  $\dot{\mathbf{x}}(t)$ , to the next position (i.e. the velocity,  $\mathbf{v}(t)$ , of the particle at time,  $t$ ).  $\theta$  is the change in angle, from which can be calculated the angular velocity  $\omega(t)$ . The tangential velocity  $v_\perp(t)$  is the projection of the velocity vector,  $\dot{\mathbf{x}}(t)$  onto the basis vector that is perpendicular to the radius,  $\mathbf{x}(t)$ .

Areal velocity is a convenient parameter because of its ease of calculation. It can be calculated directly as the area of the region (*red triangle*, **Figure 5-2**) bounded by the 2-D position vector at a given time-sample,  $\mathbf{x}_\rho(t)$ , and the 2-D velocity vector at that sample,  $\mathbf{v}_\rho(t)$ , where

$$\mathbf{v}_\rho(t) = \dot{\mathbf{x}}_\rho(t), \quad (5.4)$$

$$= \mathbf{x}_\rho(t + 1) - \mathbf{x}_\rho(t) \quad (5.5)$$

In other words, the velocity function can simply be calculated as the derivative,  $\dot{\mathbf{x}}_\rho(t)$ , of the position function. The areal velocity function (*red triangle*) can then simply be calculated geometrically as the cross-product between the position and velocity vectors at a given time. That is to say,

$$\mathbf{a}_\rho(t) = \frac{\mathbf{x}_\rho(t) \times \dot{\mathbf{x}}_\rho(t)}{2}, \quad (5.6)$$

where  $\times$  denotes the vector cross-product.

Strictly speaking, the cross-product is defined only in three-dimensional space, and its result is a vector which points in the direction orthogonal to both input vectors. In the case of our state-space data, the input vectors only have two dimensions (PC1 and PC2); thus the third input dimension is zero, and the areal velocity output vector points perpendicular to the plane of rotation (either ‘out of’ [positive] or ‘into’ [negative] the plane). Therefore, when we refer to the areal velocity,  $\mathbf{a}_\rho(t)$ , we are actually referring to the (signed) *scalar magnitude* of the areal velocity, but this is implicit.

### **5.1.6 *The properties of these oscillations suggest that they reflect intrinsic dynamics of the motor cortex.***

As mentioned above, we found that faster wrist submovements were associated with ‘bigger’ rotations in state space. To now state this more precisely: we found that the areal velocity of the *lf*-LFP state space rotation in motor cortex was proportional to the speed of submovement at the wrist (**Figure 5-3a,b,d,e**).

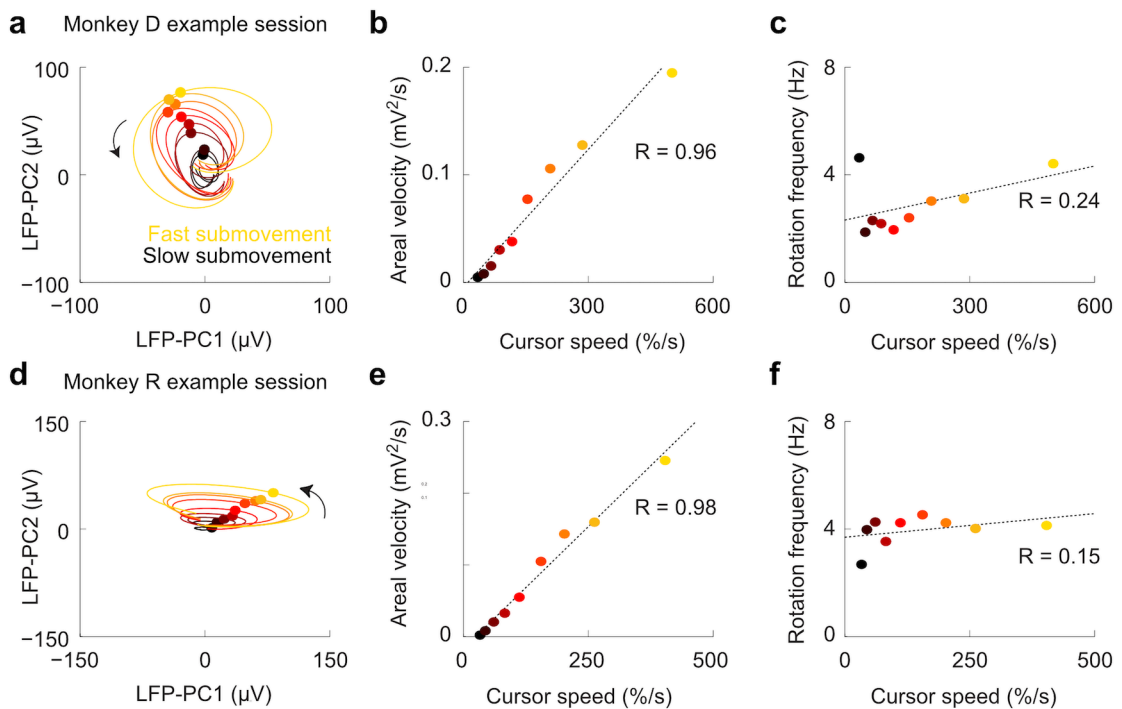


**Figure 5-3** Properties of low-frequency rotations with submovements of varying speed.

- (a) Average state space rotations (PC1 vs. PC2) of the *lf*-LFP space of Monkey D with submovements of varying speed. Submovements are classified into 9 categories according to cursor speed. (Colours as per panel b.)
- (b) Average areal velocity vs. average cursor speed for nine categories of submovement speed. Fitted line shows least-squares regression line and corresponding Pearson's  $R$  value.
- (c) Same as b, but for average rotational frequency (proportional to angular velocity).
- (d-f) Same as a-c, but for an example session from Monkey R.

— Figure adapted from Hall, De Carvalho and Jackson (2014) *Neuron* **83**, Figure 2 (Cell Press)  
Figure produced originally by A. Jackson.

Importantly, the angular velocity of *lf*-LFP state space rotations was relatively constant across this wide range of cursor speeds (**Figure 5-3c,f**), indicating that the frequency of oscillations remained relatively constant. Therefore, the increase in areal velocity associated with faster submovements was primarily mediated by an increase in the radius of rotation (amplitude of oscillation), rather than a change in angular velocity (frequency of oscillation).

These findings suggest that the generation of these oscillatory features may be intrinsic to the physiology of the motor cortex. In other words, the hypothesis would be that there are some intrinsic constraints on the dynamics of the motor cortical networks, which impose a low-frequency rhythmicity on the cortical LFP, and on the periodicity of submovements.

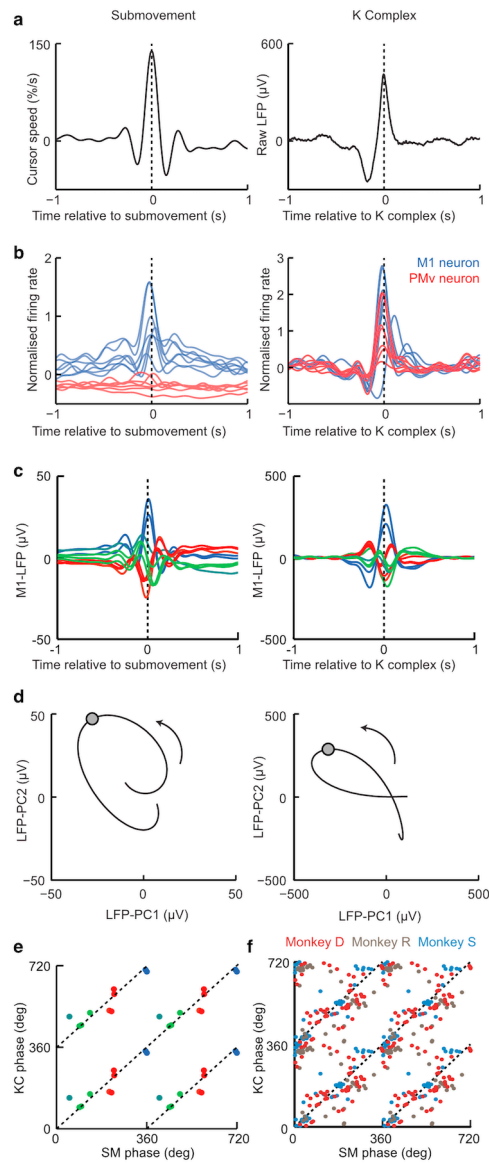


**Figure 5-4** *LFP dynamics during sleep: Submovement- and K complex-related activity share a common low-frequency phase structure.*

- (a) *Left*: average cursor speed aligned to a peak speed of 2,063 submovements. *Right*: average surface-referenced unfiltered LFP aligned to the peak of 197 K complexes. Data are from monkey D.
- (b) Average normalized firing rate of seven neurons in M1 (*blue*) and six neurons in PMv (*red*) relative to submovement (*left*) and K complex (*right*).
- (c) Average mean-subtracted *lf*-LFP from ten M1 electrodes relative to submovement (*left*) and K complex (*right*). Traces in both plots are colour-coded according to phase relative to submovements.
- (d) Average submovement-triggered (*left*) and K complex-triggered (*right*) *lf*-LFP-PC trajectories, plotted over 200 ms on either side of the trigger event (indicated by circles). All data are projected onto the PC axes determined from LFPs recorded during isometric task performance.
- (e) LFP phase relative to submovement (SM) phase plotted against LFP phase relative to K complex (KC) phase for each M1 electrode (unwrapped over two full cycles). Dashed lines indicate equality. Points are colour-coded according to LFP phase relative to submovements.
- (f) SM phase plotted against KC phase for all LFP recordings over 13 sessions in three monkeys.

— Figure reproduced from Hall, De Carvalho and Jackson (2014) *Neuron* **83**, Figure 4 (Cell Press).  
 Figure produced originally by A. Jackson.

In support of this hypothesis, we also performed a series of experiments on the same subjects, with the same electrode arrays, whilst the animals were at rest in the training chair, after the task was finished. These data showed that the dynamical properties of the cortical *lf*-LFPs (frequency, and phase difference between channels) were constrained in a very similar way during sleep (aligned to the K complex) as during task performance (**Figure 5-4**).

This provides strong evidence that these *lf*-LFP oscillations are not so-called ‘movement artefacts’—electrical artefacts correlated with movement, but caused by the physical movement of the body, head or recording equipment—since the animals were still during these periods, and yet the dynamics remained the same. Instead, these cyclical *lf*-LFP features appear to reflect a true physiological mechanism in the motor cortex. However, the identity and causality of this mechanism, or mechanisms, is not known, and will be discussed further in the Discussion section of this chapter.

## 5.2 Aims

Based on these previous findings, we wanted to see if the phenomenon of low-frequency cyclical oscillations in the motor cortex could be exploited for control of a BMI. Specifically, this Chapter has four main aims:

**Aim 1:** Develop approaches for building a decoder that can best extract an AV signal, using unlabelled training data.

**Aim 2:** Compare these approaches against one-another, and see how they compare to using more conventional signals, such as the power in a particular frequency band.

**Aim 3:** Test the performance of such an approach in a BMI task.

**Aim 4:** Use these data to test the hypothesis that these low-frequency dynamics are generated intrinsically to the cortex, as part of the movement-generation machinery, rather than being an artefact, or caused by some covariate.

## 5.3 Methods and Results

### 5.3.1 *Extracting dynamical features from multichannel lf-LFP —Motivation*

Having demonstrated the presence of cyclical dynamics, associated with movement, in the multichannel *lf*-LFP signal, and having identified the areal velocity (AV) as a meaningful parameter to quantify this signal, we were motivated to explore approaches for decoding this signal from the multichannel *lf*-LFP. We ideally wanted to do this using a fully-unsupervised approach: just using the available ‘signatures’ of movement, present in the *lf*-LFP, without needing to label specific task events.

As already described, the signatures of movement that we were looking for in the *lf*-LFP, occurred as cyclical activity within the  $Q$ -dimensional ( $Q$ -D) *lf*-LFP space. However, to enable us to extract an AV signal, we needed to collapse this space down, by projecting the data on to a 2-D plane. The problem could therefore be reframed as one of dimensionality reduction, where the aim was to find those planes in the data which contained the most salient AV signals.

The simplest approach to this problem is to use the first two principal component (PC) axes, to define the plane (PC1;PC2). However, whilst PCA aims to find those axes within the data that account for the highest *variance*, the plane (PC1;PC2), which accounts for the highest variance, does not necessarily contain cyclical dynamics. For example, if there is a large amount of zero-lag correlated signal (or noise) between LFP channels, the higher PCs are likely to reflect this correlation, whereas cyclical dynamics are dependent on phase-differences (non-zero-lag correlation) between channels.

We therefore used/developed two methods to extract AV signals from the higher-dimensional *lf*-LFP space. In both cases, we attempted to extract two (signed) scalar AV values from the data for further testing.

## 5.3.2 ‘jPCA’ approach

### 5.3.2.1 Introduction and principles

Our first approach was to use so-called ‘jPCA’, which is a variant of PCA developed by M Churchland and J P Cunningham in the lab of Krishnan Shenoy (Stanford, CA). (The ‘j’ in jPCA is arbitrary, but is thought to refer to one of the authors’ names.)

This group observed that low-frequency cyclical dynamics (oscillations) are a common, if not ubiquitous, feature of locomotion-generation networks in animals. In their case, they were recording the firing rates of multiple neurons. Importantly, in more complex movements, such as the hand movements of primates, they still found these ‘quasi-oscillations’, but they were hidden (or ‘latent’), within the high-dimensional neural space. That is to say, when they studied the time-series of multi-cell firing rate recordings, they needed to re-project the population data into the appropriate plane, then the low-frequency oscillatory structure become obvious, in the form of circling or elliptical paths in a 2-D state space (Churchland, Cunningham et al. 2012).

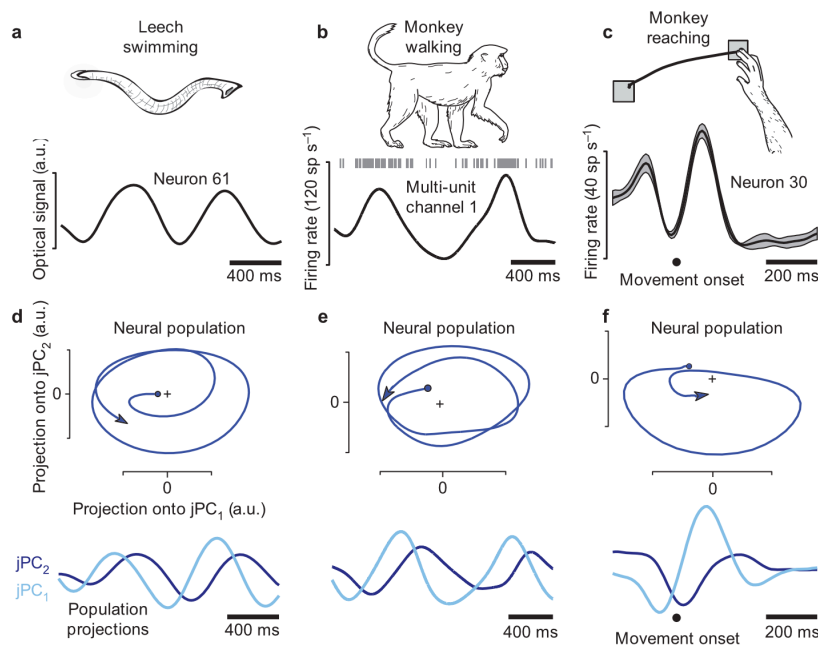


**Figure 5-5** Oscillation of neural firing rates during three movement types.

Three types of movement, in the leech, the locomoting monkey, and the reaching monkey (a–d), all reveal low-frequency oscillations in neural firing rates, and circular dynamics in 2-d projections of the neural population space (e–f). The 2-d projections shown here were generated using jPCA, which is one of the algorithms I go on to use in this thesis.

— Figure reproduced from Churchland, Cunningham et al. (2012), *Nature* **487** (Nature Publishing Group)

The jPCA algorithm begins with a standard dimensionality-reduction, into (in their case) six axes, using conventional PCA. The algorithm then finds projections of this 6-D space that capture rotational structure in the data. The approach to doing this is based on linear dynamical systems theory.

A time-invariant linear dynamical system is one in which the time-derivative (velocity) of the state-vector is a constant function of the state vector itself (radius). That is:

$$\dot{\mathbf{x}}(t) = \mathbf{f}(\mathbf{x}(t)) , \quad (5.7)$$

where  $\mathbf{f}$  is a linear function.

This can be more concisely displayed in matrix notation, by representing the data as matrix  $\mathbf{X}$ , where  $\mathbf{X} \in \mathbb{R}^{L \times n}$ ,  $L$  is the duration of the data (number of samples), and  $n = 6$ , the dimensionality of the data. Thus,

$$\dot{\mathbf{X}} = \mathbf{M}\mathbf{X} \quad (5.8)$$

Where  $\mathbf{M}$  is a square matrix of dimensions  $n \times n$ , that transforms  $\mathbf{X}$  to give  $\dot{\mathbf{X}}$ .

Equation 5.8 is a general equation describing any linear dynamical system. Therefore, matrix  $\mathbf{M}$  is a mixture of two components: a ‘symmetric’ component and a ‘skew-symmetric’ component. That is,

$$\mathbf{M} = \mathbf{M}_{symm} + \mathbf{M}_{skew} , \quad (5.9)$$

where the symmetric (‘even’) component,  $\mathbf{M}_{symm}$ , has purely real eigenvalues (and thus describes expansion/contraction), and the skew-symmetric (‘odd’) component,  $\mathbf{M}_{skew}$ , has purely imaginary eigenvalues (and thus describes rotation).

jPCA looks for rotation in the data by using gradient descent optimisation to solve for  $\hat{\mathbf{M}}$  (the hat modifier denoting an estimated variable), the least-squares solution to the problem of fitting a linear dynamical system to  $\mathbf{X}$ . However, solutions to  $\hat{\mathbf{M}}$  are constrained to be skew-symmetric, and therefore are the solutions which best describe rotations in the data.

Similar to traditional PCA, eigenvalue decomposition of matrix  $\hat{\mathbf{M}}$  allows the calculation of a ranked set of orthonormal vectors, which can be used to re-project the original data,  $\mathbf{X}$ , into

new axes. In the case of jPCA, the plane with the most rotational tendency, is that identified by the eigenvectors associated with the largest two (complex-conjugate) imaginary eigenvalues in  $\hat{\mathbf{M}}$ . Within a given jPCA plane, e.g. defined by (jPC1;jPC2), the direction of rotation is arbitrary, but is set by the algorithm to be anticlockwise (by convention).

Henceforth, this process of finding the reprojection matrix for jPCA, based on a training dataset, will be referred to as training a ‘jPCA decoder’. It is important to note, that the anticlockwise convention is set at the time of training the jPCA decoder. This means that, when using a decoder on test data, any activity in which jPC1 precedes jPC2 will produce anticlockwise rotation. However, clockwise rotation *is possible*, if the test data contains periods where activity in jPC2 precedes jPC1. Anticlockwise rotation is not a constraint of jPCA *per se*, merely a convention. Following the same convention, anticlockwise rotation in the plane (jPC1;jPC2) will produce positive values of areal velocity (vector  $\mathbf{a}(t)$  pointing out of the plane), whereas clockwise rotation in that plane will produce negative values of areal velocity (vector  $\mathbf{a}(t)$  pointing into the plane).

### 5.3.2.2 Implementation of the jPCA-based approach

To implement jPCA on our *lf*-LFP data, we used the MATLAB code package available online from Churchland and colleagues (at [http://churchlandlab.neuroscience.columbia.edu/code/jPCA\\_ForDistribution.zip](http://churchlandlab.neuroscience.columbia.edu/code/jPCA_ForDistribution.zip)), and adapted it for our specific use-case.

In the prototypical experiment, we were using 24 *lf*-LFP signals ( $Q = 24$ ). Prior to performing jPCA, we performed mean-subtraction; meaning that we subtracted the mean (across  $Q$  LFPs) *lf*-LFP signal from each of the individual *lf*-LFP signals (at each time-point). This is equivalent to re-referencing the data to a theoretical ‘average’ local reference.

For each experiment, we required up to two areal velocity (AV) signals—each AV signal requiring a 2-D plane—and we therefore needed four jPC axes (jPC1–4). For dimensionality reduction, we therefore used the first 12 principal components from the original *lf*-LFP space (usually 24 dimensions/electrodes), to generate six jPC planes, from which we used the top two: (jPC1;jPC2) and (jPC3;jPC4).

This jPCA decoder algorithm produced the orthonormal vector set to calculate these planes, which we referred to as the projection matrix,  $\mathbf{J}$ . This projection matrix was saved, and used to reproject test data into the two jPC planes. An areal velocity signal could then be calculated

from each plane by calculating the cross-product between the 2-D signal in that plane, and its own cross-product, as per Equation 5.6, to produce two AV values (known as  $AV_1$  and  $AV_2$ )

### 5.3.3 ‘Areal velocity component’ (AVC)-based approach

#### 5.3.3.1 Limitations of the jPCA approach

Whilst jPCA is theoretically a good way to find AV signals in the  $lf$ -LFP space, it has a number of mathematical constraints, with potentially undesirable outcomes.

Firstly, when going from  $Q$ -D to 2-D, jPCA may collapse informative patterns in the data into a single plane. This is best illustrated with a schematic figure:

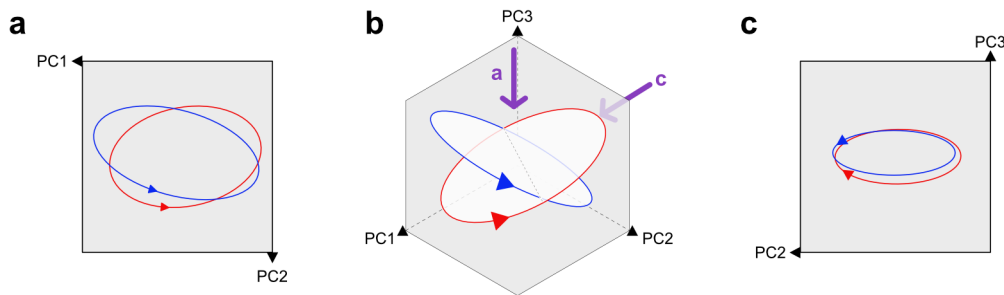


**Figure 5-6** Illustration showing the potential problems of using jPCA to find the best planes in multi-dimensional neural data

The figure shows a schematic of a hypothetical dataset in panel (b), displayed in three dimensions (PC1;PC2;PC3). This represents a single cloud of data, but, for illustrative purposes, we actually have *a priori* knowledge that there are two sources producing latent rotational patterns within those data. In (a) and (c) are shown projections of that same data onto the planes (PC1;PC2) and (PC2;PC3), respectively. Very similar anti-clockwise rotation is seen in (a), but the projection in (c) shows that a variation in the axis of rotation in (b) can produce rotations of the opposite direction (hence AV values of opposite polarity).

In **Figure 5-6b**, we display a theoretical single cloud of data, where we know *a priori* that there are two underlying sources producing latent rotational patterns (*red* and *blue*) within those data. The dominant pattern of activity is rotation in plane (PC1;PC2) (view in **Figure 5-6a**). jPCA would allocate very similar axes to the first jPC plane, (jPC1;jPC2). Essentially, the vast majority of the rotation would be collapsed into the first jPC plane.

Unfortunately, both rotations look very similar in this plane, and this is therefore not very informative for separating the activity of the two underlying sources. A highly informative plane is actually (PC2;PC3) (the view in **Figure 5-6c**), because in that plane, the two sources

rotate in the opposite direction, and would therefore produce AVs with opposite polarity. However, because of the constraints of jPCA, the second jPC plane, (jPC3;jPC4) is unlikely to reveal this counter-rotational activity: firstly, because there is no consistent direction of rotation; and secondly, because the first  $n$  jPCs form an orthonormal basis which spans the same space as the first  $n$  PCs, and the second jPC plane, (jPC3;jPC4), is already constrained by the choice of the first plane, (jPC1;jPC2), and is therefore very unlikely to capture the information seen in (PC2;PC3).

In fact, a valid criticism of jPCA is that, essentially, sources are best separated into planes according to their frequency. This is because the imaginary eigenvalues of  $\mathbf{M}_{\text{skew}}$  are fundamentally related to the frequency of rotation of the dynamical system that  $\mathbf{M}$  describes. As a result, if two sources in the  $lf$ -LFP data have the same frequency, then they are very likely to be collapsed into a single jPC plane, rather than being separated.

Results of the work from our lab already mentioned (Hall, De Carvalho, Jackson 2014) also supported our concerns that these constraints of jPCA may lead to dimensionality reduction on the multichannel  $lf$ -LFP in such a way that we would lose salient information.

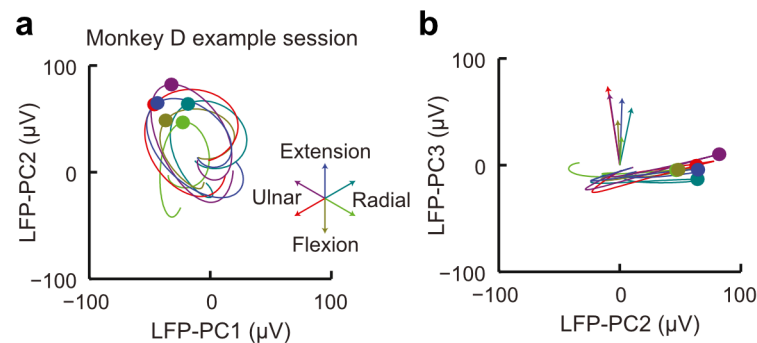


**Figure 5-7** Relationship between LFP-PCs and movement direction in three dimensions.

- (a) Average 2D LFP-PC trajectories for submovements, binned and color-coded according to the direction of cursor movement. Arrows in the inset indicate the centre-out direction of movement for each bin.
- (b) Average LFP-PC trajectories in the plane of PC2 and PC3. The trajectories revolve around slightly different angular velocity vectors, indicated by arrows.

— Figure adapted from Hall, De Carvalho and Jackson (2014) *Neuron*, Figure 2 (Cell Press).  
Figure produced originally by A. Jackson.

When Monkey D performed the isometric wrist force task, we observed that all directions of movement produced similar state-space rotations, with similar frequencies, when viewed in the first PC plane (PC1;PC2) (**Figure 5-7a**). However, when viewed in the plane (PC2;PC3)

it was clear that the axis of rotation of the activity was different for each of the different directions of movement (**Figure 5-7b**). This suggested that there may be more information about movement kinematics available from the high-dimensional *lf*-LFP space, than simply the speed of movement. Using jPCA would likely impose dimensionality reduction that would collapse all of these rotations into a single plane, and capture little of the difference between them. We therefore decided to develop a method to try and capture a richer sample of the AV signals contained within the *lf*-LFP data.

### 5.3.3.2 *Areal velocity component (AVC) principles*

We developed an alternative approach to extracting areal velocity from high-dimensional *lf*-LFP data, which did not require the definition or detection of specific 2-D planes within the data. Instead, we widened the search for salient AV signals by looking across all possible ‘areal velocity components’ within the data.

The concept of an areal velocity component (AVC) is not intuitive and requires some explanation. As inferred already in **Section 5.1.5**, the areal velocity can be thought of in geometric terms as the cross-product between two vectors in three-dimensional coordinates.

For example, the two vectors,  $\mathbf{u}$  and  $\mathbf{v}$ , can each be defined as the sum of three orthogonal components parallel to the three standard basis vectors ( $\mathbf{i}$ ,  $\mathbf{j}$  and  $\mathbf{k}$ ).

$$\begin{aligned}\mathbf{u} &= u_1\mathbf{i} + u_2\mathbf{j} + u_3\mathbf{k} \\ \mathbf{v} &= v_1\mathbf{i} + v_2\mathbf{j} + v_3\mathbf{k}\end{aligned}\tag{5.10}$$

Where  $u$  and  $v$  indicate scalar components (coefficients), by which the basis vectors are multiplied.

The cross-product,  $\mathbf{s}$ , of  $\mathbf{u}$  and  $\mathbf{v}$  can then be shown to be equal to,

$$\mathbf{s} = \mathbf{u} \times \mathbf{v} = (u_2v_3 - u_3v_2)\mathbf{i} + (u_3v_1 - u_1v_3)\mathbf{j} + (u_1v_2 - u_2v_1)\mathbf{k}\tag{5.11}$$

where  $\times$  indicates the cross-product.

This means that the resulting vector,  $\mathbf{s} = s_1\mathbf{i} + s_2\mathbf{j} + s_3\mathbf{k}$ , actually has three scalar components:

$$\begin{aligned}
s_1 &= u_2 v_3 - u_3 v_2 \\
s_2 &= u_3 v_1 - u_1 v_3 \\
s_3 &= u_1 v_2 - u_2 v_1
\end{aligned}
\tag{5.12}$$

Translating this to the situation in hand: areal velocity,  $\mathbf{a}$ , is equal to the cross-product of the position vector,  $\mathbf{x}$ , and the associated velocity vector,  $\dot{\mathbf{x}}$ . (Strictly it is equal to half of this cross product, but the factor of  $\frac{1}{2}$  is ignored to simplify the current explanation.) We can see that the areal velocity (in three dimensions) can be defined by three scalar components:

$$\begin{aligned}
a_1 &= x_2 \dot{x}_3 - x_3 \dot{x}_2 \\
a_2 &= x_3 \dot{x}_1 - x_1 \dot{x}_3 \\
a_3 &= x_1 \dot{x}_2 - x_2 \dot{x}_1
\end{aligned}
\tag{5.13}$$

One can refer to each of these scalar components as an ‘areal velocity component’. Strictly speaking, the cross-product is *only* defined for three dimensions. However, for the purposes of this methodology, we extended the concept of the areal velocity component (AVC) to higher dimensions. In a space higher than three dimensions, we defined the AVC as the relationship between any given pair of signals, and the derivative of those same two signals, such that,

$$a'_n = x_i \dot{x}_j - x_j \dot{x}_i \tag{5.14}$$

where  $a'_n$  is the areal velocity component (AVC), and  $i$  and  $j$  are indices of signals from 1 to  $N$ , where  $N$  is the dimensionality of the signal space, and  $i < j$ .

One can see from Equation 5.14, that for every pair of signals in the data, we can calculate an AVC. Hence, when calculating AVCs, we actually expand the dimensionality of the data; going from a  $N$ -dimensional input space (**Figure 5-8a**), to a  $\frac{1}{2}N(N-1)$  dimensional AVC space (**Figure 5-8c**). This gives us a much richer representation of all the possible areal velocity features within the data than we get by using orthogonal axes (like with PCA or jPCA). Once we have this rich AVC feature set, we can then generate two AV signals for future use by performing dimensionality reduction (**Figure 5-8d**) *on the AVC space* (rather than on the original data), in order to find the dominant features.

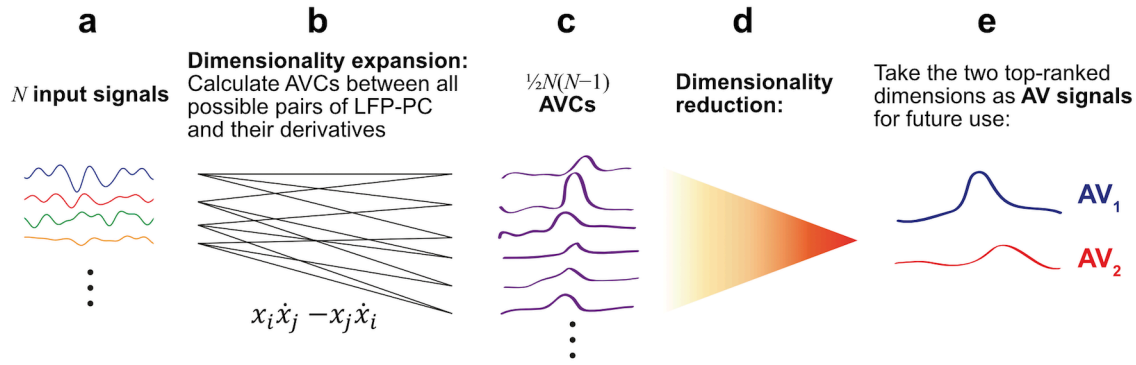


**Figure 5-8** Illustration of the steps involved in the ‘AVC’-based method of dimensionality reduction and AV signal calculation.

- (a) Selection of input signals (in our implementation, these were the PCs of *lf*-LFPs)
- (b) Calculation of areal velocity components using the equation given, for  $i = 1 \dots N$ , for  $j = 1 \dots N$ , but where  $i < j$ .
- (c) This dimensionality expansion produces  $\frac{1}{2}N(N - 1)$  AVCs.
- (d) Dimensionality reduction, e.g. through PCA.
- (e) The top two ranked signals from the dimensionality reduction can be used as AV signals (1 and 2) in later experiments.

Although this AVC-based approach has the advantage of using a richer and less-restrictive feature set than with PCA or jPCA, it does have the distinct disadvantage that AVCs (and thus the two final AV signals generated) are not representative of actual planes within the data, and therefore they cannot so easily be used to make inferences about the underlying physiology that is generating the signals. The importance of this will become clear in a later section.

### 5.3.3.3 Implementation of the AVC-based approach

In the prototypical experiment, we were using 24 *lf*-LFP signals ( $Q = 24$ ). Like with jPCA, our first step was to perform mean-subtraction of the *lf*-LFPs; meaning that we subtracted the mean (across  $Q$  LFPs) *lf*-LFP signal from each of the individual *lf*-LFP signals (at each time-point). Like with jPCA, we next performed PCA on the  $Q$ -dimensional *lf*-LFP space,  $\mathbf{y}(t)$ , to produce the  $Q$ -dimensional LFP-PC space. Like with jPCA, we took the 12 top-ranked PCs, here called  $\mathbf{z}(t)$ , as the input data for our AVC algorithm.

We calculated AVCs from the PCs, as per Equation 5.14 (with principle components,  $\mathbf{z}(t)$ , and their derivatives,  $\dot{\mathbf{z}}_n(t)$ , used as input signals, and  $N = 12$ ) to produce the 66-dimensional AVC space. It is important to note that, like a principal component, each AVC is still a function of time in the recording, so each AVC is a time series,  $a'_n(t)$ . In other words, we expanded the

12-dimensional  $\mathbf{z}(t)$  vector to produce the 66-dimensional  $\mathbf{a}'(t)$  vector. AVCs were then each normalised to unity variance.

For each experiment, we required up to two areal velocity (AV) signals. To recover these from the high-dimensional AVC space, we carried out dimensionality reduction using exploratory factor analysis (EFA; using function `factoran.m` from the Statistics and Machine Learning Toolbox in MATLAB). We used EFA rather than PCA, for largely notional reasons: that EFA is theoretically better suited to exploratory analysis for underlying/latent variables. However, we also tested PCA, and the results were so similar that the difference between EFA and PCA can largely be ignored here.

The first two ‘factor scores’ (predictions of common factors from EFA) were used as the two areal velocity signals ( $AV_1$  and  $AV_2$ ) for later experiments.

We used the loadings from factor analysis to calculate the 12-by-2 matrix,  $\mathbf{K}$ , which contained the values necessary to calculate  $AV_1$  and  $AV_2$  directly from principle components,  $\mathbf{z}_n(t)$ , and their derivatives,  $\dot{\mathbf{z}}_n(t)$ . This was saved for use in future experiments.

#### ***5.3.4 Comparing the performance of AV-based approaches to conventional methods.***

Using either of our two AV-based methods—jPCA-based or AVC-based—we were able to extract two scalar waveform signals ( $AV_1$  and  $AV_2$ ) from the  $Q$ -dimensional  $lf$ -LFP data. We hypothesised that these signals would provide a reliable method of feature-extraction of movement-related signals from motor cortical LFPs, and that these may be useful signals for a future BMI. We therefore wanted to quantify this performance in comparison to other, conventional and established methods of feature extraction from LFPs.

Because they were derived based on underlying knowledge of cortical physiology (the presence of low-frequency cortical LFP dynamics) we believed that our AV-based methods would perform better than other, conventional methods of feature extraction from LFPs. To test this, we developed an experiment to compare these different feature-extraction techniques.

To make the comparison as simple as possible, we decided to use binary classification as our test of performance. Therefore, we recorded neural signals from both cortical hemispheres of

a monkey, and recorded movements in both forelimbs. We then tested how well each of our signal extraction methods, based only on the cortical recordings, could correctly classify trials into left-handed or right-handed movements.

To the reader, this may seem like a trivial task. Left-handed movement would usually be associated with robust activity in the right M1 (and right-hand with left M1), due to the pyramidal decussation of the corticospinal tracts. However, these experiments were performed in an animal (Monkey S) whose right hemisphere electrodes had been implanted for over 15 months (475 days). Therefore, the amplitude and signal-to-noise ratio (SNR) of the LFP signals was not as large as in data presented in previous chapters.

We chose to perform this experiment in this subject, because it gave us an opportunity to test the performance of AV-based signals in chronically-implanted arrays, where conventional methods typically perform badly, due to the poor quality of recording. Whilst not a perfect analogy, this can be thought of as similar to an array chronically implanted in a patient, where the quality of signals is too poor to use for BMI control. The choice of such a *simple* bimanual task was partly a pragmatic one: that training a monkey to perform a bimanual task was extremely challenging; her having previously only performed unimanual tasks.

We hypothesised that our AV-based methods may still allow us to extract useful information, and categorise the movement correctly, even after conventional methods failed.

### 5.3.4.1 Experimental setup: task and recording

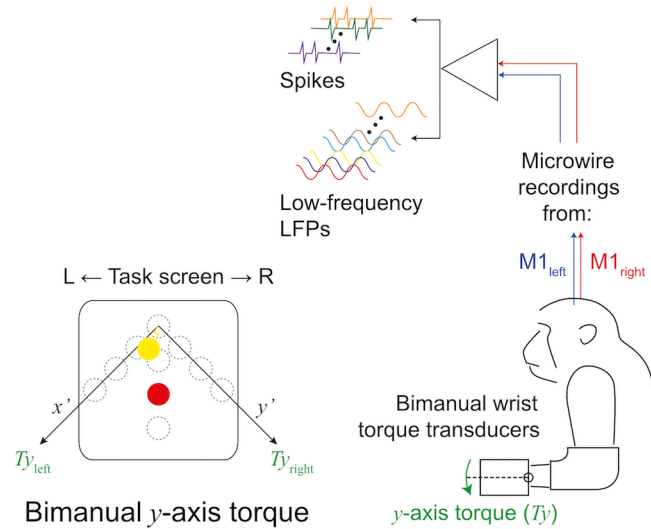


**Figure 5-9** *Bimanual wrist-torque task*

2-D cursor position was controlled by wrist torque from both wrists. The origin (home target) was at the top in the centre of the screen. Left wrist,  $y$ -axis torque (rotating and/or pushing downward) produced movement on the screen axis  $x'$  (down-and-left). Right wrist,  $y$ -axis torque produced movement on the screen axis  $y'$  (down-and-right).

#### **Task: bimanual wrist-torque task**

The task had broadly the same apparatus and setup as the unimanual, 2-D torque task introduced in **Section 2.1.2**, and the monkey's aim was the same: to move from a home target, to acquire peripheral targets. However, monkeys controlled a task in which 2-D cursor position was controlled by torque from both wrists. Subjects therefore had both of their hands in torque manipulanda. We recorded the  $y$ -axis torque ( $T_y$ ), which represents a moment acting downwards (into the manipulandum) with a pivot at the wrist.

The two axes of cursor movement on the screen were not parallel to the screen borders, but rather were rotated by 45-degrees. These rotated axes were referred to as  $(x', y')$ , as per **Figure 5-9**, and were controlled by the  $y$ -axis torque from the left wrist ( $T_{y_{left}}$ ) and right wrist ( $T_{y_{right}}$ ), respectively. The home target (relaxation) was at the centre-top of the screen, and monkeys had to acquire targets in nine different positions, at three different distances (see **Figure 5-9**), presented in pseudo-random order. To acquire the central three peripheral

targets, monkeys had to combine force from both wrists. However, for the purposes of the analysis presented here, data from the trials of the centre (bimanual) targets were ignored.

### **Electrophysiological recording**

Electrophysiological activity was recorded in the same way as documented in **Section 2.4.1**, from 12 tungsten microwire electrodes implanted in each primary motor cortex in Monkey S, using the TDT system. For this experiment, signals were low-pass filtered at 200 Hz and down-sampled and stored at 488 Hz.

In each hemisphere, there were two damaged electrodes (evident from extremely noisy signals) with unusable signals, and these channels were therefore rejected from further analysis, leaving us with a total of 20 LFP waveforms, 10 per hemisphere.

#### **5.3.4.2 Methods for extracting signals from multichannel lf-LFP**

##### **Conventional methods**

The key question we wanted to answer was whether using an AV-based approach would outperform a conventional and simple method of decoding LFP activity: using the power in a particular LFP band.

We therefore bandpass filtered the LFP signals offline using 5<sup>th</sup>-order Butterworth filters (sequential high-pass then low-pass), into three frequency categories:

- i) The *lf*-LFP (< 5 Hz), as previously (no offline high-pass);
- ii) beta band (16–30 Hz);
- iii) low-gamma band (30–60 Hz)
- iv) high-gamma band (60–200 Hz).

We quantified power using the root mean square (RMS) method. That is, using the square root of the arithmetic mean of the squares of the values in the waveform under study. To do this, continuous bandpass-filtered LFP signals were squared. The mean and square-root were then performed later on windowed chunks of data, as later described in **Section 5.3.4.4** ('ROC quantification of neural-derived signals', page 125).

## AV-based methods

We compared this conventional signal-extraction method (band power) to our AV-based methods. We implemented the jPCA-based method as per **Section 5.3.2.2** and the AVC-based method as per **Section 5.3.3.3**. However, we analysed hemispheres separately, and only extracted a single AV signal from each hemisphere (e.g. AV<sub>1</sub> from right M1; AV<sub>2</sub> from left M1). Furthermore, there were two damaged electrodes in each hemisphere, we were able to use a maximum of ten LFPs ( $Q = 10$ ) as input signals. To decide on the size of the principal component subspace used for subsequent jPCA/AVC analysis, we calculated the rank of the mean-subtracted *lf*-LFP matrix (using the built-in function `rank.m` in MATLAB), which provided an estimate of the number of linearly-independent signals.

### 5.3.4.3 Results: Extracting areal velocity-based signals from data from the bimanual wrist-torque task

Analysing periods of the bimanual torque task offline, we found that our AV-based methods successfully found periods of activity demonstrating cyclical dynamics, as evidenced by clear peaks in the AV signal, typically associated with the peak movement (torque) velocity in the contralateral wrist. For example, right hand movement (**Figure 5-10b**, *red*) was associated with robust *lf*-LFP activity in the contralateral M1 (**Figure 5-10c**, *red*). A jPCA-based feature extraction on these data was able to find a plane which successfully captured cyclical dynamics at this time (essentially due to the phase structure present in the *lf*-LFP data), and calculation of the areal velocity from this jPC plane produced a robust AV signal (**Figure 5-10c**, “AV<sub>2</sub>”, *red*).

Moreover, in the contralateral side (*blue* in all panels), the M1 LFP signals were highly attenuated, due to the age of the implant (likely because of insulation damage, as well as gliosis around the recording tip). Even so, a jPCA-based approach was still able to extract a robust AV signal. This was because there was still cyclical dynamical activity present in the multichannel *lf*-LFP (i.e. phase structure was preserved), even though the amplitude of the signals was very small.

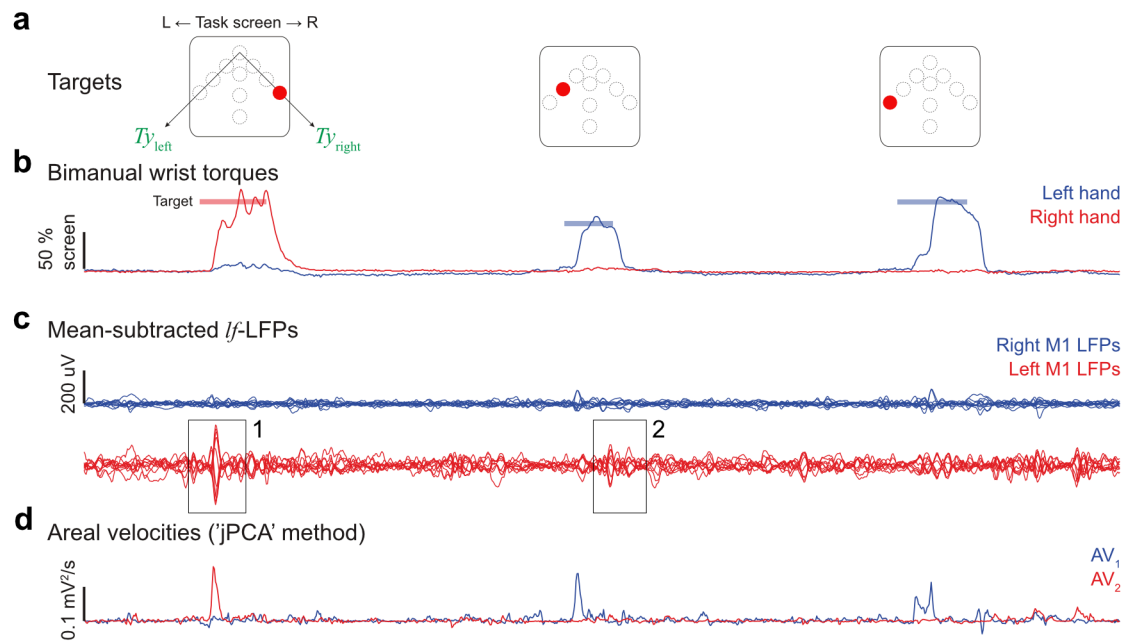


**Figure 5-10** Example section of data from the bimanual wrist-torque task

- (a) Illustration of the three targets acquired during this period of the task
- (b) Traces of  $y$ -axis wrist torque from both wrists. Bars above show period during which target was on-screen. Torque is expressed in terms of the biofeedback signal given to the subject: percentage of the screen traversed by the cursor.
- (c) Mean-subtracted  $lf$ -LFP signals from M1 in both hemispheres. At this time, the array in the right hemisphere had been implanted for 475 days (15½ months), and the array in the left hemisphere for 174 days (5½ months). Hence why the signals from the right M1 appear so attenuated. (Boxes [1] and [2], please refer to main text).
- (d) Areal velocity signals (calculated using the jPCA-based method on all 10 signals in each hemisphere), demonstrating the size of signals that could be extracted from each hemisphere, their high correlation with periods of movement, and their relative insensitivity to LFP activity un-related to movement (such as that associated with taking the reward, and chewing, between trials).

Finally, and perhaps most importantly, the AV signals were clearly highly selectively associated with periods of limb movement (e.g. **Figure 5-10c, Box 1**) on, whereas other periods of moderate amplitude  $lf$ -LFP signal (perhaps associated with chewing, or other body movement, e.g. **Figure 5-10c, Box 2**) did not have the appropriate phase structure to generate an AV signal. We believed that this feature of AV-based feature extraction, in particular, would allow us to extract signals from LFPs better than conventional power-based methods; particularly when LFP recording quality has deteriorated.

### 5.3.4.4 Quantifying classification performance of signals: Receiver-operating characteristic (ROC) analysis

To quantify the performance of a particular signal in the task of binary classification, we used the *receiver-operating characteristic* (ROC) curve. This is a method which illustrates the performance of a binary classifier as the discrimination threshold is varied, by plotting the false-positive rate (FPR) against the true-positive rate (TPR).

#### Worked example using torque signals

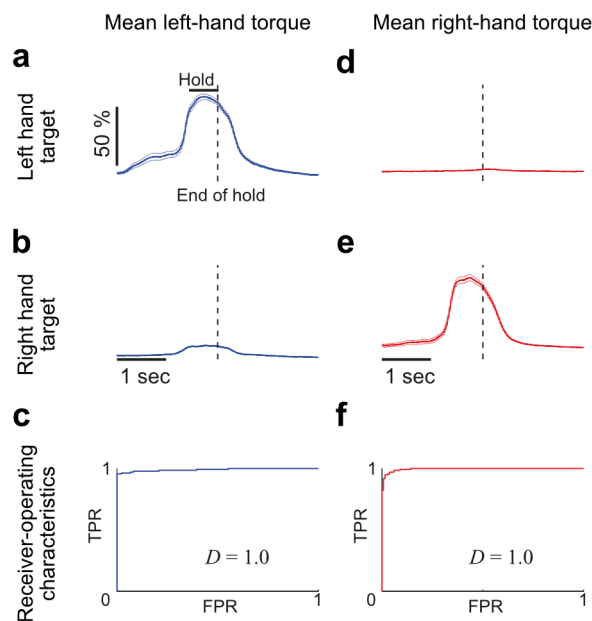


**Figure 5-11** Illustration of receiver-operating characteristics (ROC) analysis using wrist torque

- (a) Actual **left-hand** torque ( $T_{y_{\text{left}}}$ ) generated to acquire **left-side** targets. Trace represents a mean, aligned to end of the successful hold period, of all trials with a left-side target (i.e. all three of the pure  $x'$  axis targets)  $\pm$  s.e.m ( $n = 134$  trials). Torque is expressed in terms of screen cursor position (maximum 100%).
  - (b) Actual **left-hand** torque ( $T_{y_{\text{left}}}$ ) generated to acquire **right-side** targets ( $n = 134$  trials).
  - (c) Receiver-operating characteristic (ROC) curve for the performance of **left-hand torque** for classifying left- vs. right-sided targets. For this, a single metric for each signal/trial was used, of mean torque during the hold period.
  - (d) **Right-hand** torque ( $T_{y_{\text{right}}}$ ) for **left-side** targets.
  - (e) **Right-hand** torque ( $T_{y_{\text{right}}}$ ) for **right-side** targets.
  - (f) ROC curve for **right-hand torque**, classifying left- vs. right-sided targets.
- $D$  is the ROC discrimination index;  $D = 2(AUC - 0.5)$ , where AUC is area under the curve.

As a simple but useful worked example of the method, **Figure 5-11a–c** shows the binary classifier performance of the *torque from the left wrist* (from the same example session shown

in **Figure 5-10**) in classifying whether the original target was left-sided or right sided. In theory, this signal should have perfect performance, because the amplitude of left-wrist torque for left-sided targets should always be bigger than for right-sided targets, (because the left wrist only *needs* to move for left-sided targets). However, we can see from **Figure 5-11b** that the subject does sometimes move the left wrist a small amount for the right target, and this is tolerated because of the diameter of cursor/target, and overlap required by the task.

ROC analysis essentially says: for a given amplitude of response (amplitude of left-hand torque, measured as the mean during the hold period), what is the likelihood of a true positive classification (correctly classifying as a left-side target) and what is the likelihood of a false positive allocation (incorrectly classifying as a right-side target)? To express this slightly differently: if we set a threshold value of left-hand torque amplitude, and take all trials where left-hand torque amplitude was above that threshold, and call these ‘classified as left’, what proportion of those trials were *actually* left-side trials (this is the TPR), and what proportion were *actually* right-side trials (this is the FPR). Therefore, although **Figure 5-11a,b,d,e** show mean torque traces, ROC actually tests classification on a trial-by-trial basis.

**Figure 5-11c** shows the ROC curve for left-hand torque amplitude. A perfect classifier would immediately have a point at the top left of the axes, because even with the lowest amplitude threshold, all left-hand movements above this threshold would be for left-hand targets (FPR = 0; TPR = 1). However, we can see that even the torque is not a perfect classifier. There are some trials where left-hand movement is associated with right-side targets. But once the amplitude threshold is high enough, all left-hand torques above that amplitude are associated with left-side targets.

The shape of the ROC curve is difficult to summarise in a single metric, but can be satisfactorily achieved using the ‘discrimination index’,  $D$ , where,

$$D = 2(AUC - 0.5) \quad (5.15)$$

and AUC is area under the ROC curve. A perfect discrimination index is  $D = 1$ , and chance discrimination is  $D = 0$ . In our example, left-hand torque has a virtually perfect discrimination index of  $D = 1.0$ . The same pattern of results can be seen with torque from the right wrist, in (**Figure 5-11d–f**).

## ROC quantification of neural-derived signals

We used the same methods to quantify the performance of our various neural-derived signals. Data were trial-aligned to the end of the successful hold period, as above.

To give a single metric of ‘signal strength’ for each of the AV signals, for each trial, we used the mean\* amplitude of AV over an analysis window from  $-1.2$  s to  $-0.4$  s, relative to the end of the hold period. This early analysis window (relative to the hold period) was chosen because AV signal amplitude peaked during the period of highest speed of movement (as discussed previously), and subsided rapidly soon after the onset of the hold period.

To give a single metric of ‘signal strength’ for each of the power bands, for each trial, we used the mean RMS power across the 10 LFPs during over an analysis window from  $-0.8$  s to  $0$  s relative to the end of the hold period (which corresponded to when the power signal was largest). RMS power for each LFP was calculated by taking the mean, over the analysis window, of the squared-LFP signal, then taking the square root of this mean, to give a single RMS value for each LFP. The mean RMS power value was then taken across the 10 LFPs to give a single metric (per hemisphere) per trial.

It is worth noting, that the laterality labels are of course reversed for neural data, because generally, left-sided movement is associated with right-hemispheric motor cortical activity. In the following section, this logical reversal is already accounted for, and labelled appropriately in the figures.

---

\* Note: Mean across time, not across trials. Here we are calculating a metric to represent a particular trial for ROC analysis.

### 5.3.4.5 Results: Example ROC analysis for AV-based data from a single session

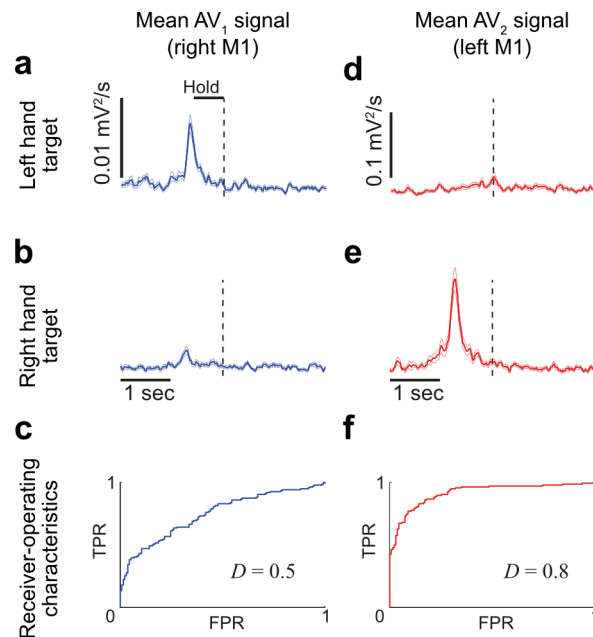


**Figure 5-12** Example ROC analysis of AV-based signals generated using the jPCA-based method

- (a) Actual **right M1** signal ( $AV_1$ ) generated when subject acquired **left-side** targets. Trace represents a mean of all trials with a left-side target  $\pm$  s.e.m. ( $n = 134$  trials).  $AV_1$  calculated from 10 right M1 *lf*-LFPs using jPCA-based method.
- (b) Actual **right M1** signal ( $AV_1$ ) generated to acquire **right-side** targets ( $n = 134$  trials).
- (c) Receiver-operating characteristic (ROC) curve for the performance of signal  $AV_1$  for classifying left vs. right-sided targets.
- (d–f) Same as a–c, but for  $AV_2$  signal.  $AV_2$  calculated from 10 left M1 *lf*-LFPs using jPCA-based method.

The jPCA-based analysis (as shown in the example above, **Figure 5-12**; same session as in **Figure 5-10**) produced signals which were relatively selective for unilateral movements although—it almost goes without saying—not as selective as the torque signals themselves (**Figure 5-11**). The discrimination indices ( $D$ ) were 0.5 and 0.8, for the right M1 and left M1 signals, respectively.

### 5.3.4.6 Comparison of areal velocity-based feature-extraction techniques to conventional, power-based techniques using ROC analysis

The AV signal represents a metric, derived *a priori* from the LFP data, which retrospectively can be seen to be informative about the movement of the subject. That is to say, the AV is derived in a totally unsupervised way from the LFP data, without a labelled ‘training set’. The

ROC is then a measure of the fully unsupervised decoding ability of the AV signal to categorise bimanual movements.

We wanted to compare the unsupervised decoding performance of AV-based methods to conventional LFP signals, and we chose to use the mean LFP power as a comparable *a priori* metric on which we could test unsupervised decoding performance. Of particular interest was whether AV-based methods would outperform power-based methods given a restricted number of LFP signals.

To test this, we took a number,  $Q$ , of LFPs from a hemisphere, and performed ROC analysis on the metrics of the six different signal types already mentioned (jPCA-based AV, AVC-based AV, delta band power, beta band power, low-gamma band power and high-gamma band power).

Specifically, we calculated the signal strength metric and performed ROC analysis, for 50 random draws of  $Q$  LFPs from the 10 LFPs in each hemisphere, for each of the six signal types. For power-based metrics, the number of LFPs,  $Q$ , ranged from 1 to 10 in each hemisphere. For the jPCA-based signal, an even number of LFP-PCs was required for each AV signal. We used the even number of LFP-PCs less than or equal to the rank of the LFP-PC matrix. Therefore, a minimum value of  $Q = 3$  LFPs was required for this analysis. For the AVC-based AV metric, we also used a minimum of  $Q = 3$  *lf-LFPs* (and then 3 LFP-PCs).

The result of ROC analysis, for each signal and for each  $Q$ , was summarised as the mean discrimination index,  $D$ , across the 50 random LFP permutations.

### 5.3.4.7 Results: Comparison of areal velocity-based feature-extraction techniques to conventional, power-based techniques using ROC analysis

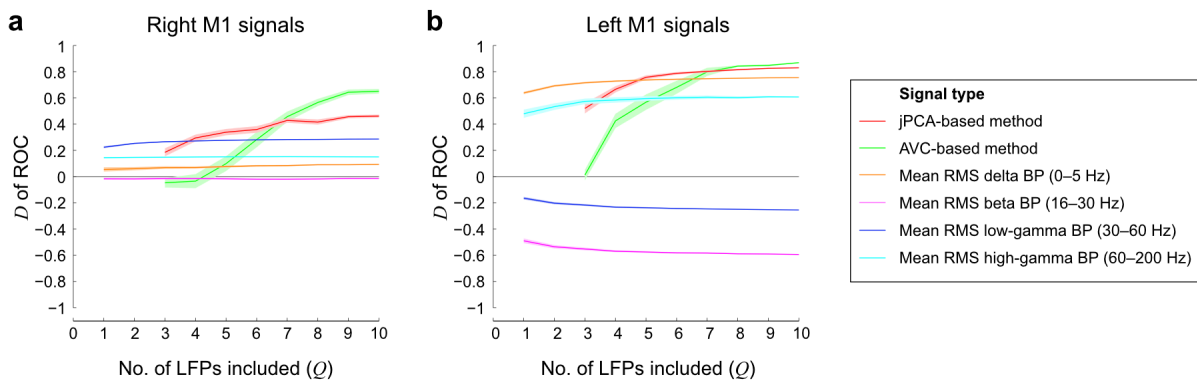


**Figure 5-13** ROC analysis comparing performance of different feature-extraction techniques, with increasing numbers of LFPs

- (a) Mean  $D$  (ROC discrimination index) values  $\pm$  s.e.m. (across 50 random draws) for each of the six signal types used, with increasing numbers of LFPs from the right M1. Negative  $D$  values indicate consistent (non-random) categorisation in the wrong direction. BP, band power.
- (b) Same as a, but for signals from the left M1.

When using signals being recorded from a relatively recently-implanted (5½ month-old) array (left M1), we found that mean RMS delta band and high-gamma band power were signal features that performed reasonably well at binary classification in our bimanual task (**Figure 5-13b**; delta band, *orange*, mean  $D$  (10 LFPs) = 0.75; high gamma-band, *cyan*, mean  $D$  (10 LFPs) = 0.61. In fact, these signal-types performed well, even when a single LFP was used. The beta-band also performed well at classification (**Figure 5-13b**; *purple*, mean  $D$  (10 LFPs) =  $-0.59$ , but classified signals in the opposite direction from the other power bands. This is not surprising, because it is known that the movement-phase of directed forelimb activity is associated with beta-band desynchronization, and reduced power (Baker et al. 2000). It is not clear why the low-gamma band also did this, but this may be due to overlap with the beta band at the lower limit of the range.

Importantly, both of the AV-based feature extraction methods (jPCA-based and AV-based) outperformed the conventional power-based methods, when 6 or more LFP signals were available. The AVC-based method out-performed all other methods, including the jPCA-based method (**Figure 5-13b**; AVC-method, *green*, mean  $D$  (10 LFPs) = 0.87; jPCA-method, *red*, mean  $D$  (10 LFPs) = 0.83).

A more interesting result was seen in the right hemisphere. The right M1 array had been implanted for over 15 months at the time of these recordings. As a result, the signal amplitudes, and more importantly, the signal-to-noise ratios were very low. Therefore, conventional, power-based feature extraction methods actually performed very poorly, even on this simple binary movement classification task (**Figure 5-13a**; all have  $D < 0.3$ ). However, AV-based methods both performed well, with AVC-based feature extraction performing surprisingly well given enough LFP inputs (**Figure 5-13a**; AVC-method, mean  $D$  (10 LFPs) = 0.65; jPCA-method, mean  $D$  (10 LFPs) = 0.46).

In summary, we found that AV-based metrics can outperform power-based metrics for the unsupervised decoding of bimanual movement, particularly when signal quality is poor. This suggests that the AV-based approach is able to extract a metric from unlabelled multichannel LFP which is not captured by the power of the LFPs. This is likely because AV-based methods allow principled identification of phase information and, specifically, progression of phase across channels, even if amplitude (and therefore power) is very small.

### ***5.3.5 Using areal velocity signals for biofeedback BMI control and exploring the underlying physiology of low-frequency cortical dynamics***

#### ***5.3.5.1 Introduction, hypothesis and predictions***

Our next aim was to investigate whether monkeys could use and modulate AV-based signals to control a biofeedback BMI task. More importantly, we wanted to see *how* they did this.

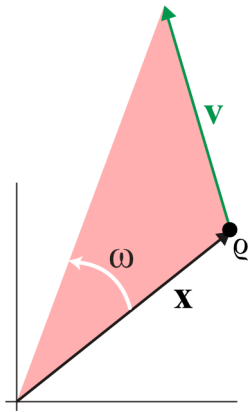


**Figure 5-14** Simple schematic of state space parameters

$q$ , particle moving in state space;  $\mathbf{x}$ , radius vector;  $\mathbf{v}$ , velocity vector;  $\omega$ , represents angular velocity; *red triangle*, represents areal velocity.

As already mentioned, there are two ways in which the areal velocity (size of the *red triangle*) can be modulated within a defined 2-D plane (**Figure 5-14**):

- i) By modulating the radius of the rotation,  $|\mathbf{x}|$ , where vertical bars indicate the modulus (length) of the vector; and
- ii) By modulating the angular velocity (angle subtended per unit time),  $\omega$ , of the rotation, which is inversely proportional to the frequency ( $f$ ) of the rotation/oscillation.

Based on our previous studies, and previous data presented in this thesis, we formed the hypothesis that the oscillations producing these cyclical patterns in the multichannel  $lf$ -LFP are intrinsically-generated. This allowed us to produce two predictions that we could test quantitatively.

### **Predictions:**

1. That the direction of rotation (which is dependent on the relative phase-shift between LFP channels) is constrained by internal dynamics, and that the subject therefore should not use negative AV signals to complete the task.
2. That the frequency of these oscillations is constrained by cortical dynamics, which are imposed by the internal physiology of the motor cortex, and that the subject will therefore find it easier (and tend to) modulate the radius of the oscillation, rather than the frequency/angular velocity.

A biofeedback BMI task uniquely allowed us to quantitatively test these predictions, because we could explicitly set the signal-to-effector relationship, and the observe how the signal was modulated in a highly controlled way. To be clear, the task would not constrain the method by which the subject ‘chose’ to perform the task; the subject was free to perform the task in whichever way they find easiest; but we could directly test the properties of the cortical dynamics under different conditions.

It was essential to use a jPCA-based method for extracting AV signals for this experiment. jPCA provides a true 2-D plane, from which the parameters shown in **Figure 5-14** could be calculated – allowing us to quantitatively test the above predictions. The AVC-based method would not provide this, since AVCs (areal velocity components) are not calculated from true projections of the data onto a 2-D plane.

### 5.3.5.2 General methods for AV-based biofeedback BMI experiments

#### Experimental setup

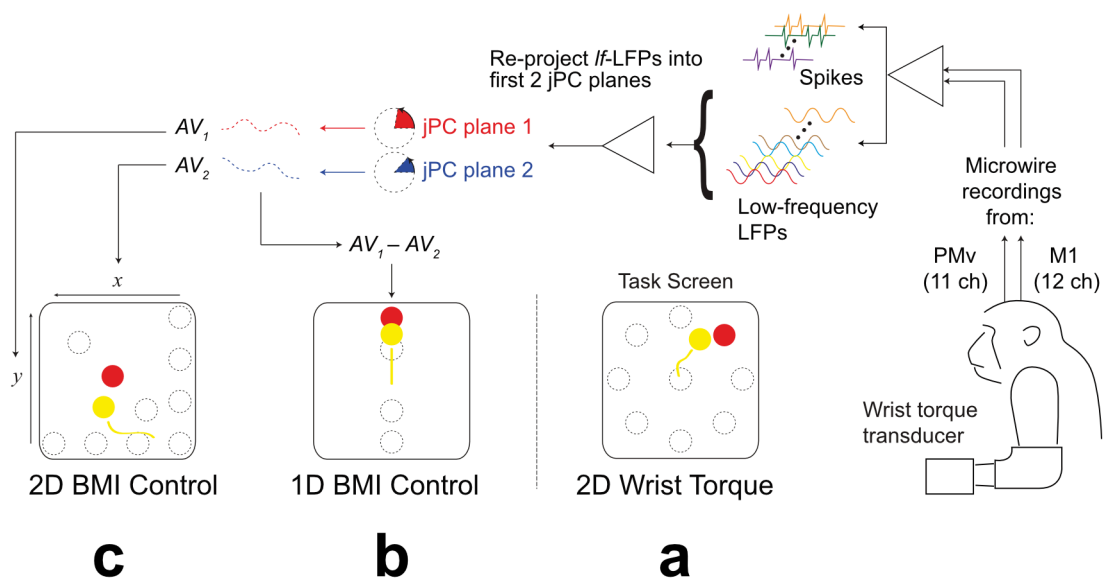


**Figure 5-15** Schematic of experimental setup for areal-velocity (AV)-controlled BMI task

- (a) Left wrist-torque controlled task
- (b) 1-D AV-controlled biofeedback BMI task (2:1 signal to task-axis mapping)
- (c) 2-D AV-controlled biofeedback BMI task (2:2 mapping)

These experiments were all performed in Monkey D. Each experiment began with 50 trials of the wrist torque-tracking task with the left wrist (**Figure 5-15a**), and we recorded from both PMv and M1, as previously described in **Chapter 2**.

### **jPCA-based decoder training**

After recording for 50 trials of the torque-tracking task, we used data from that recording to train a jPCA-based *lf*-LFP decoder. We followed the method described already in **Section 5.3.2.2**, except that one electrode in PMv was damaged (noisy signal), so the input to the decoder consisted of 23 *lf*-LFPs. We used 12 LFP-PCs, allowing 6 jPC planes. We only used the top two jPC planes, (jPC1;jPC2) and (jPC3;jPC4), from which we calculated signals AV<sub>1</sub> and AV<sub>2</sub>, respectively.

The reprojection matrices (**J**<sub>1</sub> and **J**<sub>2</sub>) were stored and transferred to the TDT-RZ2 system, which allowed us to reproject *lf*-LFPs into jPC planes, and calculate AV signals in near-realtime, as data came in from the recording system. The two resulting AV signals were normalised, using their relative standard deviations, so that the signals spanned a comparable range and could be mapped to screen dimensions in the BMI task. They were then smoothed online using an exponential decay filter with a decay constant  $\lambda = 0.25$  s. Cursor position was then controlled in near-realtime using these normalised, smoothed AV<sub>1</sub> and AV<sub>2</sub> signals, in two different biofeedback BMI tasks: a 1-D task and a 2-D task.

## 1-D BMI task

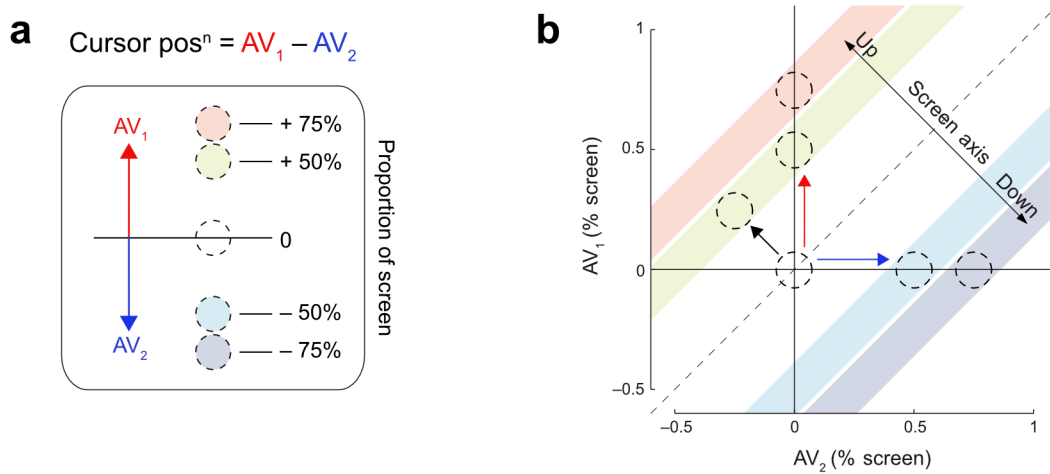


**Figure 5-16** 1-D BMI task and possible strategies to the redundant 2:1 mapping

- (a) Schematic illustrating the control mapping of the biofeedback cursor in the 1-D AV-control BMI task. We used a 2:1 mapping, where the cursor position was controlled by the difference between the two AV signals. Colours of the targets are just labels for descriptive purposes.
- (b) Schematic of the ‘solution space’. Coloured bars indicate the possible solutions to each of the targets, coloured using the same code as in a. Because there is a redundant 2:1 mapping, there are multiple redundant solutions to the task, and the subject is free to use any strategy. See text for more details, and descriptions of the arrows.

This experimental paradigm (**Figure 5-15b** and **Figure 5-16a**) was broadly the same as the two-cell BMI control described in Section 2.1.3.1. Targets appeared at four positions:  $-75\%$ ,  $-50\%$ ,  $50\%$  and  $75\%$ . Cursor position,  $c$ , was defined by  $c = (AV_1 - AV_2)/\sqrt{2}$ . We presented 75 trials per target, pseudorandomly interleaved, giving a total of 300 trials in this phase of the experiment.

Because of the redundant 2:1 mapping in this task arrangement, there are multiple redundant solutions to acquiring each target, and it is up to the subject to use the strategy which they find easiest. For example, in theory, the shortest distance from the origin to the green (up 50%) target in the 2-D AV ‘solution space’ (**Figure 5-16b**) is according to the *black* arrow shown. However, this requires that the subject’s motor cortex is able to generate a negative  $AV_2$  signal (clockwise, as opposed to anticlockwise, rotation in the jPC plane). However, we hypothesise (Prediction 1, **Section 5.3.5.1**) that the physiology of the cortex constrains AV signals to be positive. This generates the prediction that the strategy used would be that indicated by the *blue* and *red* arrows: only using positive  $AV_1$  and  $AV_2$  signals.

## 2-D BMI task

As well as differentially controlling AV signals, we also wanted to test whether the subject was able to combine the two signals, by using a 2-D control biofeedback task.

Normalised, smoothed, AV<sub>1</sub> and AV<sub>2</sub> signals controlled the 2-D coordinates (the horizontal and vertical position, respectively) of the screen cursor. 9 targets were placed at a radial screen distance of 30%, 60% and 90% away from an origin in the bottom-right of the screen (**Figure 5-15c**). Acquisition of the three targets on the diagonal required simultaneous generation of AV<sub>1</sub> and AV<sub>2</sub>. 39 trials per target were presented, pseudorandomly interleaved, giving a total of 351 trials in this phase of the experiment.

### 5.3.5.3 Results: One-dimensional (2:1 mapping) BMI biofeedback task using areal velocity signals

An *lf*-LFP decoder was trained on torque-tracking data using the jPCA-based method. jPCA planes and AVs were then calculated and used to provide feedback as the cursor position in near-realtime. Monkey D was able to control AV<sub>1</sub> and AV<sub>2</sub> independently, in order to acquire targets in this 1-D biofeedback BMI task (two example trials are shown in **Figure 5-17**).

It is clear even from this short segment of data (see **Figure 5-17a** and **b**), that jPC plane 1 (AV<sub>1</sub>) predominantly reflected a ~3–4 Hz oscillation/rotation present within the M1 *lf*-LFPs, whereas jPC plane 2 (AV<sub>2</sub>) predominantly reflected a slightly slower oscillation/rotation within the PMv *lf*-LFPs. This was confirmed when we looked at the weighting coefficients of *lf*-LFPs in the jPCA projection matrices for plane 1 and plane 2 (**Figure 5-18**).

It is important to note that this ‘separation’ of M1 and PMv LFPs between the jPC planes was not due to an imposed constraint, but rather, revealed itself as a finding from unconstrained jPCA across all 23 *lf*-LFPs. This suggests that, in this dataset at least, there may be cyclical dynamical structure within the PMv LFPs that operates at a different (lower) frequency than one within the M1 LFPs. jPCA allocates these rotations (‘M1’ rotation and ‘PMv’ rotation to the top two planes, because they represent the two dominant (but unique) cyclical features within the *lf*-LFP data.

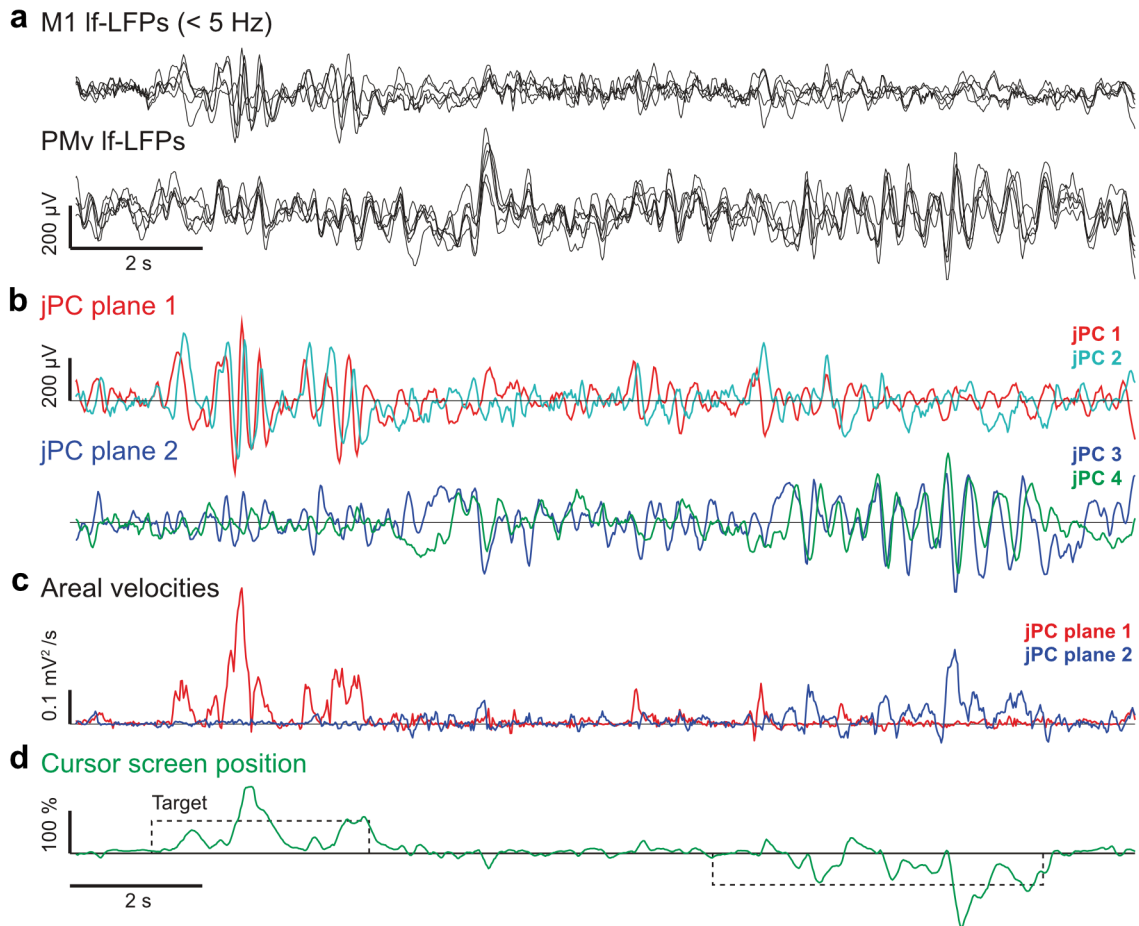


**Figure 5-17** Example data from 1-D (2:1 mapping) AV-control BMI biofeedback task

- (a) 12 lf-LFPs recorded from M1 (top) and 11 lf-LFPs from PMv (bottom).
- (b) Projections of those lf-LFPs into the first two jPC planes. jPC plane 1 (top) has axes (jPC1;jPC2) and jPC plane 2 (bottom) has axes (jPC3;jPC4).
- (c) Areal velocity signals, AV<sub>1</sub> (red) and AV<sub>2</sub> (blue), as calculated by the cross-product method from jPC plane 1 and 2, respectively.
- (d) Cursor screen position, as seen by the monkey. This is calculated in near-realtime as AV<sub>1</sub> – AV<sub>2</sub>. There is a very short processing delay, and a longer smoothing delay evident.

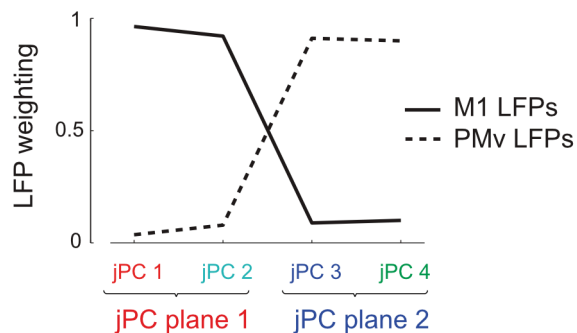


**Figure 5-18** Weighting coefficients for each jPC plane.

Mean weighting coefficients across M1 lf-LFPs and PMv lf-LFPs for each jPC axis.

### 5.3.5.4 Methods for exploring how the subject modulates areal velocity during the 1-D biofeedback BMI task

#### Secondary parameter calculation

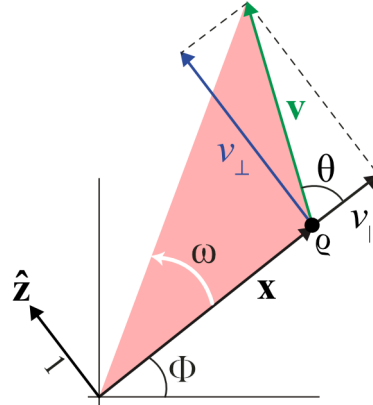


**Figure 5-19** Illustration of the various parameters related to the areal velocity

$q$ , particle moving in state space;  $\mathbf{x}$ , radius vector;  $\mathbf{v}$ , velocity vector;  $v_{\parallel}$ , radial velocity component (parallel to  $\mathbf{x}$ );  $v_{\perp}$ , tangential (cross-radial) velocity component (perpendicular to  $\mathbf{x}$ );  $\hat{\mathbf{z}}$ , unit vector perpendicular to  $\mathbf{x}$ ;  $\omega$ , represents angular velocity; *red triangle*, represents areal velocity.

In order to test Prediction 2 (Section 5.3.5.1; that the subject will tend to modulate the radius of the rotation to modulate areal velocity, rather than the angular velocity), we needed to compare the individual contribution of the radius,  $|\mathbf{x}|$ , and angular velocity,  $\omega$ , to the modulation of AV during the biofeedback task. To do this required the *post hoc* calculation of a number of secondary parameters (Figure 5-19) from the 1-D AV-control BMI data.

Firstly,  $v_{\perp}$ , the ‘tangential’ (or ‘cross-radial’) velocity, which is the component of the velocity vector  $\mathbf{v}$  perpendicular to  $\mathbf{x}$ .

$$v_{\perp} = |\mathbf{v}| \sin(\theta) \quad (5.16)$$

Angular velocity is related to tangential velocity by,

$$\omega = \frac{v_{\perp}}{|\mathbf{x}|} \quad (5.17)$$

We found that an instantaneous (sample-by-sample) estimate of  $\omega$  was extremely noisy, because during periods of the recording with low LFP activity, as  $|\mathbf{x}| \rightarrow 0$ , then  $\omega \rightarrow \infty$ ,

producing a very erratic signal. We therefore elected not to measure  $\omega$  on a trial-by-trial basis, but rather to measure  $v_{\perp}$  (which is not susceptible to this noise issue), and use the gradient relationship between  $v_{\perp}$  and  $|\mathbf{x}|$  to study the constancy of  $\omega$ .

We calculated  $v_{\perp}$  directly (without using  $\theta$ ) as a projection of  $\mathbf{v}$ ,

$$v_{\perp} = \mathbf{v} \cdot \hat{\mathbf{z}} \quad (5.18)$$

Where the dot operator indicates the vector dot-product, and  $\hat{\mathbf{z}}$  is the unit vector perpendicular to the vector  $\mathbf{x}$ . (As a projection onto a unit vector [a component],  $v_{\perp}$  is scalar.)

### **Graphical evaluation of changes in angular velocity over a range of AV values**

For each of the 300 trials, aligned to the end of the successful hold period (0 s), the mean (over time) values of AV,  $|\mathbf{x}|$  and  $v_{\perp}$  were calculated over an analysis window from  $-0.6$  to  $0$  s. These values were used as trial-by-trial metrics of AV,  $|\mathbf{x}|$  and  $v_{\perp}$  for the remainder of this analysis.

We plotted  $v_{\perp}$  (abscissa) against  $|\mathbf{x}|$  (ordinate) for each trial. The gradient of such a plot ( $\Delta v_{\perp} / \Delta |\mathbf{x}|$ ) is proportional to the angular velocity ( $\omega$ , radians/second) of the underlying rotation, and this is also proportional to the frequency (Hz), since  $f = \omega / 2\pi$ .

By having a biofeedback task, which explicitly requires the subject to modulate AV over a wide range (to acquire the different targets), we were able to observe the relationship between  $|\mathbf{x}|$  and  $\omega$ . Prediction 2 would predict that AV is only modulated by  $|\mathbf{x}|$ , in which case, there would be a constant  $\omega$  over a range of AV value. And there would therefore be a straight-line relationship (theoretically passing through zero) between  $v_{\perp}$  and  $|\mathbf{x}|$ .

**5.3.5.5 Results: Modulation of areal velocity, radius and angular velocity during the 1-D (2:1 mapping) AV-control biofeedback BMI task**

**Trial-averaged, event-aligned data**

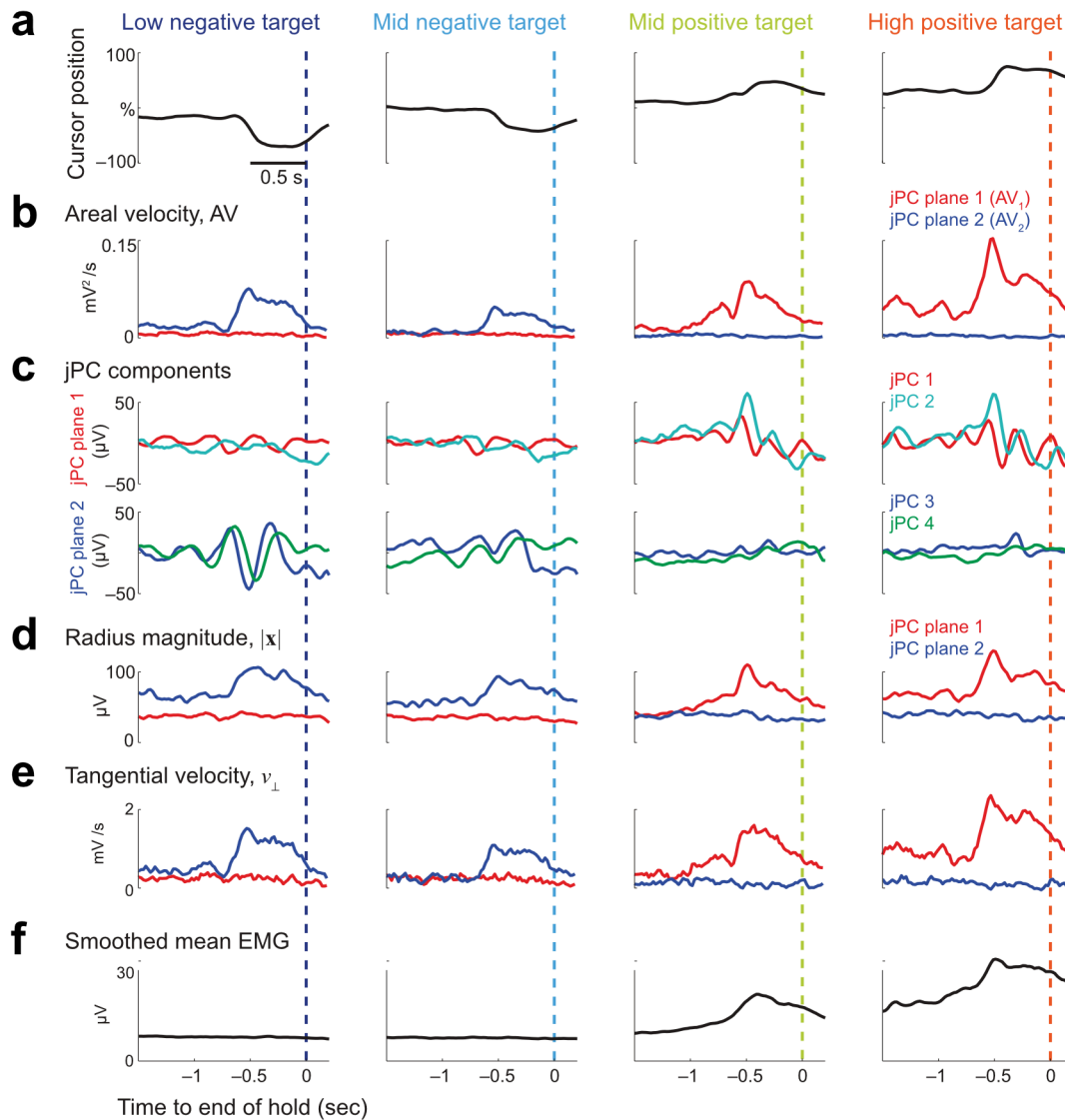


**Figure 5-20** Trial-averaged data from the 1-D (2:1 mapping) AV-control biofeedback BMI task, aligned to the end of the successful hold period

In each panel, each trace shows the mean over  $n = 75$  trials.

- (a) Trial-averaged cursor position.
- (b) Trial-averaged areal velocity (AV) signal for each jPC plane
- (c) *Top*: Trial-averaged  $lf$ -LFP signal projected onto the first two jPC axes (1 and 2), i.e. jPC plane 1  
*Bottom*: The same for jPC axes 3 and 4 (jPC plane 2)
- (d) Trial-averaged magnitude of the radius,  $|x|$  (distance from the origin in the jPC plane)
- (e) Trial-averaged tangential velocity,  $v_{\perp}$
- (f) Trial-averaged, smoothed, mean EMG signal from muscles in the left (controlling) arm

Trial-averaged data confirmed that the subject was able to control the two AV signals independently, with negative targets being acquired almost exclusively with signal in jPC plane 1, and positive targets with signal in plane 2 (**Figure 5-20b**). Although a ‘mean’ jPC signal itself is not very meaningful (because the AV signal is dependent on within-trial phase differences between the two jPCs, which may not be locked to the task), it was interesting to see the clear modulation, and surprisingly consistent phase relationships aligned to the task event (**Figure 5-20c**). As expected, both radius,  $|\mathbf{x}|$ , and tangential velocity,  $v_{\perp}$ , were modulated during the generation of AV signals (**Figure 5-20d–e**).

Finally, we noted that  $AV_1$  signal (essentially right M1 LFP activity) was associated with movement and EMG activity in the contralateral (recorded) limb (**Figure 5-20f**), whereas  $AV_2$  signal was largely associated with relaxation of the left limb (minimal EMG activity). This was compatible with the behaviour of the subject at the time. She would make clear movements of her left wrist to acquire the positive ( $AV_1$ ) targets, and actually make movements with her right limb, and postures with her body, to acquire the negative ( $AV_2$ ) targets. Unfortunately, we did not have implanted EMG or kinematic monitoring in the right limb to enable us to quantify this.

**Testing Prediction 1: ‘The subject will use only positive AV signals in their task strategy.’**

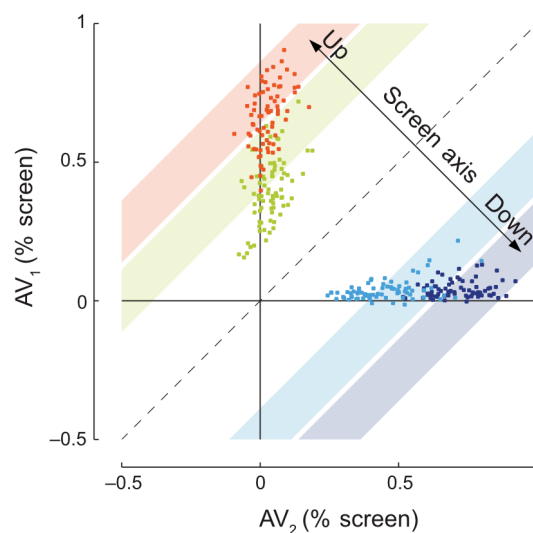


**Figure 5-21** ‘Solution space’ plot for the 1-D (2:1 mapping) biofeedback BMI task

The coordinates of each datum-point show the mean (over a 0.6 s analysis window) areal velocity signals ( $AV_1$  and  $AV_2$ ) generated to successfully complete a particular trial. Coloured bars show the possible solutions to the four target positions. Data-points are coloured according to target position on that trial (orange, +75%; green, +50%; cyan, -50%; purple, -75%).

We found that it was certainly possible for negative areal velocities (state-space counter-rotations) to be generated by the brain, particularly in the case of  $AV_2$  (e.g. see **Figure 5-17c** and **Figure 5-21**). However, on average, we found that the strategy overwhelmingly preferred by the subject was to use positive  $AV_1$  signals in trials to acquire upward targets (**Figure 5-21**; *green* and *orange* data-points) and to use positive  $AV_2$  signals in trials to acquire downward targets (**Figure 5-21**; to the right; *cyan* and *purple* data-points). It was very unusual to see negative  $AV_1$  signals, but negative  $AV_2$  signals were slightly more common, and this occasionally appears to have contributed to the acquisition of upward targets (**Figure 5-21**; *orange* and *green* data-points to the left of the vertical axis).

**Testing Prediction 2: ‘The subject will modulate AV signals by modulating  $|\mathbf{x}|$ , and  $\omega$  will remain constant.’**

We found that there was a clear positive correlation between  $v_{\perp}$  and  $|\mathbf{x}|$ , but it would be incorrect to claim that the relationship was linear because, particularly in the case of  $AV_1$  (**Figure 5-22a**), it appeared that the gradient  $\Delta v_{\perp}/\Delta|\mathbf{x}|$  increased with  $|\mathbf{x}|$ ; suggesting that the angular velocity,  $\omega$ , (and thus the frequency,  $f$ ) did increase slightly with increasing AV.

It was also clear that simple linear regression through the data in either **Figure 5-22a** or **b** would not pass through the origin. However, performing simple linear regression (no constraint to origin) produced gradients of: jPC plane 1 (**Figure 5-22a**),  $\omega = 23.2 \text{ rad s}^{-1}$ , thus  $f = 3.7 \text{ Hz}$ ; and jPC plane 2 (**Figure 5-22b**),  $\omega = 18.2 \text{ rad s}^{-1}$ , thus  $f = 2.9 \text{ Hz}$ . Unfortunately, it is difficult to comment formally on these values, other than to say that they are consistent with our observations of the frequency of  $lf$ -LFP activity that we see associated with movement (typically 2–4 Hz), and with the observation that the rotation in jPC plane 2 (mainly PMv activity) is slower than that in jPC plane 1 (mainly M1 activity).

The reason for the offset in  $|\mathbf{x}|$  (but not in  $v_{\perp}$ ) is likely a technical issue with this analysis approach. Noise in the jPC signals is likely to manifest as small, random movements around the origin. The distance,  $|\mathbf{x}|$ , around the origin will—by definition—always be positive, and positive on average over time; whereas the tangential velocity will be randomly positive and negative (depending on direction of rotation), and will average to zero over time.

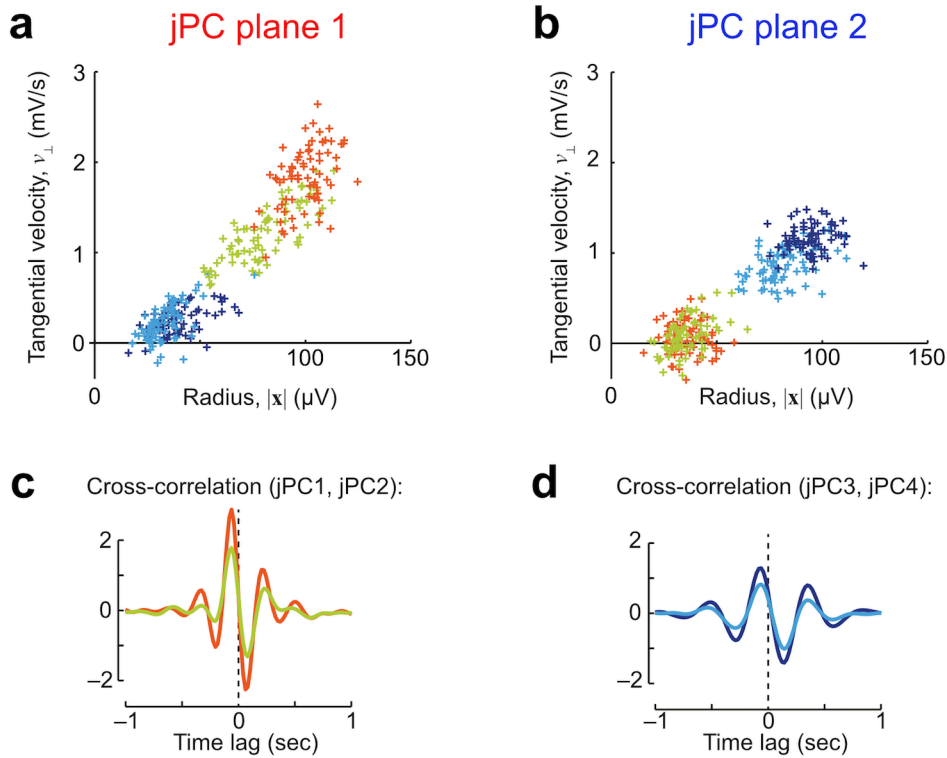


**Figure 5-22** *The mechanisms of modulation of areal velocity in the 1-D (2:1 mapping) biofeedback BMI task.*

- (a) Scatter plot of radius,  $|x|$ , versus tangential velocity,  $v_{\perp}$  in jPC plane 1. Each datum-point shows the mean parameter value for an individual trial (over the 0.6 s analysis window). Data-points are coloured according to the target-location for that trial. Gradient is proportional to angular velocity,  $\omega$  (which is also proportional to frequency,  $f$ , of the rotation).
- (b) The same as a, but for jPC plane 2.
- (c) Cross-correlation between components jPC1 and jPC2 (i.e. jPC plane 1), over the duration of the recording, for each of the two upward targets (*green*, +50% target; *orange*, +75% target).
- (d) Cross-correlation between components jPC3 and jPC4 (i.e. jPC plane 2), over the duration of the recording, for each of the two downward targets (*cyan*, -50% target; *purple*, -75% target).

In order to avoid these effects, we also studied the jPCs directly in the time-domain, by calculating the cross-correlation between the two jPCs in each jPC plane, for each of the two targets where substantial signal was being generated (e.g. positive targets for jPC plane 1). In jPC plane 1 (**Figure 5-22c**), for the +50% target, we saw an oscillation with a frequency of 3.3 Hz and a lag of 0.07 s (jPC1 leading). For the +75% target, the peaks of the cross-correlation function were extremely similar, and the frequency was 3.6 Hz. In jPC plane 2 (**Figure 5-22d**), for the -50% target, we saw an oscillation with a frequency of 2.4 Hz and a lag of 0.07 s (jPC1 leading). For the -75% target, the peaks of the cross-correlation function were extremely similar, and the frequency was also 2.4 Hz.

To summarise, whilst we can't conclusively claim that the frequency (angular velocity) of the *lf*-LFP rotations associated with movement is fixed, it seems that the dominant parameter that modulates areal velocity is the radius (amplitude) of the rotation.

### 5.3.5.6 Two-dimensional biofeedback BMI using areal velocity signals

#### Behaviour of AV signals separately and in combination

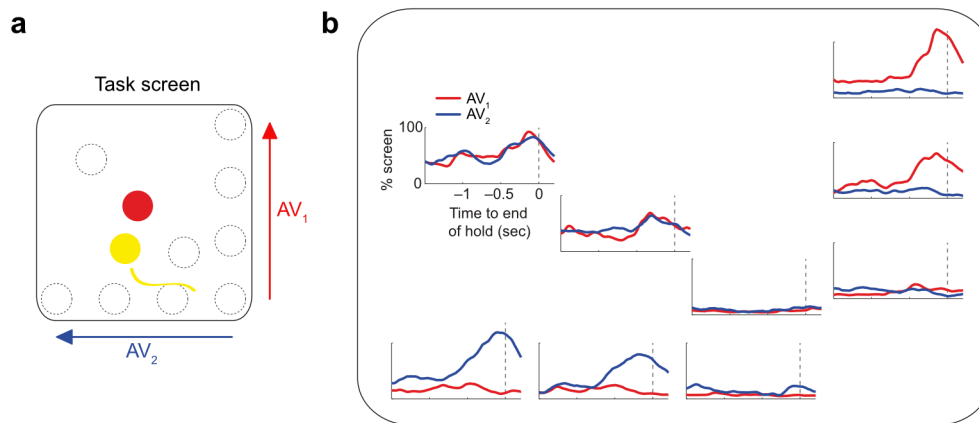


**Figure 5-23** Areal velocity during 2-D AV-control biofeedback BMI task

- (a) Screen mapping of AV signals to a 2-D task with 9 targets.
- (b) Mean  $AV_1$  and  $AV_2$  signals, aligned to end of the successful hold period, for each of the 9 target locations (mean across  $n = 39$  trials per target). Panel location represents target location. AV signals are both expressed in terms of screen proportion (%).

We found that the subject was able to both separate and combine the generation of areal velocity in the two planes, to acquire positive targets in the 2-D biofeedback task (**Figure 5-23**).

**Testing Prediction 2 in two dimensions: ‘The subject will modulate AV signals by modulating  $|x|$ , and  $\omega$  will remain constant.’**

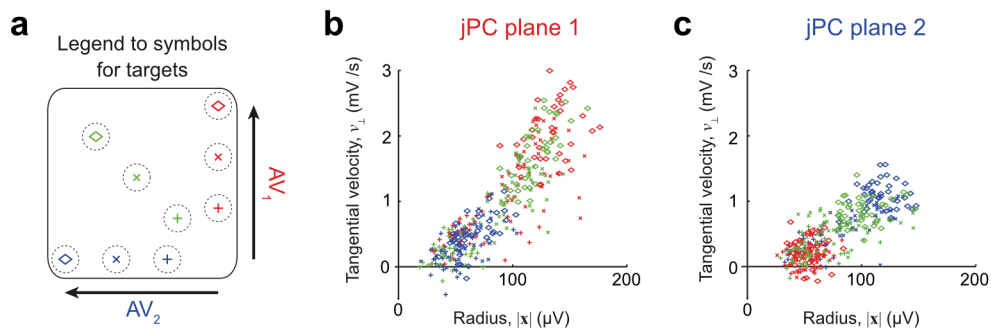


**Figure 5-24** *The mechanisms of modulation of areal velocity in the 2-D biofeedback BMI task.*

- (a) Legend for the figures to the right, indicating the marker used for each target.
- (b) Scatter plot of radius,  $|x|$ , versus tangential velocity,  $v_{\perp}$  in jPC plane 1. Each datum-point shows the mean parameter value for an individual trial (over the 0.6 s analysis window). Data-points are coloured according to the target-location for that trial. Gradient is proportional to angular velocity,  $\omega$  (which is also proportional to frequency,  $f$ , of the rotation).
- (c) The same as b, but for jPC plane 2.

We saw a very similar relationship between  $v_{\perp}$  and  $|x|$  in the 2-D BMI task as we did in the 1-D task. Again, there was a suggestion in jPC plane 1 that angular velocity (gradient) did increase as AV increased (more distant targets). But these data also suffered from the same issues discussed previously in **Section 5.3.5.5** (‘Testing Prediction 2’, page 140). Simple linear regression (no constraint to the origin) through the data gave gradients of: jPC plane 1 (**Figure 5-24b**),  $\omega = 21.4 \text{ rad s}^{-1}$ , thus  $f = 3.7 \text{ Hz}$ ; and jPC plane 2 (**Figure 5-24c**),  $\omega = 13.8 \text{ rad s}^{-1}$ , thus  $f = 2.2 \text{ Hz}$ . These values are broadly consistent with those in the 1-D task.

**Behaviour of the local neurons during the 2-D AV-control biofeedback BMI task**

So far, we have demonstrated indirect evidence of two separate dynamical systems in two separate areas of motor cortex—M1 and PMv—operating at different frequencies, and capable of being controlled separately and in combination by the subject. Whilst our experiments did not allow us to provide direct evidence of the neural substrate of these sources of activity, we were able to study the behaviour of the neurons which we recorded simultaneously to the LFPs, from both areas.

We recorded a total of 15 neurons during 2-D AV-control BMI experiment; 8 from M1 and 7 from PMv. Firing rates were calculated offline by binning spikes into 20.5 ms bins (to match the sampling interval of the *lf*-LFPs), and low-pass filtering at 5 Hz (Butterworth filter, as previously). Firing rates were normalised to zero mean and unity variance, and aligned to the end of the successful hold periods from the underlying AV-controlled task. A mean firing rate was calculated for each neuron, for each target, over a 0.6 s analysis window prior to the end of the hold period. For each neuron, we then performed multiple linear regression, with 2-D target screen co-ordinates as predictor variables (regressors), and mean firing rate as the response variable (regressand). This gave us a regression coefficient for each of the dimensions of the task (as well as a constant, which we ignored for this particular analysis).

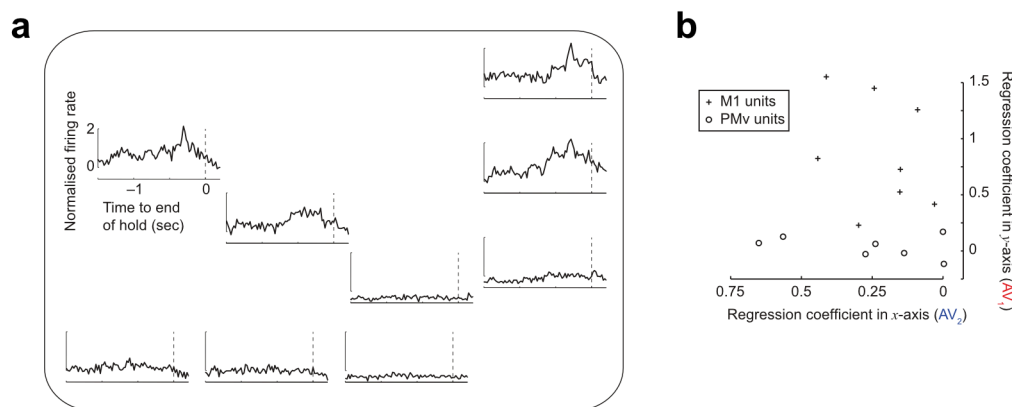


**Figure 5-25** Behaviour of the local neurons during the 2-D AV-control biofeedback BMI task

- (a) Example firing rate profiles of one M1 neuron for each of the 9 targets. Panel location in the figure represents target location in the task. Important to note that the cursor is still controlled by the AV signals, not by the firing rate. Firing rate is simply measured concurrently.
- (b) Regression coefficients for 15 neurons (8 M1, 7 PMv). A neuron with a high regression coefficient associated with  $y$ -axis targets has a firing rate which is strongly modulated when the cursor moves upwards on the screen (i.e. when the brain is generating  $AV_1$  signal via rotation in jPC plane 1). The neuron in panel a is such an example. A neuron with a high regression coefficient associated with  $x$ -axis targets has a firing rate which is strongly modulated when the cursor moves leftwards on the screen (i.e. when the brain is generating  $AV_2$  signal via rotation in jPC plane 2).

Firing rates of PMv neurons (*open circles* in **Figure 5-25b**) were highly associated with state-space rotation in jPC plane 2 (leftward target locations). This is consistent with previous observations, including LFP weightings (**Figure 5-18**), which indicated that jPC plane 2 rotation predominantly reflected PMv LFP activity. M1 neurons (*crosses* in **Figure 5-25b**) were more variable—showing some association with both target axes—but they were predominantly associated with rotation in jPC plane 1 (upward target locations). This is

consistent with LFP weightings which indicated that jPC plane 1 rotation predominantly reflected M1 LFP activity.

We know that the recorded neurons must be within their respective cortical areas (because neural recordings require micro-metre proximity). These findings therefore support the belief that the rotational features we see in the *lf*-LFP are generated locally by cortical ensembles within their respective cortical areas (rather than arising from a global phenomenon being propagated, or transmitted by volume conduction, across wide areas of cortex).

## 5.4 Discussion

Neuronal action potentials (spikes) have an all-or-nothing nature (making the separation of signal from noise very intuitive); they have a tangible physical origin (a neuron); and their signals demonstrate clear ‘features’ associated with movement – namely modulation of firing rate, and directional tuning. These factors have, for good reason, biased motor neuroscience researchers towards using the firing rates of neurons when trying to decode motor intention from wide-band cortical recordings.

LFPs have long been recognised as an alternative to spikes for decoding movement-related cortical activity, and providing control signals to BMI devices. However, in comparison to spikes, the origin of field potentials is more complex and less well understood.

Separating out a biologically or behaviourally relevant signal is arguably more challenging with LFPs than with spikes. There is an accepted method — thresholding — for at least separating spike events from other ‘unwanted’ activity. In comparison, what neuroscientists call an ‘LFP’ recording, consists of a complex mixture of a multitude of continuous signals. Separating a signal of interest in an LFP recording from irrelevant ‘noise’ (e.g. electronic recording noise, movement artefacts, cardio-respiratory noise), let alone from other genuine neural signals, is notoriously difficult. Also, LFPs represent a complex mixture of the activity of a network of tens of thousands of neurons, and the effects of volume conduction, propagation and intrinsic filtering all combine to make the LFP relatively complex and non-intuitive to analyse. Specifically, LFPs recorded simultaneously on multiple electrodes cannot be treated as independent channels of information.

There is currently no consensus on exactly which features of the LFP are best suited to extracting a movement-related signal, suitable for BMI control, and this therefore remains a challenge to the field.

We used an unsupervised decoder approach to test the performance of a metric based solely on LFP power at classifying bimanual movement. As expected, in a relatively recently-implanted cortical electrode array (left hemisphere, 5½ months old), both low-frequency (< 5 Hz) and gamma-band power performed well at movement classification. It is perhaps surprising to note that beta-band power also performed well at binary classification, but in the opposite direction to the other bands. In fact, this can be explained very simply, because it reflects a pattern of *depression* of beta-band LFP power in the motor cortex during movement, which is consistent with the literature (Baker et al. 1997).

More importantly, in the other (right) hemisphere, where the cortical electrode array had been implanted for much longer (15½ months), power-based unsupervised decoding of movement laterality performed extremely poorly (**Figure 5-13a**). As can be seen in the example data plotted in **Figure 5-10c**, this is not surprising, given the very low amplitude, and very low signal-to-noise ratio of the LFP signals in the right hemisphere (*blue traces*), compared to the left hemisphere (*red traces*).

The power of a signal is only dependent on its amplitude, but there is evidence that significant additional information is available in the LFP from the instantaneous phase of the signal. For example, a number of groups have found that the local motor potential (LMP; preserving phase information) out-performs delta-band power (removing phase information) when decoding EMG (Flint, Ethier et al. 2012) or movement (Rickert et al. 2005, Bansal et al. 2012).

Such studies also demonstrate that decoding performance is significantly better when movement is decoded using multiple *lf*-LFPs, rather than a single signal (Rickert et al. 2005), and when field recordings are made from within the cortex (LFPs) rather than just from the surface (ECoG/EEG) (Mehring et al. 2004). Bansal and colleagues, for example, explicitly comment on the variation in timing between their *lf*-LFP signals, and the relative independence of their *lf*-LFPs (Bansal et al. 2011).

These previous reports are consistent with the idea that we have already evidenced in previous chapters: that *lf*-LFP signals recorded from within a motor cortical region (e.g. M1) are not

redundant (as one might expect from the association of delta waves with periods of sleep or rest). Instead, multichannel *lf*-LFP contains a complex mixture of phases, which likely reflect the mixing of signals from a number of underlying sources. Resolving these underlying sources from the recorded data is an example of the ‘inverse problem’, commonly referred to as the ‘cocktail party problem’.

In **Chapter 3**, we demonstrated one approach to this problem, which enabled us to make use of the phase-structure within multichannel *lf*-LFP to estimate the firing rate of motor cortical neurons. In the current Chapter, we aimed to extract movement-related signals from the multichannel *lf*-LFP *without* any prior information about spiking, and *without* any information about kinematics (that is to say, using unlabelled data to train a model in an unsupervised fashion).

Our approach was based on the observation that the target-directed movement we recorded in monkeys contained subtle but consistent periodicity, termed ‘submovements’ (Hall, De Carvalho & Jackson 2014). Unpublished results from our laboratory (Susilaradeya et al. NCM poster) and previous literature (Miall et al. 1993) also indicate that similar submovements are seen in forelimb movements in humans. In monkeys, we saw that this periodicity was coherent with *lf*-LFP oscillations, but importantly, that there was variation in phase of these oscillations across different electrodes within M1 (e.g. **Figure 5-1**). Looking at these data in a reduced set of principal components (PCs), it became clear that these phase differences reflected a consistent dynamical structure within the *lf*-LFP, the activity of which was related closely to movement, and was seen as rotation in a low-dimensional state-space projection. Similar movement-related rotational structure has also been observed in multichannel neural recordings (Churchland, Cunningham et al. 2012).

We chose the areal velocity (AV) as a simple metric to capture the properties of this rotational structure in the high-dimensional LFP. We then used two different methods to extract AV signals from *lf*-LFPs. The first of these was jPCA, which explicitly reprojects the data onto 2-D planes which best capture the rotation. The second of these introduced a novel concept, the ‘areal velocity component’ (AVC), which is an abstraction of areal velocity calculation (cross-product) in three dimensions, to a situation where a pairwise AVC is calculated for all possible unique pairs of principal components.

Both of our AV-based feature extraction methods out-performed power based methods when sufficient (approximately six) *lf*-LFPs were included. More importantly, our AV-based methods were able to extract useful information, and hence classify correctly, using signals from electrodes where signal power alone performed extremely poorly.

It is important to reiterate and discuss further the distinction between supervised and unsupervised decoding. All of the studies cited above (page 143) detect features from their LFP data by using supervised/machine learning methods to learn which features of the LFP are most informative to movement decoding, based on labelled data from a ‘training set’. If we were to perform multivariate *supervised* decoding using multichannel LFP band-power, it would clearly perform significantly better at classification than simply using the mean LFP power (as was used in **Figure 5-13**). Having said this, supervised decoding of the high-dimensional AV space would likely also yield significantly better performance than unsupervised decoding. For example, it would appear from **Figure 5-7** that the multidimensional AV contains information about movement direction. Indeed, previously we have demonstrated that movement direction can be decoded in a supervised fashion from the orientation of the 3D AV vector (derived from the LFP-PC space) (Hall et al 2014, Figure 2N). Performance was not much better than chance, but it is possible that more sophisticated supervised learning methods, perhaps using the expanded-dimensionality AVC space could yield much better performance.

However, the critical and exciting property of AV-based metrics that I have shown in this chapter, is that they can be derived *a priori* from multi-channel LFP, without knowledge or labelling of the associated behaviour; then even in this unsupervised scenario, they can successfully allow decoding of simple movements. This property may be useful in patients who are completely paralyzed, and don’t exhibit any residual limb movement, therefore cannot provide a training dataset. Further work will be required to investigate whether AV-based methods could still extract (in an unsupervised fashion) a useable signal from brain recordings from such patients.

Our method based on areal velocity components (‘AVC-based’ method) performed slightly better than the jPCA-based method. This may be because jPCA looks explicitly for rotation within the PCs, meaning that projections of the data which would otherwise be informative for making subtle distinctions between movements, are often collapsed down into a single plane. In contrast, the AVC-based method actually expands the dimensionality of the feature

search-space, increasing the chances that pairs of PCs which contribute particularly rich areal velocity signals are more likely to be featured in the output signal.

Areal velocity signals seem particularly well-suited to BMI applications, because they are intrinsically robust to the two main types of noise which typically affect multichannel LFP recordings: uncorrelated and correlated noise. Uncorrelated noise across LFPs produces a mean areal velocity of zero, because it produces no consistent direction of rotation about the origin. Correlated noise is also rejected from the areal velocity signal, because correlated signals, regardless of their amplitude, produce only reciprocation, rather than rotation, in state space. Reciprocation involves only back-and-forth movement along a single axis, and therefore the area swept out is zero. The areal velocity is therefore effective at selecting only those physiological sources that produce consistent phase differences within the multichannel LFP. AV-based methods can therefore out-perform power-based methods in situations of poor signal-to-noise ratio, as long as phase structure is preserved and consistent.

Conceptually, the AVC-based method can be considered an extension of the concept of a differential recording (**Figure 5-26**). Whilst a differential recording is able to reject common (identical) noise between channels, the AVC can also reject all in-phase correlated components (regardless of amplitude), making the AV signal relatively insensitive to distant or external sources of noise.

Next, to test the feasibility of an AV-based BMI, we used the jPCA-based method to extract two AV signals simultaneously, and without supervision, from LFPs recorded across M1 and PMv. We found that the first jPC plane corresponded mostly to M1 LFPs, while the second plane corresponded mainly to PMv LFPs. That is to say, the algorithm found, and was able to separate the dynamics associated with each area. This separation took place largely on the basis of frequency, with PMv LFP dynamics demonstrating a slightly lower frequency of rotation ( $\sim 2\text{--}3$  Hz) than the M1 LFPs ( $\sim 3\text{--}4$  Hz).

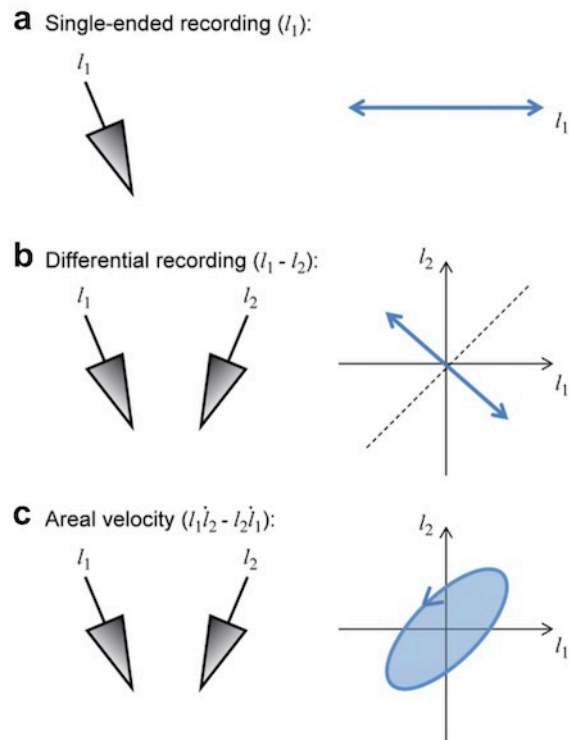


**Figure 5-26** Comparison of different signal types from LFP recording

Single-ended recordings are relative to ground. Differential recordings can reject signal components that are common to two LFPs (anything that falls along the axis  $I_1=I_2$ ). Areal velocity calculation rejects any in-phase oscillatory components in the two LFPs, as well as having zero mean for uncorrelated noise.

— Figure reproduced from Jackson & Hall (2016), IEEE TNSRE, Figure 4.  
Figure produced originally by A. Jackson.

To our knowledge, this is the first time that such differences in LFP dynamics have been described in motor cortex. However, the frequencies we observed are highly consistent with those seen in neural data, as is the observation that rotations tend to be faster in M1 than in premotor areas. Churchland and colleagues report that “... *the angular velocity of the rotations was in each case slightly higher for M1* [than for dorsal premotor cortex]. *We suspect that this effect may be real. It is consistent with our informal observations, notable in every dataset we have inspected so far, that neurons recorded in posterior sites [M1] are more likely to exhibit high-frequency response features.*” (Churchland, Cunningham et al. 2012, Supplementary Figure 5).

In a realtime, closed-loop biofeedback experiment, we found that the subject was able to control our two AV-signals simultaneously, both independently (in the 1-D experiment) and in combination (in the 2-D experiment). This behaviour was associated with relatively distinct modulation of neuronal firing rates in M1 and PMv. Given that neuronal signals are well-

localised to cortical area, this suggests that each area is able to generate independent low-frequency neural dynamics, that can be detected and exploited via the multichannel *lf*-LFP.

By using a biofeedback BMI, we were able to ask questions of the data that would not be possible with a ‘black box’ biomimetic set-up, or simply by using data from the torque-task. The relationship between the recorded brain signals and the cursor position was explicitly set by (and therefore known to) us. By observing the strategy that the subject used to perform the tasks, we were therefore able to test specific predictions that we had made, based on our hypothesis of the underlying physiology of AV signals.

Our hypothesis was that *lf*-LFP dynamics (and therefore areal velocity) would be constrained by the intrinsic cortical dynamics of a cortical area. Our first prediction from this was that the direction of rotation in state space would be constrained (because relative *lf*-LFP phase relationships remain consistent), and therefore the subject would only be able to generate positive AV signals. We could test this in our 1-D task, because it had a redundant 2-D solution space.

We found that the subject was able to generate small, negative AV signals, but that the clearly preferred strategy was to use positive AV signals. A consistent polarity of AV indicates that the phase relationships between *lf*-LFPs remain robust, despite the differing requirements of each target in the task. This supports our hypothesis that *lf*-LFP phase relationships are constrained by cortical physiology. However, we certainly cannot claim that this is proof that *lf*-LFP relationships are fixed. The subject chose a strategy for the task in which she moved her left hand to acquire ‘M1-dominant’ targets, but produced right forelimb movement and other body posturing to acquire the ‘PMv-dominant’ targets. It may therefore be coincidence that these particular behaviours correspond to positive dynamical rotations in their respective cortical areas of activity. This experiment should therefore be repeated in further subjects. In addition, it would be important to record LFPs from other cortical areas (for example dorsal premotor cortex, supplementary motor area) to see whether each area displays its own unique pattern of LFP dynamics.

Our second prediction was that increases in areal velocity would be mediated by increases in radius (amplitude) rather than increases in angular velocity (frequency), on the basis that the frequency of the cortical dynamics within a particular area is constrained. This prediction proved harder to test than we anticipated, because of background noise. Although the AV

signal itself is relatively robust to background noise, the *angular velocity* signal becomes very erratic, and also the mean radius signal becomes non-zero.

Broadly speaking, we found that the angular velocity (thus frequency) was relatively constant over a wide range of AV values, and this was supported by time-domain analysis (cross-correlation). However, we did consistently see increases in the gradient of the  $\Delta v_{\perp}/\Delta|\mathbf{x}|$  plots with higher values of AV, suggesting that the angular velocity (thus frequency) of the cortical dynamics can, and probably does, increase when the brain is generating output to produce fast movements of the forelimb.

There is no reason, from physiological first-principles, to assume that the frequency of cortical dynamics should be constrained to a specific frequency. The physiological nature of the sources that contribute to the LFP at these frequencies is still highly speculative. For example, if they are a manifestation of simple pharmacological phenomena, or sensory feedback loops, then one might expect latencies (and therefore frequency) to be relatively fixed. However, if they are a manifestation of a more complex internal cortical model of the physics of movement, then one might expect the frequency of the system to have some variability with movements of different speeds. Future work on this is already being carried out in our lab (Susilaradeya & Jackson) by introducing artificial delays into the visual feedback of a torque task (in both monkeys and humans), and measuring the effects of these feedback delays on submovements and on cortical dynamics.

We propose that areal velocity signals may, both conceptually and practically, be a useful tool when trying to extract features from LFPs. They certainly have some desirable features for use as BMI control signals, particularly in ‘real-world’ experiments, where signal amplitude and recording noise levels (i.e. signal-to-noise ratio) are often an issue, or there may be other external sources of correlated noise (e.g. movement of cables). AV signals are also very simple to calculate, and therefore to implement in low-power hardware.

In this work, we have only considered AV signals associated with low-frequency LFPs. However, areal velocity based signals should also be explored for other LFP frequency bands in the future.

Whilst AV-based approaches are conceptually attractive, and their simplicity is desirable, it is also important to acknowledge that the true underlying physiology of *lf*-LFP generation in motor cortex is undoubtedly far more complex than the areal velocity can capture. Areal

velocity is a relatively simple non-linear transformation of LFP data, based on a simplistic assumption that the dynamics of the motor cortex can be modelled as a linear dynamical system. Such simple models may be useful for providing reliable BMI signals, but future work will need to explore more sophisticated non-linear models of *lf*-LFP dynamics.

Furthermore, with regards the generalizability of our findings, it is important to note that all of the relationships studied in this thesis were recorded in the laboratory environment, with an animal highly trained to perform particular types of movement with one limb (although the other limbs were free, and did move frequently). It remains to be seen whether the robust LFP relationships which we observe in the lab hold true during natural behaviour – for example, jumping around in the home-cage environment. It may be that the relationships between LFPs change, and thus the informative (non-redundant) dimensions of the LFP space also change. Indeed, it is clear that relationships between LFPs *do* change with different directions of movement, and the dynamical system approaches that we use in this chapter may collapse a lot of this information down (thus making it effectively redundant). For example, in **Figure 5-7**, we see that by only using the first PCs of the LFP space, we lose the information that varies with movement direction. Our ‘AVC’ method was an attempt to extract more than two useful signals using an areal velocity-based approach, and hence capture more of this information. However, we were only consistently able to extract two signals. Further work will be required to develop approaches to extract more of this non-redundant information.

Finally, as already discussed in previous chapters, our data strongly suggest that recording from a variety of cortical depths is critical to capturing the local structure of the *lf*-LFP. Unfortunately, the most commonly-used arrays in human patients (and NHP experiments) are planar silicon arrays, which are optimised for spike recording, but tend to capture LFPs from a single layer of the cortex. The data presented in this thesis so far suggest that the information content of *lf*-LFP recordings could be improved by placing electrodes at specific depths, to optimally capture distinct SRSP components, and reduce the redundancy of recordings. Unfortunately, the moveable microwires we have used so far in this thesis do not allow us to document recording site location; nor do they provide a geometric electrode arrangement that allows us to perform spatial analysis. In the next Chapter, we discuss the design of a geometric array to address these limitations, and present some preliminary data from such an array.

## 5.5 Chapter summary

- Cyclical patterns of activity in motor cortex can be seen in low-dimensional projections of low-frequency LFPs, and are linked to movement kinematics.
- We observed (at least) two planes with rotational structure, corresponding broadly to distinct M1 and PMv activity.
- A monkey was able to use the areal velocities of these rotations to control a biofeedback BMI task in one and two dimensions.
- A consistent direction of rotation and largely consistent frequency of rotation within each plane suggests that these LFP dynamics may reflect intrinsic network properties of cortex.
- Areal velocity is relatively insensitive to both correlated and uncorrelated noise: useful properties for LFP-controlled chronic BMIs.
- The use of non-linear transformations such as areal velocity can expand the dimensionality of the feature space (since  $N$  LFP channels yields  $\frac{1}{2}N(N-1)$  LFP pairs), and produce a conceptually new type of signal for future BMI experiments.

# Chapter 6. Hybrid geometric/moveable arrays for investigating the spatial nature of *lf*-LFPs in motor cortex.

*In which we describe design and implantation of, and preliminary data from, a new design for a hybrid electrode array – featuring fixed, regularly-spaced electrodes and moveable microwire electrodes.*

## 6.1 Introduction

In previous chapters, we have mentioned that we are unable to comment on the spatial nature of SRSPs and other *lf*-LFP features, because we do not know the locations of the tips of our tungsten microwire electrodes in the brain; other than knowing that they are in the cortical area of interest, based on the location of implantation.

The majority of studies that use chronic cortical implants for performing BMI experiments in monkeys (and in humans) use high-density, rigid, silicone multielectrode arrays (MEAs) – most commonly ‘Utah’ arrays (Blackrock Microsystems). Typically, around 96 electrodes are implanted directly into the cortex in a single-stage surgery. The aim of the implant is generally to maximise the number of cortical neurons that are recorded from the ‘output’ layer of the cortex, and so the recording sites are found in a single plane, at the tips of 1.0–1.5 mm-long shanks, where it is hoped that a large number will end up in layer V of the motor neocortex, recording from pyramidal neurons (**Figure 6-1**).

Typically, all the electrodes in a rigid MEA are in a single plane. For physiological studies, this has the advantage that the recording sites are geometrically arranged, and the relative spatial relationships of the recorded signals are known. However, this likely produces a disadvantage for extracting useful BMI-control signals from LFPs on these arrays, because LFPs are also only recorded from a 2-D plane, at a single depth. The findings presented in this thesis, as well as other studies (e.g. Einevoll et al. 2007; Markowitz et al. 2011) indicate that decoding of movement (or neural firing rate, or EMG) is more successful when LFPs are recorded from multiple depths; in other words, from a 3-D volume of cortex.

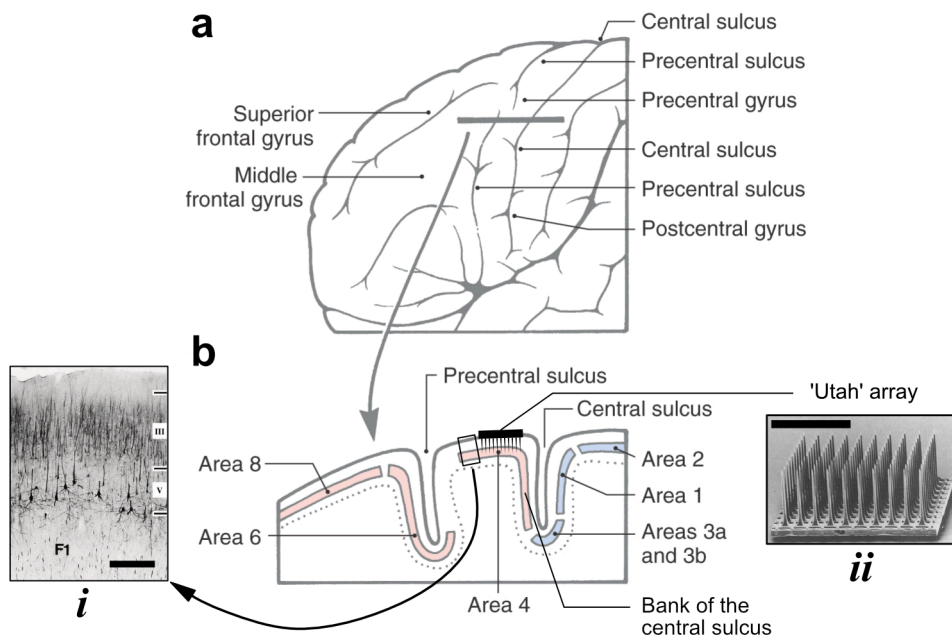


**Figure 6-1** *Anatomy and histology around the central sulcus, and example MEA implantation*

- (a) Schematic lateral view of the left hemisphere (human), showing the major sulci and gyri of the frontal lobe. Grey bar indicates line of sagittal section shown below, in b.
- (b) Schematic sagittal section through precentral and central sulci. Brodmann ‘Area 4’ corresponds to primary motor cortex (M1). Pink region indicates the approximate depth of layer V (pyramidal cell, primary output layer) in pre-central motor areas. Areas 1, 2, 3a and 3b are primary somatosensory cortex. Black box indicates area enlarged in Inset *i*: example histology (SMI-32 immuno-architecture) of M1 (here labelled as F1), showing prominent pyramidal cells in layer V, with layer III above (layer IV is absent in agranular cortex). Scale bar: 500  $\mu$ m. Inset *ii*: A typical 96-electrode rigid silicone MEA (‘Utah’ array). Scale bar: 2 mm. The silhouette in the main panel shows a typical implant location.

— Panels **a** and **b** adapted from Haines & Mihailoff, *The Telencephalon*, from Haines (ed.) (2017) *Fundamental Neuroscience for Basic and Clinical Applications* (Elsevier Health)

Inset *i* adapted from Geyer et al (2000), *Anat Embryol* **202** (Springer-Verlag)

Inset *ii* adapted from Campbell et al (1991), *IEEE TBME* **38** (IEEE press)

Rigid MEAs also have a number of other disadvantages:

- i) Silicone electrodes are rigid, as is the square base-plate of the typical MEA. This means that any translational or rotational movement of the implant relative to the brain can put shearing stress on the surrounding neural tissue, which can be particularly damaging.
- ii) Once an MEA is implanted in a particular location, the recording sites cannot be moved, without performing another surgery and completely re-implanting the array.

This can be a problem if the array is not implanted correctly (which can happen for a variety of reasons) or if reactive gliosis makes the recording sites unusable.

- iii) Electrodes cannot be moved independently, so any adjustment to the array means losing all recording locations, both good and bad.
- iv) Recording sites tend to be small (to optimise isolation of single-unit recordings) so impedances tend to be relatively high ( $\geq 400 \text{ k}\Omega$ ; commonly  $> 1 \text{ M}\Omega$ ).

Our moveable microwire electrodes (as used in this thesis; designed by A. Jackson and E. Fetz, and described in **Chapter 1**) do have a number of advantages over ‘Utah’ arrays, as follows:

- i) Individual electrodes are moveable, so once a recording site becomes unusable—due to gliosis, or neuron loss around the contact site—the electrode can be withdrawn or advanced into a new recording location.
- ii) Electrode impedance is relatively low, around 100–200 k $\Omega$ ; reducing noise in recordings, which is particularly important in the LFP.
- iii) The microwire array bundle can be implanted into the skull before the electrodes are advanced, allowing local healing of the surgical site to take place prior to advancement of the electrodes. Anecdotally, this seems to reduce the inflammatory response to electrode insertion (A. Jackson, personal communication).

However, despite these advantages, microwires have the considerable disadvantage (compared to silicone arrays) that we don’t know the precise location of the recording sites, even after post-mortem histology. This is because the moveable tungsten wires, whilst stiff, don’t necessarily take straight paths through the cortex, making tract reconstruction impossible. Moreover, during one monkey’s lifetime, electrodes are moved multiple times, and recordings are therefore made at different depths from multiple, crossing tracks.

In order to further investigate the anatomy of the *lf*-LFP and SRSP we designed a ‘hybrid’ array. This combined the main benefit of using moveable tungsten microwires—being able to move electrodes and acquire new neurons—with a geometric design for recording LFPs. For our geometric arrays, rather than using silicone electrode technology, we used *linear microelectrode arrays* (LMAs, Microprobes for Life Sciences, Inc., MD, USA).

As we can see from **Figure 6-1b**, primary motor cortex (M1; Brodmann Area 4) is not limited to the surface of brain. A significant proportion of M1 (in particular, forelimb and hand areas)

is found within the anterior (rostral) bank of the central sulcus (Geyer et al. 2000). During our experiments where we have inferred that cortical “depth” produces phase and polarity shifts within the *lf*-LFP/SRSP (e.g. **Figure 3-6**, page 44), we need to accept that our electrodes may not be travelling transversely through cortical layers, but rather, may be travelling down the anterior (rostral) bank of the central sulcus. We therefore set out to design a hybrid array that would allow us to record signals from the bank, as well as from the gyral convexity.

Finally, as we discussed in **Chapter 1**, one potential application of *lf*-LFP-based decoders of cortical motor activity, is as control signals for ultra-low power BMIs. As well as minimising the sampling rate of such a device, another simple way to reduce the overall data acquisition rate (and hence power consumption) of a BMI is to reduce the number of channels of recording. This would be possible if one could work out which electrodes were critical to the decoding process (for example, which LFPs were essential to estimating a particular firing rate). We therefore also wanted to see what mixtures of electrodes, from which areas (e.g. surface, gyral convexity, bank of M1) were most informative for estimating firing rates.

## 6.2 Aims

**Aim 1:** Design and manufacture a hybrid electrode array, combining moveable tungsten microwires with linear microelectrode arrays.

**Aim 2:** Make use of the geometric arrangement of LFP recording sites, to better understand the depth profile of the *lf*-LFP and SRSP. Specifically, study differences between LFPs recorded *down the anterior (rostral) bank* of the central sulcus, versus LFPs recorded perpendicular to the cortical surface, *across different cortical layers* in the gyral convexity.

**Aim 3:** Analyse the optimum locations to have electrodes, given a limited number of recording channels.

**The reader should please note** that this Chapter only represents preliminary work towards addressing these aims. It has not been possible to perform formal analyses of these data during the period of this PhD studentship, and that will therefore constitute future work. However, the novel hybrid electrode design is certainly relevant to this thesis, and the analysis

presented here is not meant to provide conclusive results, but rather, illustrative examples of preliminary findings, which the reader will hopefully find stimulating.

## 6.3 Methods and Results

### 6.3.1 *Hybrid electrode design and construction*

Our hybrid electrode (see **Figure 6-2**) was a modification of the original moveable microwire design by Jackson & Fetz (2007), through incorporation of four linear microelectrode arrays (LMAs, made by Microprobes).

We added two “long” (7.5 mm active area) and two “short” (4 mm active area) LMAs to a moveable microwire array of 12 tungsten microwires (**Figure 6-2b**). Each LMA had 15 platinum/iridium contacts of diameter 25  $\mu\text{m}$  (impedance 0.7–1  $\text{M}\Omega$ ) plus a sharp tungsten tip that was also an active recording site (impedance < 0.1  $\text{M}\Omega$ ) (**Figure 6-2a**). There were thus 76 recording channels per array: 12 microwires + (16  $\times$  4) LMA contacts.

LMAs were placed in a square of sides 3 mm, with the microwire bundle in the centre of the square. The microwire guide tubes were aligned as described previously (Jackson & Fetz 2007), and larger polyimide guide tubes (310  $\mu\text{m}$  internal diameter, Cole Parmer, UK) were arranged in a surrounding square, using tungsten alignment rods (Advent Research Materials, UK). The components of the array, including the supplied LMAs, were then sterilised with ethylene oxide treatment.

The final stage of construction took place the day prior to cortical implant surgery. Under sterile conditions, the microwires were inserted (as per Jackson & Fetz 2007). The four LMAs were then inserted in turn into their respective guide tubes, such that their contact sites faced inwards towards the microwire bundle, and fixed in place at the top with dental cement. The base and tops of the guide tubes were then sealed with two-part silicone (*Kwik-Sil*, World Precision Instruments, UK).

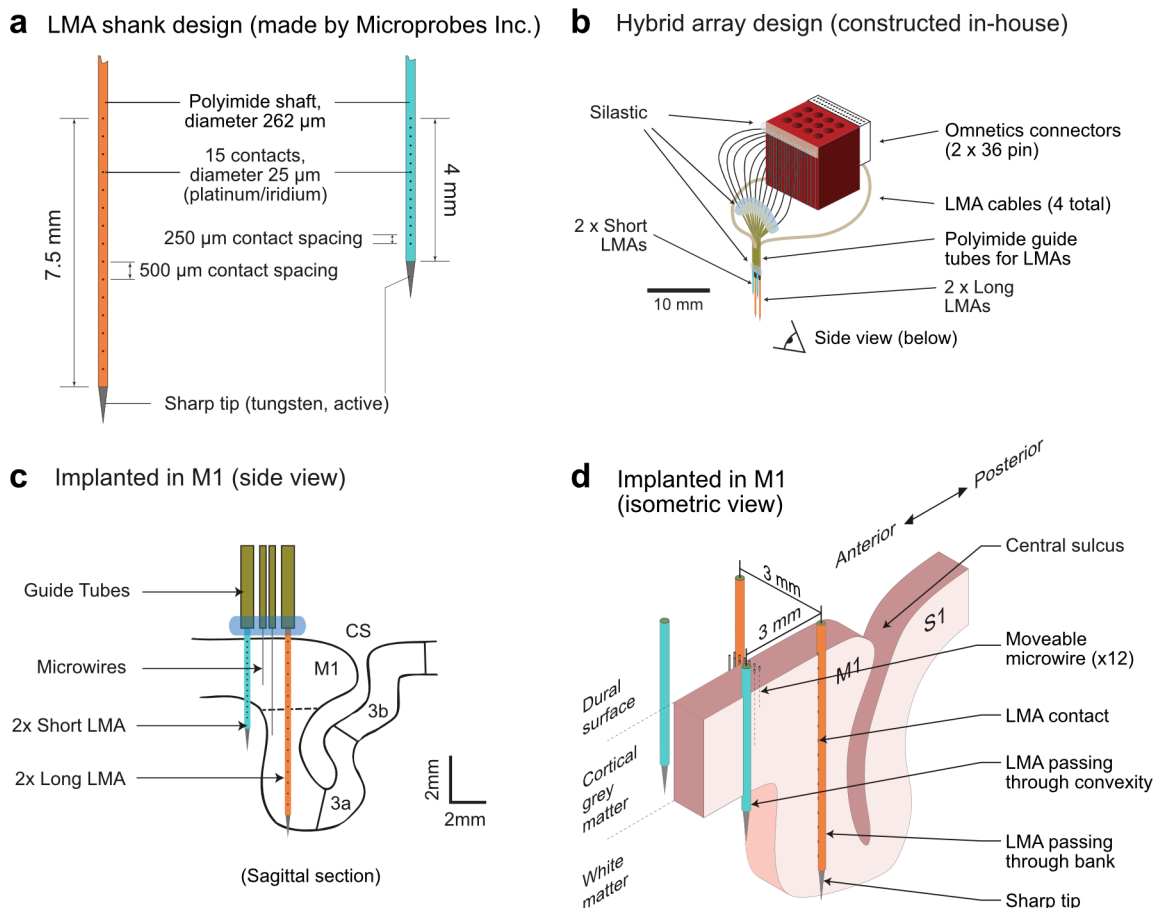


**Figure 6-2** Design of dual-shank LMA plus tungsten microwire hybrid array.

- (a) Illustration of LMA shank design (constructed off-site by Microprobes For Life Science, MD, USA). See **Appendices I & II** for detailed specifications of the LMAs.
- (b) Illustration of the method of integration of four LMAs into a hybrid array. LMAs sat in front of (anterior/rostral to) and behind (posterior/occipital to) the  $6 \times 2$  microwire array. The microwires were still moveable using forceps, as previously.
- (c) 2-D sectional illustration of the theoretical location of the four LMAs (side view so only two visible), and the microwire bundle, anterior to the central sulcus. The anterior (rostral) LMAs pass through the gyral convexity and into the white matter. The posterior (occipital) LMAs pass down the anterior bank of the central sulcus. Slice profile is traced from actual macaque histology, but not from the Monkey used in this study.
- (d) 3-D isometric illustration of the theoretical location of LMAs and microwires following implantation.

— Slice profile in panel c adapted from an image kindly provided by C. Witham from Fig. 3 in Witham & Baker (2012), *J Neurophysiol* **108** (American Physiological Society)

### **6.3.2 *Surgical implantation***

One subject (Monkey U) was implanted with this hybrid array, in the right M1. The surgical procedures were the same as described in **Section 2.3**. The array was rotated approximately 30 degrees about the vertical axis, towards the midline, to account for the angle of the central sulcus. The long LMAs were implanted just anterior to the central sulcus, such that their shanks ran down into the anterior (rostral) bank of the central sulcus. The short LMAs were therefore 3 mm anterior to this, passing through the gyral convexity (**Figure 6-2c,d**). The microwires were advanced at the time of surgery, since it was felt that the cortex was well fixated by the placement of the four LMAs. The array and connectors were fixed to the skull with dental cement. A protective titanium cranial implant was fixed to the skull as described in **Section 2.3**.

### **6.3.3 *Task and electrophysiological recording.***

Monkey U performed the wrist-controlled torque task with her left wrist, as described in **Section 2.1.2**. Electrophysiological recordings were made using the TDT-based recording system, as per **Section 2.4.1**. Signals were referenced to a separate surface electrode (a de-insulated tungsten microwire). Signals were recorded in groups of 16 channels. The channel mapping was as per **Table 6-1**, and this information is also shown schematically in **Figure 6-3**. *Lf*-LFPs were calculated offline by low-pass filtering at 5 Hz. Spikes were occasionally seen transiently on LMA channels, but were very unstable. However, spikes were recorded successfully, as previously, on a number of microwire channels.

Recording channels	Electrode/shank type
1 - 12	Tungsten microwires
(13 - 16)	(Not connected)
17 - 32	Short LMA "L" (lateral)
33 - 48	Short LMA "M" (medial)
49 - 64	Long LMA "L" (lateral)
65 - 80	Long LMA "M" (medial)

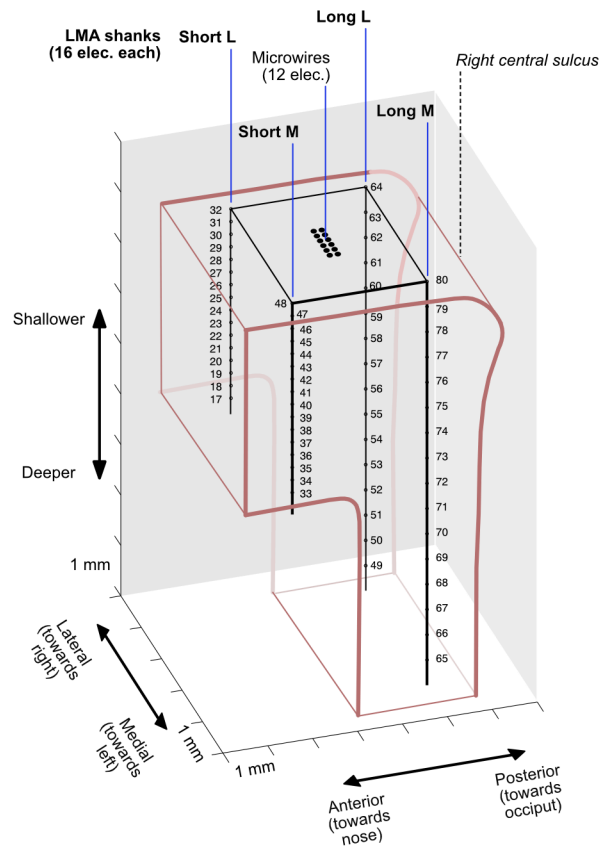


**Table 6-1** (left) Channel mapping in Monkey U. Note that channels 13–16 were not connected.

**Figure 6-3** (right) Schematic of relative locations of recording sites in Monkey U. (To scale.)

Long LMAs passed down the anterior (rostral) bank of the right central sulcus. Short LMAs passed through the gyral convexity. Note that the electrode locations are only illustrative, and not based on histological analysis. Tungsten tip electrodes were 17, 33, 49 and 65.

## 6.3.4 Event-triggered average profiles across LMAs

### 6.3.4.1 Method

For the purposes of displaying the task-related structure of the *lf*-LFP data across all 76 electrodes, we used the submovement-triggered average, as described in Hall, De Carvalho and Jackson (2014). Briefly, we identified submovements in the cursor trajectory during the wrist-torque task as peaks in the radial speed of the cursor. We used these peaks as events to perform event-triggered averaging of each of the *lf*-LFP channels, using the iterative approach described in **Figure 3-1** (page 38), but with submovement events rather than spike events.

### 6.3.4.2 Results

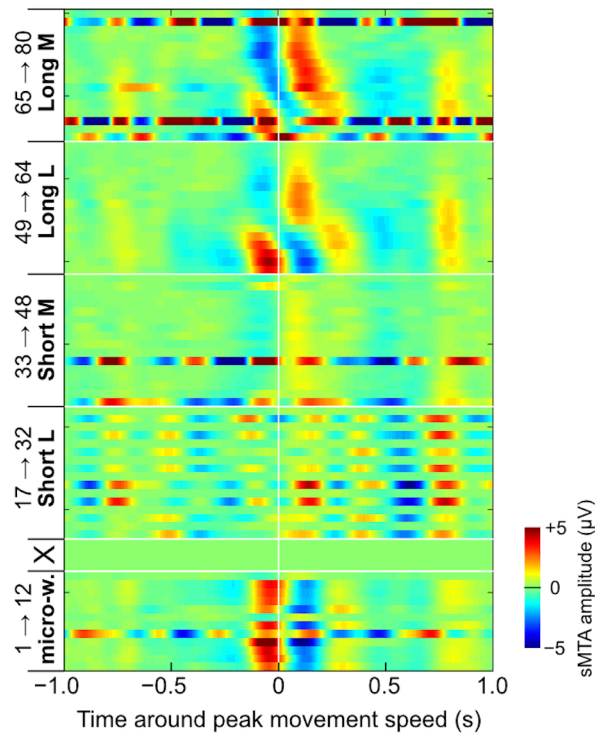


**Figure 6-4** Example submovement-triggered average from 76 electrodes in MI in Monkey U.

Plot of submovement triggered averages (sMTAs), where colour depth represents amplitude of the sMTA. Channel numbers are given on the left, and correspond to those given in the previous figure. Unstable or broken electrodes can be identified by very large artefacts (e.g. channel 79). X indicates four channels in group one that were not recorded. In each LMA, the lowest-numbered channel is the tungsten tip.

Unfortunately, we had a number of broken or unstable recording channels in the LMAs. These are evident from large artefacts in the submovement-triggered average. In this particular recording, we also saw an unusually small amount of variation in signal phase and amplitude across the tungsten microwires, compared to previous experience in other animals. The reason for this is unclear, but it may be because the microwires were all at a similar depth at the time of this recording.

Most interestingly, we saw a large amount of structure in the *lf*-LFP in the long LMAs, which passed down the anterior (rostral) bank of the central sulcus. In the long-lateral LMA in particular (**Figure 6-4**, “Long L”), where there were no broken recording channels, we saw very clear evidence of strong changes in signal amplitude, phase and polarity across the LMA. This was in contrast to the short LMAs (e.g. **Figure 6-4**, “Short M”), where we saw relatively little signal variation between channels.

### 6.3.5 *Estimating neural firing rates with a minimal number of LFPs*

We wanted to know the answer to the following question: if one only had a limited number of recording channels, due to the constraints of an ultra-low power implanted device, which electrodes would be optimal to record from? For example, is it better to have electrodes near the surface, deep in the anterior (rostral) bank of the central sulcus, in the gyral convexity, or distributed over multiple sites?

Based on the findings of **Chapter 4** of this thesis—that estimated firing rates may be a valuable form of control signal in *lf*-LFP-controlled BMIs—we used the estimation of the firing rate of a single neuron (recorded on a microwire) to quantify the importance of individual LFPs, and combinations of LFPs.

#### 6.3.5.1 *Methods*

We recorded the spiking of a single neuron on a microwire (channel 2), and *lf*-LFPs on all 64 LMA channels. We built models to estimate the firing rate of the neuron (as described in **Section 3.3.5.1**), but using only three *lf*-LFPs. We validated these models within-recording using Pearson's correlation coefficient,  $r$ , on the last 25% of the data (as described in **Section 3.3.5.2**). We did this for every one of the 41,664 ' $k$ -combinations' of 3 LFPs from the set of 64 LMA LFPs (using  $b = \text{nchoosek}(64,3)$  in MATLAB, where  $b = n!/((n-k)! k!)$ ). For each LMA channel, we took the mean  $r$ -value across all combinations which included that channel, and used that as a measure of the importance of that channel to the estimation of the neuronal firing rate.

Note that it is the combination of channels included that determines the overall performance of our firing rate estimation model (for example, including channels with phase differences), not necessarily the inclusion of a particular channel. The mean  $r$ -value associated with a particular channel may therefore be misleading. We therefore also looked at which particular combinations of LMA channels performed well.

#### 6.3.5.2 *Results*

We found that LMA channels on the long LMAs (down the rostral bank of the central sulcus) tended, on average, to be associated with better estimates of the firing rate than the LMAs that spanned the gyral convexity (**Figure 6-5**). Inclusion of deeper channels on the long-lateral

LMAs (e.g. 49–57) seemed to be particularly associated with good estimation performance. But one particular LMA contact on the long-medial LMA (electrode 69) stood out as being the channel associated with the highest performance of firing rate estimation (**Figure 6-5**).

It is interesting to note that channels around 53–55 seem to be associated with the largest changes in the submovement-triggered average in **Figure 6-4**. However, from this finding for a single neuron, in a single animal, it is not possible to conclude anything comprehensively without further analysis. It is unclear why a uniquely high mean  $r$ -value is associated with 69, as this channel did not stand out as having a distinctive submovement-triggered average (**Figure 6-4**).

To explore this in more detail, we looked at the best-performing combinations of neurons from across the LMAs (**Table 6-2**).

Row ID	Category	Max. $r$ -value	LFP 1	LFP 2	LFP 3
1	All 64 channels	0.375	35	53	69
2	Both long LMAs	0.360	49	52	69
3	Just Long M	0.352	68	69	76
4	Just Long L	0.323	49	52	63
5	Both short LMAs	0.264	17	20	37
6	Just Short L	0.252	17	19	20
7	Just Short M	0.24	36	37	38

**Table 6-2** Performance of the best combination of channels from each category in firing rate estimation with three LMA channels.

Rows are sorted by column three (maximum  $r$ -value for that category). Remaining columns then list the three LFPs which produce that best  $r$ -value.

Interestingly, with across all 64 electrodes, the best firing rate estimate was provided by LFPs taken from three different LMAs: two deep channels in the bank, and one deep channel in the convexity. In both cases where laterality was a variable (rows 2 and 5), the best model included at least one channel from both LMAs. Finally, the long LMAs clearly performed better than the short LMAs, but the cases restricted to single long LMAs (rows 3 and 4) both included one shallow channel. Beyond these superficial observations, it is not possible to make specific inferences from this limited analysis. Overall, however, it is noteworthy that the best combinations of three LFPs tended to include a channel that was remote from the other two channels (either in laterality, depth, or gyrus/convexity), and not a channel that you would necessarily predict based on **Figure 6-5**.

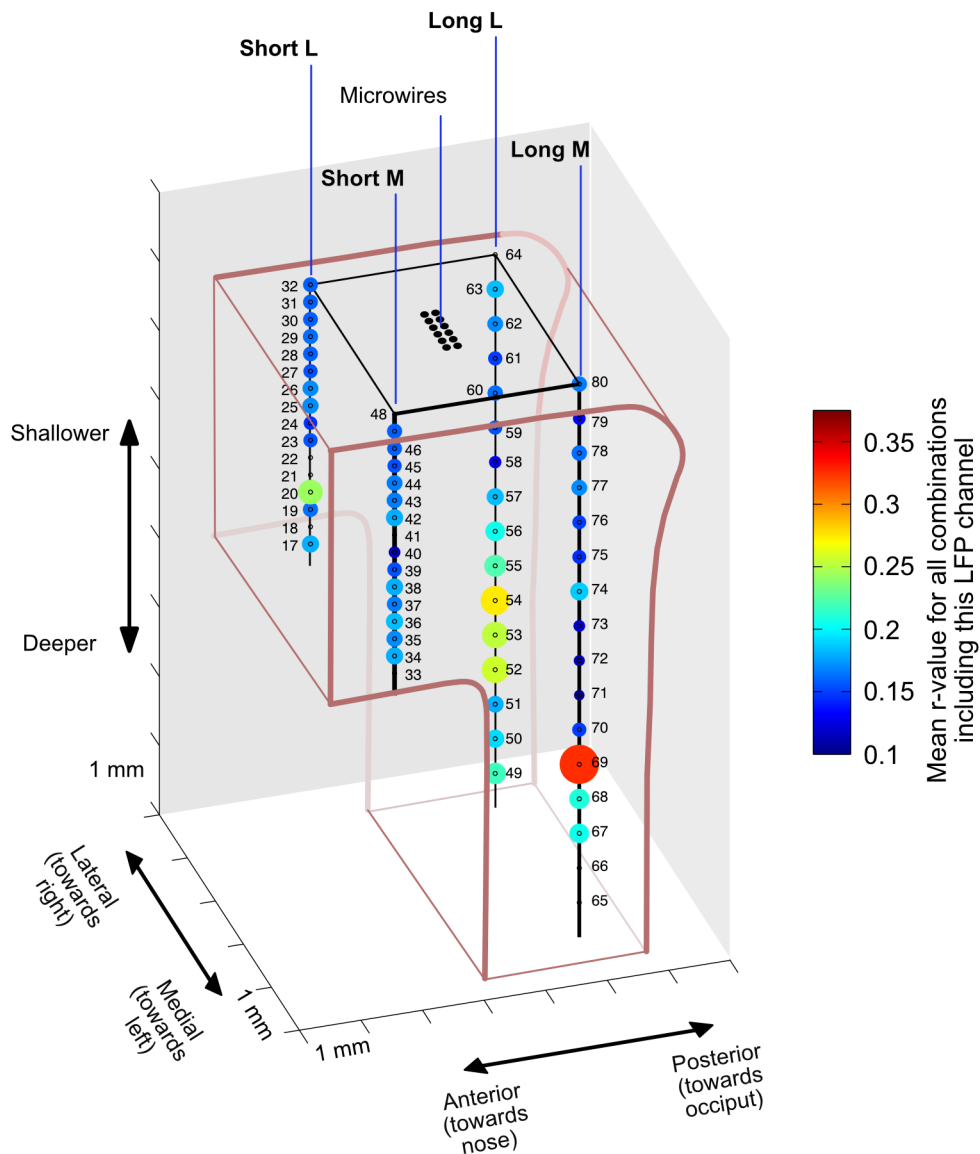


**Figure 6-5** Example of using a minimal number (three) LFPs to estimate the firing rate of a single neuron recorded on a separate microwire. (To scale.)

The size and colour of the sphere plotted at a particular electrode location indicates its mean  $r$ -value in estimating the neuron-of-interest, across all possible combinations of three LFPs that include that LMA channel. Numbers next to data-points indicate channel numbers, as per **Figure 6-3**. Because the neuron-of-interest was recorded on a microwire, it was unfortunately not possible to know its precise geometric location.

## 6.4 Discussion

In this chapter, we have shown the design, development, construction and implantation of a novel type of ‘hybrid’ electrode array. This array is designed to allow the stable recording of single neurons—using proven moveable microwire technology—with the geometric recording of LFPs – using linear microelectrode arrays (LMAs).

Based on the limited findings we have presented here, the proposed applications of this array in future work are as follows:

*a) Investigating the depth profile of the SRSP and its components.*

To date, our lack of defined recording geometry and post-mortem histological tract reconstruction has limited our abilities to correlate the spike-related sources we see in the *lf*-LFP with the anatomy of the cortex. In this chapter, we have not studied the SRSP (or STA) specifically, but it is interesting to note that the submovement-triggered average *lf*-LFP shows considerably more structure across a depth profile of the anterior (rostral) bank of the central sulcus, than it does across the laminar profile of gyral M1. Certainly, forearm movement-related neurons, particularly those associated with the most distal extremities, are known to be found in this rostral bank (Geyer et al. 2000). Therefore, it is possible that we have misinterpreted our previous depth profiles (e.g. **Figure 3-6**, page 44) as laminar profiles, when in fact they are depth profiles down the rostral bank, and hence parallel with laminar boundaries, rather than perpendicular. Our finding that the ‘long’ LMAs are most informative for estimating the firing rate of an M1 neuron would also support this alternative theory. However, we cannot draw any meaningful conclusions from this single datum.

Further work is needed to explore the depth profile of the SRSP across ‘short’ and ‘long’ LMAs. This should include analysis of SRSP components: specifically, whether different SRSP components have differing depth profiles, as this could hint at their origins. Multiple neurons will be required in at least two animals to reach meaningful conclusions. Ideally for this analysis, one would also know the locations of the neurons as well as the LFPs. Unfortunately, we have found recordings of neuronal spiking on our LMA contacts to be extremely rare, and generally unstable when present.

Future array designs can be informed by some of the issues and limitations we have experienced in this subject. Contact sizes, materials and impedances may need to be modified

to maximise the chances of recording neurons on our linear arrays, as precise knowledge of the location of neurons would allow use to use source-localisation techniques that are currently not an option, for dissecting the *lf*-LFP/SRSP. We have also had issues with unstable LMA channels in this subject, perhaps suggesting poor electrical contacts or damaged insulation. Given the rich dataset that each LMA is able to provide, and the even richer possibilities of having multiple fully-functioning LMAs, it will be important in the future to discuss the design of LMAs with Microprobes Inc., in order to maximise the number of channels we can record from every implant. This is particularly important in primate subjects, in whom every implant is both scientifically and ethically critical.

*b) Investigating the origin of low-frequency cortical dynamics.*

There remains considerable debate in the field as to whether features within the LFP which vary in phase or polarity between separated electrodes represent interactions between distinct sources within the cortex (Ray & Maunsell 2011; Kajikawa & Schroeder 2011), or the effect of ‘traveling waves’ that propagate across the cortex (Rubino et al. 2006; Nauhaus et al. 2009; Nauhaus et al. 2012). Whilst broadly we feel our data support the former theory, we have not been able to investigate this specifically to date, due to the unknown geometry of our arrays. The use of geometric arrays of contacts, spanning both the depth of the sulcus, and laminar thickness of the cortex, will allow us to further investigate whether the phenomena we have reported here and elsewhere (Hall, De Carvahó & Jackson 2014) demonstrate evidence of travelling waves.

*c) Selecting electrode locations for brain-machine interfaces.*

As already mentioned, one of the dominant limitations of all BMIs—spike based or otherwise—is the huge bandwidth of data that needs to be streamed from the implant to the recording equipment. One solution is to put more of the signal processing, such as spike sorting, on the implant, so that a lower bandwidth of data has to be transmitted (e.g. Peng et al. 2009). The main solution we have proposed here, is to use very low frequency brain signals, either by exploiting their intrinsic dynamical features, or their relationships to underlying neural spiking.

However, in this chapter, we have also demonstrated in principle, that very few LFPs (perhaps as few as three) might be needed to accurately provide a firing rate estimate, or other appropriate signal for biofeedback BMI control. If only three *lf*-LFP signals were needed for a

BMI control signal, and each of those signals could be sampled at rates as low as tens of Hertz, it could potentially reduce the energy demands of a simple BMI by many, many orders of magnitude. The critical factor is *where* those LFP electrodes are located.

Here, we have shown one example, in which we have provided (admittedly, very limited) evidence that informative *lf*-LFP channels are most commonly found relatively deep in the rostral bank of the central sulcus. Having said this, it also seems important to combine such channels with at least one electrode located elsewhere. Clearly, to form firm conclusions on these points, significantly more analysis of existing data is needed, as well as replication of any findings in at least one other subject.

We can envisage two scenarios. Firstly, if findings are very repeatable, it may be that we can design simple and reliable electrodes, with very few contacts, but appropriate geometry, to specifically target the ‘best’ locations for either firing rate estimation, or some other form of low-frequency feature extraction. However, between-subject variability is likely to be extremely high with these phenomena, due to the large number of uncontrollable variables and individual differences. Therefore, we may never reach a point where we can say exactly where the ‘best’ locations are, prior to surgery.

The second scenario would be one in which multichannel electrodes are implanted, and recordings are initially performed in the lab. Analysis of these data could then allow us to identify the most valuable recording sites for feature extraction. At that point, we could move over to a neuroprosthetic device which *only* records and processes those channels which we have identified, whilst other channels are ignored. Such a device would be highly amenable to miniaturisation, because it could have very low power consumption, and therefore require a very small battery, which could even be implanted subcutaneously.

## 6.5 Chapter summary

- We have designed and manufactured a hybrid electrode array, combining moveable tungsten microwires (to enable acquisition of new spikes) and linear microelectrode arrays (to provide geometrically-arranged contacts for LFP recordings).
- Preliminary analysis suggests that an optimal subset of LFPs for estimating firing rates would include contacts from deep in the rostral bank of the central sulcus, combined with at least one channel in another location.

- These arrays will be used for future experiments to investigate the physiology and depth profile of the  $\beta$ -LFP, and to further explore the optimal locations for electrodes for low-power BMIs.

# Chapter 7. General Discussion

## 7.1 Summary and implications for the field

Neural interfaces (including brain-machine interfaces, BMIs) are a technology on the cusp of delivering a step-change in neurology and rehabilitation: providing treatment to large numbers of people with a wide range conditions that cause life-changing arm and hand paralysis – a particularly important example being spinal cord injury. There has been enormous progress over the last decade in the development of chronic, ‘invasive’ neural interface devices, which record the spiking activity (action potentials) of hundreds of neurons in motor cortex using implanted electrodes, and decode these signals, to control external effectors, or stimulation of the muscles or spinal cord.

However, it can legitimately be argued that the limitations inherent in using neuronal spike signals are placing bottlenecks on progress towards true ‘clinical’ BMIs: low-maintenance systems which could be used by patients in their own homes for many years or decades. Firstly, instability of neuronal recording means that firing rate-based decoders can be capricious. Secondly, the biological response to implanted electrodes means that action potential recordings cannot be maintained for sufficient periods. And thirdly, the high-frequency nature of spikes places high power-demands on hardware, which means that sufficient miniaturisation of electronics and batteries, and development of ‘wireless’ solutions, is currently limited.

Continuous, lower-frequency field recordings from the brain—LFPs (intracortical), ECoG (brain surface) and EEG (scalp surface)—have long been recognised as an alternative to spikes for decoding movement-related cortical activity, and providing control signals to BMI devices. However, in comparison to spikes, the origin of field potentials—from the underlying network activity of at least thousands of neurons—is less well understood.

With action potentials, there is a near-universally accepted method of separating signal (spike events) from noise. It is also very widely accepted, that the firing rate of a neuron (or of many neurons) is a meaningful parameter, which reflects underlying brain function. Firing rates have been used as a feature of brain activity when investigating behaviours in nearly every imaginable modality. Finally, it is known that the firing rates of single (e.g. Fetz 1969) or

multiple (e.g. Ganguly et al. 2011) neurons can be subject to operant conditioning in closed-loop BMIs.

In contrast, there is less agreement on how to identify and separate ‘signal’ from ‘noise’ in LFPs. Moreover, there is not broad scientific consensus on what is the best way to extract meaningful *features* from the LFP. Finally, it is not clear which of these features might be most amenable to learning through biofeedback in a closed-loop BMI.

A variety of recent studies have demonstrated that low-frequency signals (*lf*-LFPs; < 5 Hz; also termed local motor potentials, LMPs) are particularly informative for both offline decoding of kinematics (e.g. Rickert et al 2005) and online control of LFP-based motor BMIs (e.g. Flint et al. 2013), particularly if multiple channels of *lf*-LFP (Rickert et al. 2005) are available from different depths within the cortex (Mehring et al. 2004). However, there is still no consensus on which low-frequency features are best suited to closed-loop BMI control.

In this thesis, we hypothesised that, if we could identify *lf*-LFP components in macaque motor cortex with a strong and consistent relationship to the firing rates of local neurons, then these should be amenable to operant conditioning and therefore provide useful features for closed-loop LFP-based BMIs. Using spike-triggered averaging, we identified the presence of low-frequency spike-related LFP features, which we termed spike-related slow potentials (SRSPs) (**Chapter 3**). We used these features to develop simple linear models of the relationships between multichannel *lf*-LFP and the firing rates of local neurons. Using such models, we were able to estimate the firing rates of single neurons, and our estimates typically captured around 25% of the variance of instantaneous firing rates and 75–85% of trial-averaged profiles. Further work is needed to better understand the underlying physiology of the SRSP, as this was limited by the unknown geometry of our microwires. Pharmacological experiments, including perhaps *in vitro* experiments, will also be required to fully understand the synaptic and receptor-level mechanisms that underlie low-frequency spike-related features.

SRSP-based models were able to significantly estimate the firing rates of the majority of simultaneously-recorded local neurons, and firing rate estimates were stable over weeks to months (**Chapter 4**). On trial-averaged data, remarkably, LFP-based firing rate estimates performed as well as actual firing rates at reconstructing the task relationship of individual neurons (taking the ‘ground truth’ as the task relationship on day zero). In fact, task

relationships could be reconstructed from LFP-based estimates long after the actual neuron was lost. Furthermore, the dimensionality of LFP-based firing rate estimates was comparable to the dimensionality of the associated neural space, and LFP-based firing rate estimates generalised reasonably well across behaviours with different patterns of neural correlation.

It is important to reiterate that we are not claiming that the SRSP reflects the contribution of a single neuron to the *lf*-LFP. Rather, it must (because of its amplitude) represent the activity of an ensemble of many cortical neurons, of which the activity of the selected neuron is representative. Our approach is therefore likely to be limited in its ability to resolve single units as the density of electrode arrays increases. Most likely, greater single-unit resolution will ultimately reveal tightly correlated ensembles beyond which SRSP-based separation becomes impossible.

Despite these likely limitations, we found that our models were sufficiently accurate and specific to permit operant conditioning of individual neuron firing rates using realtime biofeedback *based solely* on *lf*-LFPs (**Chapter 4**). This indicates that our approach is capable of separating the unique task-related activity of the neuron of interest (and its ensemble) from the broader task-related activity of other neurons in that area of motor cortex (for either M1 or PMv).

We propose a scenario in which, soon after electrode implantation, while clean spike recordings can be obtained from many neurons, model parameters that relate the firing rates of these neurons to *lf*-LFPs should be calculated. Such an approach may allow firing rate estimation also to be performed after spike recordings have substantially deteriorated. Future work will need to explore whether this approach proves more or less stable and reliable than the most common current alternative: using unsorted threshold crossings (so-called ‘multi-unit spikes’) for BMI control once single neurons are lost (Gilja et al. 2012).

We next endeavoured to develop a method for extracting movement-related features from multichannel *lf*-LFP without the prior need for recording spikes at all. We based this method on the observation that low-frequency intrinsic cortical dynamics appear to underlie the generation of periodic submovements in forelimb movement (Hall, De Carvalho & Jackson 2014). We characterised the magnitude of these dynamical LFP features using ‘areal velocity’ (AV), and developed two methods for extracting AV-based signals from motor cortical *lf*-LFPs (**Chapter 5**). AV-based methods appeared to out-perform conventional methods of

feature extraction (band-power), particularly when the signal amplitude was very small, on chronically-implanted electrodes.

A monkey was able to use these AVs (extracted using the jPCA-based method) to control a biofeedback BMI task in one and two dimensions, and the consistent direction of rotation, and largely consistent frequency of rotation within each plane, supported the hypothesis that LFP dynamics reflect intrinsic properties of motor cortical networks, rather than low-frequency artefacts resulting from overt movement. Having said this, these biofeedback experiments have only been reported from a single animal, and therefore further experiments and analysis will be required to corroborate these findings.

The ‘areal velocity component’ (AVC) can be thought of as a novel type of signal that can be derived from the *lf*-LFP (**Chapter 5**). Compared to a differential signal, it is theoretically less sensitive to both correlated and uncorrelated noise. These are particularly useful properties for LFP-controlled chronic BMIs, where noise is likely to be a considerable issue. Calculation of the AVC can also expand the dimensionality of the LFP feature space (since  $N$  LFP channels yields  $\frac{1}{2}N(N-1)$  LFP pairs). However, it is likely that activity will be constrained to only a small portion of this high-dimensional space. An important area of future research will therefore be to determine which and how many combinations of these areal velocity features are under volitional control.

In order to further investigate the physiological nature of the SRSP and of low-frequency cortical dynamics, we developed a new type of hybrid electrode array (**Chapter 6**), which incorporates moveable microwires (to allow stable single-unit recording) and four linear microelectrode arrays (to provide a geometric profile of the LFP both across the layers of M1 in the gyral convexity, and down the rostral bank of the central sulcus). We explored the use of a minimal subset of LFPs from the available channels. Preliminary analysis involving firing rate estimation of a single neuron using only three *lf*-LFPs, suggests that channels located deep in the central sulcus may be particularly informative, but particularly when combined with at least one channel in a different location (**Chapter 6**). We propose that even greater energy savings (on top of those achieved by using low sampling rates) could be achieved in BMI applications, by careful selection and recording of only an optimal subset of channels from those available. Further analysis, and replication in another subject, will clearly be required before we can formalise these ideas. Histological analysis of post-mortem tissue from the subjects will also be critical, to reconstruct the anatomical locations of our LMA

contacts, and this will also provide insights into the physiology of the SRSP and other low-frequency phenomena.

## **7.2 Future directions**

The work presented in this thesis potentially contributes towards the development of a low-power, chronically implanted neural interface, which uses low-frequency multichannel LFP activity as its input, and computationally simple approaches to signal processing.

Such a device could parsimoniously address the three main limitations of current neural interfaces: long-term stability, power consumption and implantability. Reducing sampling frequency to tens of Hertz, and using simple on-board processing could significantly help address the latter two limitations, because it would dramatically reduce the power consumption of the device, in turn reducing battery size and facilitating miniaturisation for subcutaneous implantation. Once the recording and processing equipment can be subcutaneously implanted, this paves the way for development of fully-implantable neural interfaces, which could produce their effects by delivering electrical stimulation to implanted electrodes in the muscles, or in the spinal cord, below the level of injury. An exciting area for future research is therefore to explore how best low-frequency signals can be decoded for control of such stimulation.

Power consumption could be reduced even further by reducing the absolute number of channels which are needed to control a neural interface device. Our preliminary results suggest that this should be possible if electrodes are located in optimal locations, or if an approach can be developed to identify the optimal subset of electrodes from those available. Ultra-low bandwidth devices are a particularly exciting avenue for future work, because they open up the possibility of wireless communication between an implanted device and the outside world.

In summary, we envisage a situation within the next twenty years, in which production of a fully-implantable neural interface device becomes possible, which is affordable enough to be offered to patients with spinal cord injury (or other conditions) via the National Health Service, or other healthcare systems. I hope that the research presented in this thesis represents a positive contribution to the body of research that allows this to happen.



# References

- Abiri, P., Abiri, A., et al., 2017. Inductively powered wireless pacing via a miniature pacemaker and remote stimulation control system. *Scientific Reports*, Article number: 6180.
- Aflalo, T.N. & Graziano, M.S.A., 2006. Partial tuning of motor cortex neurons to final posture in a free-moving paradigm. *Proceedings of the National Academy of Sciences of the United States of America*, 103(8), pp.2909–2914.
- Amar, A.B., Kouki, A.B. & Cao, H., 2015. Power approaches for implantable medical devices. *Sensors*, 15(11), pp.28889–28914.
- Andersen, R.A., Burdick, J.W., et al., 2004. Cognitive neural prosthetics. *Trends in Cognitive Sciences*, 8(11), pp.486–493.
- Andersen, R.A., Musallam, S. & Pesaran, B., 2004. Selecting the signals for a brain-machine interface. *Current Opinion in Neurobiology*, 14(6), pp.720–726.
- Antonic, A. et al., 2013. Stem cell transplantation in traumatic spinal cord injury: a systematic review and meta-analysis of animal studies. *PLoS Biology*, 11(12), p.e1001738.
- Arora, P. 2016. FPGA-based design for low system power consumption. Power Electronics. [www.powerelectronics.com](http://www.powerelectronics.com); published 7 April 2016, accessed 20 May 2018.
- Asher, I. et al., 2007. Comparison of direction and object selectivity of local field potentials and single units in macaque posterior parietal cortex during prehension. *Journal of Neurophysiology*, 97(5), pp.3684–3695.
- Baker, S.N., Olivier, E. & Lemon, R.N., 1997. Coherent oscillations in monkey motor cortex and hand muscle EMG show task-dependent modulation. *The Journal of Physiology*, 501(1), pp.225–241.
- Baker, S.N., Kilner, J.M., Pinches, E.M. & Lemon, R.N., 1999. The role of synchrony and oscillations in the motor output. *Experimental Brain Research*, 128, pp.109–117.
- Baker, S.N., 2011. The primate reticulospinal tract, hand function and functional recovery. *The Journal of Physiology*, 589(Pt 23), pp.5603–5612.
- Bansal, A.K. et al., 2011. Relationships among low-frequency local field potentials, spiking activity, and three-dimensional reach and grasp kinematics in primary motor and ventral premotor cortices. *Journal of Neurophysiology*, 105(4), pp.1603–1619.
- Barrese, J.C. et al., 2013. Failure mode analysis of silicon-based intracortical microelectrode arrays in non-human primates. *Journal of Neural Engineering*, 10(6), p.066014.
- Belitski, A. et al., 2008. Low-Frequency Local Field Potentials and Spikes in Primary Visual Cortex Convey Independent Visual Information. *Journal of Neuroscience*, 28(22), pp.5696–5709.

- Bellman, R., 1957. *Dynamic Programming*. North Chelmsford, MA: Courier Corporation.
- Bensmaia, S.J. & Miller, L.E., 2014. Restoring sensorimotor function through intracortical interfaces: progress and looming challenges. *Nature Reviews Neuroscience*, 15(5), pp.313–325.
- Berens, P. et al., 2008. Comparing the feature selectivity of the gamma-band of the local field potential and the underlying spiking activity in primate visual cortex. *Frontiers in systems neuroscience*, 2, pp.1–11.
- Bhagat, N.A. et al., 2016. Design and Optimization of an EEG-Based Brain Machine Interface (BMI) to an Upper-Limb Exoskeleton for Stroke Survivors. *Frontiers in Neuroscience*, 10, p.122.
- Biran, R., Martin, D.C. & Tresco, P.A., 2005. Neuronal cell loss accompanies the brain tissue response to chronically implanted silicon microelectrode arrays. *Experimental neurology*, 195(1), pp.115–126.
- Boudrias, M-H., McPherson, R.L., Frost, S.B. & Cheney, P.D., 2009. Output properties and organization of the forelimb representation of motor areas on the lateral aspect of the hemisphere in rhesus macaques. *Cerebral Cortex*, 20, pp.169–186.
- Bradberry, T.J., Gentili, R.J. & Contreras-Vidal, J.L., 2010. Reconstructing three-dimensional hand movements from noninvasive electroencephalographic signals. *Journal of Neuroscience*, 30(9), pp.3432–3437.
- Brosch, M., Budinger, E. & Scheich, H. 2002. Stimulus-related gamma oscillations in primate auditory cortex. *Journal of Neurophysiology*, 87(6), pp.2715–2725.
- Buzsáki, G., 2004. Neuronal Oscillations in Cortical Networks. *Science*, 304(5679), pp.1926–1929.
- Buzsáki, G., Anastassiou, C.A. & Koch, C., 2012. The origin of extracellular fields and currents — EEG, ECoG, LFP and spikes. *Nature Reviews Neuroscience*, pp.1–14.
- Campbell, P.K. et al., 1991. A silicon-based, three-dimensional neural interface: manufacturing processes for an intracortical electrode array. *IEEE Transactions on Bio-medical Engineering*, 38(8), pp.758–768.
- Canolty, R.T. et al., 2010. Oscillatory phase coupling coordinates anatomically dispersed functional cell assemblies. *Proceedings of the National Academy of Sciences of the United States of America*, 107(40), pp.17356–17361.
- Carmena, J.M., 2013. Advances in neuroprosthetic learning and control. *PLoS Biology*, 11(5), p.e1001561.
- Carmena, J.M. et al., 2003. Learning to Control a Brain–Machine Interface for Reaching and Grasping by Primates. *PLoS Biology*, 1(2), pp.194–208.
- Carracedo, L.M. et al., 2013. A neocortical delta rhythm facilitates reciprocal interlaminar interactions via nested theta rhythms. *Journal of Neuroscience*, 33(26), pp.10750–10761.

- Chao, Z.C., Nagasaka, Y. & Fujii, N., 2010. Long-term asynchronous decoding of arm motion using electrocorticographic signals in monkeys. *Frontiers in Neuroengineering*, 3, p.3.
- Chauvette, S. et al., 2011. Properties of slow oscillation during slow-wave sleep and anesthesia in cats. *Journal of Neuroscience*, 31(42), pp.14998–15008.
- Cherry, E.C., 1953. Some experiments on the recognition of speech, with one and with two ears. *Journal of the Acoustical Society of America*, 25(5), pp.975–979.
- Churchland, M.M. et al., 2010. Cortical Preparatory Activity: Representation of Movement or First Cog in a Dynamical Machine? *Neuron*, 68(3), pp.387–400.
- Churchland, M.M. et al., 2012. Neural population dynamics during reaching. *Nature*, 487, pp.51–56.
- Colgin L.L. & Moser E.I., 2012. Gamma oscillations in the hippocampus. *Physiology*, 25(5), pp.319–329.
- Cunningham, J.P. & Yu, B.M., 2014. Dimensionality reduction for large-scale neural recordings. *Nature Publishing Group*, 17(11), pp.1500–1509.
- Daly, J.J. & Wolpaw, J.R., 2008. Brain-computer interfaces in neurological rehabilitation. *Lancet Neurology*, 7(11), pp.1032–1043.
- Dayan, P. & Abbott, L.F., 2005. Neural Encoding I: Firing Rates and Spike Statistics. In P. Dayan & L. F. Abbott, eds. *Theoretical Neuroscience: Computational and Mathematical Modeling of Neural Systems*. Cambridge MA: MIT Press, pp. 1–42.
- Destexhe, A., 1998. Spike-and-wave oscillations based on the properties of GABAB receptors. *Journal of Neuroscience*, 18(21), pp.9099–9111.
- Destexhe, A., Contreras, D. & Steriade, M., 2001. LTS cells in cerebral cortex and their role in generating spike-and-wave oscillations. *Neurocomputing*, 38, pp.555–563.
- Dine, J. et al., 2014. Optogenetic evocation of field inhibitory postsynaptic potentials in hippocampal slices: a simple and reliable approach for studying pharmacological effects on GABAA and GABAB receptor-mediated neurotransmission. *Frontiers in Cellular Neuroscience*, 8, pp.1–8.
- Dlugosz, R.T. & Iniekski, K. 2006. Ultra low power current-mode algorithmic analog-to-digital converter implemented in 0.18/spl mu/m CMOS technology for wireless sensor network. *MIXDES 2006, Proceedings of the International Conference*, Gdynia, Poland
- Einevoll, G.T. et al., 2007. Laminar population analysis: estimating firing rates and evoked synaptic activity from multielectrode recordings in rat barrel cortex. *Journal of Neurophysiology*, 97(3), pp.2174–2190.
- Einevoll, G.T. et al., 2013. Modelling and analysis of local field potentials for studying the function of cortical circuits. *Nature Reviews Neuroscience*, 14(11), pp.770–785.

- Engelhard, B. et al., 2013. Inducing Gamma Oscillations and Precise Spike Synchrony by Operant Conditioning via Brain-Machine Interface. *Neuron*, 77(2), pp.361–375.
- Ethier, C. et al., 2012. Restoration of grasp following paralysis through brain-controlled stimulation of muscles. *Nature*, 485(7398), pp.368–371.
- Fabiani, G.E. et al., 2004. Conversion of EEG activity into cursor movement by a brain-computer interface (BCI). *IEEE Transactions on Neural Systems and Rehabilitation Engineering*, 12(3), pp.331–338.
- Fagg, A.H. et al., 2007. Biomimetic brain machine interfaces for the control of movement. *Journal of Neuroscience*, 27(44), pp.11842–11846.
- Fan, J.M. et al., 2014. Intention estimation in brain-machine interfaces. *Journal of Neural Engineering*, 11(1), p.016004.
- Fetz, E.E., 1969. Operant conditioning of cortical unit activity. *Science*, 163(3870), pp.955–958.
- Fetz, E.E. & Baker, M.A., 1973. Operantly conditioned patterns on precentral unit activity and correlated responses in adjacent cells and contralateral muscles. *Journal of Neurophysiology*, 36(2), pp.179–204.
- Flesher, S.N. et al., 2016. Intracortical microstimulation of human somatosensory cortex. *Science Translational Medicine*, 8(361), p.361ra141.
- Flint, R.D. et al., 2013. Long term, stable brain machine interface performance using local field potentials and multiunit spikes. *Journal of Neural Engineering*, 10(5), p.056005.
- Flint, R.D. et al., 2016. Long-Term Stability of Motor Cortical Activity: Implications for Brain Machine Interfaces and Optimal Feedback Control. *Journal of Neuroscience*, 36(12), pp.3623–3632.
- Flint, R.D., Ethier, C., et al., 2012. Local field potentials allow accurate decoding of muscle activity. *Journal of Neurophysiology*, 108(1), pp.18–24.
- Flint, R.D., Lindberg, E.W., et al., 2012. Accurate decoding of reaching movements from field potentials in the absence of spikes. *Journal of Neural Engineering*, 9(4), p.046006.
- Flint, R.D., Wright, Z.A. & Slutzky, M.W., 2012. Control of a biomimetic brain machine interface with local field potentials: performance and stability of a static decoder over 200 days. In Conference proceedings: Engineering in Medicine and Biology Society (EMBC), 2012 34th Annual International Conference of the IEEE. San Diego, pp. 6719–6722.
- Galán, F. et al., 2008. A brain-actuated wheelchair: asynchronous and non-invasive Brain-computer interfaces for continuous control of robots. *Clinical Neurophysiology*, 119(9), pp.2159–2169.
- Ganguly, K. & Carmena, J.M., 2009. Emergence of a stable cortical map for neuroprosthetic control. *PLoS Biology*, 7(7), p.e1000153.

- Ganguly, K. et al., 2011. Reversible large-scale modification of cortical networks during neuroprosthetic control. *Nature Neuroscience*, 14(5), pp.662–667.
- Georgopoulos, A.P. et al., 1982. On the relations between the direction of two-dimensional arm movements and cell discharge in primate motor cortex. *Journal of Neuroscience*, 2(11), pp.1527–1537.
- Geyer, S. et al., 2000. Functional neuroanatomy of the primate isocortical motor system. *Anatomy and embryology*, 202(6), pp.443–474.
- Gilja, V. et al., 2012. A high-performance neural prosthesis enabled by control algorithm design. *Nature Neuroscience*, 15(12), pp.1752–1757.
- Gilja, V. et al., 2015. Clinical translation of a high-performance neural prosthesis. *Nature medicine*, 21(10), pp.1142–1145.
- Green, A.M. & Kalaska, J.F., 2011. Learning to move machines with the mind. *Trends in Neurosciences*, 34(2), pp.61–75.
- Hall, T.M., de Carvalho, F. & Jackson, A., 2014. A common structure underlies low-frequency cortical dynamics in movement, sleep, and sedation. *Neuron*, 83(5), pp.1185–1199.
- Hall, T.M., Nazarpour, K. & Jackson, A., 2014. Real-time estimation and biofeedback of single-neuron firing rates using local field potentials. *Nature communications*, 5, p.5462.
- Hart, C.B. & Giszter, S.F., 2010. A neural basis for motor primitives in the spinal cord. *Journal of Neuroscience*, 30(4), pp.1322–1336.
- Henze, D.A. et al., 2000. Intracellular features predicted by extracellular recordings in the hippocampus in vivo. *Journal of Neurophysiology*, 84(1), pp.390–400.
- Hermes, D. Miller, K.J. & Wandell, B.A., 2015. Gamma oscillations in visual cortex: The stimulus matters. *Trends in Cognitive Sciences*, 19(2), pp.57–58.
- Hochberg, L.R. et al., 2006. Neuronal ensemble control of prosthetic devices by a human with tetraplegia. *Nature*, 442(7099), pp.164–171.
- Hochberg, L.R. et al., 2012. Reach and grasp by people with tetraplegia using a neurally controlled robotic arm. *Nature*, 485(7398), pp.372–375.
- Hutcheon, B., Miura, R.M. & Putil, E., 1996. Subthreshold membrane resonance in neocortical neurons. *Journal of Neurophysiology*, 76(2), pp.683–697.
- Hwang, E.J. & Andersen, R.A., 2009. Brain control of movement execution onset using local field potentials in posterior parietal cortex. *Journal of Neuroscience*, 29(45), pp.14363–14370.
- Hwang, E.J. & Andersen, R.A., 2013. The utility of multichannel local field potentials for brain–machine interfaces. *Journal of Neural Engineering*, 10(4), p.046005.

- Hwang, E.J., Bailey, P.M. & Andersen, R.A., 2013. Volitional control of neural activity relies on the natural motor repertoire. *Current biology*, 23(5), pp.353–361.
- Intan Technologies, LLC, 2013. RHD2000 Series Digital Electrophysiology Interface Chips: RHD2216, RHD2132. *www.intantech.com*, version: 5 September 2013, accessed: 15 May 2018.
- Ito, J., 2015. Spike-Triggered Average. In D. Jaeger & R. Jung, eds. *Encyclopedia of Computational Neuroscience*. Berlin, Germany: Springer.
- Jackson, A. & Fetz, E.E., 2007. Compact Movable Microwire Array for Long-Term Chronic Unit Recording in Cerebral Cortex of Primates. *Journal of Neurophysiology*, 98(5), pp.3109–3118.
- Jackson, A. & Fetz, E.E., 2011. Interfacing With the Computational Brain. *IEEE Transactions on Neural Systems and Rehabilitation Engineering*, 19(5), pp.534–541.
- Jackson, A. & Hall, T.M., 2017. Decoding Local Field Potentials for Neural Interfaces. *IEEE Transactions on Neural Systems and Rehabilitation Engineering*, 25(10), pp.1705–1714.
- Jackson, A. & Zimmermann, J.B., 2012. Neural interfaces for the brain and spinal cord--restoring motor function. *Nature Reviews Neurology*, 8(12), pp.690–699.
- Kajikawa, Y. & Schroeder, C.E., 2011. How Local Is the Local Field Potential? *Neuron*, 72(5), pp.847–858.
- Katzner, S. et al., 2009. Local Origin of Field Potentials in Visual Cortex. *Neuron*, 61(1), pp.35–41.
- Kaufman, M.T. et al., 2014. Cortical activity in the null space: permitting preparation without movement. *Nature Publishing Group*, 17(3), pp.440–448.
- Kipke, D.R. et al., 2008. Advanced Neurotechnologies for Chronic Neural Interfaces: New Horizons and Clinical Opportunities. *Journal of Neuroscience*, 28(46), pp.11830–11838.
- Kokotilo, K.J., Eng, J.J. & Curt, A., 2009. Reorganization and preservation of motor control of the brain in spinal cord injury: a systematic review. *Journal of Neurotrauma*, 26(11), pp.2113–2126.
- Krasoulis, A. et al., 2014. Generalizability of EMG decoding using local field potentials. *Conference proceedings: Annual International Conference of the IEEE Engineering in Medicine and Biology Society. IEEE Engineering in Medicine and Biology Society. Annual Conference*, 2014, pp.1630–1633.
- Kreiman, G. et al., 2006. Object selectivity of local field potentials and spikes in the macaque inferior temporal cortex. *Neuron*, 49(3), pp.433–445.
- Leach, J.B., Achyuta, A.K.H. & Murthy, S.K., 2010. Bridging the Divide between Neuroprosthetic Design, Tissue Engineering and Neurobiology. *Frontiers in Neuroengineering*, 2, pp.1–19.

- Lebedev, M.A. & Nicolelis, M.A.L., 2006. Brain–machine interfaces: past, present and future. *Trends in Neurosciences*, 29(9), pp.536–546.
- Lemon, R.N. et al., 2004. Direct and indirect pathways for corticospinal control of upper limb motoneurons in the primate. In *Progress in Brain Research*. Progress in Brain Research. Elsevier, pp. 263–279.
- Łęski, S. et al., 2013. Frequency dependence of signal power and spatial reach of the local field potential. *PLoS Computational Biology*, 9(7), p.e1003137.
- Leuthardt, E.C. et al., 2004. A brain–computer interface using electrocorticographic signals in humans. *Journal of Neural Engineering*, 1(2), pp.63–71.
- Levine, S.P. et al., 2000. A direct brain interface based on event-related potentials. *IEEE Transactions on Rehabilitation Engineering*, 8(2), pp.180–185.
- Logothetis, N.K., 2003. The underpinnings of the BOLD functional magnetic resonance imaging signal. *Journal of Neuroscience*, 23(10), pp.3963–3971.
- Markowitz, D.A. et al., 2011. Optimizing the decoding of movement goals from local field potentials in macaque cortex. *Journal of Neuroscience*, 31(50), pp.18412–18422.
- McFarland, D.J. et al., 2008. Emulation of computer mouse control with a noninvasive brain–computer interface. *Journal of Neural Engineering*, 5(2), pp.101–110.
- Mehring, C. et al., 2004. Comparing information about arm movement direction in single channels of local and epicortical field potentials from monkey and human motor cortex. *Journal of Physiology - Paris*, 98(4-6), pp.498–506.
- Miall, R.C., Weir, D.J. & Stein, J.F., 1993. Intermittency in human manual tracking tasks. *Journal of motor behavior*, 25(1), pp.53–63.
- Moritz, C.T. & Fetz, E.E., 2011. Volitional control of single cortical neurons in a brain–machine interface. *Journal of Neural Engineering*, 8(2), p.025017.
- Moritz, C.T., Perlmutter, S.I. & Fetz, E.E., 2008. Direct control of paralysed muscles by cortical neurons. *Nature*, 456(7222), pp.639–642.
- Nauhaus, I. et al., 2012. Robustness of traveling waves in ongoing activity of visual cortex. *Journal of Neuroscience*, 32(9), pp.3088–3094.
- Nauhaus, I. et al., 2009. Stimulus contrast modulates functional connectivity in visual cortex. *Nature Neuroscience*, 12(1), pp.70–76.
- NSCISC, 2017. National Spinal Cord Injury Statistical Center, Facts and Figures at a Glance. *National Spinal Cord Injury Statistical Center*. Available at: <https://www.nscisc.uab.edu/> [Accessed October 21, 2017].
- O'Leary, J.G. & Hatsopoulos, N.G., 2006. Early visuomotor representations revealed from evoked local field potentials in motor and premotor cortical areas. *Journal of Neurophysiology*, 96(3), pp.1492–1506.

- Okun, M., Naim, A. & Lampl, I., 2010. The subthreshold relation between cortical local field potential and neuronal firing unveiled by intracellular recordings in awake rats. *Journal of Neuroscience*, 30(12), pp.4440–4448.
- Pendegrass, C.J. et al., 2008. Sealing the skin barrier around transcutaneous implants: in vitro study of keratinocyte proliferation and adhesion in response to surface modifications of titanium alloy. *The Bone and Joint Journal*, 90(1), pp.114–121.
- Peng, C.-C., Xiao, Z. & Bashirullah, R., 2009. Toward energy efficient neural interfaces. *IEEE Transactions on Bio-medical Engineering*, 56(11 Pt 2), pp.2697–2700.
- Penttonen, M., & Buzsáki, G., 2003. Natural logarithmic relationship between brain oscillators. *Thalamus Relat. Syst.*, 2, pp.145–152.
- Perge, J.A. et al., 2013. Intra-day signal instabilities affect decoding performance in an intracortical neural interface system. *Journal of Neural Engineering*, 10(3), p.036004.
- Perreault, E.J., Kirsch, R.F. & Acosta, A.M., 1999. Multiple-input, multiple-output system identification for characterization of limb stiffness dynamics. *Biological cybernetics*, 80(5), pp.327–337.
- Pesaran, B. et al., 2002. Temporal structure in neuronal activity during working memory in macaque parietal cortex. *Nature Neuroscience*, 5(8), pp.805–811.
- Pfurtscheller, G. et al., 2003. “Thought” control of functional electrical stimulation to restore hand grasp in a patient with tetraplegia. *Neuroscience letters*, 351(1), pp.33–36.
- Polikov, V.S., Tresco, P.A. & Reichert, W.M., 2005. Response of brain tissue to chronically implanted neural electrodes. *Journal of Neuroscience Methods*, 148(1), pp.1–18.
- Rasch, M.J. et al., 2008. Inferring Spike Trains From Local Field Potentials. *Journal of Neurophysiology*, 99(3), pp.1461–1476.
- Rasch, M.J., Logothetis, N.K. & Kreiman, G., 2009. From Neurons to Circuits: Linear Estimation of Local Field Potentials. *Journal of Neuroscience*, 29(44), pp.13785–13796.
- Ray, S. & Maunsell, J.H.R., 2011. Network rhythms influence the relationship between spike-triggered local field potential and functional connectivity. *Journal of Neuroscience*, 31(35), pp.12674–12682.
- Ray, S. & Maunsell, J.H.R., 2014. Do gamma oscillations play a role in cerebral cortex? *Trends in Cognitive Sciences*, 19(2), pp.78–85.
- Rickert, J. et al., 2005. Encoding of Movement Direction in Different Frequency Ranges of Motor Cortical Local Field Potentials. *Journal of Neuroscience*, 25(39), pp.8815–8824.
- Rosenberg, J.R. et al., 1989. The Fourier approach to the identification of functional coupling between neuronal spike trains. *Progress in biophysics and molecular biology*, 53(1), pp.1–31.
- Rouse, A.G. & Schieber, M.H., 2015. Advancing brain-machine interfaces: moving beyond linear state space models. *Frontiers in systems neuroscience*, 9, p.108.

- Rubino, D., Robbins, K.A. & Hatsopoulos, N.G., 2006. Propagating waves mediate information transfer in the motor cortex. *Nature Neuroscience*, 9(12), pp.1549–1557.
- Sadtler, P.T. et al., 2014. Neural constraints on learning. *Nature*, 512(7515), pp.423–426. Available at: <https://www.ncbi.nlm.nih.gov/pmc/articles/PMC4393644/>.
- Scheid, M.R., Flint, R.D. & Wright, Z.A., 2013. Long-term, stable behavior of local field potentials during brain machine interface use. In Conference proceedings: Engineering in Medicine and Biology Society (EMBC), 2013 35th Annual International Conference of the IEEE. Osaka, pp. 307–310.
- Schwartz, A.B. et al., 2006. Brain-Controlled Interfaces: Movement Restoration with Neural Prosthetics. *Neuron*, 52(1), pp.205–220.
- Serruya, M.D. et al., 2002. Instant neural control of a movement signal. *Nature*, 416(6877), pp.141–142.
- Simeral, J.D. et al., 2011. Neural control of cursor trajectory and click by a human with tetraplegia 1000 days after implant of an intracortical microelectrode array. *Journal of Neural Engineering*, 8(2), p.025027.
- Slutzky, M.W. et al., 2011. Decoding the rat forelimb movement direction from epidural and intracortical field potentials. *Journal of Neural Engineering*, 8(3), p.036013.
- So, K. et al., 2014. Subject-specific modulation of local field potential spectral power during brain-machine interface control in primates. *Journal of Neural Engineering*, 11(2), p.026002.
- Spinal Research, 2017. Spinal Research. *International Spinal Research Trust*. Available at: <https://www.spinal-research.org/> [Accessed October 21, 2017].
- Srinivasan, R., Nunez, P.L. & Silberstein, R.B., 1998. Spatial filtering and neocortical dynamics: estimates of EEG coherence. *IEEE Transactions on Bio-medical Engineering*, 45(7), pp.814–826.
- Stavisky, S.D. et al., 2015. A high performing brain-machine interface driven by low-frequency local field potentials alone and together with spikes. *Journal of Neural Engineering*, 12(3), p.036009.
- Steriade, M., Timofeev, I. & Grenier, F., 2001. Natural waking and sleep states: a view from inside neocortical neurons. *Journal of Neurophysiology*, 85(5), pp.1969–1985.
- Sun, T., Xie, X. & Wang Z., 2013. Design challenges of wireless power transfer for medical microsystems. *IEEE International Wireless Symposium (IWS), 2013*, Beijing, pp.1–4.
- Suner, S. et al., 2005. Reliability of signals from a chronically implanted, silicon-based electrode array in non-human primate primary motor cortex. *IEEE Transactions on Neural Systems and Rehabilitation Engineering*, 13(4), pp.524–541.
- Taylor, D.M., Tillery, S.I.H. & Schwartz, A.B., 2002. Direct cortical control of 3D neuroprosthetic devices. *Science*, 296(5574), pp.1829–1832.

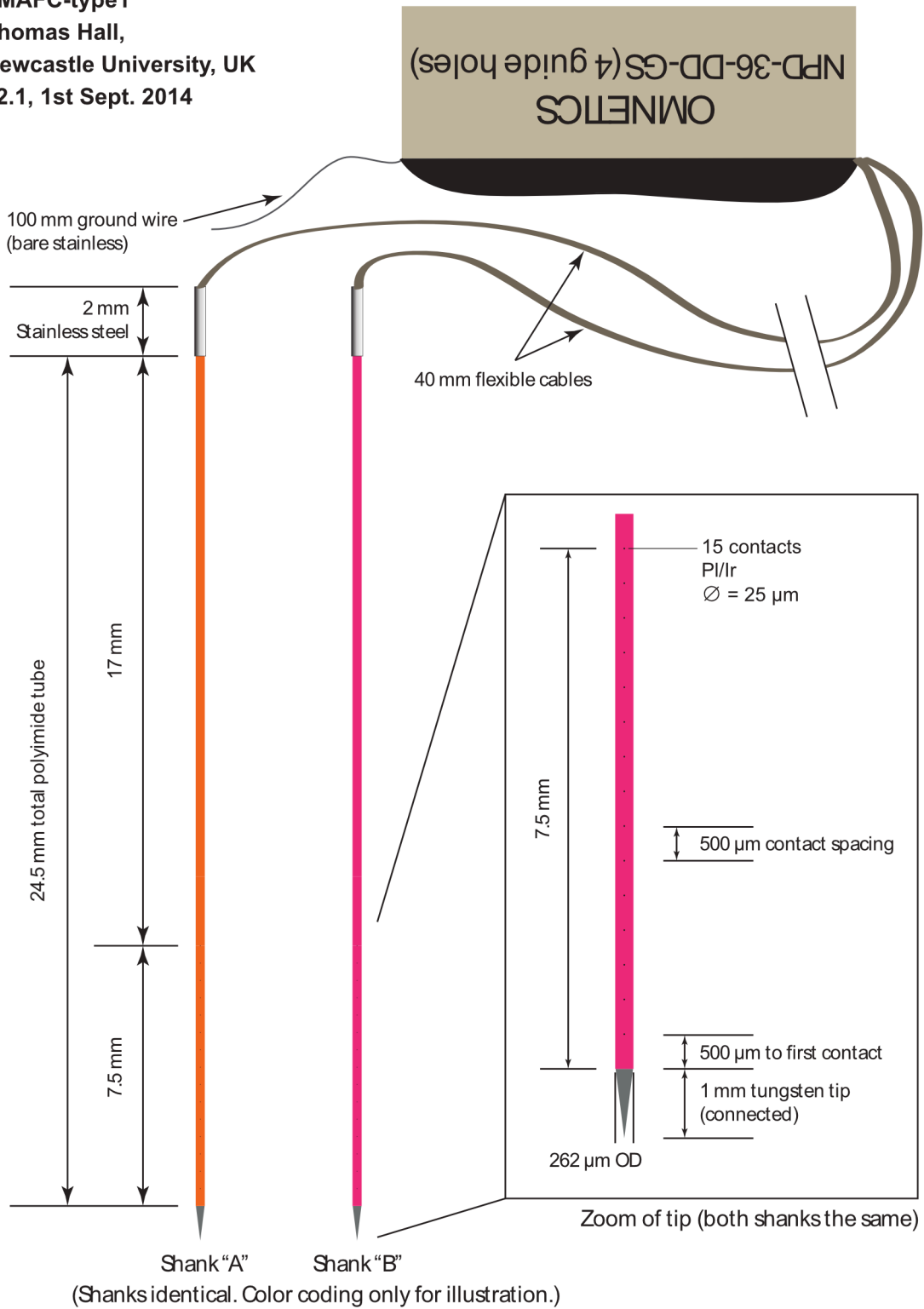
- Tseng, P., Chang, Y-T., Fang, C-F., Liang, W-K. & Juan C-H., 2016. The critical role of phase difference in gamma oscillation within the temporoparietal network for binding visual working memory. *Scientific Reports*, 6, Article number: 32138.
- Velliste, M. et al., 2008. Cortical control of a prosthetic arm for self-feeding. *Nature*, 453(7198), pp.1098–1101.
- Waldert, S. et al., 2008. Hand movement direction decoded from MEG and EEG. *Journal of Neuroscience*, 28(4), pp.1000–1008.
- Waldert, S., Lemon, R.N. & Kraskov, A., 2013. Influence of spiking activity on cortical local field potentials. *Journal of Physiology*, 591(21), pp.5291–5303.
- Wang, D. et al., 2014. Long-term decoding stability of local field potentials from silicon arrays in primate motor cortex during a 2D center out task. *Journal of Neural Engineering*, 11(3), p.036009.
- Wessberg, J. et al., 2000. Real-time prediction of hand trajectory by ensembles of cortical neurons in primates. *Nature*, 408(6810), pp.361–365.
- Westwick, D.T. et al., 2006. Identification of multiple-input systems with highly coupled inputs: application to EMG prediction from multiple intracortical electrodes. *Neural computation*, 18(2), pp.329–355.
- WHO, 2013. Spinal cord injury: Factsheet No. 384. *World Health Organization*. Available at: <http://www.who.int/mediacentre/factsheets/fs384/en/> [Accessed October 21, 2017].
- Witham, C.L. & Baker, S.N., 2012. Coding of digit displacement by cell spiking and network oscillations in the monkey sensorimotor cortex. *Journal of Neurophysiology*, 108(12), pp.3342–3352.
- Xing, D., Yeh, C.-I. & Shapley, R.M., 2009. Spatial spread of the local field potential and its laminar variation in visual cortex. *Journal of Neuroscience*, 29(37), pp.11540–11549.
- Young, N.A., Collins, C.E. & Kaas, J.H., 2013. Cell and neuron densities in the primary motor cortex of primates. *Frontiers in neural circuits*, 7, p.30.
- Zanos, S. et al., 2012. Relationships between spike-free local field potentials and spike timing in human temporal cortex. *Journal of Neurophysiology*, 107(7), pp.1808–1821.
- Zanos, S. et al., 2011. The Neurochip-2: an autonomous head-fixed computer for recording and stimulating in freely behaving monkeys. *IEEE Transactions on Neural Systems and Rehabilitation Engineering*, 19(4), pp.427–435.
- Zhang, D. 2014. Ultra-low-power analog-to-digital converters for medical applications. *Linköping University Institute of Technology*, Doctoral Dissertation.
- Zimmermann, J.B., Seki, K. & Jackson, A., 2011. Reanimating the arm and hand with intraspinal microstimulation. *Journal of Neural Engineering*, 8(5), p.054001.

# Appendices

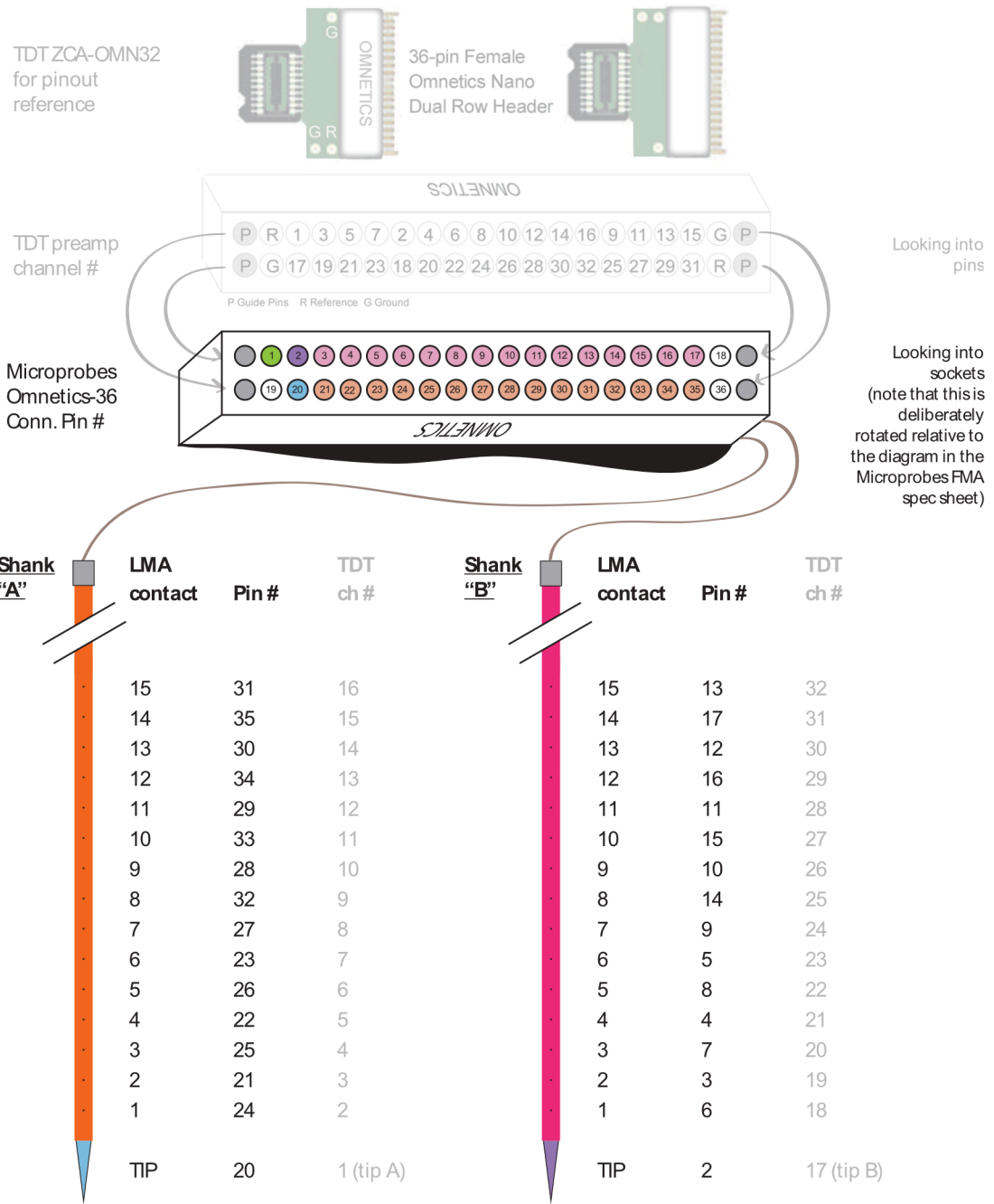
## **Appendix I: Specifications of dual “Long”-shank LMA**

- The following designs were sent to: Microprobes For Life Science, 18247 Flower Hill Way D, Gaithersburg, MD 20879, USA
- They were produced by Brian and Martin Bak of Microprobes, to our specifications.
- Impedances after implantation were typically in the range 300–700 k $\Omega$  at 1000 Hz.

LMAFC-type1  
Thomas Hall,  
Newcastle University, UK  
v2.1, 1st Sept. 2014



**Pinout Specification of LMAFC-type1**  
**Thomas Hall, Newcastle University, UK**  
**v2.1, 1st Sept. 2014**



Single ground wire to pin #1. No reference wires. (Pins 18, 19 and 36 deliberately empty.)

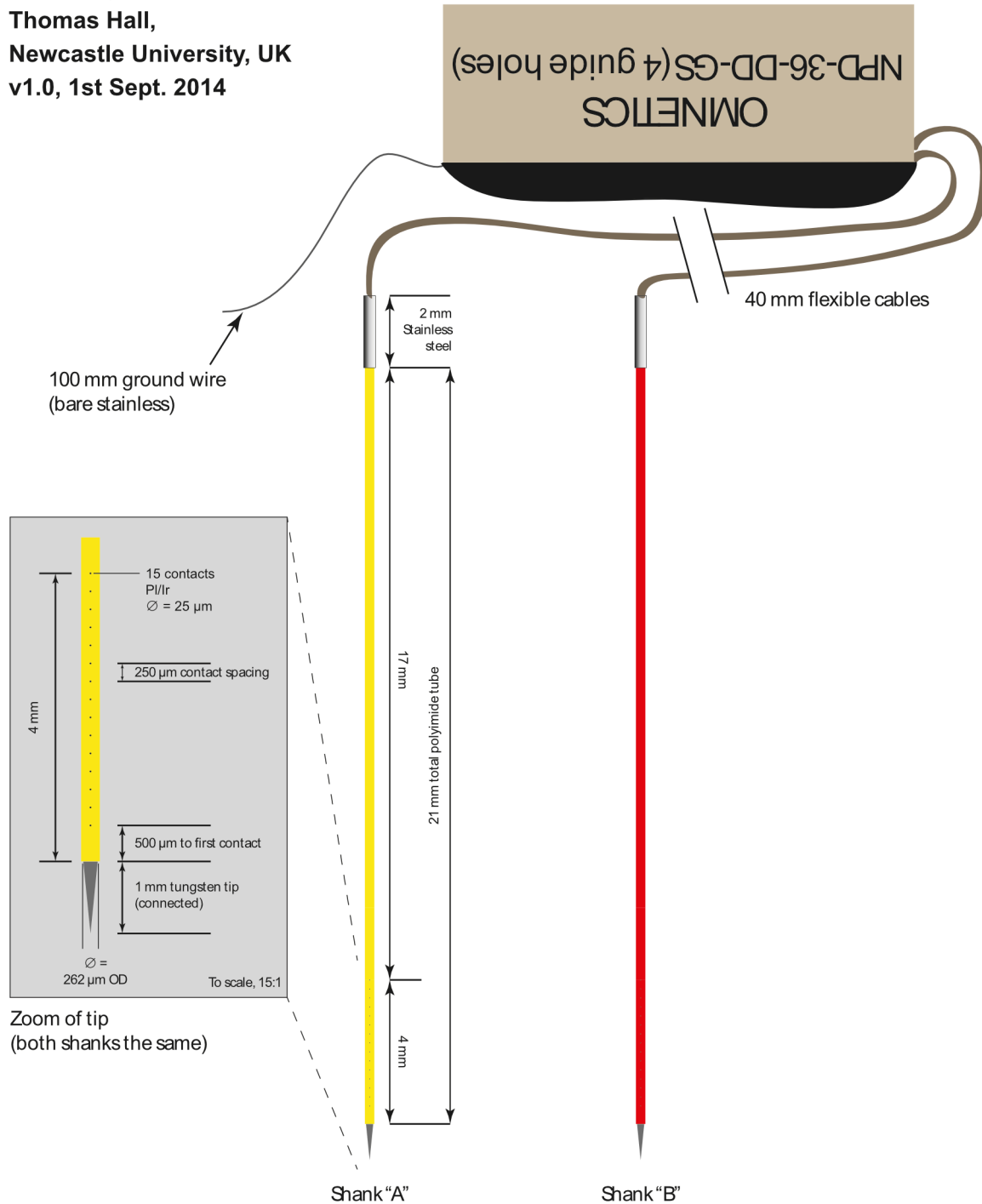
## Appendix II: Specifications of dual “Short”-shank LMA

- Production and approximate impedances, as above.

LMAFC-type4

Thomas Hall,  
Newcastle University, UK  
v1.0, 1st Sept. 2014

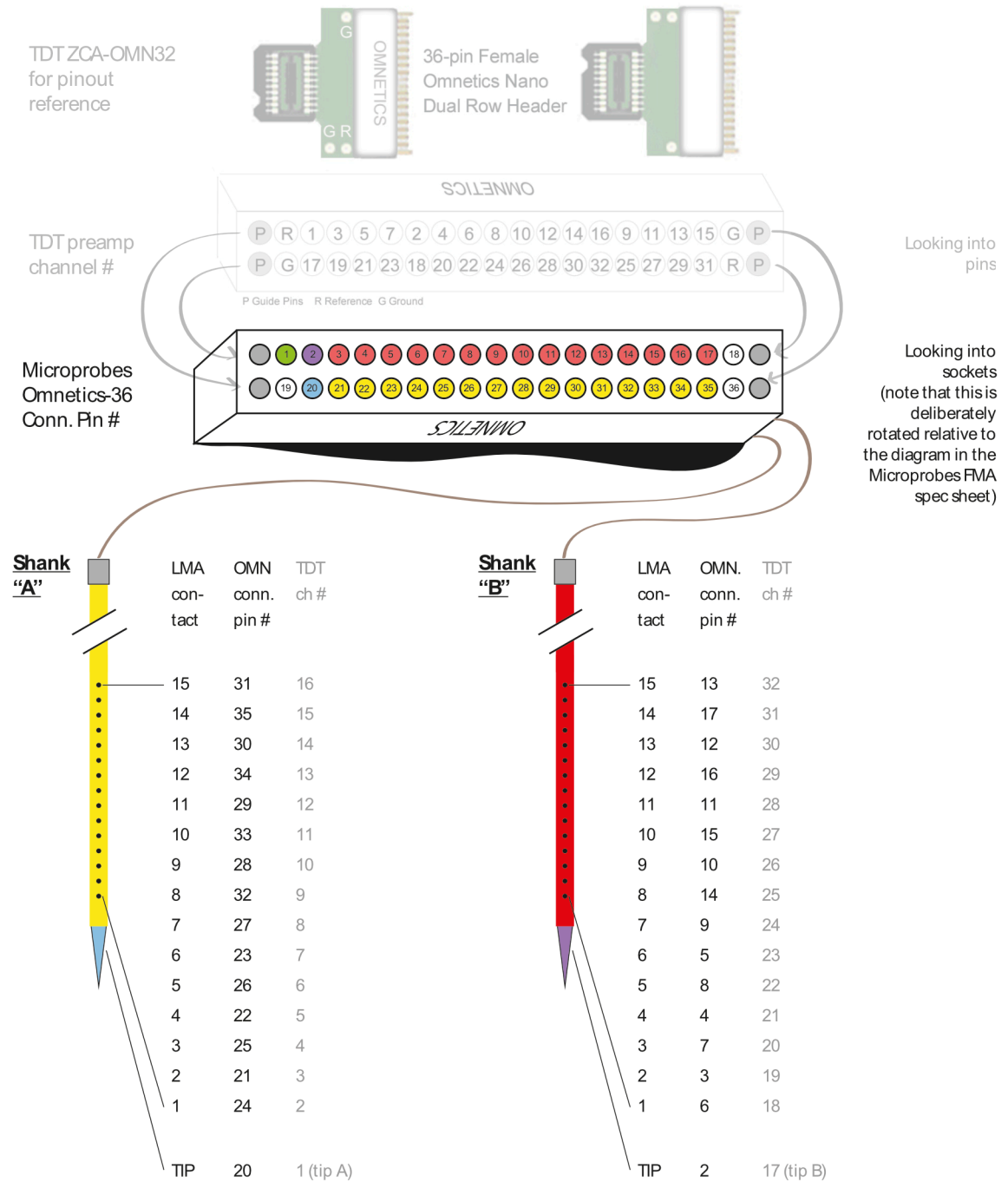
To scale, 7.5:1



Color coding only for illustration. Both shanks identical.

**Pinout specification for LMAFC-type4**  
**Thomas Hall, Newcastle University, UK**  
**v1.0, 1st Sept. 2014**

Not to scale



Single ground wire to pin #1. No reference wires. (Pins 18, 19 and 36 deliberately empty.)



# Indices

## Index of acronyms and abbreviations

<b>Abbreviation</b>	<i>Page where first defined:</i>
1-D/2-D/3-D; One/two/three-dimensional .....	22
AC, Alternating current .....	31
ANOVA; Analysis of variance .....	77
BCI; Brain-computer interface .....	1
BMI; Brain-machine interface .....	1
CED, Cambridge Electronic Design (recording systems) .....	30
CNS; Central nervous system .....	1
DOF; Degree of freedom .....	91
ECoG, Electrocortico-gram/-graphy (dural surface) .....	13
EEG, Electroencephalo-gram/-graphy (scalp surface) .....	3
EMG, Electromyo-gram/-graphy .....	28
GABA <sub>B</sub> ; <i>gamma</i> -Aminobutyric acid receptor type B .....	57
jPCA; A variant of PCA, which explicitly looks for planes in the data with rotational tendency .....	109
<i>lf</i> -LFP, Low-frequency local field potential (< 5 Hz) .....	13
LFP, Local field potential .....	6
M1, Primary motor cortex .....	3
MIMO; Multiple-input, multiple-output (model) .....	40
MRI, Magnetic resonance imaging .....	26
PC(A); Principal component (analysis) .....	46
s.d.; Standard deviation .....	48
s.e.m.; Standard error of the mean .....	39
SNR, Signal-to-noise ratio .....	7
SRSP; Spike-related slow potential .....	39

STA, Spike-triggered average.....	37
TDT, Tucker-Davis Technologies (recording systems).....	30
TMI; Torque modulation index.....	81

## Conventions for mathematical variables

$x(t)$ , (italic); Scalar variable (or function of time)
$\mathbf{x}(t)$ , (bold lower-case); Vector variable
$\mathbf{X}$ , (bold upper-case); Matrix variable
$x \in \mathbb{R}$ , (blackboard bold); Number set (e.g. $x$ is a member of the real number set)
$\bar{x}$ , (bar modifier); Mean value of variable
$\dot{x}$ , (dot modifier); First derivative
$\hat{a}(t)$ , (hat modifier); Estimated variable from model
$ a $ , (pipe brackets); Absolute value of variable
$\mathbf{a}_{\text{val}}$ , (subscript 'val'); Indicates validation data.

## Index of common terms

Common Term	Page where first defined:
$a'_n$ ; Areal velocity component (AVC) calculated from a pair of input signals.....	115
$\mathbf{a}_q(t)$ ; Scalar magnitude (signed) of the areal velocity of particle $q$ in state space.....	104
$c$ , Cursor position (percentage of screen).....	23
$C(\tau)$ , Spike-triggered average function (Volts), in timebase $\tau$ .....	37
$D$ ; Receiver-operating characteristic (ROC) discrimination index.....	124
$F_{i,j}$ ; F-statistic from ANOVA, with degrees of freedom within and between groups as subscript, respectively.....	78
$\mathbf{H}(\tau)$ ; $Q$ -by- $P$ finite impulse response filter kernel matrix.....	40
$\mathbf{h}'_p(\tau)$ ; Vector of six filter kernels for estimating neuron $p$ .....	47
$h_{pq}(\tau)$ ; Individual element of $\mathbf{H}(\tau)$ , with matrix location $(p, q)$ .....	41

<b>J</b> ; Projection matrix produced by jPCA. ....	111
<b>K</b> ; Matrix output from areal velocity component (AVC) analysis algorithm .....	117
$\hat{\mathbf{M}}$ ; Estimated transformation matrix describing linear dynamical system in jPCA.....	110
$\mathbf{M}_p$ ; <i>lf</i> -LFP reprojection matrix for estimating neuron $p$ .....	48
$p$ (decimal); Probability of Type 1 error (range 0 to 1).....	41
$p$ (index); Index of neuron in model. $p = 1, \dots, P$ .....	47
$P$ ; Number of neurons in model .....	40
$q$ ; Index of LFP in model. $q = 1, \dots, Q$ .....	40
$Q$ ; Number of LFPs in model. ....	40
$r$ (-value); Pearson's correlation coefficient .....	42
$\mathbf{s}_p(t)$ ; 'Source estimate' vector for $p^{\text{th}}$ neuron.....	48
$T$ , Duration of the recording (seconds).....	37
$T_y$ ; $Y$ -axis (downward) torque at the wrist .....	119
$\mathbf{v}_\varrho(t)$ ; 2-d velocity vector of particle $\varrho$ in state space .....	103
$\hat{x}(t)$ , Estimated neuronal firing rate function (Hertz), from model .....	24
$\mathbf{x}(t)$ , Multichannel neuronal firing rate vector .....	40
$x(t)$ ; Actual neuronal firing rate function (Hertz) .....	23
$\mathbf{x}_\varrho(t)$ ; 2-d position vector of particle $\varrho$ in state space .....	103
$y(t)$ , Local field potential waveform function (Volts) .....	37
$\hat{\mathbf{y}}(t)$ , Multichannel estimated <i>lf</i> -LFP vector, from model.....	41
$\mathbf{y}(t)$ , Multichannel LFP waveform vector .....	40
$\mathbf{y}'_p(t)$ ; 'Source projection' vector of LFP data for estimation of neuron $p$ .....	48
$\mathbf{z}(t)$ ; Principal component projection of the <i>lf</i> -LFP space (where relevant) .....	116
$\boldsymbol{\kappa}_p(\tau)$ , Inverse filter kernels for estimating firing rates from 'source projections' .....	48
$\lambda$ ; Decay constant (seconds) .....	23
$\varrho$ ; Label for a theoretical particle in higher dimensional LFP space.....	102
$\sigma$ ; Proportion of spikes retained in simulation of noisy spike trains (%). ....	75
$\tau$ , Time around spike event (seconds).....	37